University of Alaska

Coastal Marine Institute

Wind Field Representations and Their Effect on Shelf Circulation Models: A Case Study in the Chukchi Sea

Andrey Yu. Proshutinsky, Principal Investigator
University of Alaska Fairbanks

Final Report

February 2000

OCS Study MMS 2000-011

This study was funded in part by the U.S. Department of the Interior, Minerals Management Service (MMS), through Cooperative Agreement No. 14-35-01-98-CA-30909, Task Order No. 14194, between the MMS, Alaska Outer Continental Shelf Region, and the University of Alaska Fairbanks.

OCS Study MMS 2000-0011

Final Report

Wind Field Representations and Their Effect on Shelf Circulation Models: A Case Study in the Chukchi Sea

by

Andrey Yu. Proshutinsky, Principal Investigator
Tatiana Proshutinsky
Thomas J. Weingartner

Institute of Marine Science
University of Alaska Fairbanks
Fairbanks, AK 99775-7220

E-mail: prosh@ims.uaf.edu

February 2000

Table of Contents

List of Tables iv
List of Figures v
Abstract 1
1.0 Introduction 2
2.0 Sources of Atmospheric Pressure Data 3
  2.1 NCAR Data 3
  2.2 FNOC Data 3
  2.3 ECMWF 3
  2.4 Sources of Observational Data 4
    2.4.1 Observed wind data 4
    2.4.2 Observed buoy motion 4
    2.4.3 Observed ocean currents 4
3.0 Methods 5
  3.1 The 2-D Coupled Ice–Water Model 5
    3.1.1 Model equations 5
    3.1.2 Initial and boundary conditions 8
  3.2 The 3-D Ocean Model 9
  3.3 Simulation of the Surface Buoy Motion 9
  3.4 Data for the Models 9
4.0 Results 10
  4.1 Comparison Among the NCAR, FNOC, and ECMWF Data Sets 10
    4.1.1 Atmospheric pressure 10
    4.1.2 Geostrophic wind 10
  4.2 Comparison Between Observed and Simulated Winds 10
    4.2.1 Barrow 10
    4.2.2 Kotzebue 14
  4.3 Observed and Simulated Buoy Drift 14
  4.4 Observed and Simulated Currents 17
  4.5 Bering Strait Water Transport 20
  4.6 Results of Circulation Simulation Using a 3-D Barotropic Model 20
  4.7 Seasonal Variability 22
  4.8 Comparisons of Water Trajectories 23
5.0 Conclusions 24
6.0 Recommendations 24
Acknowledgements 25
References 25
Figures 27
Appendix. Project-Related Publications and Presentations 136

List of Tables

Table 1. Moorings in the Chukchi Sea 5

Table 2. Coefficients of correlation and root mean square errors among NCAR, NFOC, and ECMWF sea level atmospheric field data in 1991–1992 12

Table 3. Coefficients of correlation and root mean square errors among NCAR, FNOC, and ECMWF geostrophic winds in 1991–1992 13

Table 4. Results of simulation of buoy drift in 1992 using the Thorndike–Colony empirical model 15

Table 5. Results of simulation of buoy drift in 1991 using the Thorndike–Colony empirical model 15

Table 6. Results of simulation buoy drift in 1991 using a 2-D coupled ice–ocean model 16

Table 7. Results of simulation buoy drift in 1992 using a 2-D coupled ice–ocean model 16

Table 8a. Comparison between observed and simulated annual mean currents in 1991–1992 17

Table 8b. Comparison between observed and simulated annual mean currents in 1991–1992 18

Table 9a. Results of simulated currents using a 2-D coupled ice–ocean model. Standard deviation 18

Table 9b. Results of simulation of currents using a 2-D coupled ice–ocean model. Root mean square error 19

Table 9c. Results of simulation of currents using a 2-D coupled ice–ocean model. Correlation coefficient 19

Table 10a. Comparison between observed and simulated 3-D annual mean bottom currents in 1991–1992. 3-D currents are averaged in the vertical direction 20

Table 10b. Comparison between observed and simulated 3-D annual mean currents 1991–1992. 3-D currents are averaged in the vertical direction 21

Table 11a. Bottom velocities. Results of simulation currents using the 3-D ocean barotropic model. Standard deviations 21

Table 11b. Results of simulation of currents using the 3-D coupled ice–ocean model. Root mean square errors 21

Table 11c. Results of simulation of currents using the 3-D barotropic model. Correlation coefficients 22

Figure Legends

Figure 1. Bathymetric map of the Chukchi Sea 27

Figure 2. Location of moorings used for comparison with the model results 27

Figure 3. NCAR octagonal grid (47 x 51) for sea surface atmospheric pressure fields. Solid, thick, black line shows boundaries of the area under research 29

Figure 4. ECMWF and FNOC (13 x 41) 2.5° resolution grid for sea surface atmospheric pressure fields 30

Figure 5. ECMWF 1.125° resolution grid for sea surface atmospheric pressure fields 30

Figure 6. Spatial distribution of correlation coefficients and spatial distribution of RMS among NCAR, FNOC, and ECMWF sea level atmospheric pressure fields in January of 1991 31

Figure 7. Spatial distribution of correlation coefficients and spatial distribution of RMS among NCAR, FNOC, and ECMWF sea level atmospheric pressure fields in February of 1991 32

Figure 8. Spatial distribution of correlation coefficients and spatial distribution of RMS among NCAR, FNOC, and ECMWF sea level atmospheric pressure fields in March of 1991 33

Figure 9. Spatial distribution of correlation coefficients and spatial distribution of RMS among NCAR, FNOC, and ECMWF sea level atmospheric pressure fields in April of 1991 34

Figure 10. Spatial distribution of correlation coefficients and spatial distribution of RMS among NCAR, FNOC, and ECMWF sea level atmospheric pressure fields in May of 1991 35

Figure 11. Spatial distribution of correlation coefficients and spatial distribution of RMS among NCAR, FNOC, and ECMWF sea level atmospheric pressure fields in June of 1991 36

Figure 12. Spatial distribution of correlation coefficients and spatial distribution of RMS among NCAR, FNOC, and ECMWF sea level atmospheric pressure fields in July of 1991 37

Figure 13. Spatial distribution of correlation coefficients and spatial distribution of RMS among NCAR, FNOC, and ECMWF sea level atmospheric pressure fields in August of 1991 38

Figure 14. Spatial distribution of correlation coefficients and spatial distribution of RMS among NCAR, FNOC, and ECMWF sea level atmospheric pressure fields in September of 1991 39

Figure 15. Spatial distribution of correlation coefficients and spatial distribution of RMS among NCAR, FNOC, and ECMWF sea level atmospheric pressure fields in October of 1991 40

Figure 16. Spatial distribution of correlation coefficients and spatial distribution of RMS among NCAR, FNOC, and ECMWF sea level atmospheric pressure fields in November of 1991 41

Figure 17. Spatial distribution of correlation coefficients and spatial distribution of RMS among NCAR, FNOC, and ECMWF sea level atmospheric pressure fields in December of 1991 42

Figure 18. Spatial distribution of correlation coefficients and spatial distribution of RMS among NCAR, FNOC, and ECMWF speed of geostrophic winds in January of 1991 43

Figure 19. Spatial distribution of correlation coefficients and spatial distribution of RMS among NCAR, FNOC, and ECMWF speed of geostrophic winds in February of 1991 44

Figure 20. Spatial distribution of correlation coefficients and spatial distribution of RMS among NCAR, FNOC, and ECMWF speed of geostrophic winds in March of 1991 45

Figure 21. Spatial distribution of correlation coefficients and spatial distribution of RMS among NCAR, FNOC, and ECMWF speed of geostrophic winds in April of 1991 46

Figure 22. Spatial distribution of correlation coefficients and spatial distribution of RMS among NCAR, FNOC, and ECMWF speed of geostrophic winds in May of 1991 47

Figure 23. Spatial distribution of correlation coefficients and spatial distribution of RMS among NCAR, FNOC, and ECMWF speed of geostrophic winds in June of 1991 48

Figure 24. Spatial distribution of correlation coefficients and spatial distribution of RMS among NCAR, FNOC, and ECMWF speed of geostrophic winds in July of 1991 49

Figure 25. Spatial distribution of correlation coefficients and spatial distribution of RMS among NCAR, FNOC, and ECMWF speed of geostrophic winds in August of 1991 50

Figure 26. Spatial distribution of correlation coefficients and spatial distribution of RMS among NCAR, FNOC, and ECMWF speed of geostrophic winds in September of 1991 51

Figure 27. Spatial distribution of correlation coefficients and spatial distribution of RMS among NCAR, FNOC, and ECMWF speed of geostrophic winds in October of 1991 52

Figure 28. Spatial distribution of correlation coefficients and spatial distribution of RMS among NCAR, FNOC, and ECMWF speed of geostrophic winds in November of 1991 53

Figure 29. Spatial distribution of correlation coefficients and spatial distribution of RMS among NCAR, FNOC, and ECMWF speed of geostrophic winds in December of 1991 54

Figure 30. Seasonal variability of observed monthly mean wind speed at Barrow. Data are averaged for the period 1948–1989. Numbers (1, 2, ... 12) depict months 55

Figure 31. Same as Figure 30 except for NCAR simulated wind 56

Figure 32. Same as Figure 30 except for ECMWF simulated wind and period from 1991 through 1994 57

Figure 33. Same as Figure 30 except for FNOC simulated wind and period from 1991 through 1994 58

Figure 34. Time series of observed and simulated wind speed and wind direction at Barrow for 1991. Temporal resolution of the atmospheric fields is 12 hours 59

Figure 35. Same as Figure 34 except the temporal resolution between atmospheric fields is six hours 60

Figure 36. Times series of simulated ECMWF, NCAR, and FNOC wind at Barrow with a 12-hour temporal resolution for 1991 61

Figure 37. Seasonal variability of observed monthly mean wind speed at Kotzebue. Data are averaged for the period from 1945 through 1991. Numbers (1, 2, ... 12) depict months 62

Figure 38. Same as Figure 37 except for ECMWF simulated wind and period from 1991 through 1994 63

Figure 39. Same as Figure 37 except for FNOC simulated wind and period from 1991 through 1994 64

Figure 40. Same as Figure 37 except for NCAR simulated wind and period from 1946 through 1988 65

Figure 41. Time series of observed and simulated wind speed and wind direction at Kotzebue for 1991. Temporal resolution of the atmospheric fields is 12 hours 66

Figure 42. Times series of simulated ECMWF, NCAR, and FNOC wind at Kotzebue with a 12-hour temporal resolution for 1991 67

Figure 43. Ice surface buoy (International Arctic Buoy Program) trajectories in the Chukchi and Beaufort Sea in 1991. Numbers show buoy number at the beginning of each trajectory. The end of the trajectory is marked by the letter "E" 68

Figure 44. Same as Figure 43 for the year 1992 68

Figure 45. Observed and simulated components of the ice surface buoy drift. Buoy # 12782. Simulated ice drift is based on the Thorndike–Colony empirical model using NCAR atmospheric pressure fields 69

Figure 46. Same as Figure 45 except for FNOC atmospheric pressure data 70

Figure 47. Same as Figure 45 except for ECMWF atmospheric pressure data 71

Figure 48. Observed and simulated components of the ice surface buoy drift. Buoy # 12806. Simulated ice drift is based on Thorndike–Colony empirical model using NCAR atmospheric pressure fields 72

Figure 49. Same as Figure 48 except for FNOC atmospheric pressure data 73

Figure 50. Same as Figure 48 except for ECMWF atmospheric pressure data 74

Figure 51. Observed and simulated components of the ice surface buoy drift. Buoy # 12801. Simulated ice drift is based on Thorndike–Colony empirical model using NCAR atmospheric pressure fields 75

Figure 52. Same as Figure 51 except for FNOC atmospheric pressure data 76

Figure 53. Same as Figure 51 except for ECMWF atmospheric pressure data 77

Figure 54. Observed and simulated components of the ice surface buoy drift. Buoy # 12807 in 1991. Simulated ice drift is based on 2-D coupled ice–ocean model using FNOC atmospheric pressure fields 78

Figure 55. Same as Figure 54 for the year 1992 79

Figure 56. Same as Figure 54 except for buoy # 12820 in 1992 80

Figure 57. Time series of observed and simulated currents at the mooring BSE. Calculated velocities are obtained using 2-D coupled ice-ocean model and NCAR atmospheric pressure fields 81

Figure 58. Same as Figure 57 except for the FNOC atmospheric pressure data 82

Figure 59. Same as Figure 57 except for the ECMWF atmospheric pressure data 83

Figure 60. Comparison of FNOC- and ECMWF-based components of currents at mooring BSE 84

Figure 61. Time series of observed and simulated currents at the mooring BSN. Calculated velocities are obtained using 2-D coupled ice–ocean model and NCAR atmospheric pressure fields 85

Figure 62. Same as Figure 61 except for the FNOC atmospheric pressure data 86

Figure 63. Same as Figure 61 except for the ECMWF atmospheric pressure data 87

Figure 64. Comparison of FNOC- and ECMWF-based components of currents at mooring BSN 88

Figure 65. Time series of observed and simulated currents at mooring EP3. Calculated velocities are obtained using a 2-D coupled ice–ocean model and NCAR atmospheric pressure fields 89

Figure 66. Same as Figure 57 except for the FNOC atmospheric pressure data 90

Figure 67. Same as Figure 57 except for the ECMWF atmospheric pressure data 91

Figure 68. Comparison of FNOC- and ECMWF-based components of currents at mooring EP3 92

Figure 69. Time series of observed and simulated currents at mooring BP12. Calculated velocities are obtained using a 2-D coupled ice–ocean model and NCAR atmospheric pressure fields 93

Figure 70. Same as Figure 69 except for the FNOC atmospheric pressure data 94

Figure 71. Same as Figure 69 except for the ECMWF atmospheric pressure data 95

Figure 72. Comparison of FNOC- and ECMWF-based components of currents at mooring BP12 96

Figure 73. Time series of observed and simulated currents at mooring CP3. Calculated velocities are obtained using a 2-D coupled ice–ocean model and NCAR atmospheric pressure fields 97

Figure 74. Same as Figure 73 except for the FNOC atmospheric pressure data 98

Figure 75. Same as Figure 73 except for the ECMWF atmospheric pressure data 99

Figure 76. Comparison of FNOC- and ECMWF-based components of currents at mooring CP3 100

Figure 77. Daily Bering Strait simulated water transport (results of 2-D coupled ice–ocean model) based on ECMWF (solid line), FNOC (dotted line), and NCAR (dashed line) sea level atmospheric pressure fields 101

Figure 78. Time series of observed and simulated surface currents at mooring BSE. Calculated velocities obtained using a 3-D ocean barotropic model and ECMWF atmospheric pressure fields 102

Figure 79. Same as Figure 78 for mooring BSN 103

Figure 80. Same as Figure 78 for mooring AP18 104

Figure 81. Same as Figure 78 for mooring EP3 105

Figure 82. Same as Figure 78 for mooring BP12 106

Figure 83. Same as Figure 78 for mooring CP3 107

Figure 84. Time series of observed and simulated near bottom currents at mooring BSE. Calculated velocities obtained using 3-D ocean barotropic model and ECMWF atmospheric pressure fields 108

Figure 85. Same as Figure 84 for mooring BSN 109

Figure 86. Same as Figure 84 for mooring AP18 110

Figure 87. Same as Figure 84 for mooring EP3 111

Figure 88. Same as Figure 84 for mooring BP12 112

Figure 89. Same as Figure 84 for mooring CP3 113

Figure 90. Surface circulation and atmospheric pressure distribution in the Chukchi Sea in October 1991. Results of simulation using a 3-D barotropic model and NCAR atmospheric pressure data 114

Figure 91. Surface circulation and atmospheric pressure distribution in the Chukchi Sea in October 1991. Results of simulation using a 3-D barotropic model and FNOC atmospheric pressure data 114

Figure 92. Surface circulation and atmospheric pressure distribution in the Chukchi Sea in October 1991. Results of simulation using a 3-D barotropic model and ECMWF atmospheric pressure data 115

Figure 93. Surface circulation and atmospheric pressure distribution in the Chukchi Sea in November 1991. Results of simulation using a 3-D barotropic model and NCAR atmospheric pressure data 115

Figure 94. Surface circulation and atmospheric pressure distribution in the Chukchi Sea in November 1991. Results of simulation using a 3-D barotropic model and FNOC atmospheric pressure data 116

Figure 95. Surface circulation and atmospheric pressure distribution in the Chukchi Sea in November 1991. Results of simulation using a 3-D barotropic model and ECMWF atmospheric pressure data 116

Figure 96. Surface circulation and atmospheric pressure distribution in the Chukchi Sea in December 1991. Results of simulation using a 3-D barotropic model and NCAR atmospheric pressure data 117

Figure 97. Surface circulation and atmospheric pressure distribution in the Chukchi Sea in December 1991. Results of simulation using a 3-D barotropic model and FNOC atmospheric pressure data 117

Figure 98. Surface circulation and atmospheric pressure distribution in the Chukchi Sea in December 1991. Results of simulation using a 3-D barotropic model and ECMWF atmospheric pressure data 118

Figure 99. Surface circulation and atmospheric pressure distribution in the Chukchi Sea in January 1992. Results of simulation using a 3-D barotropic model and NCAR atmospheric pressure data 118

Figure 100. Surface circulation and atmospheric pressure distribution in the Chukchi Sea in January 1992. Results of simulation using 3-D a barotropic model and FNOC atmospheric pressure data 119

Figure 101. Surface circulation and atmospheric pressure distribution in the Chukchi Sea in January 1992. Results of simulation using a 3-D barotropic model and ECMWF atmospheric pressure data 119

Figure 102. Surface circulation and atmospheric pressure distribution in the Chukchi Sea in February 1992. Results of simulation using a 3-D barotropic model and NCAR atmospheric pressure data 120

Figure 103. Surface circulation and atmospheric pressure distribution in the Chukchi Sea in February 1992. Results of simulation using a 3-D barotropic model and FNOC atmospheric pressure data 120

Figure 104. Surface circulation and atmospheric pressure distribution in the Chukchi Sea in February 1992. Results of simulation using a 3-D barotropic model and ECMWF atmospheric pressure data 121

Figure 105. Surface circulation and atmospheric pressure distribution in the Chukchi Sea in April 1992. Results of simulation using a 3-D barotropic model and NCAR atmospheric pressure data 121

Figure 106. Surface circulation and atmospheric pressure distribution in the Chukchi Sea in April 1992. Results of simulation using a 3-D barotropic model and FNOC atmospheric pressure data 122

Figure 107. Surface circulation and atmospheric pressure distribution in the Chukchi Sea in April 1992. Results of simulation using a 3-D barotropic model and ECMWF atmospheric pressure data 122

Figure 108. Surface circulation and atmospheric pressure distribution in the Chukchi Sea in June 1992. Results of simulation using a 3-D barotropic model and NCAR atmospheric pressure data 123

Figure 109. Surface circulation and atmospheric pressure distribution in the Chukchi Sea in June 1992. Results of simulation using a 3-D barotropic model and FNOC atmospheric pressure data 123

Figure 110. Surface circulation and atmospheric pressure distribution in the Chukchi Sea in June 1992. Results of simulation using a 3-D barotropic model and ECMWF atmospheric pressure data 124

Figure 111. Bottom circulation and sea level (cm) distribution in the Chukchi Sea in November 1991. Results of simulation using a 3-D barotropic model and NCAR atmospheric pressure data 124

Figure 112. Bottom circulation and sea level (cm) distribution in the Chukchi Sea in November 1991. Results of simulation using a 3-D barotropic model and FNOC atmospheric pressure data 125

Figure 113. Bottom circulation and sea level (cm) distribution in the Chukchi Sea in November 1991. Results of simulation using a 3-D barotropic model and ECMWF atmospheric pressure data 125

Figure 114. Bottom circulation and sea level (cm) distribution in the Chukchi Sea in December 1991. Results of simulation using a 3-D barotropic model and NCAR atmospheric pressure data 126

Figure 115. Bottom circulation and sea level (cm) distribution in the Chukchi Sea in December 1991. Results of simulation using a 3-D barotropic model and FNOC atmospheric pressure data 126

Figure 116. Bottom circulation and sea level (cm) distribution in the Chukchi Sea in December 1991. Results of simulation using a 3-D barotropic model and ECMWF atmospheric pressure data 127

Figure 117. Bottom circulation and sea level (cm) distribution in the Chukchi Sea in January 1992. Results of simulation using a 3-D barotropic model and NCAR atmospheric pressure data 127

Figure 118. Bottom circulation and sea level (cm) distribution in the Chukchi Sea in January 1992. Results of simulation using a 3-D barotropic model and FNOC atmospheric pressure data 128

Figure 119. Bottom circulation and sea level (cm) distribution in the Chukchi Sea in January 1992. Results of simulation using a 3-D barotropic model and ECMWF atmospheric pressure data 128

Figure 120. Bottom circulation and sea level (cm) distribution in the Chukchi Sea in February 1992. Results of simulation using a 3-D barotropic model and NCAR atmospheric pressure data 129

Figure 121. Bottom circulation and sea level (cm) distribution in the Chukchi Sea in February 1992. Results of simulation using a 3-D barotropic model and FNOC atmospheric pressure data 129

Figure 122. Bottom circulation and sea level (cm) distribution in the Chukchi Sea in February 1992. Results of simulation using a 3-D barotropic model and ECMWF atmospheric pressure data 130

Figure 123. Simulated trajectories of water particles released in the Bering Strait on October 1, 1991. Solid, dotted, and dashed lines show trajectories of particles simulated using, respectively, FNOC, ECMWF, and NCAR atmospheric pressure data. Trajectories of particles moving with surface currents are shown. B is a releasing point. E, E1 and E2 denote locations of particles on September 29, 1992 for the FNOC, ECMWF and NCAR simulations, respectively 131

Figure 124. Same as Figure 123, for particles moving with vertically mean currents 132

Figure 125. Same as Figure 123, for particles moving with bottom currents 133

Figure 126. Simulated trajectories of water particles (moving with vertically averaged water velocities) released in the Bering Strait for anticyclonic circulation regimes of circulation (ACCR) in the left column (for years 1946–1952, 1957–1962, 1972–1979 and 1984–1988, respectively). In the right column the trajectories of parcels released in the Bering Strait in the years of cyclonic regime of circulation regime (CCR) are shown (1953–1956, 1963–1971, 1980–1983, and 1989–1996) 134

Figure 127. Same as Figure 126, for ice particles 135

Abstract

Arctic pollutant transport models use winds obtained from forecasts of surface atmospheric pressure fields. Uncertainties inherent in these forecast pressure fields lead to errors in the calculation of surface winds, and therefore, to errors in circulation-model results dependent upon them. We have investigated the differences among three nominally identical wind field representations derived from surface atmospheric pressure fields prepared by:

- the European Center for Medium Weather Range Forecasting (ECMWF),
- the U.S. Navy's Fleet Numerical Oceanography Center (FNOC), and
- the National Centers for Environmental Predictions and the National Center for Atmospheric Research (NCEP/NCAR).

We have analyzed:

- wind and surface atmospheric pressure data from the National Weather Service offices at Barrow, Alaska, and Kotzebue, Alaska, to examine differences between observed and estimated winds;
- ice-drifting buoy data from the International Arctic Buoy Program (IABP), to examine differences between observed and interpolated surface atmospheric pressures, and to examine differences between observed and simulated ice drift; and
- differences in shelf circulation, as predicted by 2-D and 3-D barotropic shelf circulation models when forced by the three wind field representations.

This study has demonstrated that ECMWF sea level atmospheric pressure data with a spatial resolution of 1.125° and a temporal resolution of six hours can be recommended as the best source of wind forcing data. The FNOC atmospheric pressure fields with a spatial resolution of 2.5° and a temporal resolution of six hours can be recommended as well, in the absence of ECMWF data. NCAR data with a spatial resolution of about 350 km and a temporal resolution of 12 hours can be used successfully for climatological simulations.

1.0 Introduction

Mean flow on the Chukchi shelf (Figure 1) is nominally northward (e.g., from the southern Chukchi Sea to the Arctic Ocean) and is forced by the mean sea level drop (secular pressure gradient) between the Pacific and Arctic oceans. This flow persists even though the mean winds are northeasterly and tend to establish an opposing pressure gradient and a southward oceanic flow. However, the circulation varies considerably on time scales ranging from days to interannual periods (Coachman et al., 1975; Aagaard, 1988; Coachman and Aagaard, 1988). Much of this flow variability is significantly coherent (in the statistical sense) with variations in the regional wind field (Weingartner and Proshutinsky, 1998). Our results (Weingartner and Proshutinsky, 1998) imply that a first-order description of the circulation field and its variability can be obtained using a barotropic model forced by winds and the secular pressure gradient. Models such as this are frequently used to predict pollutant transport.

With past CMI support we used an ocean circulation model developed by Proshutinsky (1986) and adapted for the Chukchi Sea shelf to explore the dynamics governing the Chukchi shelf circulation, and to examine, in a retrospective sense, the interannual circulation variability of this shelf. The model is a coupled ice–ocean two-dimensional (2-D), nonlinear barotropic model driven by winds and atmospheric pressure. Variants of this model have been used to study the Arctic Ocean's tides (Kowalik and Proshutinsky, 1994) and its large-scale, wind-driven circulation (Proshutinsky and Johnson, 1997). We reconfigured the model for application to the Chukchi Sea shelf with a grid size of 7 km, and we forced it with the surface winds calculated from the atmospheric pressure fields of the U.S. Navy's Fleet Numerical Oceanography Center (FNOC). These fields, prepared at six-hour intervals, are interpolated onto a 2.5° grid.

The results from this model, as with other models (Overland and Roach, 1987; Spaulding et al., 1987), depend to a sensitive degree on the forcing of the wind field (a surface boundary condition). One reviewer of our CMI-funded proposal recommended that we use the ECMWF (European Center for Medium Weather Range Forecasting) surface pressure fields and pressure fields that are being used by Rutgers University (RU) researchers to drive their circulation model. The latter fields provide input into the Minerals Management Service (MMS) oil spill risk analysis as an alternative estimate for the surface winds that force the model. This reviewer further suggested that the results from the model forced by the ECMWF winds be compared with those forced by FNOC and RU winds. Such a comparison would be particularly useful because the procedures for forecasting the pressure fields are different among the three sources of data; consequently, the three surface atmospheric pressure and wind fields, although nominally identical, could be quite different from one another. Circulation predictions based upon these atmospheric data sets would, therefore, also be quite different. By quantifying the differences among the three atmospheric or wind fields and the model results from these wind fields, we will better understand the uncertainties in pollutant transport models.

The winds used by the Rutgers modelers are computed from either the International Arctic Buoy Program or the NCEP/NCAR reanalysis fields. These fields are a product of an NCEP/NCAR reanalysis project, which is developing a hindcast numerical weather prediction model using all conventional meteorological observations. Therefore, instead of using Rutgers' wind data, which strongly depend on their model of the surface air boundary layer and are related to direct measurements of vertical air temperature stratification, we used the NCEP/NCAR (hereafter, NCAR) atmospheric pressure fields, and investigated the differences among three nominally identical wind field representations derived from surface atmospheric pressure fields prepared by ECMWF, FNOC, and NCAR weather centers.

We have analyzed wind data from the National Weather Service offices at Barrow and Kotzebue, Alaska, to examine differences between observed and estimated winds, and we have used ice-drifting buoy data from the International Arctic Buoy Program to examine differences between observed and simulated ice drift. Current-meter data (Figure 2) and differences in shelf circulation, as predicted by barotropic shelf circulation models when forced by the three wind fields, have also been investigated and analyzed.

This study provides a better understanding of the uncertainties in wind fields and the circulation predictions that rely on those wind fields. Major aspects of the Chukchi Sea circulation regime and its seasonal and interannual variability have been discussed by Weingartner and Proshutinsky (1998); here we have paid more attention to the quality of simulations and the accuracy of the obtained results. An additional goal of this project has been to improve the results of numerical simulations of the Chukchi Sea circulation. We have used the 3-D Princeton University Model (Blumberg and Mellor, 1983) for this purpose.

2.0 Sources of Atmospheric Pressure Data

2.1 NCAR Data

At least two data sets represent sea surface atmospheric pressure fields for the Northern Hemisphere. The first data set is on a CD-ROM prepared by the University of Washington in 1986. The last edition of the CD-ROM presents information for the period 1946–1993. This CD-ROM contains a selected subset of the National Meteorological Center's (NMC) Northern Hemisphere octagonal grid data, as archived at NCAR. This is an update of the original NMC grid point CD-ROM produced in 1986. The NMC octagonal grid is a 1977-point grid (Figure 3) whose points are equally spaced when viewed on a polar stereographic grid centered on the North Pole (spatial resolution 350 km). The data are recorded at 12-hour intervals.

A second data set, archived at NCEP/NCAR, can be obtained by ftp. The sea surface atmospheric pressure fields in this data set are the result of a modern reanalysis project. These data, covering the period from 1973 through 1997, are in the same format as the CD-ROM data.

2.2 FNOC Data

The FNOC data base contains the sea surface atmospheric pressure fields generated by the U.S. Navy's Fleet Numerical Oceanography Center. These fields, prepared at six-hour intervals, are interpolated onto a 2.5° grid (spherical coordinate system, see Figure 4). We obtained and used a subset of FNOC data covering the 1981–1995 period.

2.3 ECMWF Data

Important notice: ECMWF data sets can be used only by U.S. scientists working for the government or a university; by scientists visiting such U.S. institutions; or by Canadian scientists affiliated with University Corporation for Atmospheric Research (UCAR) member organizations. Users must sign and return a permission form before NCAR can process requests.

We used two data sets of sea surface atmospheric pressures from ECMWF. The first data set (ds111.1) is a high-resolution (1.125°) global surface analysis with six-hour intervals. The second (ds111.2) has 2.5° spatial resolution and 12-hour intervals. The original data sets, which are available from NCAR, cover a period from 1985 through 1997: ftp://ncardata.ucar.edu/datasets/ds111.1 . We obtained and used a subset of ECMWF data covering the 1991–1994 period.

2.4 Sources of Observational Data

The three data sets helped us to estimate the quality of the atmospheric pressure fields and their representations of wind conditions in the Chukchi Sea.

2.4.1 Observed wind data

We compared the computed winds with measurements of surface winds from the Barrow and Kotzebue meteorological stations. The atmospheric pressures and wind records for these areas are available from the state climatologist's data base at the University of Alaska Geophysical Institute. These wind measurements are collected at the coast, far from mountain ranges or hills, so they are relatively free from orographic influence (Schwerdtfegger, 1975; Pacific Northwest Laboratory, 1983).

Barrow station, which is well exposed to winds from all directions, represents conditions along the Chukchi Sea coast; it is the more reliable station, with observations averaging 24 per day. Kotzebue Sound is well represented by the Kotzebue National Weather Service station on the Baldwin Peninsula. This station is exposed to winds from all directions, averaging 21 observations per day during the summary period.

2.4.2 Observed buoy motion

Another source of observed data was the International Arctic Ocean Buoy Program (IABP, Thorndike and Colony, 1982). The surface-drifting buoys measure surface atmospheric pressure and their coordinates (as a measure of the ice-drift motion under wind forcing). These data, available for all years since 1979, are based on a 12-hour interval.

2.4.3 Observed ocean currents

The third source of information for the model calibration, and for indirect evaluation of the accuracy of the atmospheric pressure fields, was a measurement of ocean currents. Model winds can be calibrated indirectly in terms of the accuracy of simulated currents, but we used observations on current velocities obtained during several expeditions to the Chukchi Sea (Weingartner and Proshutinsky, 1998). A scheme showing the locations of the moorings is presented in Figure 2 and the information about these data is presented in Table 1.

Table 1. Moorings in the Chukchi Sea.

Mooring	Latitude	Longitude	Depth	Beginning	Ending
BSE	65.78	–168.60	45/53	9/28/91	9/20/92
BSN	66.30	–169.98	45/53	9/28/91	9/22/92
MA190	65.95	–169.42	41/50	9/25/90	9/23/91
MA290	65.77	–168.58	44/52	9/11/90	9/15/91
MA390	66.29	–168.95	47/58	9/5/90	9/4/91
AP18	71.33	–158.17	117/122	10/1/91	9/31/92
BP12	71.05	–159.55	82/85	10/1/91	9/4/92
MK190	71.03	–159.69	71/79	9/17/90	9/21/91
EP3	69.02	–166.97	42/45	9/29/91	9/23/92
MC690	69.02	–166.95	38/45	9/09/90	9/21/91
MC490	68.85	–169.59	44/52	9/23/90	9/3/91
MC390	68.60	–171.07	47/54	9/23/90	9/24/91
MC290	68.33	–172.49	42/50	9/23/90	9/18/91
MC190	67.94	–174.55	35/42	9/23/90	10/4/91
ME290	70.49	–178.44	37/44	9/21/90	9/29/91
MF290	70.95	–174.18	40/48	9/22/90	9/29/91
CP3	70.67	–167.03	49/54	10/2/91	9/27/92

3.0 Methods

We used correlation analyses (see section 4) for numerous comparisons among the atmospheric pressures and derived winds. These techniques allowed us to contrast the differences among the data sets. We used methods of numerical modeling to simulate surface winds and ocean currents. These modeling methods are described in the following subsection.

3.1 The 2-D Coupled Ice–Water Model

3.1.1 Model equations

The ocean model was formulated on a stereographic polar coordinate system centered at the North Pole. This system is very similar to a rectangular coordinate system except for the presence of the map coefficient m, which varies from 1 at the North Pole to 1.071 at 60°N. This coefficient describes a correction from a spherical to a polar stereographic projection. We based the model on the vertically averaged momentum and continuity equations for coupled water–ice motion:

$$\frac{d\vec{U}}{dt} + f\vec{k} \times \vec{U} = -gDm\nabla\xi + N_h m^2 \nabla^2 \vec{U} + \frac{c\vec{T}_i + (1-c)\vec{T}_s - \vec{T}_b}{\rho} \quad (1)$$

$$\frac{\partial \xi}{\partial t} = m^2 \nabla \left(\frac{\vec{U}}{m} \right) \quad (2)$$

$$\frac{d\vec{u}_i}{dt} + f\vec{k} \times \vec{u}_i = -gm\nabla\xi + \frac{\vec{T}_{is} - \vec{T}_i}{\rho_i h_i} + \vec{F}_i \quad (3)$$

$$\frac{\partial c}{\partial t} = -m^2 \nabla \left(\frac{\vec{u}_i c}{m} \right) \quad (4)$$

where, x and y are the lateral coordinates, with their origin at the North Pole;

t is time;

ξ denotes free surface elevation;

$\vec{U}$ is a vector of volume transport with components U and V along x and y directions;

$\vec{u}_i$ is a vector of ice velocity;

$\vec{T}_i$ is a vector of ice stress between water and ice;

$\vec{T}_{is}$ is a vector of ice stress between atmosphere and ice;

$\vec{T}_b$ is a vector of bottom stress;

$\vec{T}_s$ is a vector of water stress between atmosphere and water;

$\vec{F}_i$ is a vector of internal ice forces;

ρ_i and ρ are ice and water density;

N_h is a horizontal eddy viscosity coefficent;

$\vec{k}$ is a unit vector along the vertical direction.

$$\vec{T}_s = \rho_\alpha R_\alpha \vec{W} |W| \quad (5)$$

where $\vec{W}$ is a vector of surface wind, and ρ_α and R_α are air density and a friction coefficient respectively.

In the above equations, *c* is ice concentration; h_i is ice thickness, and $D=h+\xi$, where *h* is the ocean depth.

The surface wind was determined from geostrophic relationships, with consideration of the transitional coefficient μ and angle of deviation of surface wind from the geostrophic direction λ. Implemented in the model calculations is the algorithm in which

$\mu = 0.7$ if $W < 15$ m/s;

$\lambda = 30°$ if $W < 15$ m/s;

$\mu = 0.8$ if $W > 15$ m/s; and

$\lambda = 20°$ if $W > 15$ m/s.

The surface wind transitional coefficients and turning angles are based on the model calibration, and on diagnostic and prognostic simulations of ice drift and storm surges in the Kara, Laptev, East Siberian, and Chukchi seas (Proshutinsky, 1978, 1986, 1988).

The air–water drag coefficient, R_α is a function of the wind speed (Proshutinsky, 1978, 1986, 1988).

$$R_\alpha = (1.1 + 0.04 \mid W \mid) \times 1000 \qquad (6)$$

Bottom stress is described by

$$T_b = \rho R_b \frac{|\vec{U}|\vec{U}}{D^2} \qquad (7)$$

where R_b is a bottom friction coefficient ($= 2.6 \cdot 10^{-3}$).

The interaction of ice and atmosphere is described by:

$$T_{is} = \rho_a R_{i\alpha} \vec{W} \mid \vec{W} \mid \qquad (8)$$

In a first approximation the ice–atmosphere drag coefficient, $R_{i\alpha}$, is equal to the air–water friction coefficient R_α. The interaction of ice and water is described by:

$$T_i = \rho R_i \mid \vec{u}_i - \frac{\vec{U}}{D} \mid (\vec{u}_i - \frac{U}{D}) \qquad (9)$$

We used the ice–water drag coefficient R_i (= 5.5E3) estimated by McPhee (1980). To describe internal ice forces, the nonlinear viscous constitutive law proposed by Rothrock (1975) and applied by Kowalik (1981) to model storm surges and tides in the Arctic Ocean, was used:

$$F_i = \eta m^2 \nabla^2 \vec{u}_i + \Lambda m^2 \nabla(\nabla \vec{u}_i - m \nabla p) \qquad (10)$$

where $\nabla(\nabla \vec{u}_i) = \text{grad}(\text{div } \vec{u}_i)$.

Rothrock (1975) suggested that the tensile stress in ice is negligible compared with compressive stress. Pressure p is given by:

$$p = -A_p m \nabla \vec{u}_i \;\text{ if }\; \nabla \bar{u}_i < 0 \tag{11}$$

$$p = 0 \;\text{ if }\; \nabla \bar{u}_i \geq 0 \tag{12}$$

In the above equations, both bulk Λ and shear η viscosity coefficients are taken to be equal (= 10E7 square cm/s); A_p (= 10E8 square cm/s) is the ice pressure coefficient. The magnitude of the horizontal frictional coefficients used should result in numerical stability and reasonable reproduction of the turbulent processes in the water and ice.

3.1.2 Initial and boundary conditions

Initially, the dependent variables in the integration domain were taken as zero:

$$\xi(x,y)_{t=0} = 0; \;\; \vec{U}(x,y)_{t=0} = 0; \;\; \vec{u}_i(x,y)_{t=0} = 0 \tag{13}$$

Along the solid boundary S we assumed a no-slip condition for water transport and ice velocity:

$$\vec{U}(x,y,t)_S = 0; \qquad V(x,y,t)_S = 0 \tag{14}$$

In ice-free areas, equations of motion and continuity were solved subject to the boundary condition at the bottom. The same equations were used for under the shore-fast ice. Ice velocity was set to zero and compactness c was set to 1. In the areas covered by pack ice, the full system of equations was used to obtain a solution. A series of numerical experiments were carried out with different versions of the model in order to study the effects of internal ice stresses, ice distribution, ice-water friction, and ice thickness. We discuss, in this paper, results from only one numerical experiment where the ice thickness and ice concentration were explicitly prescribed. We solved only the dynamical ice equations without including the effects of ice formation and ice melting. We artificially prescribed the variability of ice concentration and thickness as external parameters based on observations (monthly data from the Navy–NOAA Joint Ice Center). The ice thickness was prescribed according to ice age.

At the open boundary of the model domain we prescribed sea level variations:

$$\xi_O = \xi(x, y, t) \tag{15}$$

Along the northern open boundary a radiation condition was prescribed as:

$$\vec{U} = \pm \xi_{in} (gH)^{-2} \tag{16}$$

where ξ_{in} is sea level along the first line parallel to the open boundary.

For ice cover at the open boundary the following conditions were prescribed:

$$\frac{\partial u_i}{\partial n} = 0; \qquad \frac{\partial c}{\partial n} = 0 \tag{17}$$

Along the open boundaries in the North Pacific we prescribed sea level. Along the open boundaries in the Arctic Ocean (northern part of the Chukchi Sea) we prescribed the radiation condition. These conditions established the sea slope between the Pacific and Arctic oceans. This slope forces the mean inflow from the Bering Sea into the Arctic Ocean (about 1 Sv) and supports stable circulation in the northern Bering Sea and the Chukchi Sea (Proshutinsky, 1986). Recent estimates (Roach et al., 1995) have given an average permanent transport of about 0.8 SV in the Bering Strait. To include river runoff we prescribed water transport (U or V) for model rivers (Mackenzie, Kolyma), although river input did not have a significant influence on the results presented here.

3.2 The 3-D Ocean Model

One of the goals of this project has been to improve the results of numerical simulation of the Chukchi Sea circulation. To do this we have used a 3-D Princeton University model (Blumberg and Mellor, 1983). Most observations of the currents in the Chukchi and Beaufort seas were obtained from current meters located close to the bottom. The 3-D model allowed us to obtain more realistic results. We forced this model with the same surface winds that were used for the 2-D ocean circulation model. A detailed description of the model is presented in Blumberg and Mellor (1983) and a computer code is available via anonymous ftp at: http://www.aos.princeton.edu/WWWPUBLIC/htdocs.pom .

3.3 Simulation of the Surface Buoy Motion

To test how well the model simulates ice motion, we used the empirical relationship described by Thorndike and Colony (1982) for ice drift and geostrophic winds in the Arctic Ocean, based on 1979 and 1980 data from an array of surface-drifting buoys. The relationship among the ice velocity u, the geostrophic wind G, and the mean ocean current c was examined in the form

$$\vec{u} = A\vec{G} + C + \varepsilon \qquad (18)$$

where A is a complex constant and the vectors $\vec{u}$, $\vec{G}$, $\vec{c}$, and ε are thought of as complex numbers.

The complex coefficient A involves a scaling factor | A | and a turning angle Θ.

$$A = | A \mid e^{-i\Theta} \qquad (19)$$

Thorndike and Colony have shown that in the absence of a steady ocean current, sea ice moves about 8° to the right of the geostrophic wind at 0.008 times its speed (i.e., $\Theta = 8°$ and $| A | = 0.008$). Although the model is simple, it describes 70% of the variance of the ice velocity, leaving residuals with a standard deviation of 0.04 m/s (Thorndike and Colony, 1982).

3.4 Data for the Models

To define the model's 21-km spatial grid, we subsampled the 14-km spatial grid and bathymetry prepared by Kowalik and Proshutinsky (1994) for their tidal model of the Arctic Ocean. Figure 5 shows the computational domain. To define the model's 7-km spatial grid we digitized Russian navigational charts which are available now at the Institute of Marine Science (IMS), University of Alaska Fairbanks.

4.0 Results

4.1 Comparison Among the NCAR, FNOC, and ECMWF Data Sets

4.1.1 Atmospheric pressure

Figures 6–17 show spatial correlation and root mean square (RMS) errors among NCAR and FNOC; NCAR and ECMWF; and ECMWF and FNOC atmospheric pressure fields. The numbers under the figures show maximum and minimum coefficients of correlation between corresponding atmospheric pressure fields, and maximum and minimum RMS errors (mb) among these fields. Table 2 shows these extrema for every month of 1991 and 1992. These were used for analysis of possible seasonal variability. The correlation is very high between pairs of pressure fields from different centers of atmospheric analyses. Maximum errors are usually located at the centers of the cyclones and anticyclones. FNOC atmospheric pressure in these cases is significantly different from the atmospheric pressures given by NCAR and ESMWF data centers. Usually this happens when the atmospheric pressure in the center of the cyclone is less than 950 mb. Possibly this problem is the result of a procedure that the FNOC computer managing team used to prepare data for our purposes. We did not have this problem in the FNOC pressure fields before 1987. Coefficients of correlation between ECMWF (2.5° and 1.125° spatial resolutions) are very high, which allowed us to conclude that they describe practically identical synoptic variability in the sea level atmospheric pressures. No seasonal variability is visible in the coefficients of correlation or RMS errors, which means the accuracy of the atmospheric pressure prediction has no relation to the seasons.

4.1.2 Geostrophic wind

Figures 18–29 and Table 3 show correlation coefficients and RMS differences in the geostrophic winds calculated using NCAR, FNOC, and ECMWF sea surface atmospheric pressure fields. There was less correlation among geostrophic winds than among corresponding atmospheric pressure fields. Coefficients of correlation between NCAR and ECMWF winds were higher than they were between those for NCAR and FNOC, or ECMWF and FNOC. We used two data sets (Barrow and Kotzebue) to estimate the accuracy of the simulated winds. The statistical structure of the real winds and the results of comparison between observed and simulated winds at Barrow and Kotzebue are described in the following sections.

4.2 Comparison Between Observed and Simulated Winds

4.2.1 Barrow

Observed and simulated wind roses for Barrow are shown in Figures 30–33. Seasonal variability of the observed monthly mean wind at Barrow is presented in Figure 30. East and west are the major directions of wind in Barrow; higher wind velocity occurs from September through November and a minimum of wind is observed during April through July. In Figures 31–33 the simulated winds (based on NCAR, ECMWF, and FNOC sea surface atmospheric fields) are shown. Simulated winds do not adequately reproduce wind conditions at Barrow. First, NCAR wind roses show that the major wind direction is east; second, summer winds are very weak; and third, northwest winds are not represented as well as those from ECMWF, which show two major wind directions for Barrow (east and west). However, the ECMWF summer winds are poorly reproduced. FNOC data are similar to those for ECMWF wind distribution. Comparison among NCAR, ECMWF, FNOC, and observed winds in 1992 are shown in Figures 34, 35, and 36. Correlation between observed and simulated winds is very low. On the other hand, correlation among NCAR, FNOC and ECMWF simulated winds is very high, which demonstrates that FNOC, NCAR, and ECMWF sea level atmospheric fields are very similar. It is difficult to evaluate which source of data is better for modeling needs. At least two possible reasons can be found for a disagreement between observed and simulated wind at Barrow. The first is that we used a very simple model, which may not work well for Chukchi Sea wind calculations. The second reason is related to a local effect. Local winds cannot be simulated based only on geostrophic balance and empirical relationships; a strong air temperature gradient exists between land and sea during summer, and this gradient, or thermal effect, generates sea breezes during open-water months. Kozo (1979, 1982, 1984), and Kozo and Robe (1986) have reported thermal effects in their description of mesoscale meteorology of the Beaufort Sea and Norton Sound region. According to Kozo, the pure sea breeze effects control 23% of the measured wind velocities, and the thermal contrast between the ocean and land would act in a 20-km coastal zone. Aagaard, Pease, and Salo (1990) reached a similar conclusion in reference to the meteorological stations of the Beaufort and Chukchi seas. They correlated meteorological parameters (atmospheric pressure, air temperature, and surface winds) between data from the Barter, Resolution, Lonely, and Barrow stations, and data from FNOC. High correlations between observed atmospheric pressure and FNOC atmospheric pressure, and between observed air temperature and FNOC air temperature were demonstrated, but the wind velocity correlation was less than 0.5, which was explained by local sea breeze effects.

Table 2. Coefficients of correlation and root mean square errors among NCAR, FNOC, and ECMWF sea level atmospheric field data in 1991–1992.

Month	**Source of data**	**Coefficient of correlation**		**Root mean square error**	
		Maximum	**Minimum**	**Maximum**	**Minimum**
January	NCAR – FNOC	0.99/1.00	0.74/0.89	11.5/5.4	1.6/1.0
January	NCAR – ECMWF	0.99/1.00	0.74/0.29	10.7/13.8	1.6/0.9
January	FNOC – ECMWF	1.00/1.00	0.94/0.29	5.5/13.7	0.4/0.6
February	NCAR – FNOC	1.00/1.00	0.95/0.91	4.0/4.4	0.7/0.8
February	NCAR – ECMWF	1.00/1.00	0.93/0.91	6.8/4.4	0.8/0.8
February	FNOC – ECMWF	1.00/1.00	0.92/0.92	4.0/5.6	0.7/0.8
March	NCAR – FNOC	1.00/1.00	0.92/0.90	4.0/6.2	0.8/0.5
March	NCAR – ECMWF	1.00/1.00	0.93/0.92	4.9/5.3	0.8/0.8
March	FNOC – ECMWF	1.00/1.00	0.91/0.91	5.2/4.2	0.3/0.6
April	NCAR – FNOC	1.00/1.00	0.94/0.88	3.6/4.8	0.8/0.5
April	NCAR – ECMWF	1.00/1.00	0.90/0.94	3.3/4.6	0.6/0.7
April	FNOC – ECMWF	1.00/1.00	0.94/0.94	3.2/3.8	0.4/0.7
May	NCAR – FNOC	1.00/1.00	0.90/0.92	3.3/3.8	0.7/0.6
May	NCAR – ECMWF	1.00/1.00	0.91/0.97	3.6/2.4	0.6/0.4
May	FNOC – ECMWF	1.00/1.00	0.89/0.88	3.0/4.0	0.3/0.4
June	NCAR – FNOC	1.00/1.00	0.82/0.86	3.8/3.6	0.7/0.6
June	NCAR – ECMWF	1.00/1.00	0.88/0.92	2.9/2.4	0.7/0.5
June	FNOC – ECMWF	1.00/1.00	0.86/0.84	3.8/3.2	0.3/0.5
July	NCAR – FNOC	1.00/0.99	0.92/0.90	3.4/3.1	0.6/0.9
July	NCAR – ECMWF	1.00/1.00	0.95/0.95	3.1/3.1	0.6/0.9
July	FNOC – ECMWF	1.00/0.99	0.89/0.89	3.8/2.9	0.3/0.7
August	NCAR – FNOC	1.00/0.98	0.92/0.80	3.4/4.1	0.6/1.3
August	NCAR – ECMWF	1.00/0.92	0.92/0.92	3.1/3.5	0.7/0.7
August	FNOC – ECMWF	1.00/0.96	0.91/0.83	3.4/4.2	0.4/1.2
September	NCAR – FNOC	1.00/0.99	0.95/0.80	3.5/4.7	0.6/1.4
September	NCAR – ECMWF	1.00/1.00	0.93/0.93	3.2/3.2	0.5/0.6
September	FNOC – ECMWF	1.00/0.98	0.91/0.83	3.4/4.2	0.4/1.2
October	NCAR – FNOC	1.00/0.98	0.94/0.89	4.3/5.3	0.7/1.8
October	NCAR – ECMWF	1.00/1.00	0.96/0.90	4.4/3.1	0.7/0.7
October	FNOC – ECMWF	1.00/0.99	0.92/0.89	4.5/5.1	0.5/1.6
November	NCAR – FNOC	1.00/0.99	0.97/0.80	4.1/6.1	0.8/2.0
November	NCAR – ECMWF	1.00/1.00	0.97/0.62	5.3/12.2	0.8/0.7
November	FNOC – ECMWF	1.00/0.99	0.95/0.57	5.2/13.6	0.5/1.4
December	NCAR – FNOC	1.00/0.95	0.95/0.60	5.7/12.0	0.6/1.6
December	NCAR – ECMWF	1.00/0.94	0.94/0.10	6.0/11.3	0.8/2.3
December	FNOC – ECMWF	1.00/0.98	0.92/0.09	6.4/12.4	0.5/1.9

Table 3. Coefficients of correlation and root mean square errors among NCAR, FNOC, and ECMWF geostrophic winds in 1991–1992.

Month	Source of data	Coefficient of correlation		Root mean square error	
		Maximum	Minimum	Maximum	Minimum
January	NCAR – FNOC	0.94/0.93	0.10/0.09	11.3/10.4	2.3/1.8
January	NCAR – ECMWF	0.95/0.92	–0.21/0.09	12.4/10.8	1.9/1.3
January	FNOC – ECMWF	0.98/0.92	0.09/0.18	12.4/13.7	1.9/2.1
February	NCAR – FNOC	0.98/0.93	0.24/0.12	11.1/12.4	1.3/1.8
February	NCAR – ECMWF	0.98/0.98	0.12/0.13	11.1/12.0	1.3/1.5
February	FNOC – ECMWF	0.98/0.97	–0.16/0.09	9.9/9.0	1.3/1.7
March	NCAR – FNOC	0.98/0.95	0.37/0.24	7.4/8.0	2.1/2.5
March	NCAR – ECMWF	0.98/0.99	0.08/0.02	10.4/10.6	1.8/2.8
March	FNOC – ECMWF	0.97/0.98	0.22/0.28	11.1/10.7	1.4/1.2
April	NCAR – FNOC	0.96/0.99	0.24/0.32	7.1/6.8	1.8/1.5
April	NCAR – ECMWF	0.97/0.93	0.04/0.00	9.5/9.4	1.5/1.7
April	FNOC – ECMWF	0.98/0.98	0.17/0.18	9.2/8.8	1.3/1.3
May	NCAR – FNOC	0.97/0.99	0.29/0.33	5.7/4.6	1.5/0.9
May	NCAR – ECMWF	0.98/0.97	–0.25/0.09	10.3/9.4	1.5/1.4
May	FNOC – ECMWF	0.97/0.99	0.12/0.23	10.0/9.9	1.1/1.4
June	NCAR – FNOC	0.95/0.98	0.12/0.26	5.9/4.6	1.5/2.6
June	NCAR – ECMWF	0.97/0.97	–0.01/0.02	10.7/12.4	1.4/2.5
June	FNOC – ECMWF	0.97/0.95	–0.10/0.04	8.9/11.2	1.3/2.5
July	NCAR – FNOC	0.96/0.97	0.26/0.24	5.7/6.1	1.4/1.9
July	NCAR – ECMWF	0.97/0.94	0.18/0.15	9.0/10.1	1.4/1.9
July	FNOC – ECMWF	0.95/0.99	0.10/0.19	8.3/7.9	1.4/0.9
August	NCAR – FNOC	0.98/0.98	0.49/0.34	5.3/5.1	1.6/1.3
August	NCAR – ECMWF	0.98/0.92	0.47/0.42	7.6/7.5	1.6/1.7
August	FNOC – ECMWF	0.97/0.98	0.41/0.43	8.7/8.2	1.4/1.2
September	NCAR – FNOC	0.98/0.99	0.60/0.50	6.4/6.7	1.3/1.4
September	NCAR – ECMWF	0.98/0.98	0.22/0.23	8.1/7.2	1.3/1.6
September	FNOC – ECMWF	0.98/0.99	0.27/0.34	8.6/9.3	1.4/1.2
October	NCAR – FNOC	0.97/0.89	0.69/0.59	4.8/5.3	1.7/1.8
October	NCAR – ECMWF	0.98/1.00	0.31/0.30	9.3/9.9	1.7/1.7
October	FNOC – ECMWF	0.97/0.99	0.43/0.49	9.0/7.1	1.4/1.1
November	NCAR – FNOC	0.97/0.95	0.60/0.30	7.7/6.1	1.5/2.0
November	NCAR – ECMWF	0.97/0.94	0.32/0.32	11.1/12.2	1.7/2.1
November	FNOC – ECMWF	0.97/0.99	0.26/0.57	11.5/9.6	1.5/0.4
December	NCAR – FNOC	0.98/0.95	0.57/0.33	8.5/9.7	1.7/2.2
December	NCAR – ECMWF	0.98/0.98	–0.33/0.10	13.7/11.3	1.7/2.3
December	FNOC – ECMWF	0.98/0.91	–0.21/0.03	15.3/12.4	1.3/1.9

4.2.2 Kotzebue

Observed and simulated wind roses for Kotzebue are shown in Figures 37–42. Seasonal variability of the observed monthly mean winds at Kotzebue (Figure 36) is similar to variability of winds at Barrow. Here we can reach the same conclusion as in the previous section; i.e., that local wind effects dominate at the coastal stations, and that they cannot be used as sources for estimation of the accuracy of NCAR, FNOC, and ECMWF data.

4.3 Observed and Simulated Buoy Drift

We have simulated buoy drift in the Chukchi and Beaufort seas using empirical relationships proposed by Thorndike and Colony and a 2-D coupled ice–ocean model. NCAR, FNOC, and ECMWF sea surface atmospheric pressure fields for 1991 and 1992 were used for these calculations. Trajectories of the surface-ice buoys for 1991 and 1992 are shown in Figures 43 and 44, respectively. We have analyzed results of simulations only for moving buoys. Some of the buoys were trapped by fast ice and did not drift at all. Several buoys that drifted with the ice experienced the influence of strong internal ice forces due to ice-floe interactions and lateral friction. This usually happens in the vicinity of land, at a distance of about 400 km. The Thorndike–Colony empirical model does not take into account these effects. Our 2-D coupled ice–ocean model does contain these forces; it takes into account a permanent current generated by the sea level slope between the Pacific and Atlantic oceans, and therefore, would theoretically simulate buoy drift better than the Thorndike–Colony empirical model used in the vicinity of the coast. Figures 45–53, for example, show results of buoy velocity simulations using the Thorndike–Colony empirical model. U and V components of ice drift are presented for each buoy for which motion was simulated using NCAR, FNOC, and ECMWF atmospheric data. Coefficients of correlation among simulated and observed buoy velocities and root mean square errors for all buoys are given in Tables 4–7. From these results we have concluded that all of the atmospheric pressure fields give more or less similar accuracy, but that ECMWF's data are better than FNOC's, and FNOC's atmospheric pressure data are better than NCAR's. The advantage of the ECMWF atmospheric pressure fields is their higher resolution, which allows us to simulate less smoothed winds. As shown in Figures 45–53, the ECMWF-based simulations resolve maximums and minimums of the ice drift much better than NCAR- and FNOC-based calculations. Observed and simulated U and V ice velocities obtained with a 2-D coupled ice–ocean model of the Chukchi Sea are presented in Figures 54–57 and in Tables 8–9. Again, we can conclude that ECMWF-based simulations are better than simulations of ice drift using FNOC and NCAR sea–surface atmospheric pressure data.

Table 4. Results of simulation of buoy drift in 1992 using the Thorndike–Colony empirical model.

Buoy number	Correlation coefficient between observed and simulated ice drift U/V			Root mean square error of simulated buoy drift U/V		
	NCAR	FNOC	ECMWF	NCAR	FNOC	ECMWF
1836	0.92/0.68	0.90/0.64	0.92/0.66	9.9/6.9	9.1/8.3	6.9/7.6
1837	0.88/0.77	0.88/0.74	0.85/0.72	15.3/12.6	12.8/13.7	15/5/14.8
2386	0.88/0.87	0.84/0.84	0.82/0.71	15.5/19.4	16.3/20.3	16.4/36.3
2388	0.86/0.85	0.82/0.81	0.80/0.80	13.2/17.3	14.1/20.9	15.4/21.9
7100	0.88/0.79	0.87/0.75	0.86/0.75	15.2/14.1	14.5/15.9	14.2/15.9
7101	0.90/0.48	0.88/0.42	0.89/0.46	14.9/10.3	14.2/12.2	12.0/12.0
7102	0.77/0.79	0.78/0.76	0.78/0.78	64.4/17.8	60.3/20.3	55.2/18.2
9786	1.00/1.00	1.00/1.00	1.00/1.00	0.1/8.6	0.9/15.4	2.2/3.3
10667	0.77/0.78	0.90/0.83	0.80/0.78	26.3/27.5	24.2/22.5	32.3/29.0
11251	0.89/0.69	0.87/0.65	0.85/0.63	69.7/29.6	61.5/31.6	59.7/33.2
11252	0.84/0.80	0.86/0.78	0.87/0.76	33.9/20.7	31.9/21.1	21.8/22.6
12790	0.87/0.82	0.83/0.75	0.83/0.78	12.1/13.6	14.5/17.3	14.7/15.3
12800	0.90/0.78	0.90/0.76	0.89/0.82	12.1/12.3	10.4/14.5	11.8/10.7
12801	0.63/0.71	0.63/0.74	0.73/0.77	11.5/12.5	11.2/11.6	14.6/11.5
12806	0.79/0.74	0.80/0.69	0.79/0.74	36.3/14.3	32.2/15.8	31.6/14.1
12820	0.90/0.80	0.90/0.73	0.90/0.79	12.3/19.2	12.3/21.6	10.6/17.3
12821	0.80/0.80	0.79/0.83	0.79/0.82	9.8/15.3	11.7/12.9	13.6/13.6

Table 5. Results of simulation of buoy drift in 1991 using the Thorndike–Colony empirical model.

Buoy number	Correlation coefficient between observed and simulated ice drift U/V			Root mean square error of simulated buoy drift U/V		
	NCAR	FNOC	ECMWF	NCAR	FNOC	ECMWF
7100	0.79/0.71	0.87/0.75	0.80/0.79	40.4/27.1	14.5/15.9	32.5/25.4
7414	0.90/0.72	0.92/0.68	0.92/0.72	17.6/20.6	12.7/20.5	16.8/18.6
9784	0.68/0.72	0.71/0.68	0.59/0.68	46.5/50.3	40.5/54.0	52.3/49.6
12782	0.77/0.34	0.94/0.74	0.94/0.87	35.3/46.2	33.6/19.8	16.4/8.9
12783	0.78/0.57	0.77/0.50	0.70/0.56	56.2/22.7	51.4/29.8	59.1/25.3
11252	0.84/0.80	0.86/0.78	0.83/0.74	33.9/20.7	31.9/21.1	16.9/18.8
12800	0.81/0.77	0.82/0.72	0.83/0.78	18.0/17.6	16.4/20.9	14.7/15.3
12807	0.90/0.78	0.90/0.76	0.78/0.66	12.1/12.3	10.4/14.5	16.5/42.5
12806	0.81/0.82	0.80/0.72	0.82/0.79	14.5/13.9	15.6/21.1	14.9/14.3

Table 6. Results of simulation buoy drift in 1991 using a 2-D coupled ice-ocean model.

Buoy number	**Correlation coefficient between observed and simulated ice drift U/V**			**Root mean square error of simulated buoy drift U/V**		
	NCAR	**FNOC**	**ECMWF**	**NCAR**	**FNOC**	**ECMWF**
7100	0.65/0.80	0.68/0.81	0.72/0.81	25.6/49.3	26.1/50.2	24.1/47.1
7101	0.58/0.52	0.57/0.65	0.60/0.64	18.7/22.5	17.2/21.1	17.0/20.1
7102	0.81/0.74	0.82/0.77	0.82/0.79	23.8/312	22.1/293	20.5/250
7103	0.74/0.89	0.74/0.89	0.72/0.92	17.2/210	17.3/218	16.3/165
7104	0.75/0.62	0.75/0.53	0.76/0.67	10.9/182	10.5/177	12.0/165
7105	0.68/0.59	0.69/0.72	0.72/0.72	24/368	25.0/220	23.0/198
7414	0.66/0.80	0.65/0.78	0.50/0.35	17.6/19.4	18.0/20.2	20.4/32.0
9784	0.32/0.69	0.44/0.82	0.45/0.82	36.0/64.0	30.3/56.1	29.2/50.1
12782	0.22/0.72	0.39/0.79	0.45/0.77	18.5/9.0	16.3/8.2	17.0/8.0
12783	0.56/0.64	0.56/0.64	0.67/0.68	12.3/119	12.3/118	11.3/95.0
12800	0.84/0.80	0.85/0.79	0.87/0.83	19.4/22.9	18.9/20.5	17.4/20.0
12801	0.87/0.82	0.84/0.87	0.85/0.86	27.0/32.5	26.1/29.1	25.9/27.7
12806	0.56/0.81	0.62/0.78	0.56/0.80	28.1/16.8	25.3/18.0	26.0/17.1
12807	0.79/0.66	0.80/0.69	0.81/0.70	20.3/25.0	19.7/23.7	18.2/21.9

Table 7. Results of simulation buoy drift in 1992 using a 2-D coupled ice-ocean model.

Buoy number	**Correlation coefficient between observed and simulated ice drift U/V**			**Root mean square error of simulated buoy drift U/V**		
	NCAR	**FNOC**	**ECMWF**	**NCAR**	**FNOC**	**ECMWF**
1836	0.43/0.84	0.45/0.83	0.65/0.91	8.4/13.7	8.2/12.8	7.1/9.6
1837	0.68/0.84	0.68/0.82	0.69/0.87	10.2/21.2	9.9/22.0	9.2/21.1
2388	0.82/0.88	0.82/089	0.83/0.92	31.4/6.8	25.1/7.0	23.1/6.5
7100	0.51/0.85	0.59/0.84	0.61/0.77	16.8/21.2	15.2/20.1	16.0/20.0
7101	0.70/0.93	0.69/0.95	0.83/0.93	6.2/43.6	5.9/41.0	4.9/43.1
7103	0.49/0.83	0.35/0.70	0.44/0.79	19.4/94.0	19.9/111	24.0/118
7104	0.02/–0.07	0.0/0.0	–0.3/0.21	42.3/226	46.1/218	49.1/187
7105	0.17/0.16	0.29/0.34	0.33/0.18	27.0/193	20.3/198	25.7/201
9784	0.85/0.77	0.85/0.77	0.87/0.80	16.0/54.8	15.2/40.9	13.2/31.9
12790	0.64/0.83	0.67/0.81	0.68/0.85	24.0/20.3	22.1/19.3	21.5/19.1
12820	0.72/0.83	0.73/0.82	0.72/0.82	13.7/37.2	13.9/35.1	12.4/34.2
12821	0.55/0.70	0.55/0.70	0.50/0.72	54.8/26.0	52.1/25.0	51.5/23.7
12828	0.76/0.80	0.74/0.88	0.77/0.86	31.4/16.9	30.5/15.9	30.1/14.5
12829	0.73/0.82	0.77/0.89	0.74/0.88	17.6/37.2	17.4/33.2	18.1/35.2

4.4 Observed and Simulated Currents

Figures 57–76 and Tables 8a through 9c show the 1991–1992 results of comparisons between observed and simulated currents using the 2-D coupled ice–ocean model. The results based on the different sources of atmospheric pressure fields are close to each other, but, on average, the NCAR-based annual mean simulated velocities (Tables 8a and 8b) are higher than the FNOC- and ECMWF-based water velocities. Direction of the observed currents is reproduced well enough by all three sources of atmospheric data. Annual mean wind over the Chukchi Sea is relatively weak and does not significantly change currents generated by the secure-level gradient between the Pacific and Arctic oceans.

Table 8a. Comparison between observed and simulated annual mean currents in 1991–1992.

Mooring	**Mean U velocity, cm/s**				**Mean V velocity, cm/s**			
	Observed	**NCAR**	**FNOC**	**ECMWF**	**Observed**	**NCAR**	**FNOC**	**ECMWF**
BSE	10.0	–3.2	–2.8	–2.8	23.1	31.2	27.8	26.4
BSN	–8.6	–3.6	–3.9	–3.0	18.4	23.4	20.7	20.6
AP18	18.0	8.0	6.1	4.8	10.5	4.1	3.3	2.7
EP3	–1.0	2.4	2.7	2.1	2.8	3.3	2.8	2.2
BP12	21.7	11.1	8.7	6.4	7.3	–3.4	–1.7	–1.0
CP3	–1.4	2.1	2.2	2.1	8.1	8.2	7.9	7.0
MA190	5.7	–12.0	–10.6	–	11.1	19.8	15.9	–
MA290	2.1	–4.5	–3.8	–	15.4	27.5	22.7	–
MA390	–8.2	–7.9	–8.5	–	20.6	24.7	19.7	–
MC290	–2.5	–5.4	–8.5	–	3.8	5.1	8.1	–
MC390	–3.3	–3.2	–4.3	–	4.1	1.1	1.2	–
MC490	–2.6	–2.7	–2.3	–	4.8	2.4	–5.0	–
MC690	0.5	3.3	2.2	–	4.1	3.8	–0.8	–
ME290	–2.8	–1.4	–0.1	–	1.3	0.2	1.6	–
MF290	–0.5	0.8	3.9	–	12.4	4.0	7.9	–
MK190	13.8	8.2	0.2	–	4.0	–2.5	0.2	–

Table 8b. Comparison between observed and simulated annual mean currents in 1991–1992.

Mooring	Direction of the current, degrees				Velocity of the current, cm/s			
	Observed	NCAR	FNOC	ECMWF	Observed	NCAR	FNOC	ECMWF
BSE	23	354	354	353	25.2	31.4	27.9	26.5
BSN	335	351	349	352	20.3	23.7	21.1	20.8
AP18	59	63	62	60	20.8	9.0	6.9	5.5
EP3	340	36	43	43	3.0	4.1	3.9	3.0
BP12	71	107	101	99	22.9	11.6	8.9	6.5
CP3	350	14	15	17	8.2	8.5	8.2	7.3
MA190	27	328	326	–	12.5	23.2	19.1	–
MA290	7	351	350	–	15.5	27.9	23.0	–
MA390	338	342	336	–	22.1	25.9	21.5	–
MC290	325	313	314	–	4.4	7.2	11.8	–
MC390	321	288	285	–	5.3	3.4	4.5	–
MC490	331	312	205	–	5.5	3.6	5.5	–
MC690	7	40	110	–	4.1	5.0	2.3	–
ME290	294	278	356	–	3.1	1.4	1.6	–
MF290	358	11	26	–	12.4	4.1	8.8	–
MK190	74	107	45	–	14.4	8.6	0.3	–

Table 9a. Results of simulated currents using a 2-D coupled ice–ocean model. Standard deviation.

Mooring	Standard deviation of U velocity, cm/s				Standard deviation of V velocity, cm/s			
	Observed	NCAR	FNOC	ECMWF	Observed	NCAR	FNOC	ECMWF
BSE	7.3	2.1	2.6	2.4	22.7	20.4	25.5	25.6
BSN	10.9	2.7	3.5	3.3	18.3	13.9	17.8	16.8
AP18	25.6	18.7	22.4	22.6	12.3	6.5	7.5	8.2
EP3	4.3	6.7	7.5	8.4	9.1	7.6	10.1	11.6
BP12	26.2	26.6	30.8	32.1	17.4	6.5	7.4	9,3
CP3	4.7	7.4	9.0	10.1	8.6	8.7	8.7	9.6
MA190	9.5	13.1	15.1	–	24.6	17.9	22.7	–
MA290	3.4	3.4	4.2	–	25.9	23.9	30.3	–
MA390	12.3	4.7	5.7	–	22.5	18.9	24.7	–
MC290	7.1	5.5	6.4	–	5.6	5.6	7.5	–
MC390	6.4	6.3	6.0	–	6.9	9.0	11.1	–
MC490	5.5	6.6	6.7	–	10.4	8.6	14.7	–
MC690	4.2	6.1	8.2	–	12.4	8.8	14.2	–
ME290	11.7	7.4	9.0	–	3.1	3.5	4.7	–
MF290	2.6	7.2	9.0	–	10.5	7.0	8.5	–
MK190	25.9	24.2	30.5	–	15.3	6.0	7.5	–

Table 9b. Results of simulation of currents using a 2-D coupled ice–ocean model. Root mean square error.

Mooring	Root mean square error (RMS) for U velocity, cm/s			Root mean square error (RMS) for V velocity, cm/s		
	NCAR	FNOC	ECMWF	NCAR	FNOC	ECMWF
BSE	15.1	14.9	14.7	15.9	17.5	15.6
BSN	12.5	12.7	12.3	11.8	12.3	11.0
AP18	18.1	18.8	19.8	10.4	10.6	10.9
EP3	9.0	9.8	10.5	6.7	8.1	9.4
BP12	18.3	21.4	23.3	23.8	24.0	24.4
CP3	9.0	10.8	12.1	7.2	7.9	9.0
MA190	27.0	27.6	–	19.0	17.9	–
MA290	7.6	7.2	–	21.4	21.2	–
MA390	10.3	10.6	–	12.8	11.7	–
MC290	6.6	9.5	–	6.6	9.9	–
MC390	6.3	6.6	–	7.9	9.4	–
MC490	5.8	6.1	–	8.5	15.1	–
MC690	7.4	9.0	–	9.6	12.7	–
ME290	13.6	14.7	–	4.3	4.9	–
MF290	7.3	9.8	–	13.9	14.7	–
MK190	18.5	24.5	–	20.3	21.0	–

Table 9c. Results of simulation of currents using a 2-D coupled ice–ocean model. Correlation coefficient.

Mooring	Coefficient of correlation between observed and simulated U velocity			Coefficient of correlation between observed and simulated V velocity		
	NCAR	FNOC	ECMWF	NCAR	FNOC	ECMWF
BSE	0.12	0.10	0.15	0.80	0.76	0.81
BSN	–0.13	–0.12	0.12	0.81	0.78	0.81
AP18	0.81	0.82	0.82	0.79	0.79	0.79
EP3	–0.09	–0.11	–0.16	0.69	0.65	0.61
BP12	0.84	0.83	0.84	–0.59	–0.53	–0.43
CP3	0.11	0.01	–0.08	0.57	0.59	0.52
MA190	–0.67	–0.62	–	0.73	0.74	–
MA290	0.34	0.40	–	0.75	0.76	–
MA390	0.58	0.51	–	0.84	0.88	–
MC290	0.58	0.41	–	0.34	0.10	–
MC390	0.52	0.45	–	0.60	0.60	–
MC490	0.56	0.52	–	0.64	0.63	–
MC690	0.14	0.11	–	0.64	0.62	–
ME290	0.06	0.05	–	0.22	0.26	–
MF290	0.18	0.22	–	0.25	–0.07	–
MK190	0.75	0.75	–	–0.54	–0.60	–

4.5 Bering Strait Water Transport

Year-to-year and seasonal fluctuations of the water transport in Bering Strait are natural indicators of large-scale circulation and the interaction between the atmosphere and ocean in the Chukchi Sea. Therefore, a comparison among simulated water transports in Bering Strait, obtained using different atmospheric pressure sources, can validate our preliminary conclusions about the accuracy of the NCAR, FNOC, and ECMWF data sets. Figure 77 shows this comparison among simulated water transports from different sources of wind forcing. Again, all of them give practically the same numbers for water transport. Maximum coefficients of correlation are between ECMWF and NCAR data. FNOC data, as we discussed before, has some problems when the atmospheric pressure is lower than 950 mb, which usually happens in fall or winter. These situations, shown in Figure 77, are visible at the beginning of 1991 and the end of 1992.

4.6 Results of Circulation Simulation Using a 3-D Barotropic Model

Some results of simulation of 3-D currents in the Chukchi Sea in 1991 and 1992 are presented in Tables 10–11 and in Figures 78–89. The new results are better than those obtained with the 2-D coupled ice–ocean model. It is important to note that the 3-D model currents can be obtained for the depth at which observations were made. This allows higher accuracy in simulated velocities. Analysis of Tables 10 and 11 shows that the differences among currents simulated using NCAR, FNOC, and ECMWF data are small; it is difficult to recommend which atmospheric field is better to use.

Table 10a. Comparison between observed and simulated 3-D annual mean bottom currents in 1991–1992. 3-D currents are averaged in the vertical direction.

Mooring	Annual mean U velocity, cm/s				Annual mean V velocity, cm/s			
	Observed	NCAR	FNOC	ECMWF	Observed	NCAR	FNOC	ECMWF
BSE	10.3	5.4	4.5	4.3	25.3	33.6	31.1	31.8
BSN	–9.0	–3.4	–2.7	–2.0	19.9	35.6	32.6	32.4
AP18	15.7	20.7	17.9	15.6	9.3	1.2	0.6	–0.1
EP3	–1.3	1.9	1.9	1.8	3.2	8.3	6.3	6.3
BP12	19.5	27.8	23.5	20.1	6.4	2.2	1.9	1.7
CP3	–1.2	3.1	3.4	3.1	7.6	7.6	7.2	8.9

Table 10b. Comparison between observed and simulated 3-D annual mean currents 1991–1992. 3-D currents are averaged in the vertical direction.

Mooring	Direction of the current, degrees				Velocity of the current, cm/s			
	Observed	NCAR	FNOC	ECMWF	Observed	NCAR	FNOC	ECMWF
BSE	22	9	8	8	27.3	34.0	31.4	32.1
BSN	335	354	355	356	21.8	35.7	32.7	32.4
AP18	59	86	88	90	18.2	20.7	17.9	15.6
EP3	337	13	17	16	3.0	8.6	6.6	6.6
BP12	71	85	85	85	20.5	27.9	23.6	20.2
CP3	350	22	25	19	7.7	8.2	8.0	9.4

Table 11a. Bottom velocities. Results of simulation currents using the 3-D ocean barotropic model. Standard deviations.

Mooring	Standard deviation of U velocity, cm/s				Standard deviation of V velocity, cm/s			
	Observed	NCAR	FNOC	ECMWF	Observed	NCAR	FNOC	ECMWF
BSE	7.6	3.1	4.6	4.8	22.4	11.9	15.7	15.8
BSN	10.7	2.6	3.7	4.7	18.4	13.0	18.0	18.6
AP18	25.1	15.1	18.6	20.3	11.9	6.7	7.1	7.5
EP3	4.0	3.8	4.0	5.4	9.3	10.3	13.4	13.6
BP12	26.2	23.8	29.0	31.5	17.9	3.1	3.4	4.0
CP3	5.0	6.3	7.9	8.9	8.7	6.7	8.7	9.6

Table 11b. Results of simulation of currents using the 3-D coupled ice–ocean model. Root mean square errors.

Mooring	Root mean square error (RMS) for U velocity, cm/s			Root mean square error (RMS) for V velocity, cm/s		
	NCAR	FNOC	ECMWF	NCAR	FNOC	ECMWF
BSE	9.7	10.6	11.0	16.9	15.5	14.9
BSN	11.2	11.1	11.2	19.1	16.9	16.5
AP18	15.4	13.2	12.3	11.7	12.0	12.5
EP3	6.4	7.0	7.6	9.7	10.8	11.0
BP12	15.8	15.0	15.4	16.3	16.5	16.3
CP3	8.9	10.7	11.7	6.1	6.3	7.4

Table 11c. Results of simulation of currents using the 3-D barotropic model. Correlation coefficients.

Mooring	Coefficient of correlation between observed and simulated U velocity NCAR	FNOC	ECMWF	Coefficient of correlation between observed and simulated V velocity NCAR	FNOC	ECMWF
BSE	–0.03	–0.06	–0.05	0.80	0.78	0.80
BSN	0.50	0.57	0.61	0.81	0.81	0.83
AP18	0.85	0.86	0.87	0.72	0.73	0.72
EP3	0.02	0.00	–0.07	0.65	0.63	0.64
BP12	0.86	0.87	0.87	0.74	0.65	0.67
CP3	0.07	–0.06	–0.15	0.72	0.74	0.68

4.7 Seasonal Variability

Monthly variability of the surface atmospheric pressure and water circulation in the Chukchi Sea, presented in Figures 90–110, is based on NCAR, FNOC, and ECMWF atmospheric pressure data. If we compare these patterns with the circulation generated by a secular sea level gradient between the Pacific and Arctic oceans (see Weingartner and Proshutinsky, 1998) we can conclude that the wind is a major factor responsible for the seasonal variability of the Bering Strait transport and the water circulation in the Chukchi Sea. In October the Alaskan branch of the Chukchi Sea current system is pronounced in all three patterns representing NCAR, FNOC, and ECMWF results (Figures 90–92). A northward transport along the depression to the east of Herald Shoal is also well defined. Differences are large among ECMWF, NCAR, and FNOC patterns in the area of Wrangel Island. The ECMWF results show a cyclonic water circulation around Wrangel Island as a part of the East Siberian coastal current, with velocities of about 30 cm/s in Long Strait. The NCAR data do not show the existence the East Siberian current at all. The FNOC data show very small velocities associated with this current.

In November (Figures 93–95) the water circulation in the Chukchi Sea is influenced by easterly winds generated by the atmospheric pressure gradient between the Aleutian Low and the Arctic High. The isobars nearly coincide with the direction of the geographical parallels. In this situation, the major flow from Bering Strait is directed toward the northwest. The Alaskan branch of the Chukchi Sea current system does not exist at this time, and the Chukchi Sea surface water penetrates to the East Siberian Sea through Long Strait. NCAR, FNOC, and ECMWF atmospheric pressure distributions and circulation patterns are very similar in November. In December (Figures 96–98) the Bering Strait surface current is practically blocked by northeast winds as a result of intensification of the Aleutian Low. The Alaskan coastal current is reversed, and there is a tendency toward formation of an anticyclonic surface water circulation around Wrangel Island. The patterns of the NCAR, FNOC, and ECMWF pressure fields and currents are similar except for some differences in the intensity of the Aleutian Low, and some differences in the location and intensity of the Arctic High. The maximum surface current velocity obtained using ECMWF data is 65 cm/s, which is 20 cm/s higher than velocities represented by the NCAR and FNOC data. Patterns of atmospheric pressure and currents in January (Figures 99–101) are very similar to distributions of atmospheric pressure and currents in November, except that the atmospheric pressure gradients are larger, resulting in higher velocities in the surface currents. The NCAR data show a maximum velocity of 65 cm/s; the FNOC and ECMWF data show 71 cm/s and 82 cm/s, respectively. February (Figures 102–104) and March (not shown) pressure distributions and currents in the Chukchi Sea are close to November patterns when the Alaskan coastal current is reversed and the major flow from Bering Strait goes along the Chukotka coastline to the East Siberian Sea. From April to September (April and June are shown in Figures 105–110) the Chukchi Sea circulation is more or less stable and is very close to the climate patterns described by Aagaard (1988), Coachman and Aagaard (1988), and many others.

Figures 111–122 show bottom circulation and sea level variability in the Chukchi Sea as derived from NCAR-, FNOC-, and ECMWF-based simulations. Bottom currents flow along depth contours. These currents are more stable than surface currents, and differences among NCAR, FNOC, and ECMWF results are much smaller than among the patterns of the surface currents. During the entire year, the bottom currents are directed toward the north through Bering Strait and do not show blockage of the Bering Strait water transport in winter.

4.8 Comparisons of Water Trajectories

Water parcel trajectories are shown in Figures 123–125 for surface, bottom, and vertically integrated currents based on simulations using the NCAR, FNOC, and ECMWF data. Water parcels were released in four points of the section across Bering Strait on 1 October 1991. Maximum divergence among trajectories of parcels representing NCAR, FNOC, and ECMWF atmospheric pressures is observed in the surface data because of the higher velocities of the surface currents. The trajectories of NCAR, FNOC, and ECMWF parcels, which represent vertical mean and bottom currents during the first month of motion, are very similar. Trajectories of the surface parcels representing NCAR, FNOC, and ECMWF data repeat each other during the first 5–8 days only. This is important for calculations of the pollutant transport because it demonstrates that all three sources (NCAR, FNOC, and ECMWF) of atmospheric pressure can be equally successfully used for prediction of contaminant motion in the Chukchi Sea.

The dependence of the trajectory on the different components of water velocity is extremely variable. In our case of the barotropic sea, there are two components of the water currents: a wind-driven current, and a current generated by the sea level slope between the Pacific and the Arctic Oceans. From experiments carried out we conclude that the role of the permanent current (the current induced by sea level slope between the Pacific and the Arctic Ocean) gradually decreases toward North from the Bering Strait area. This is very well manifested not only in the trajectories of the water parcels, which move with the bottom and vertically mean velocities but with the surface water currents as well (Figures 123–125).

The derived patterns (Figures 123–125) suggest that parcel trajectories depend strongly on initial position and time of release. The latter dependence is very important in simulations and investigations of contaminant transport.

We identify two regimes of the Arctic system decadal variability (Proshutinsky and Johnson, 1997), which correspond to the cyclonic and anticyclonic circulation of the Arctic atmosphere and ocean with “cold and dry” and “warm and wet” atmospheres, and “cold and saltier” and “warm and fresh” ocean water, respectively. Shifts from one regime to another are forced by changes in location and intensity of the Icelandic Low and the Siberian High. Wind-driven ice and water motion in the Arctic alternates between anticyclonic circulation regime (AACR) and cyclonic circulation regime (CCR), with each regime persisting for 5–7 years (period is 10–15 years). Understanding the two circulation regimes is useful for investigating the temporal and spatial variability of ice, water and pollutant transport in the Arctic Ocean and in the Beaufort and Chuckhi seas. For example, in Figure 126 and Figure 127 we present the trajectories of water and ice markers released monthly beginning in Bering Strait for a period of anticyclonic and cyclonic regimes. NCAR atmospheric pressure and a 2-D model of the entire Arctic Ocean was used for this simulation.

Water markers moving with vertically averaged velocities have comparatively stable trajectories following bathymetric features and consistent with the two circulation regimes. Parcels released in Bering

Strait have trajectories with both cyclonic and anticyclonic rotation. During anticyclonic regimes (Figure 126, left column) they move with the Alaskan Branch of coastal current and after reaching a longitude of about 140°W they become involved into the Arctic Ocean Transpolar Drift system and move generally anticyclonically. During cyclonic circulation regimes (Figure 126, right column) the water parcels again move from the Bering Strait with the Alaskan coastal current but closer to the coastline than in the case of anticyclonic circulation regime. After that they usually cross longitude 140°W and continue their motion toward straits of Canadian Archipelago or to Fram Strait along coastline of Canadian Archipelago forming a cyclonic type circulation.

Ice trajectories (Figure 127) are more variable because of the direct wind influence. Tracks of the ice motion can be found everywhere in the Arctic basin with a maximum concentration in the Beaufort Sea and along the core of the Trans-Arctic Current but one can easily distinguish between anticyclonic and cyclonic regimes of circulation. It is important for arctic studies to know which regime prevails any time.

5.0 Conclusions

We have investigated the differences among three nominally identical wind field representations derived from surface atmospheric pressure fields prepared by ECMWF, FNOC, and NCAR. We have analyzed wind data from the National Weather Service offices at Barrow and Kotzebue, Alaska, to examine differences between observed and estimated winds. We have investigated ice-drifting buoy data from the International Arctic Buoy Program to examine differences between observed and simulated ice drift, and we have used 2-D and 3-D numerical models to analyze differences in shelf circulation, as forced by the three wind fields.

The results of this study demonstrate that the ECMWF sea level atmospheric pressure data with a spatial resolution of 1.125° and a temporary resolution of six hours can be recommended as the best source of wind forcing. The FNOC atmospheric pressure fields with a spatial resolution of 2.5° and a temporal resolution of six hours can be recommended as well, in the absence of ECMWF data. NCAR data with a spatial resolution of about 350 km and a temporal resolution of 12 hours can be used successfully for climatology studies. All three sources of atmospheric pressure can be used with equal success in the Chukchi Sea for predictions of pollutant transport for a period of 5–8 days.

6.0 Recommendations

Comparison between observed and simulated currents in the Chukchi Sea demonstrates that some effects are not reproduced by the 3-D barotropic model. These effects include baroclinicity and thermodynamic processes related to ice formation and ice decay. A 3-D dynamic thermodynamic coupled ice–ocean model can be recommended for determining the seasonal and interannual variability of Chukchi Sea water dynamics and ice conditions. It will allow an investigation of variability of currents due to air–ice–ocean interactions, formation of baroclinic jets (Aagaard, 1988), and investigation of processes related to convection, water salinization, and freshening during ice formation and melting. The latter is important for simulations and predictions of pollutant transport because vertical motions play a significant role in redistribution of contaminants.

Acknowledgments

We acknowledge the support provided by the Minerals Management Service (MMS) and the Coastal Marine Institute (CMI) under task order 14194. We would like to acknowledge support for this work from the Wadati Fund (Geophysical Institute, University of Alaska Fairbanks). We extend our appreciation to Dr. Richard Prentki , contracting officer's technical representative (MMS), Dr. Susan Hills, CMI project coordinator , and reviewers of this project for very valuable comments and advises. Numerical computations were carried out using the CRAY Y-MP located at the University of Alaska Fairbanks.

References

Aagaard, K. 1988. Current, CTD, and pressure measurements in possible dispersal regions of the Chukchi Sea. Outer Continental Shelf Environmental Assessment Program (OCSEAP) Final Reports of Principal Investigators 57: 255–333.

Aagaard, K., C. H. Pease and S. A. Salo. 1990. Beaufort Sea mesoscale circulation study: Preliminary results. Outer Continental Shelf Environmental Assessment Program (OCSEAP) [1988] Final Reports of Principal Investigators 65: 137–304.

Blumberg, A. F. and G. S. Mellor. 1983. Diagnostic and prognostic numerical circulation studies of the South Atlantic Bight. J. Geophys. Res. 88(C8): 4579–4592.

Coachman, L. K. and K. Aagaard. 1988. Transports through Bering Strait: Annual and inter-annual variability. J. Geophys. Res. 93: 15535–15539.

Coachman, L. K., K. Aagaard and R. B. Tripp. 1975. Bering Strait: The Regional Physical Oceanography. University of Washington Press, Seattle. 172 pp.

Kowalik, Z. 1981. A study of the M2 tide in the ice-covered Arctic Ocean: Modeling, identification and control. Norw. Res. Bull. 2(4): 201–223.

Kowalik, Z. and A. Proshutinsky. 1994. Diurnal tides in the Arctic Ocean. J. Geophys. Res. 98(C9): 16449–16468.

Kozo, T. L. 1979. Evidence for sea breezes on the Alaskan Beaufort Sea coast. Geophys. Res. Lett. 6(11): 849–852.

Kozo, T. L. 1982. An observational study of sea breezes along the Alaskan Beaufort Sea coast: Part I. J. Appl. Meteorol. 12(7): 891–905.

Kozo, T. L. 1984. Mesoscale meteorology of the Norton Sound. Outer Continental Shelf Environmental Assessment Program (OCSEAP) Final Reports of Principal Investigators 39: 1–102.

Kozo, T. L. and R. Q. Robe. 1986. Modeling winds and open-water buoy drift along Eastern Beaufort Sea coast. J. Geophys. Res. 91(C11): 13011–13022.

McPhee, M. G. 1980. An analysis of pack ice drift in summer. Pp. 62–75 *in:* Proceedings of the AIDJEX Symposium, University of Washington Press, Seattle.

Overland, J. E. and A. T. Roach. 1987. Northward flow in the Bering and Chukchi seas. J. Geophys. Res. 92(C7): 7097–7105.

Pacific Northwest Laboratory. 1983. Wind Energy Resource Atlas, Volume 10 – Alaska. Battelle, PNL-3195 WERA-10, 183 p.

Proshutinsky, A. Y. 1978. On the problem of numerical simulation of storm surges in the shelf zone of the arctic seas. Sov. Meteorol. Hydrol., translated from Russian by Allerton Press, Inc. 1: 72–79.

Proshutinsky, A. Y. 1986. On the problem of calculating the storm surge fluctuations of sea level and water circulation in the Chukchi Sea. Sov. Meteorol. Hydrol., translated from Russian by Allerton Press, Inc. 1: 54–61.

Proshutinsky, A. Y. 1988. Modeling seasonal fluctuations of the level of the Arctic Ocean. Sov. Meteorol. Hydrol., translated from Russian by Allerton Press, Inc. 2: 57–65.

Proshutinsky, A. Y. and M. A. Johnson. 1997. Two circulation regimes of the wind-driven Arctic Ocean. J. Geophys. Res. 102(C6): 12493–12514.

Roach, A. T., K. Aagaard, C. H. Pease, S. A. Salo, T. J. Weingartner, V. Pavlov and M. Kulakov. 1995. Direct measurements of transport and water properties through the Bering Strait. J. Geophys. Res. 100: 18443–18457.

Rothrock, D. A. 1975. The mechanical behavior of pack ice. Ann. Rev. Earth Planet. Sci. 3: 317–342.

Spaulding, M., T. Isaji, D. Mendelsohn and A. C. Turner. 1987. Numerical simulation of wind-driven flow through the Bering Strait. J. Phys. Oceanogr. 17: 1799–1816.

Schwerdtfeger, W. 1985. Mountain barrier effect on the flow of stable air north of Brooks Range. Pp. 204–208 *in:* G. Weller and S. A. Bowling (eds.), Climate of the Arctic. Geophysical Institute, University of Alaska Fairbanks.

Thorndike, A. S. and R. Colony. 1982. Sea ice motion in response to geostrophic winds. J. Geophys. Res. 87: 5845–5852.

Weingartner, T. J. and T. O. Proshutinsky. 1998. Modeling the circulation of the Chukchi Sea, Final Report, OCS Study MMS 98-0017. Coastal Marine Institute, University of Alaska, Fairbanks, 75 p.

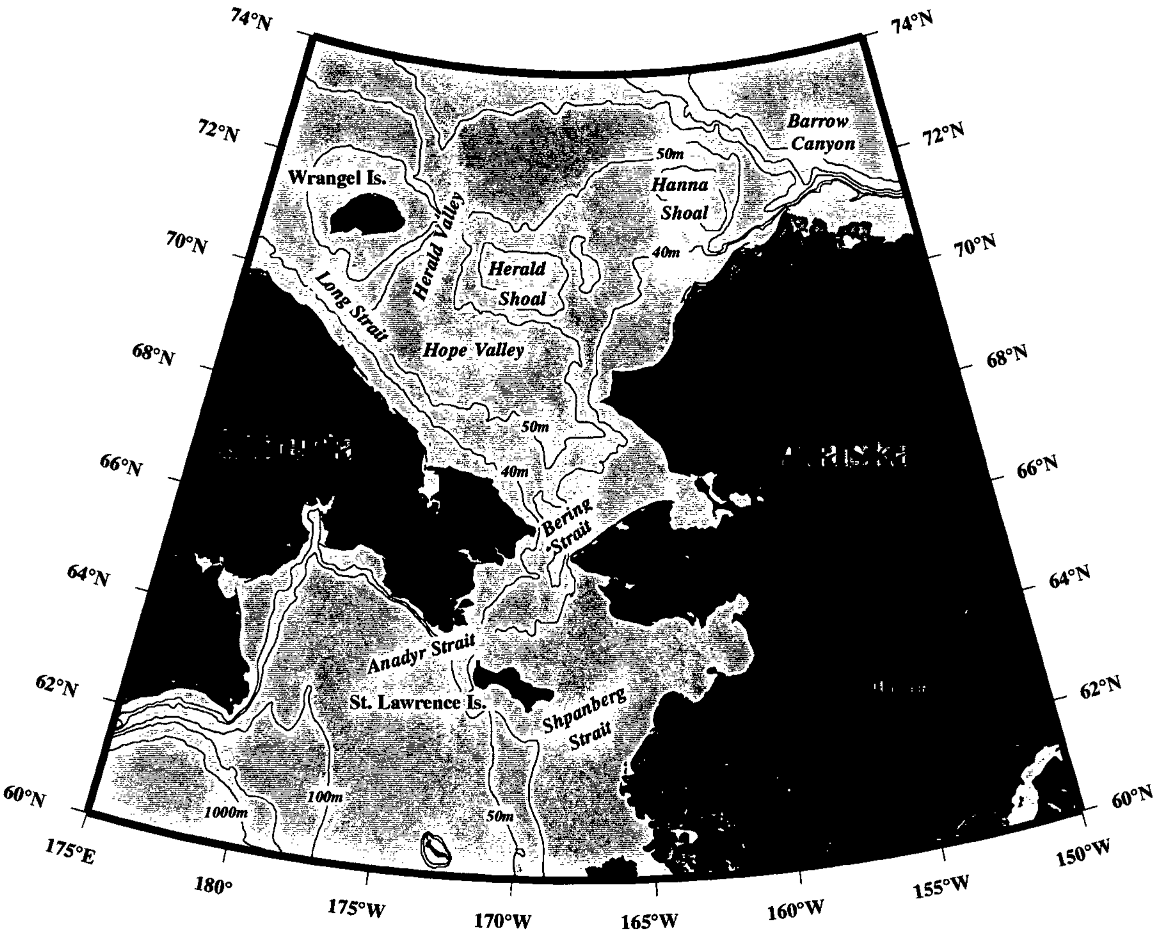

Figure 1. Bathymetric map of the Chukchi Sea.

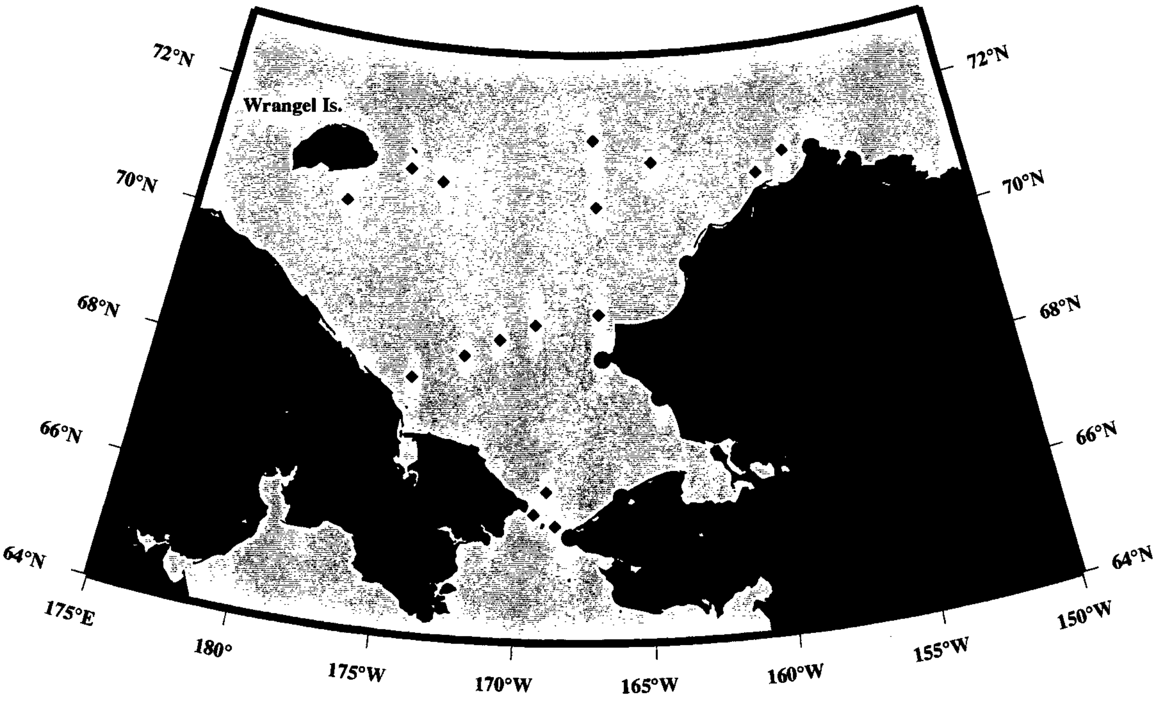

Figure 2. Location of moorings used for comparison with the model results.

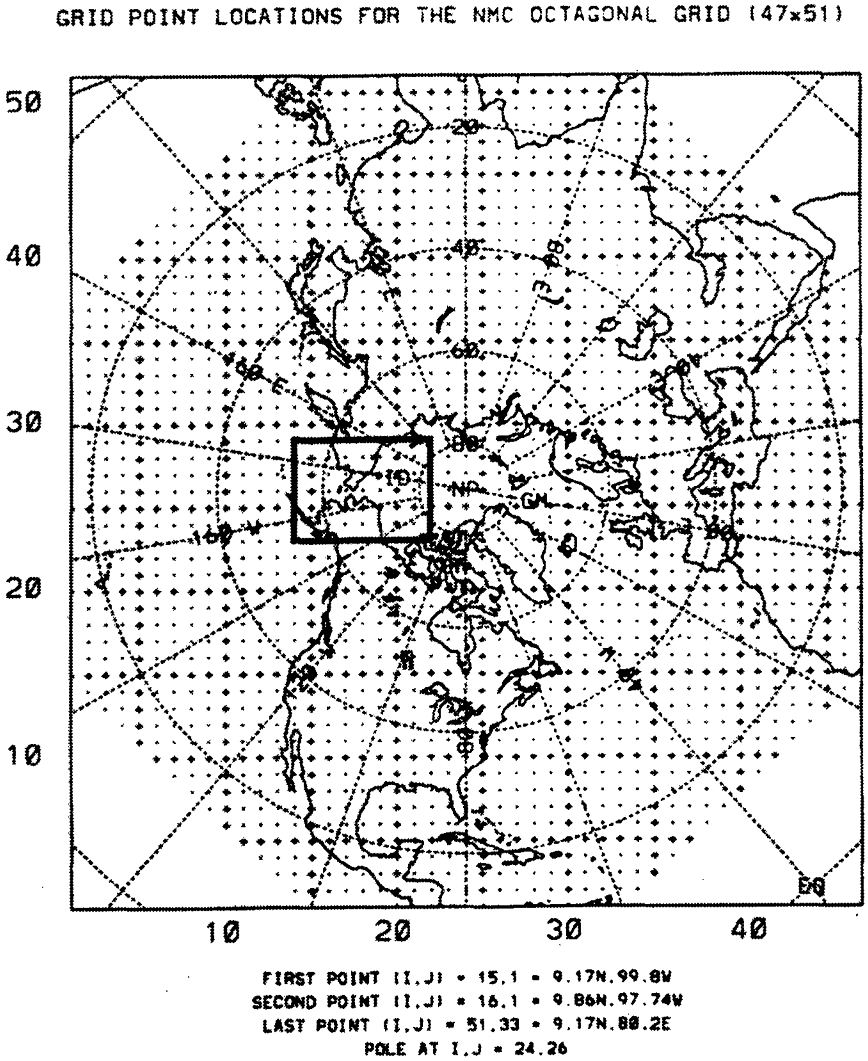

Figure 3. NCAR octagonal grid (47 x 51) for sea surface atmospheric pressure fields. Solid, thick, black line shows boundaries of the area under research.

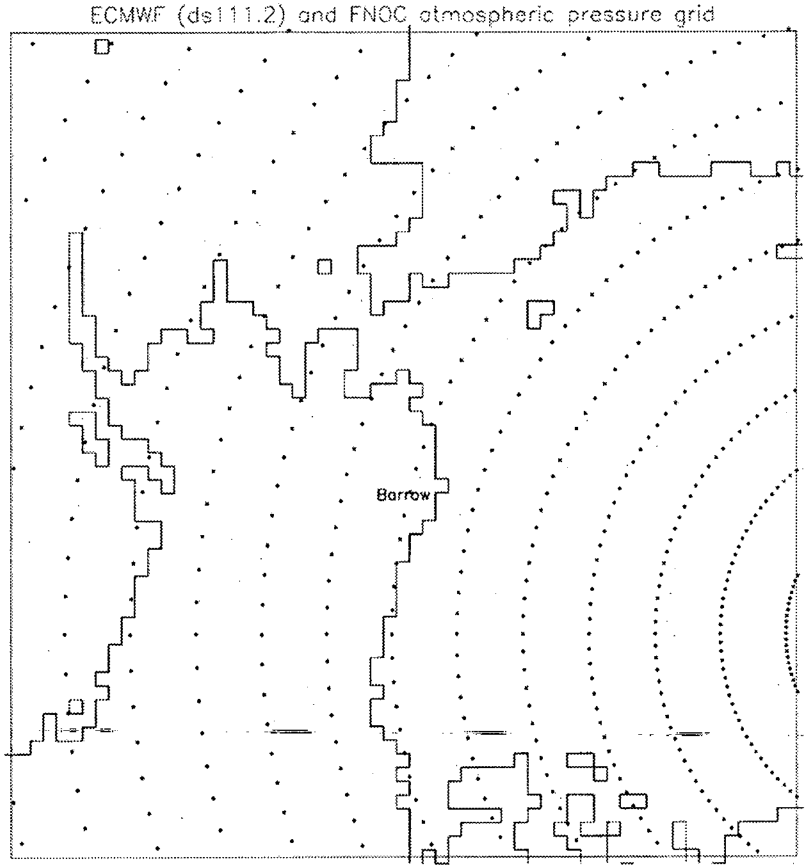

Figure 4. ECMWF and FNOC (13 x 41) 2.5° resolution grid for sea surface atmospheric pressure fields.

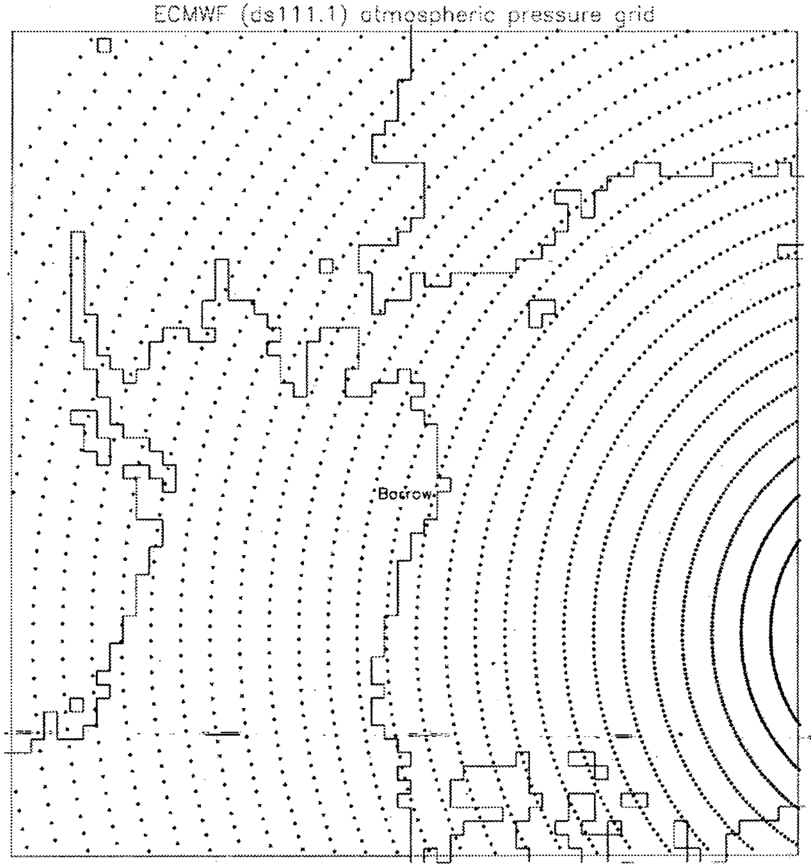

Figure 5. ECMWF 1.125° resolution grid for sea surface atmospheric pressure fields.

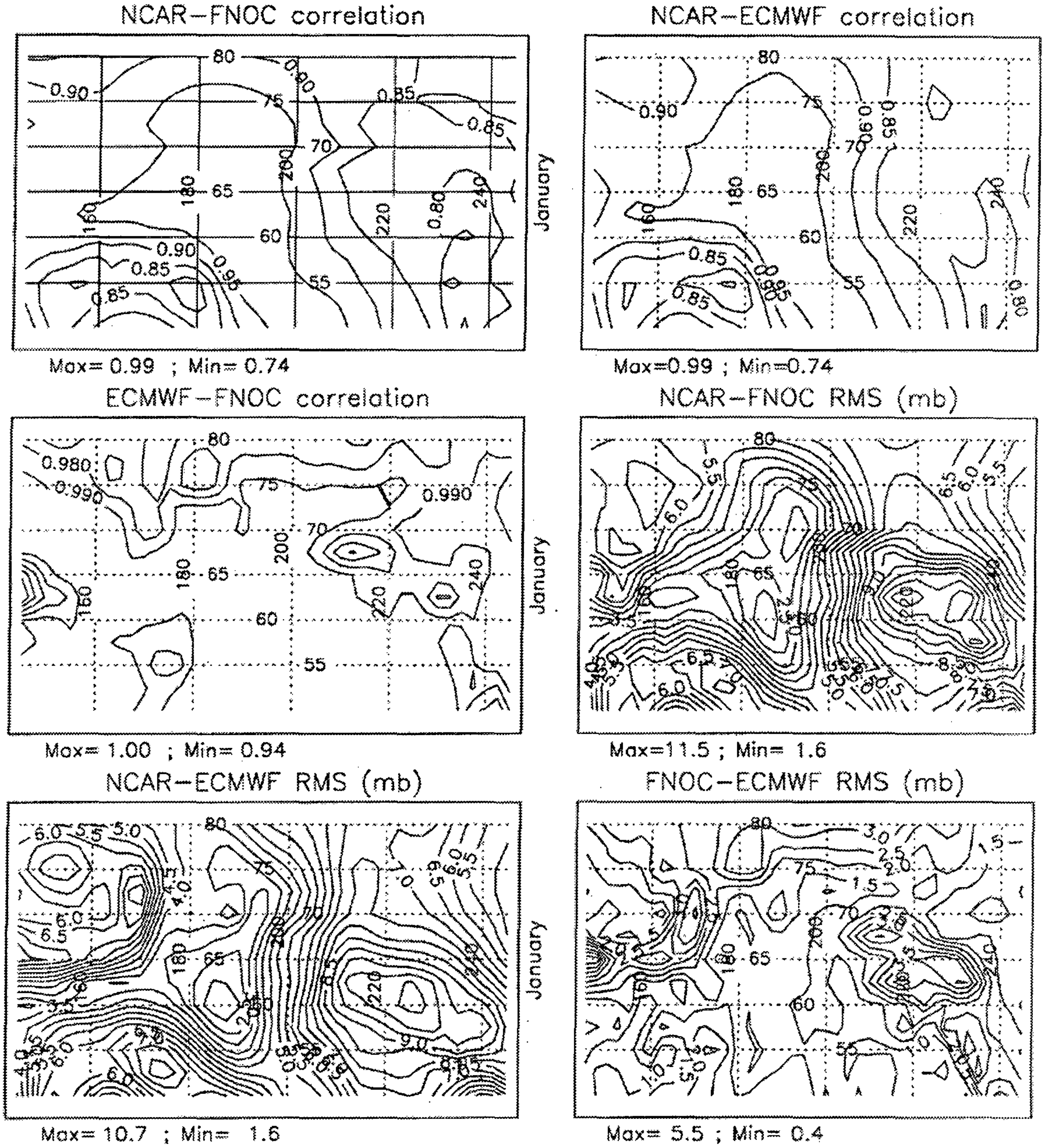

NCAR−FNOC correlation

Max= 0.99 ; Min= 0.74

NCAR−ECMWF correlation

Max=0.99 ; Min=0.74

ECMWF−FNOC correlation

Max= 1.00 ; Min= 0.94

NCAR−FNOC RMS (mb)

Max=11.5 ; Min= 1.6

NCAR−ECMWF RMS (mb)

Max= 10.7 ; Min= 1.6

FNOC−ECMWF RMS (mb)

Max= 5.5 ; Min= 0.4

Figure 6. Spatial distribution of correlation coefficients and spatial distribution of RMS among NCAR, FNOC, and ECMWF sea level atmospheric pressure fields in January of 1991.

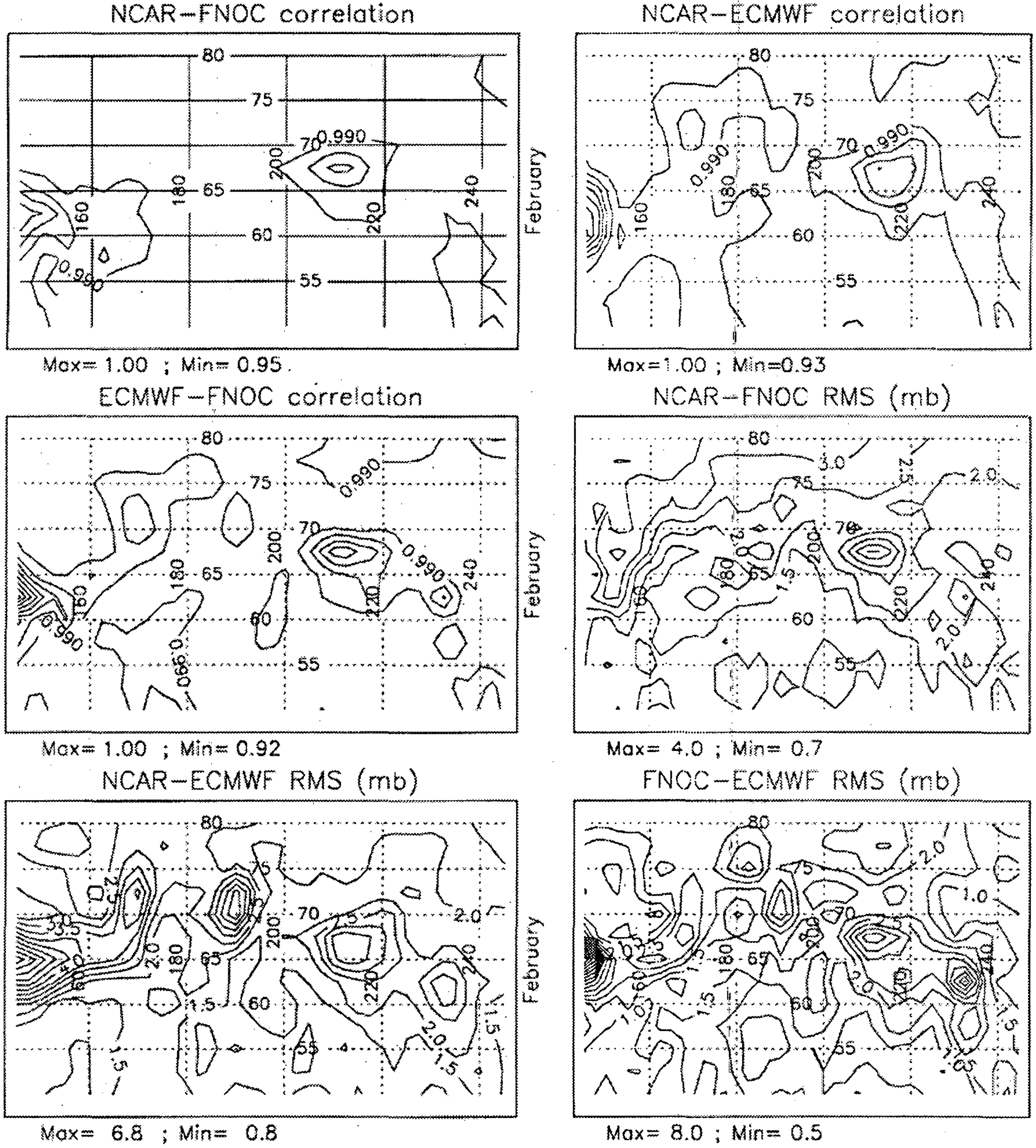

Figure 7. Spatial distribution of correlation coefficients and spatial distribution of RMS among NCAR, FNOC, and ECMWF sea level atmospheric pressure fields in February of 1991.

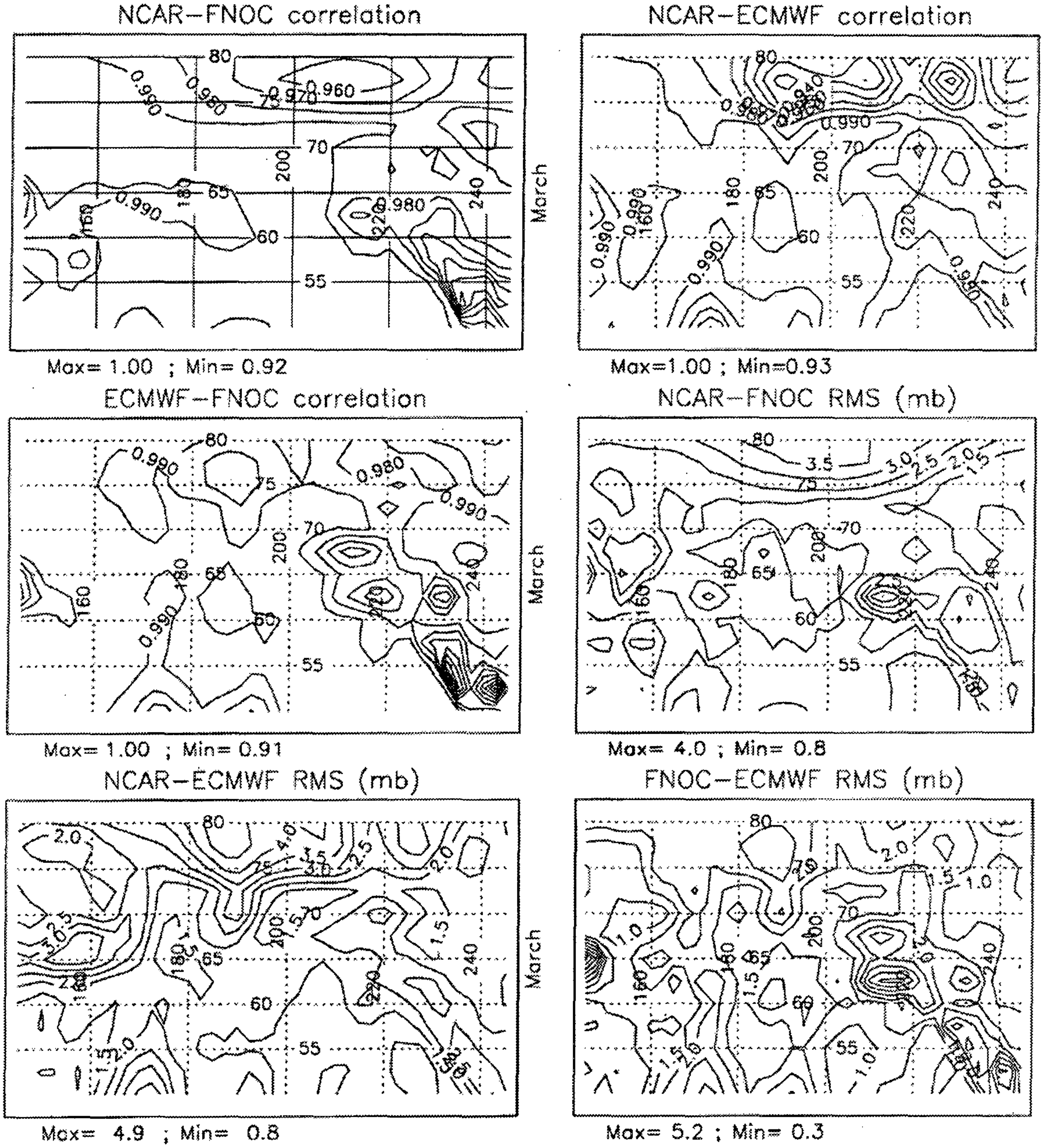

Figure 8. Spatial distribution of correlation coefficients and spatial distribution of RMS among NCAR, FNOC, and ECMWF sea level atmospheric pressure fields in March of 1991.

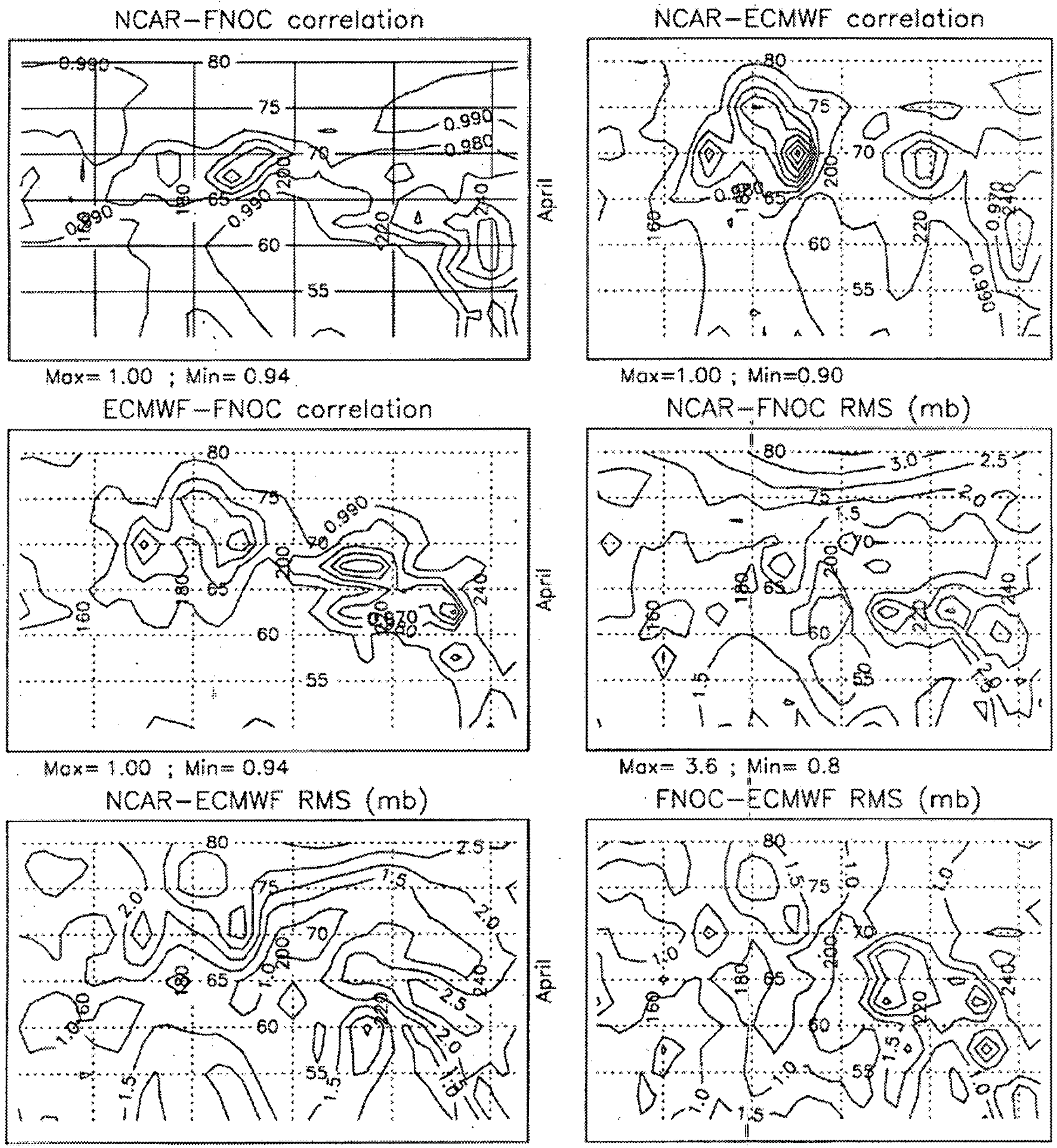
NCAR–FNOC correlation

Max= 1.00 ; Min= 0.94

NCAR–ECMWF correlation

Max=1.00 ; Min=0.90

ECMWF–FNOC correlation

Max= 1.00 ; Min= 0.94

NCAR–FNOC RMS (mb)

Max= 3.6 ; Min= 0.8

NCAR–ECMWF RMS (mb)

Max= 3.3 ; Min= 0.6

FNOC–ECMWF RMS (mb)

Max= 3.2 ; Min= 0.4

Figure 9. Spatial distribution of correlation coefficients and spatial distribution of RMS among NCAR, FNOC, and ECMWF sea level atmospheric pressure fields in April of 1991.

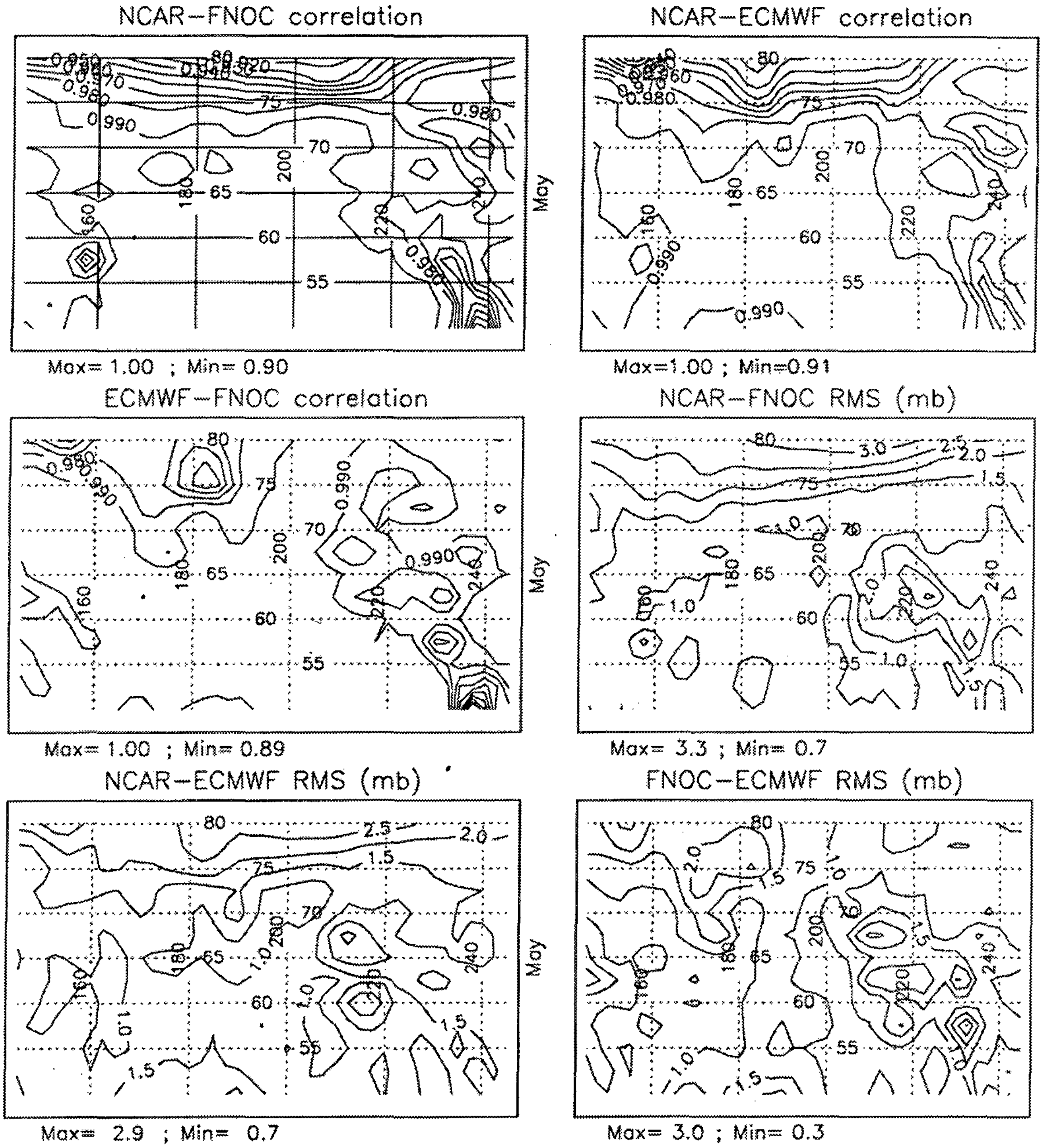

NCAR–FNOC correlation

Max= 1.00 ; Min= 0.90

NCAR–ECMWF correlation

Max=1.00 ; Min=0.91

ECMWF–FNOC correlation

Max= 1.00 ; Min= 0.89

NCAR–FNOC RMS (mb)

Max= 3.3 ; Min= 0.7

NCAR–ECMWF RMS (mb)

Max= 2.9 ; Min= 0.7

FNOC–ECMWF RMS (mb)

Max= 3.0 ; Min= 0.3

Figure 10. Spatial distribution of correlation coefficients and spatial distribution of RMS among NCAR, FNOC, and ECMWF sea level atmospheric pressure fields in May of 1991.

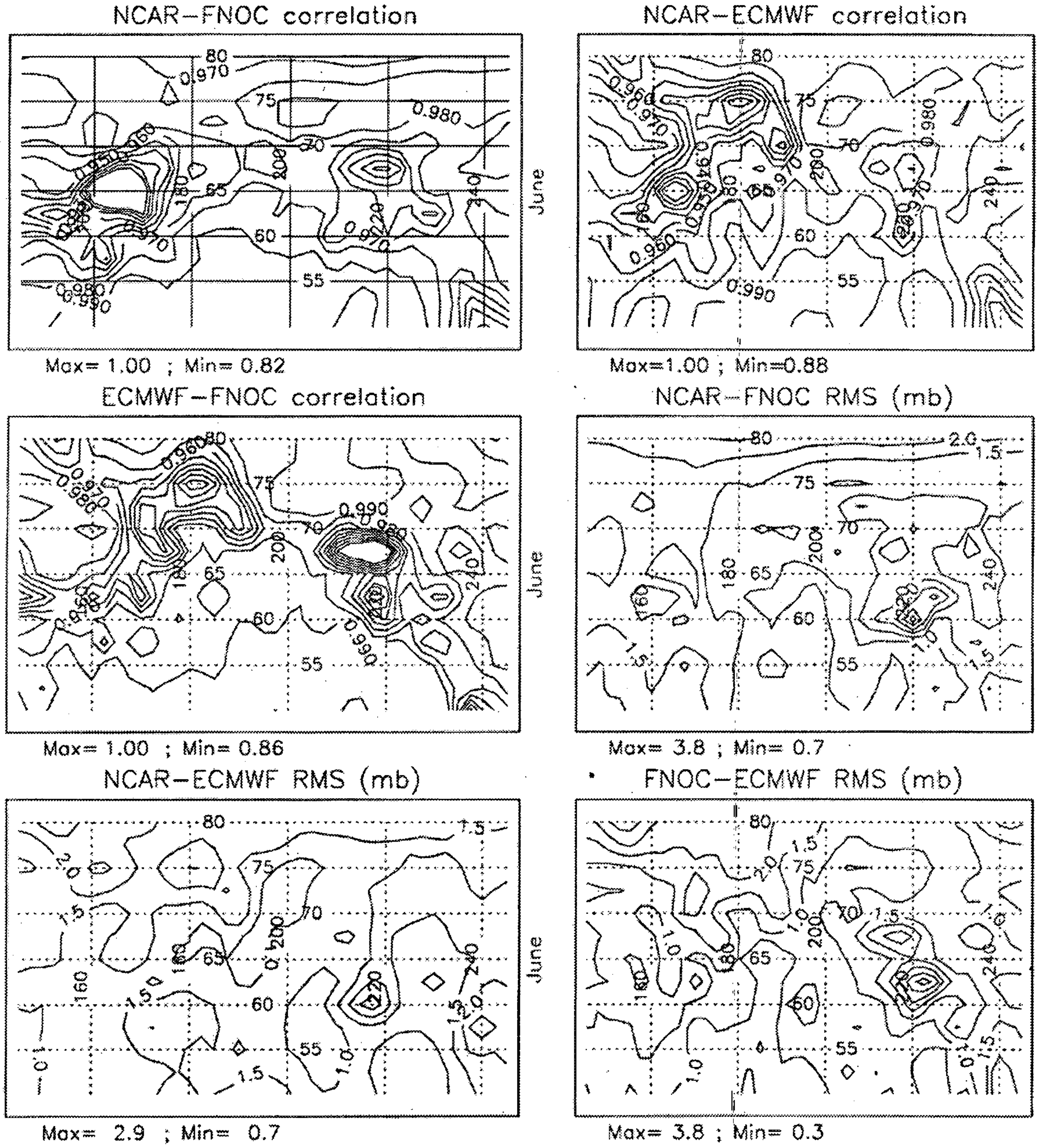

NCAR−FNOC correlation

Max= 1.00 ; Min= 0.82

NCAR−ECMWF correlation

Max=1.00 ; Min=0.88

ECMWF−FNOC correlation

Max= 1.00 ; Min= 0.86

NCAR−FNOC RMS (mb)

Max= 3.8 ; Min= 0.7

NCAR−ECMWF RMS (mb)

Max= 2.9 ; Min= 0.7

FNOC−ECMWF RMS (mb)

Max= 3.8 ; Min= 0.3

Figure 11. Spatial distribution of correlation coefficients and spatial distribution of RMS among NCAR, FNOC, and ECMWF sea level atmospheric pressure fields in June of 1991.

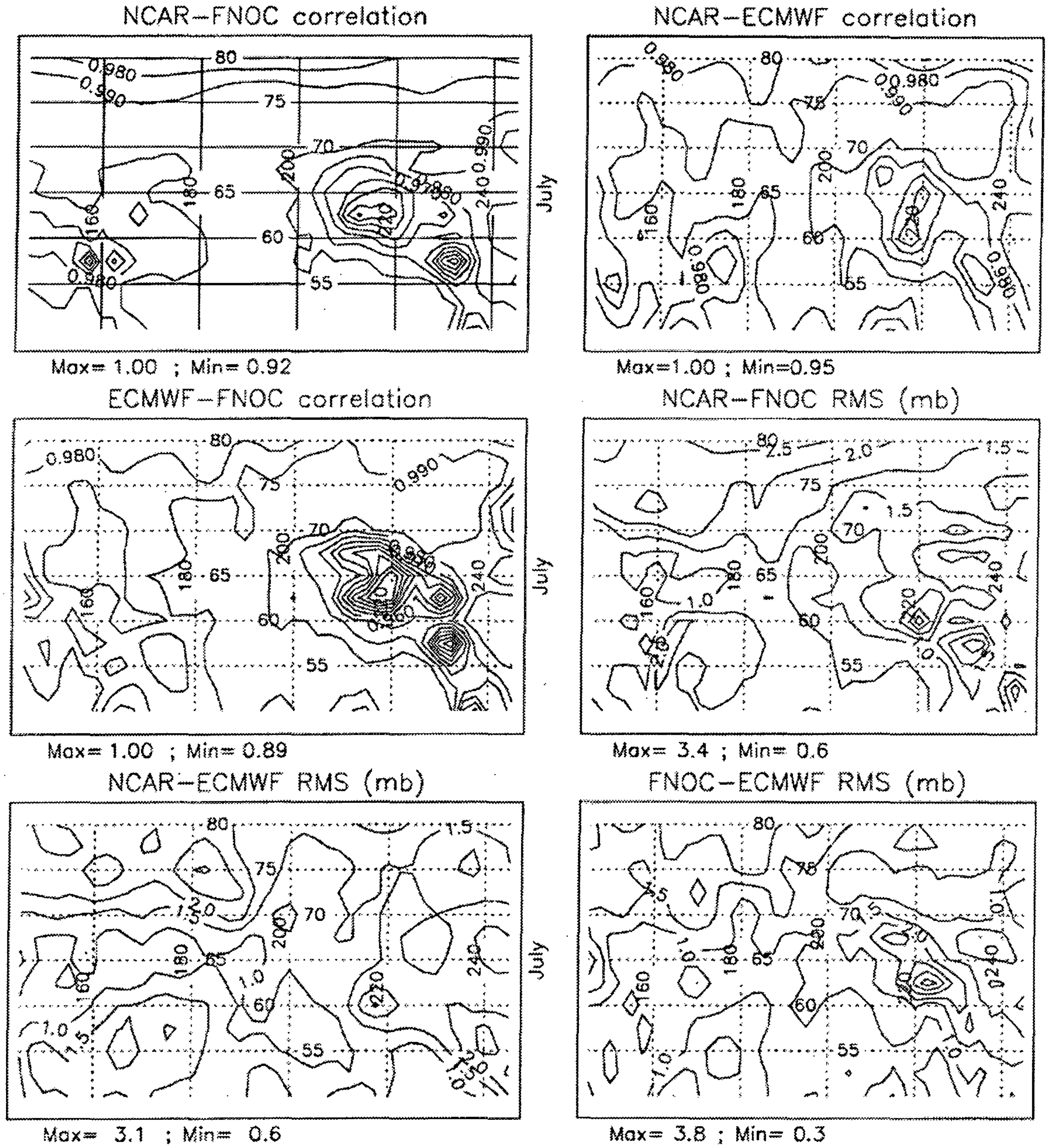

NCAR–FNOC correlation

Max= 1.00 ; Min= 0.92

NCAR–ECMWF correlation

Max=1.00 ; Min=0.95

ECMWF–FNOC correlation

Max= 1.00 ; Min= 0.89

NCAR–FNOC RMS (mb)

Max= 3.4 ; Min= 0.6

NCAR–ECMWF RMS (mb)

Max= 3.1 ; Min= 0.6

FNOC–ECMWF RMS (mb)

Max= 3.8 ; Min= 0.3

Figure 12. Spatial distribution of correlation coefficients and spatial distribution of RMS among NCAR, FNOC, and ECMWF sea level atmospheric pressure fields in July of 1991.

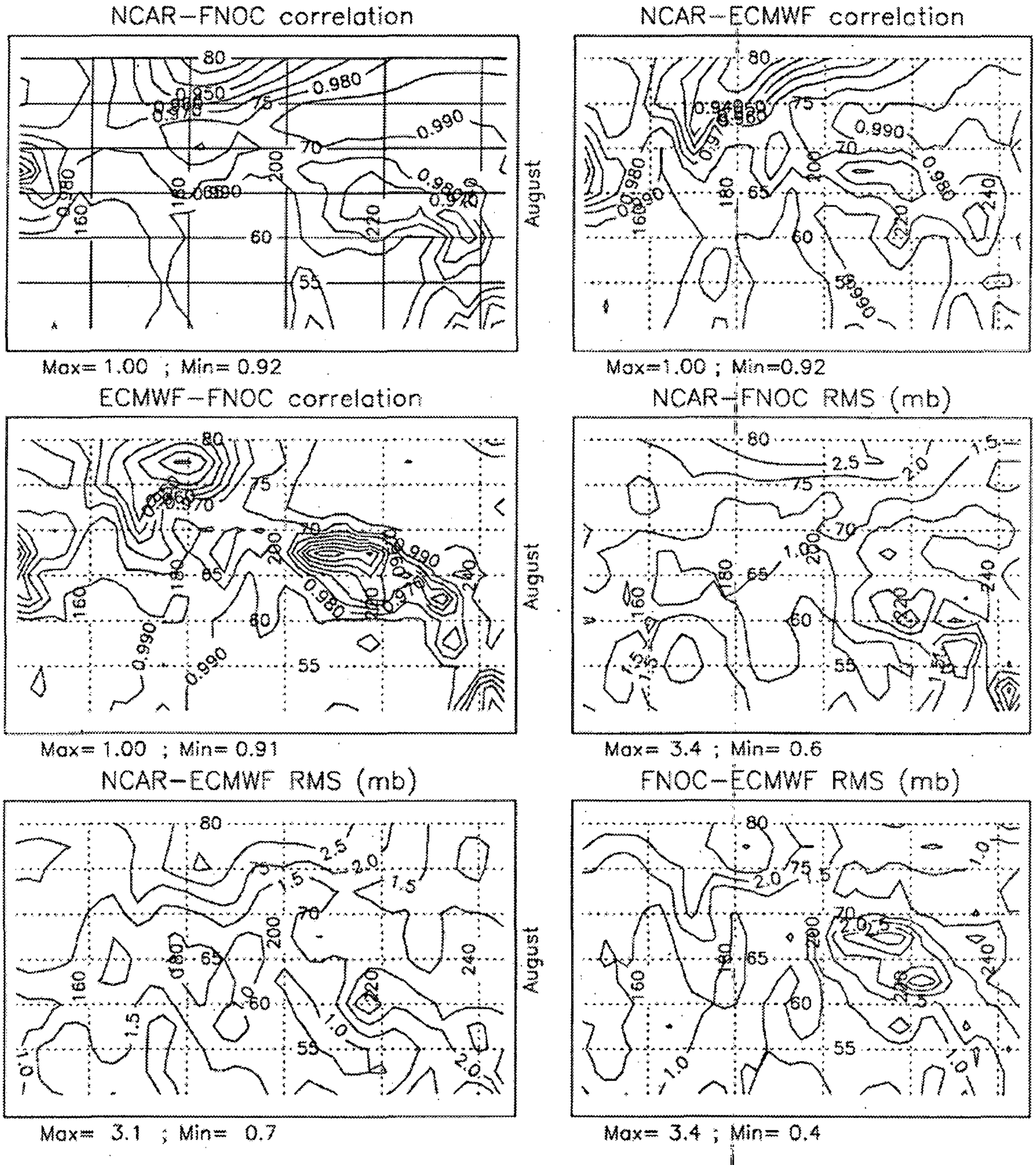

NCAR–FNOC correlation

Max= 1.00 ; Min= 0.92

NCAR–ECMWF correlation

Max=1.00 ; Min=0.92

ECMWF–FNOC correlation

Max= 1.00 ; Min= 0.91

NCAR–FNOC RMS (mb)

Max= 3.4 ; Min= 0.6

NCAR–ECMWF RMS (mb)

Max= 3.1 ; Min= 0.7

FNOC–ECMWF RMS (mb)

Max= 3.4 ; Min= 0.4

Figure 13. Spatial distribution of correlation coefficients and spatial distribution of RMS among NCAR, FNOC, and ECMWF sea level atmospheric pressure fields in August of 1991.

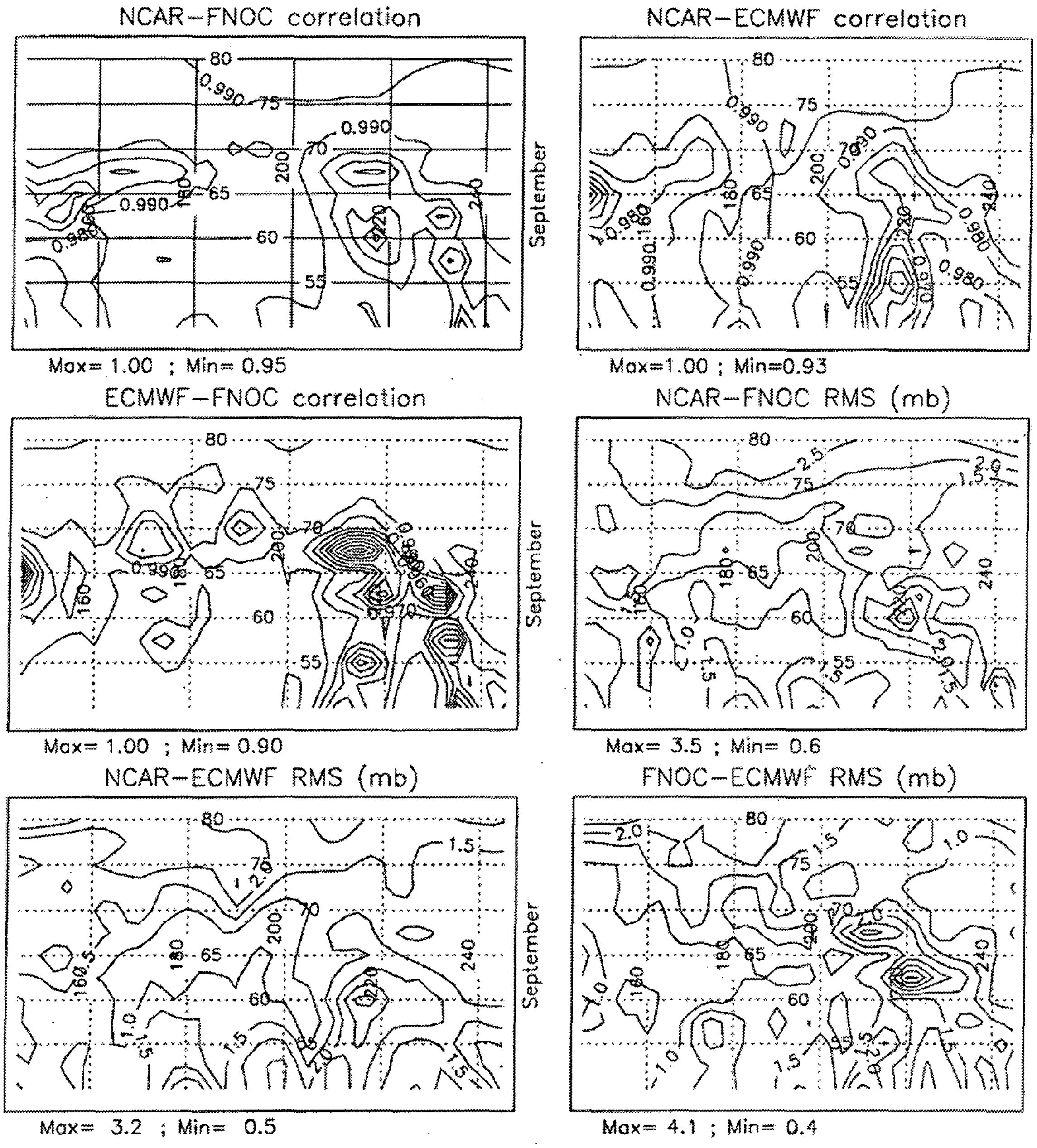

NCAR–FNOC correlation

Max= 1.00 ; Min= 0.95

NCAR–ECMWF correlation

Max=1.00 ; Min=0.93

ECMWF–FNOC correlation

Max= 1.00 ; Min= 0.90

NCAR–FNOC RMS (mb)

Max= 3.5 ; Min= 0.6

NCAR–ECMWF RMS (mb)

Max= 3.2 ; Min= 0.5

FNOC–ECMWF RMS (mb)

Max= 4.1 ; Min= 0.4

Figure 14. Spatial distribution of correlation coefficients and spatial distribution of RMS among NCAR, FNOC, and ECMWF sea level atmospheric pressure fields in September of 1991.

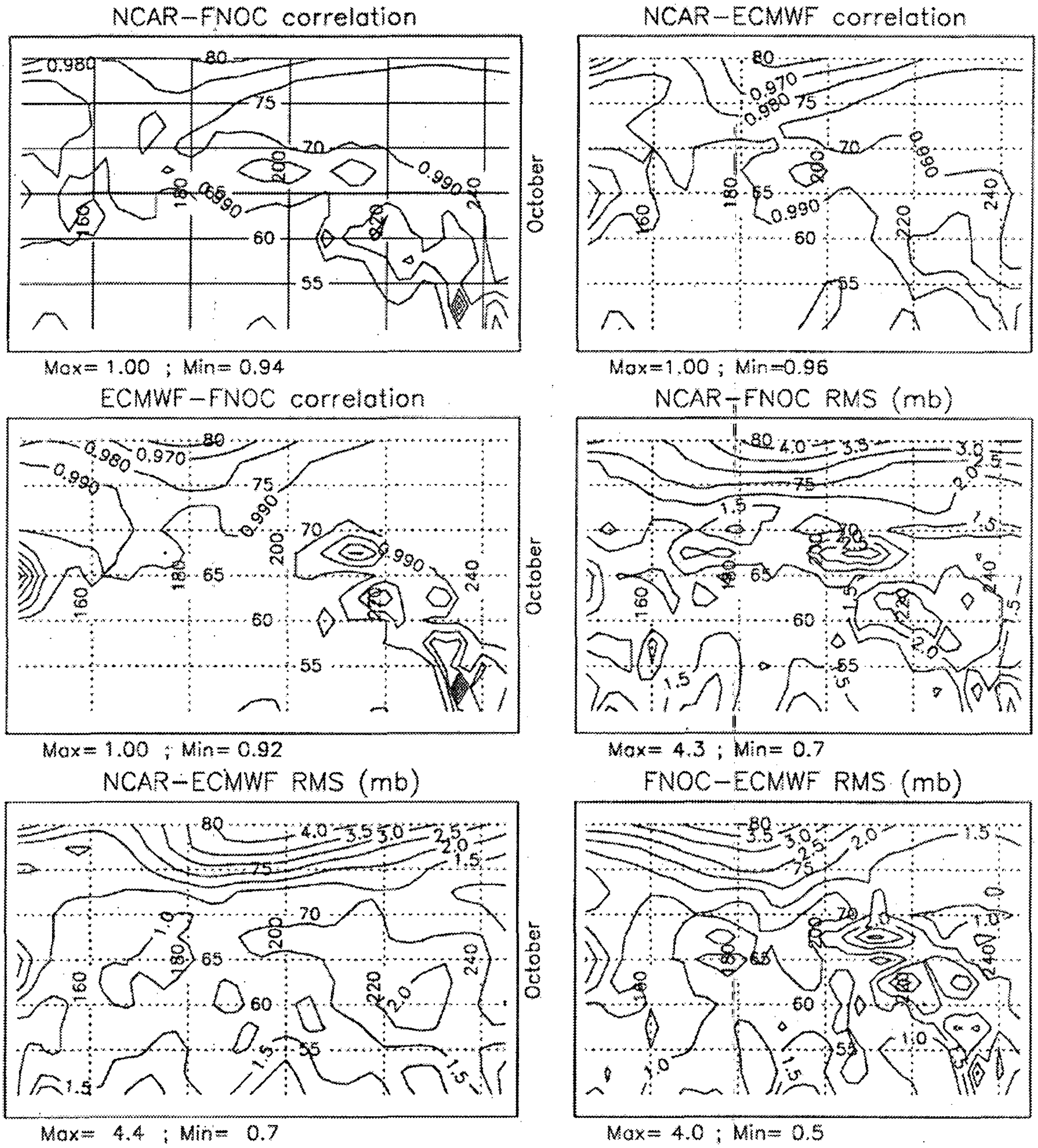

NCAR–FNOC correlation

Max= 1.00 ; Min= 0.94

NCAR–ECMWF correlation

Max=1.00 ; Min=0.96

ECMWF–FNOC correlation

Max= 1.00 ; Min= 0.92

NCAR–FNOC RMS (mb)

Max= 4.3 ; Min= 0.7

NCAR–ECMWF RMS (mb)

Max= 4.4 ; Min= 0.7

FNOC–ECMWF RMS (mb)

Max= 4.0 ; Min= 0.5

Figure 15. Spatial distribution of correlation coefficients and spatial distribution of RMS among NCAR, FNOC, and ECMWF sea level atmospheric pressure fields in October of 1991.

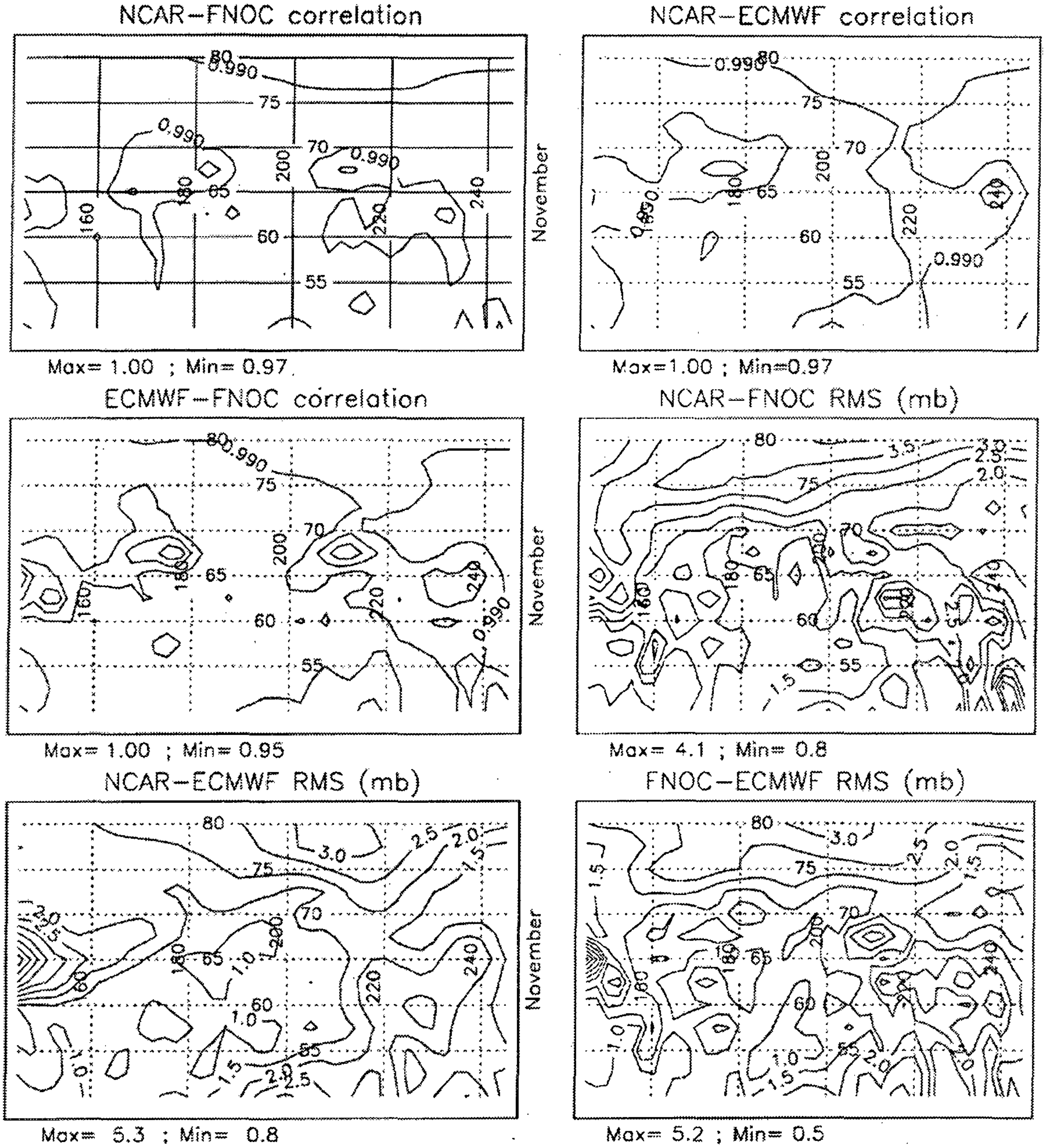

Figure 16. Spatial distribution of correlation coefficients and spatial distribution of RMS among NCAR, FNOC, and ECMWF sea level atmospheric pressure fields in November of 1991.

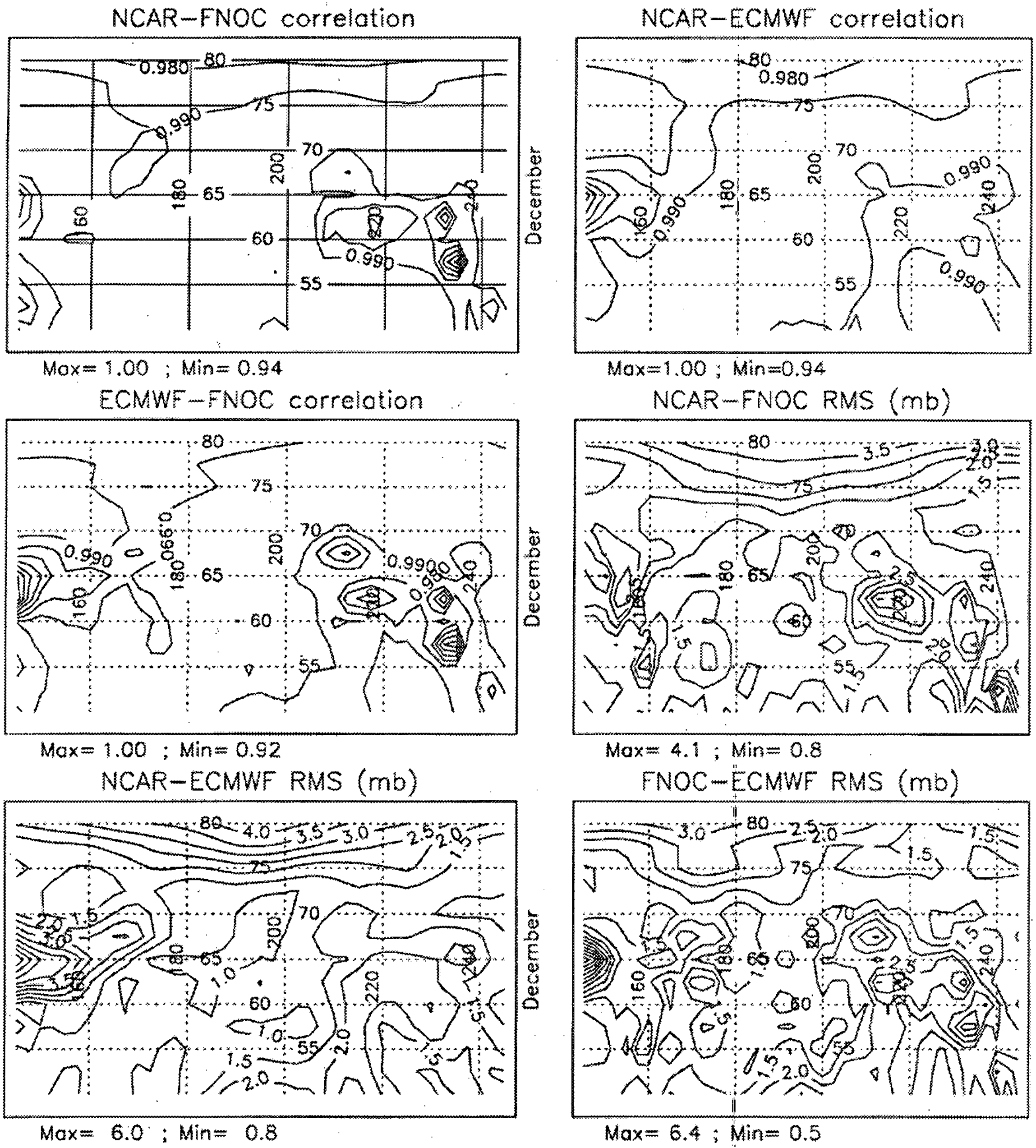

NCAR−FNOC correlation

Max= 1.00 ; Min= 0.94

NCAR−ECMWF correlation

Max=1.00 ; Min=0.94

ECMWF−FNOC correlation

Max= 1.00 ; Min= 0.92

NCAR−FNOC RMS (mb)

Max= 4.1 ; Min= 0.8

NCAR−ECMWF RMS (mb)

Max= 6.0 ; Min= 0.8

FNOC−ECMWF RMS (mb)

Max= 6.4 ; Min= 0.5

Figure 17. Spatial distribution of correlation coefficients and spatial distribution of RMS among NCAR, FNOC, and ECMWF sea level atmospheric pressure fields in December of 1991.

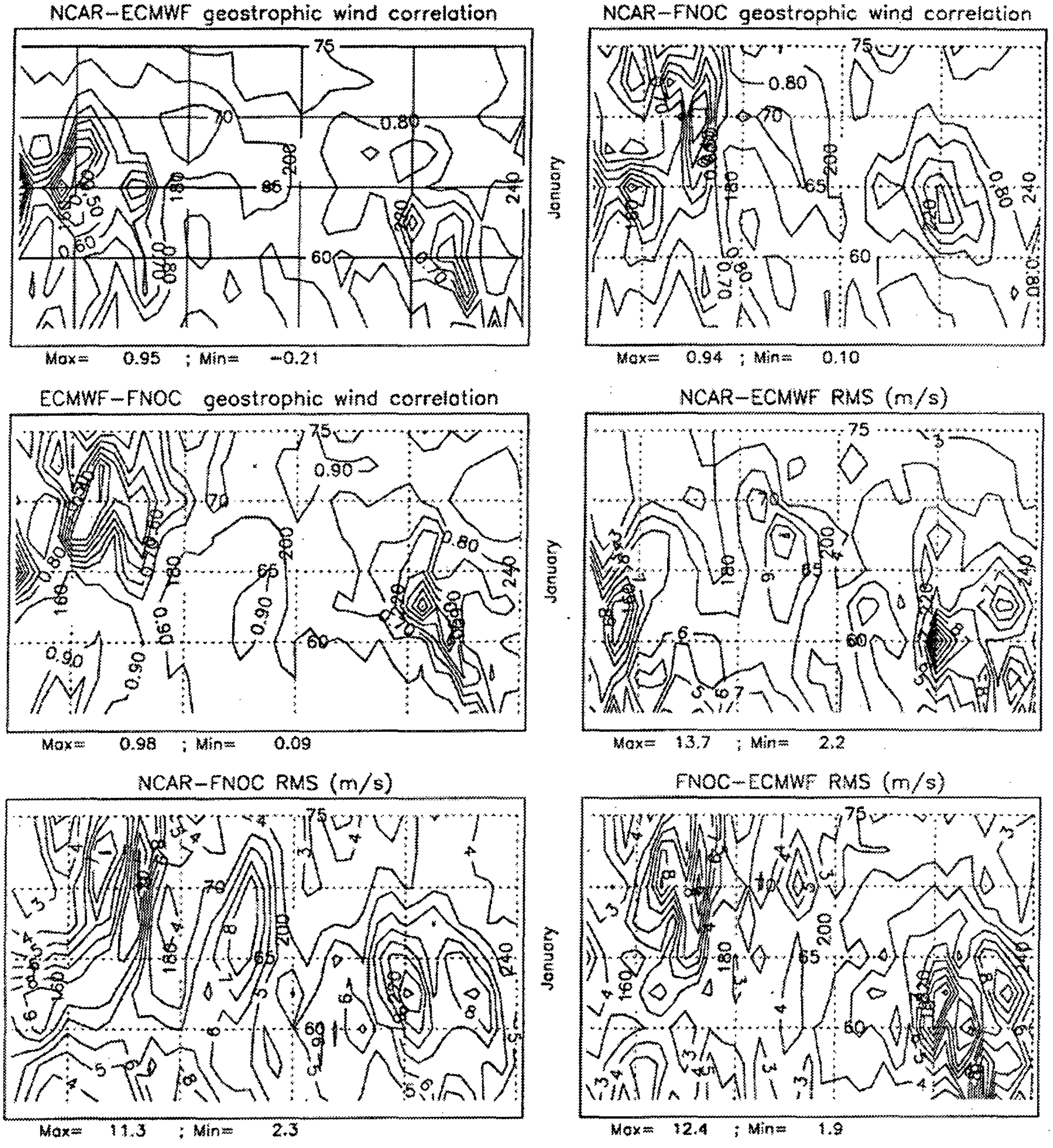

Figure 18. Spatial distribution of correlation coefficients and spatial distribution of RMS among NCAR, FNOC, and ECMWF speed of geostrophic winds in January of 1991.

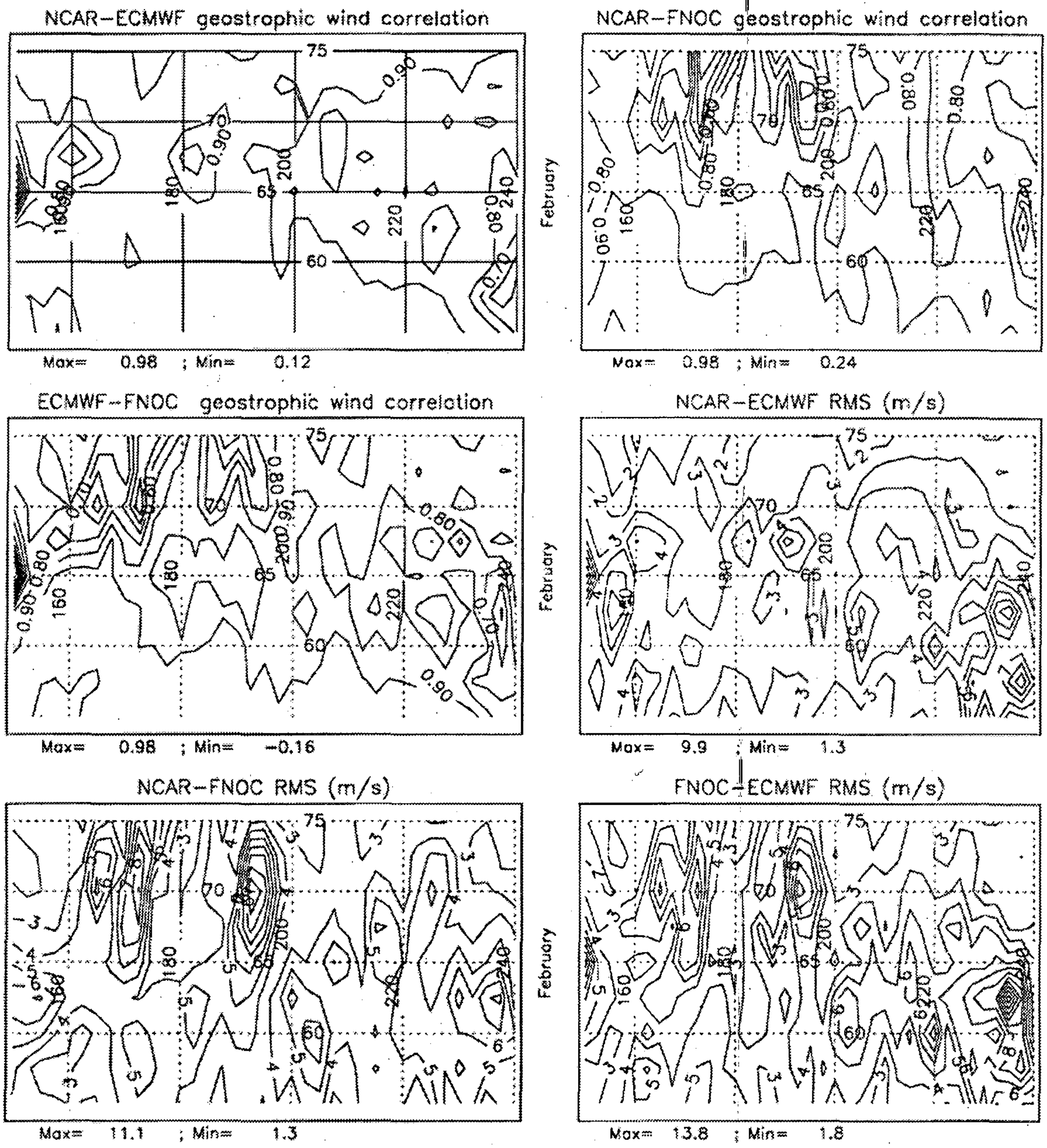

NCAR–ECMWF geostrophic wind correlation

Max= 0.98 ; Min= 0.12

NCAR–FNOC geostrophic wind correlation

Max= 0.98 ; Min= 0.24

ECMWF–FNOC geostrophic wind correlation

Max= 0.98 ; Min= −0.16

NCAR–ECMWF RMS (m/s)

Max= 9.9 ; Min= 1.3

NCAR–FNOC RMS (m/s)

Max= 11.1 ; Min= 1.3

FNOC–ECMWF RMS (m/s)

Max= 13.8 ; Min= 1.8

Figure 19. Spatial distribution of correlation coefficients and spatial distribution of RMS among NCAR, FNOC, and ECMWF speed of geostrophic winds in February of 1991.

NCAR−ECMWF geostrophic wind correlation

NCAR−FNOC geostrophic wind correlation

ECMWF−FNOC geostrophic wind correlation

NCAR−ECMWF RMS (m/s)

NCAR−FNOC RMS (m/s)

FNOC−ECMWF RMS (m/s)

Figure 20. Spatial distribution of correlation coefficients and spatial distribution of RMS among NCAR, FNOC, and ECMWF speed of geostrophic winds in March of 1991.

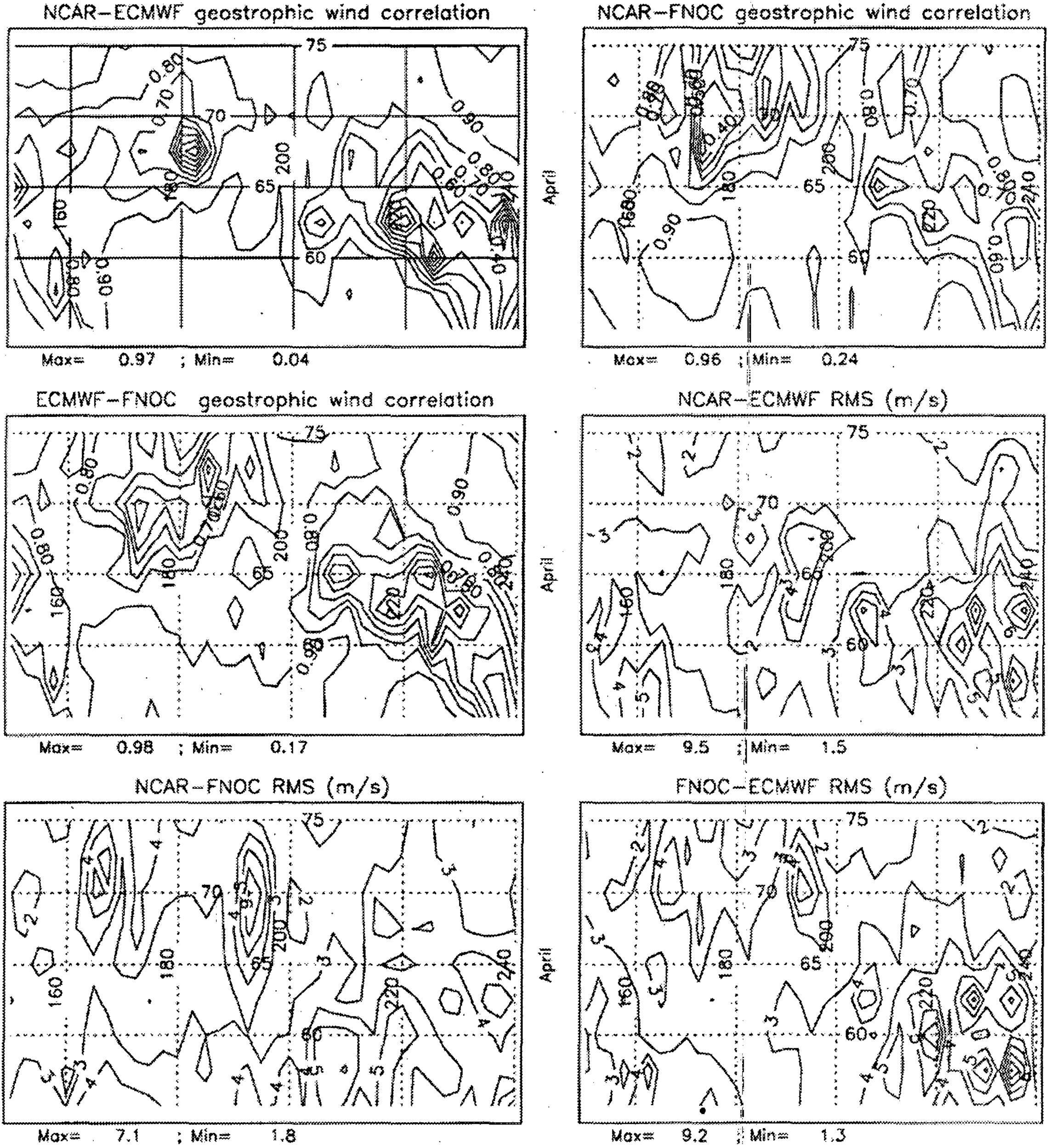
NCAR–ECMWF geostrophic wind correlation

Max= 0.97 ; Min= 0.04

NCAR–FNOC geostrophic wind correlation

Max= 0.96 ; Min= 0.24

ECMWF–FNOC geostrophic wind correlation

Max= 0.98 ; Min= 0.17

NCAR–ECMWF RMS (m/s)

Max= 9.5 ; Min= 1.5

NCAR–FNOC RMS (m/s)

Max= 7.1 ; Min= 1.8

FNOC–ECMWF RMS (m/s)

Max= 9.2 ; Min= 1.3

Figure 21. Spatial distribution of correlation coefficients and spatial distribution of RMS among NCAR, FNOC, and ECMWF speed of geostrophic winds in April of 1991.

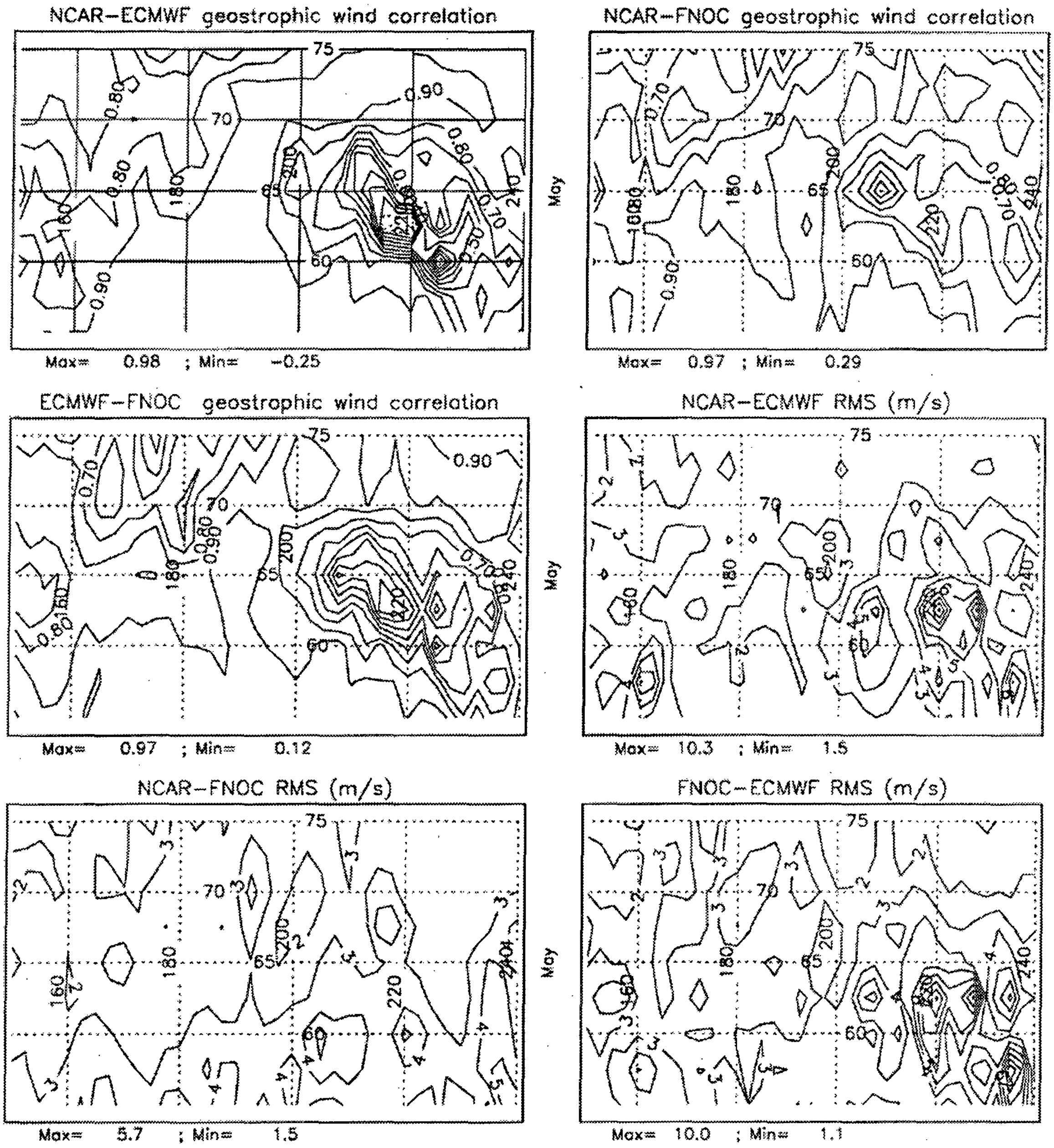
NCAR−ECMWF geostrophic wind correlation

Max= 0.98 ; Min= −0.25

NCAR−FNOC geostrophic wind correlation

Max= 0.97 ; Min= 0.29

ECMWF−FNOC geostrophic wind correlation

Max= 0.97 ; Min= 0.12

NCAR−ECMWF RMS (m/s)

Max= 10.3 ; Min= 1.5

NCAR−FNOC RMS (m/s)

Max= 5.7 ; Min= 1.5

FNOC−ECMWF RMS (m/s)

Max= 10.0 ; Min= 1.1

Figure 22. Spatial distribution of correlation coefficients and spatial distribution of RMS among NCAR, FNOC, and ECMWF speed of geostrophic winds in May of 1991.

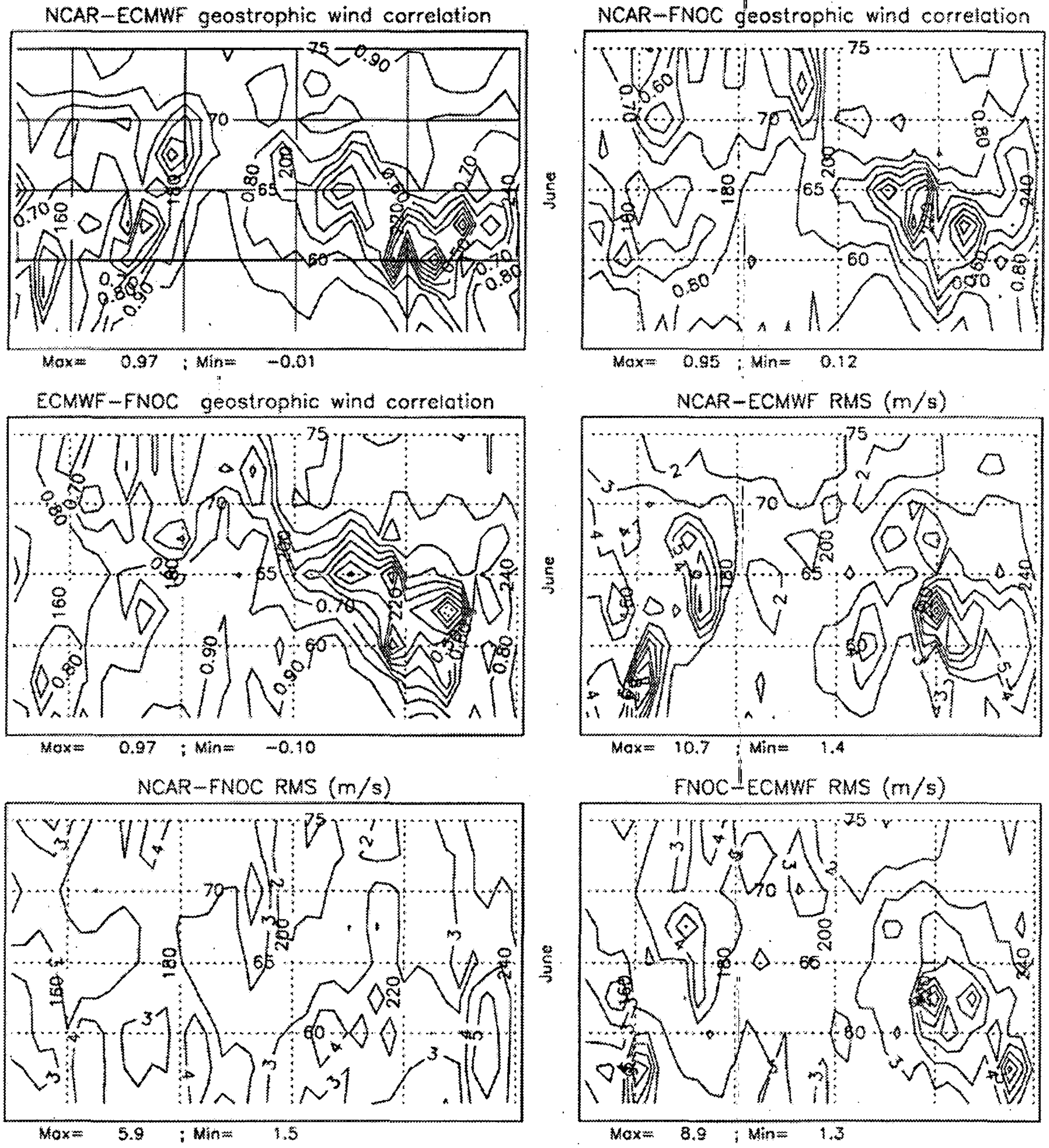

Figure 23. Spatial distribution of correlation coefficients and spatial distribution of RMS among NCAR, FNOC, and ECMWF speed of geostrophic winds in June of 1991.

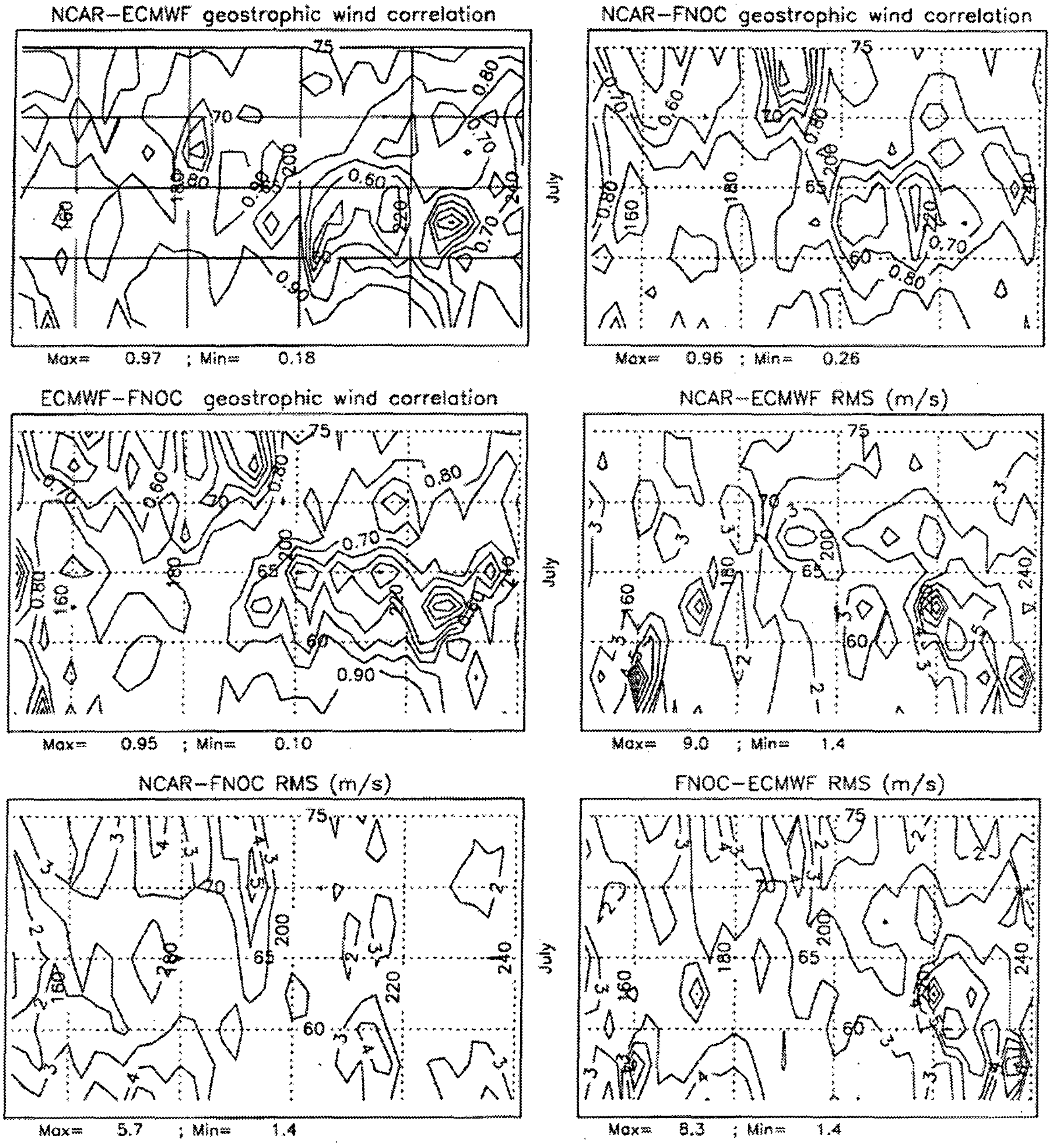
NCAR–ECMWF geostrophic wind correlation

Max= 0.97 ; Min= 0.18

NCAR–FNOC geostrophic wind correlation

Max= 0.96 ; Min= 0.26

ECMWF–FNOC geostrophic wind correlation

Max= 0.95 ; Min= 0.10

NCAR–ECMWF RMS (m/s)

Max= 9.0 ; Min= 1.4

NCAR–FNOC RMS (m/s)

Max= 5.7 ; Min= 1.4

FNOC–ECMWF RMS (m/s)

Max= 8.3 ; Min= 1.4

Figure 24. Spatial distribution of correlation coefficients and spatial distribution of RMS among NCAR, FNOC, and ECMWF speed of geostrophic winds in July of 1991.

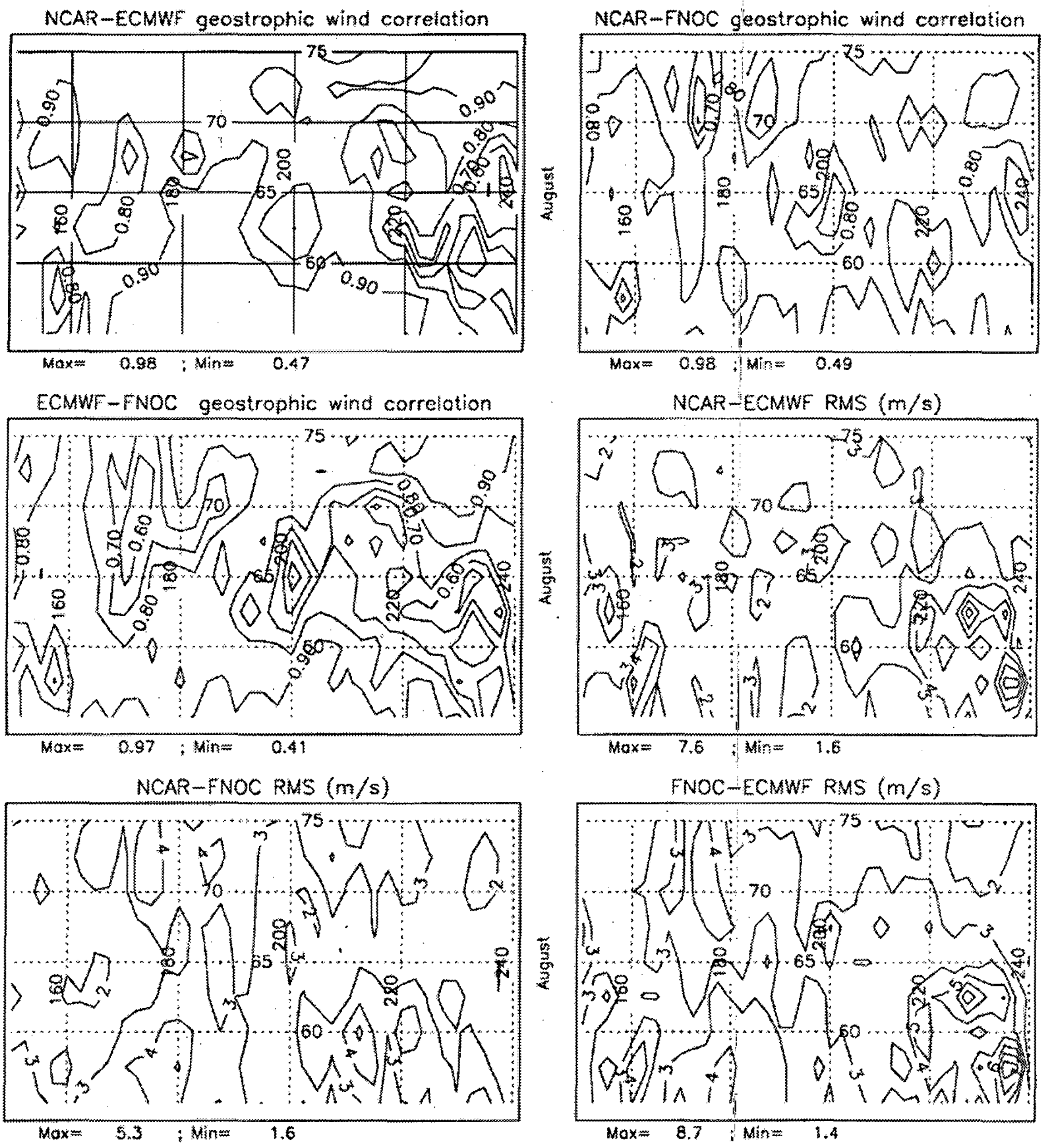
NCAR–ECMWF geostrophic wind correlation

NCAR–FNOC geostrophic wind correlation

ECMWF–FNOC geostrophic wind correlation

NCAR–ECMWF RMS (m/s)

NCAR–FNOC RMS (m/s)

FNOC–ECMWF RMS (m/s)

Figure 25. Spatial distribution of correlation coefficients and spatial distribution of RMS among NCAR, FNOC, and ECMWF speed of geostrophic winds in August of 1991.

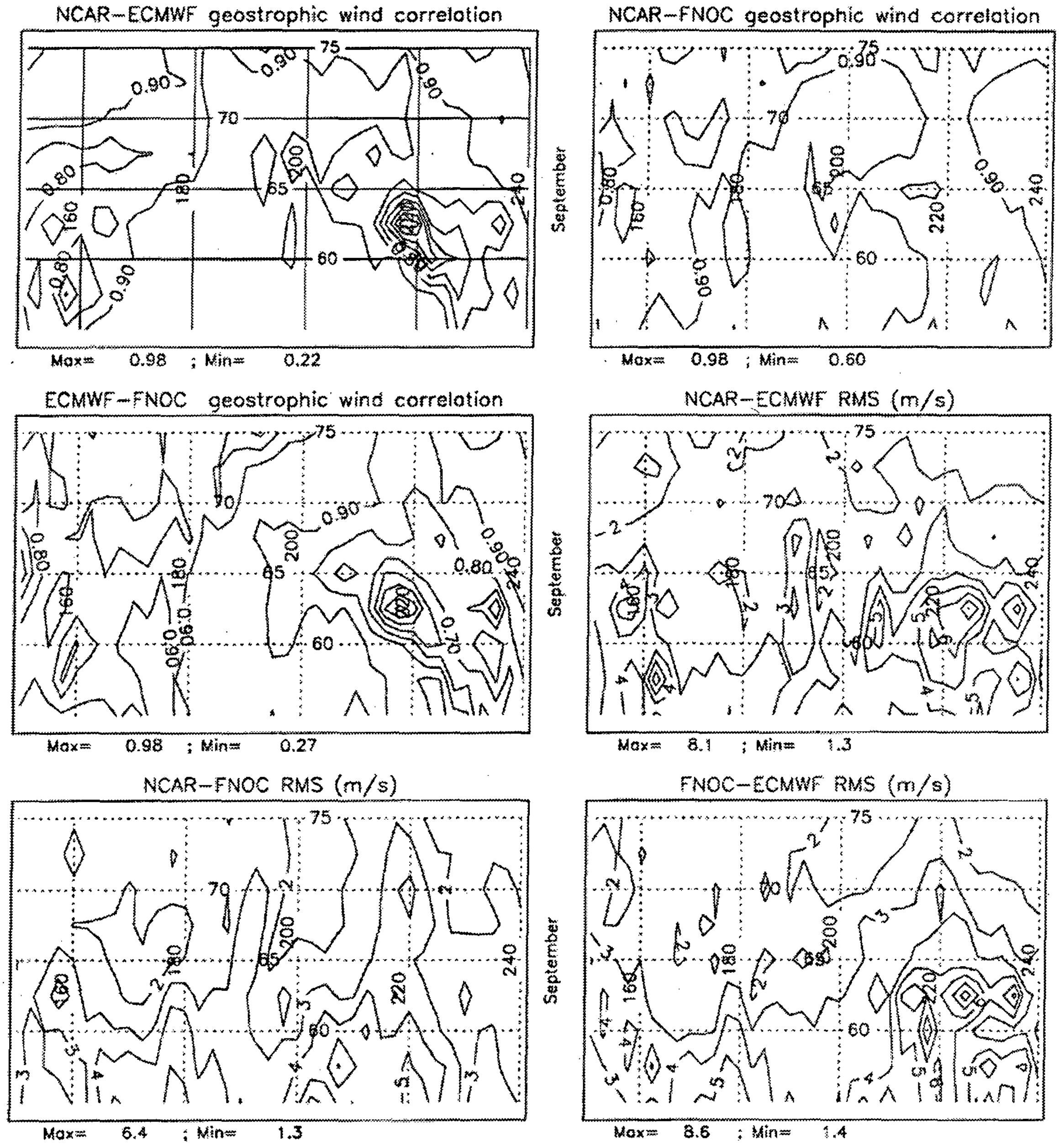

Figure 26. Spatial distribution of correlation coefficients and spatial distribution of RMS among NCAR, FNOC, and ECMWF speed of geostrophic winds in September of 1991.

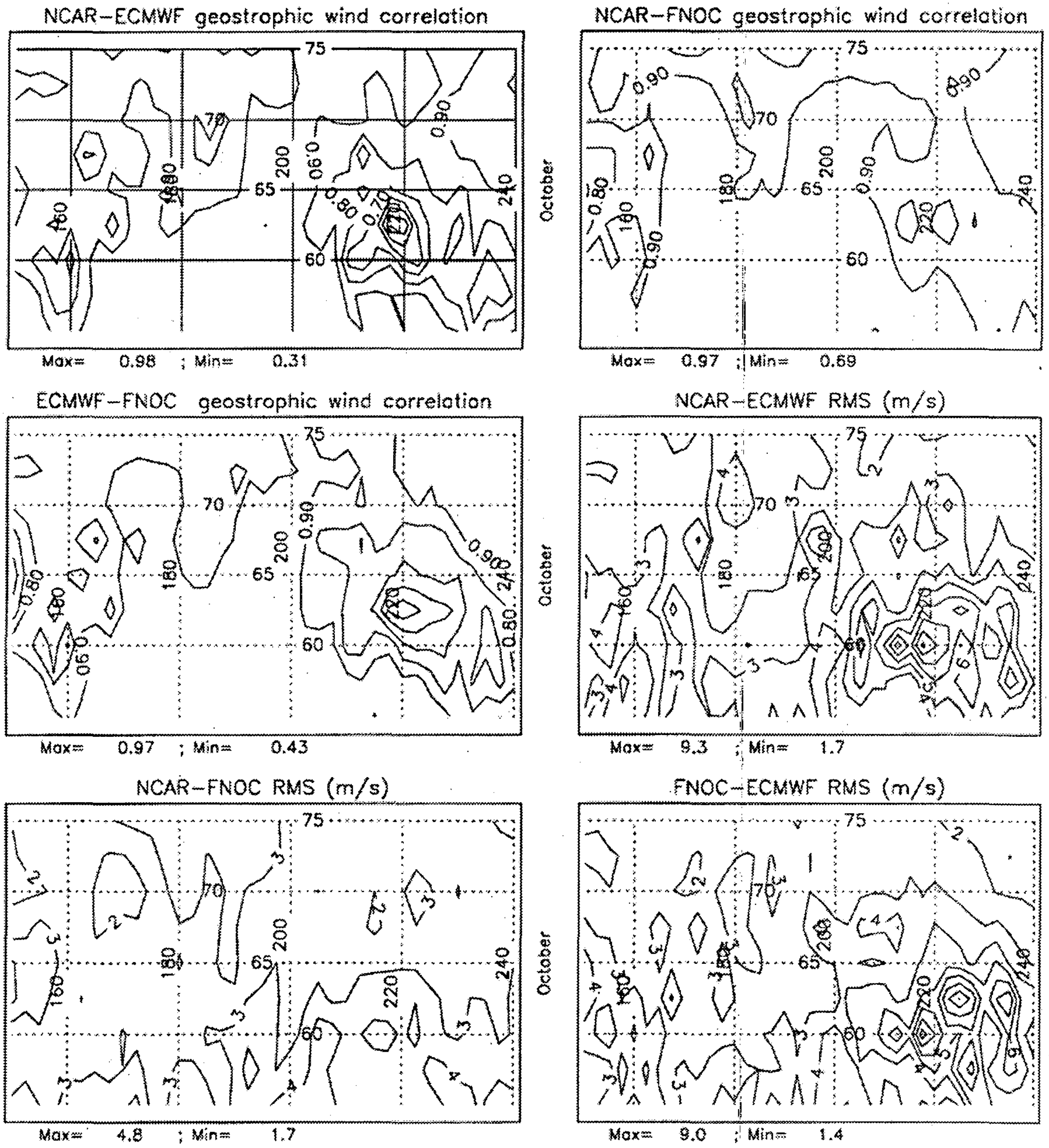
NCAR–ECMWF geostrophic wind correlation

Max= 0.98 ; Min= 0.31

NCAR–FNOC geostrophic wind correlation

Max= 0.97 ; Min= 0.69

ECMWF–FNOC geostrophic wind correlation

Max= 0.97 ; Min= 0.43

NCAR–ECMWF RMS (m/s)

Max= 9.3 ; Min= 1.7

NCAR–FNOC RMS (m/s)

Max= 4.8 ; Min= 1.7

FNOC–ECMWF RMS (m/s)

Max= 9.0 ; Min= 1.4

Figure 27. Spatial distribution of correlation coefficients and spatial distribution of RMS among NCAR, FNOC, and ECMWF speed of geostrophic winds in October of 1991.

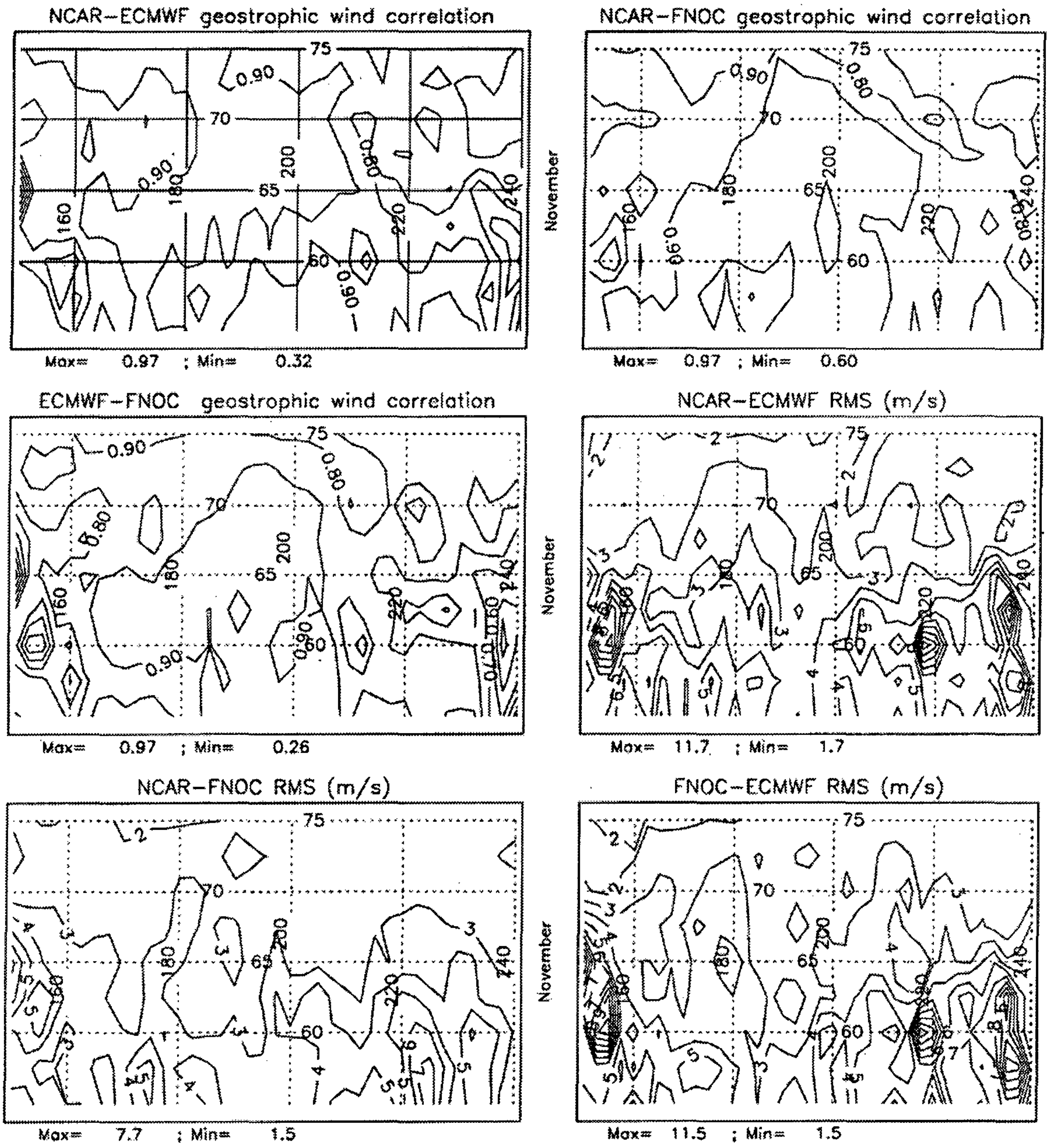

NCAR–ECMWF geostrophic wind correlation

Max= 0.97 ; Min= 0.32

NCAR–FNOC geostrophic wind correlation

Max= 0.97 ; Min= 0.60

ECMWF–FNOC geostrophic wind correlation

Max= 0.97 ; Min= 0.26

NCAR–ECMWF RMS (m/s)

Max= 11.7 ; Min= 1.7

NCAR–FNOC RMS (m/s)

Max= 7.7 ; Min= 1.5

FNOC–ECMWF RMS (m/s)

Max= 11.5 ; Min= 1.5

Figure 28. Spatial distribution of correlation coefficients and spatial distribution of RMS among NCAR, FNOC, and ECMWF speed of geostrophic winds in November of 1991.

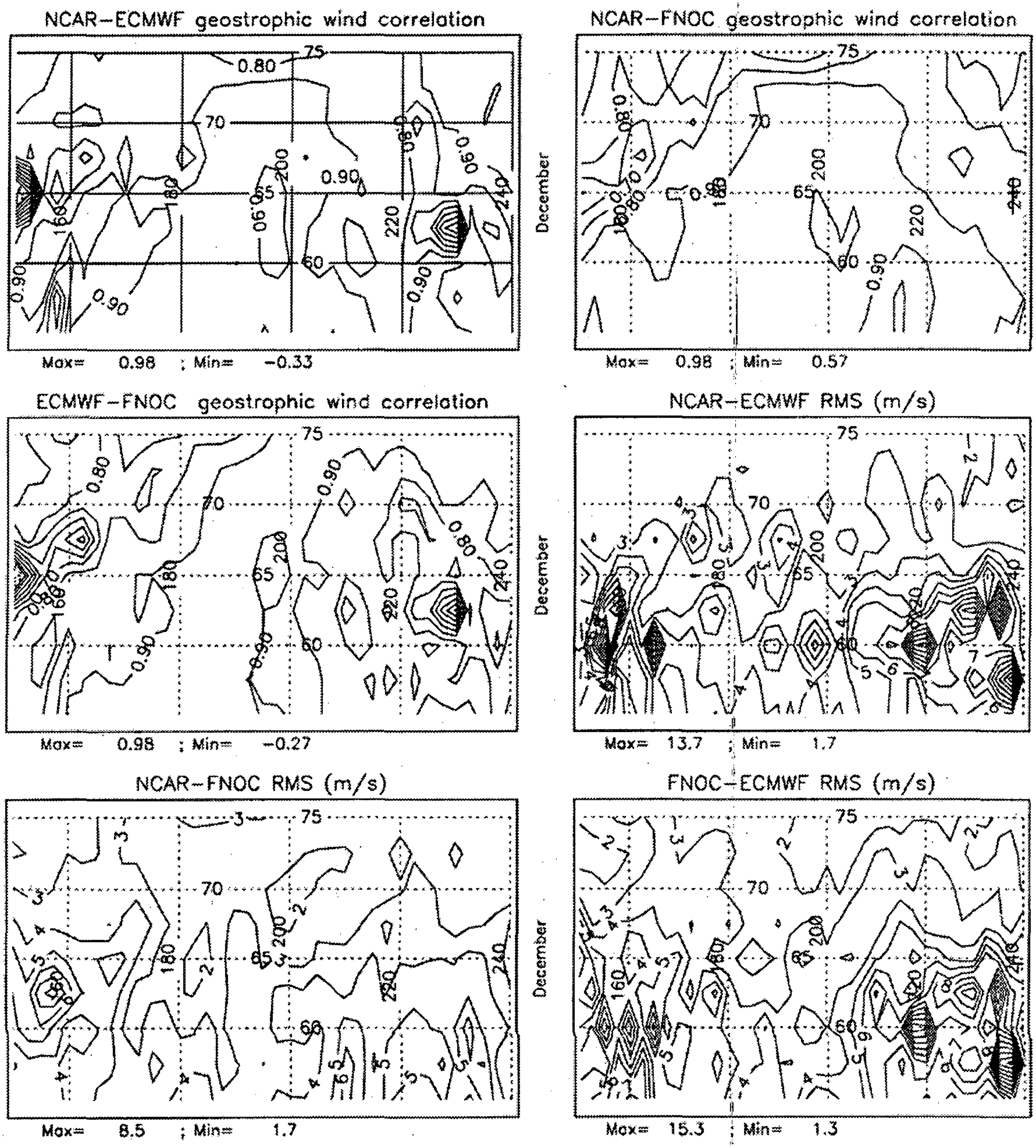

NCAR–ECMWF geostrophic wind correlation

NCAR–FNOC geostrophic wind correlation

ECMWF–FNOC geostrophic wind correlation

NCAR–ECMWF RMS (m/s)

NCAR–FNOC RMS (m/s)

FNOC–ECMWF RMS (m/s)

Figure 29. Spatial distribution of correlation coefficients and spatial distribution of RMS among NCAR, FNOC, and ECMWF speed of geostrophic winds in December of 1991.

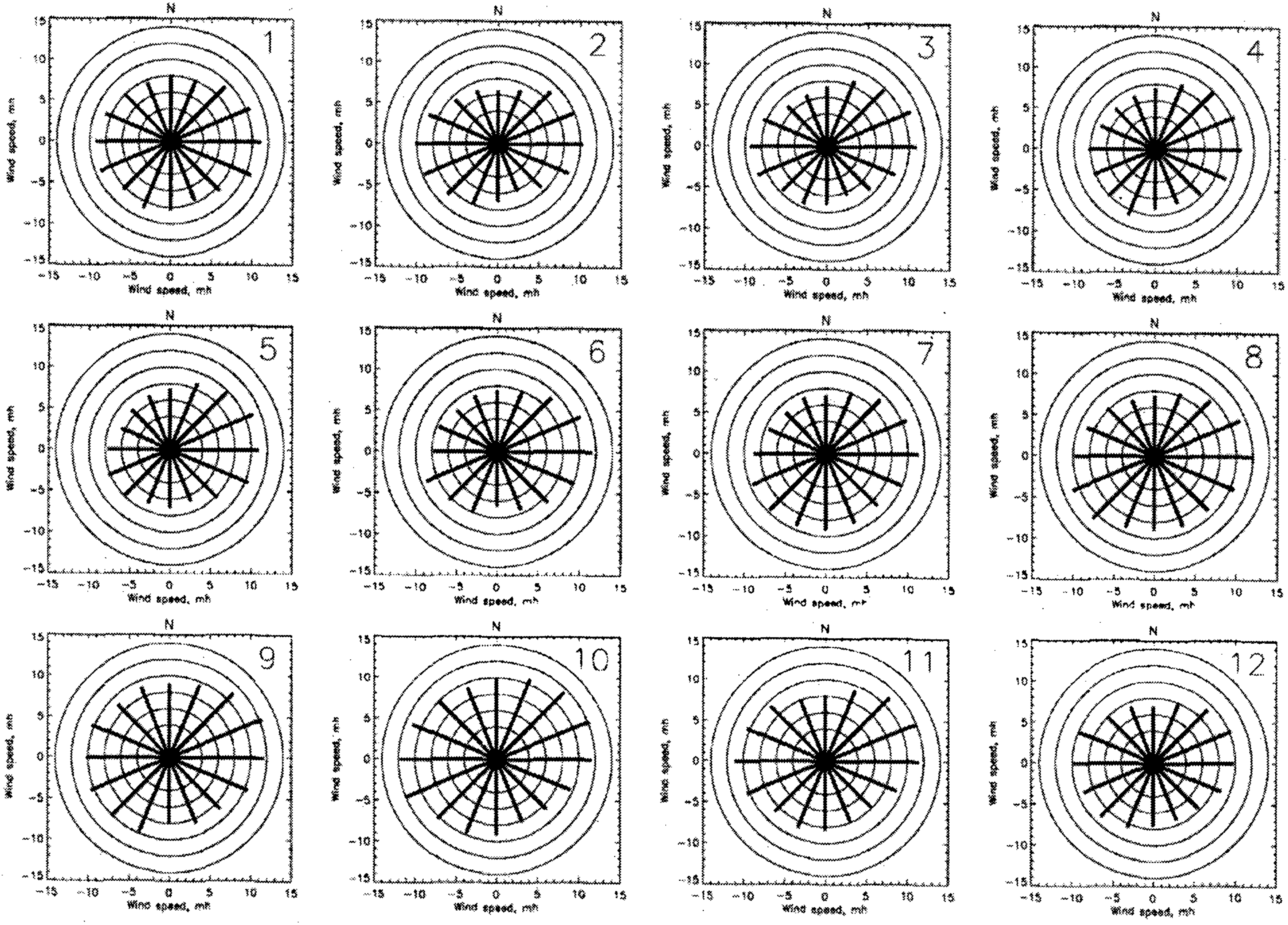

Barrow monthly mean wind speed, 1948–1989 — 1, 2, 3 ... 12 – month

Figure 30. Seasonal variability of observed monthly mean wind speed at Barrow. Data are averaged for the period 1948–1989. Numbers (1, 2, ... 12) depict months.

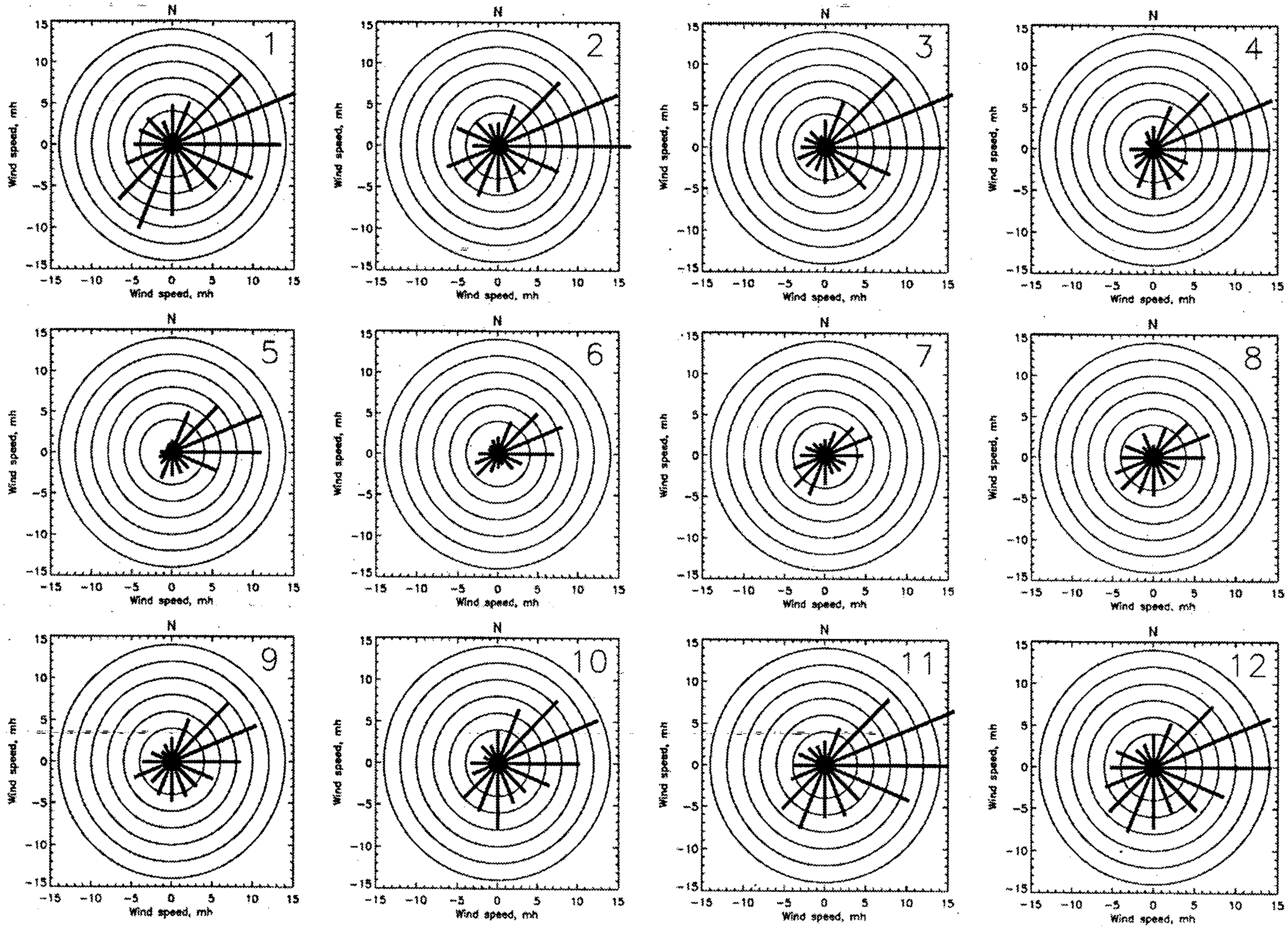

Figure 31. Same as Figure 30 except for NCAR simulated wind.

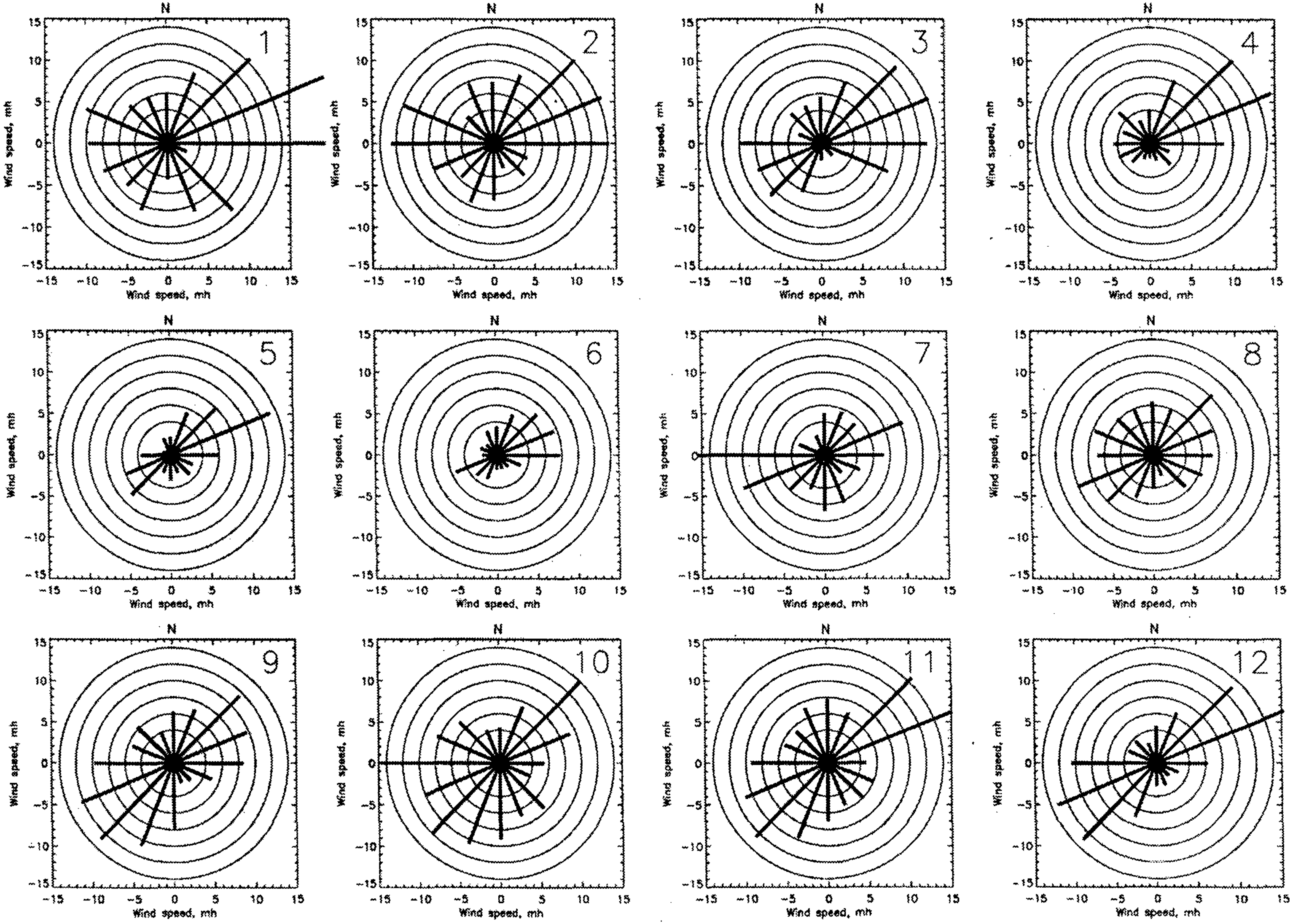

Figure 32. Same as Figure 30 except for ECMWF simulated wind and period from 1991 through 1994.

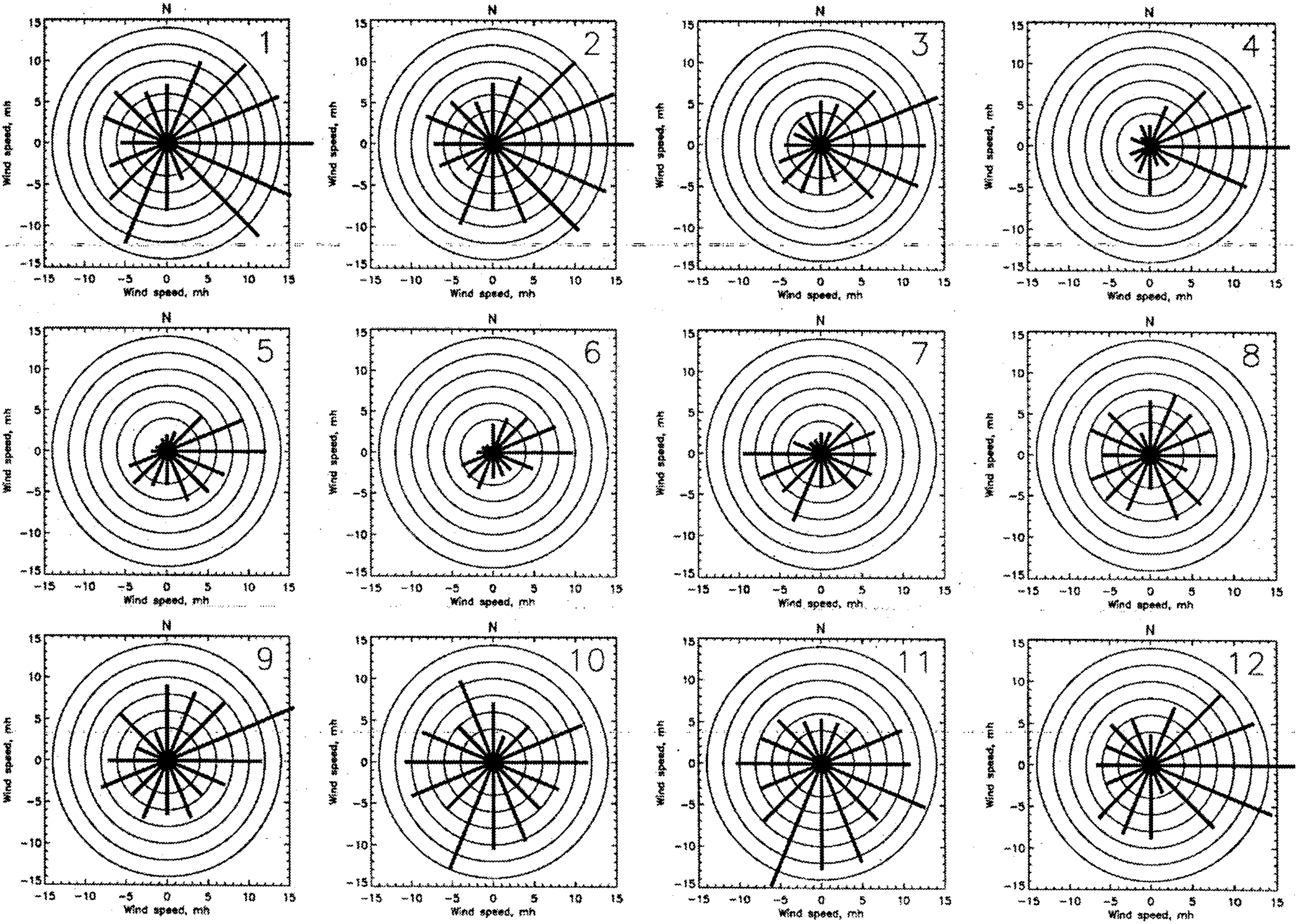

Figure 33. Same as Figure 30 except for FNOC simulated wind and period from 1991 through 1994.

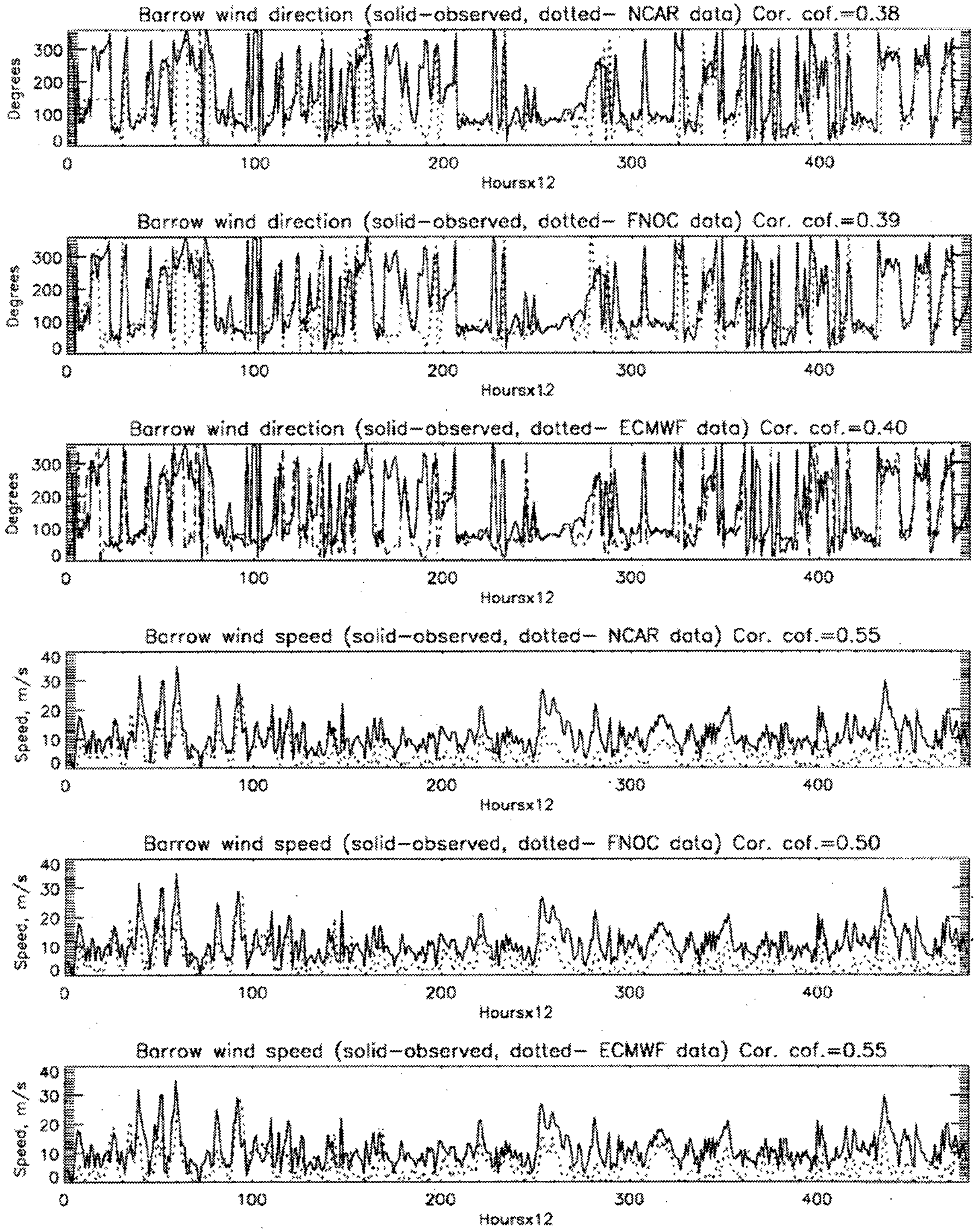
Barrow wind direction (solid–observed, dotted– NCAR data) Cor. cof.=0.38

Barrow wind direction (solid–observed, dotted– FNOC data) Cor. cof.=0.39

Barrow wind direction (solid–observed, dotted– ECMWF data) Cor. cof.=0.40

Barrow wind speed (solid–observed, dotted– NCAR data) Cor. cof.=0.55

Barrow wind speed (solid–observed, dotted– FNOC data) Cor. cof.=0.50

Barrow wind speed (solid–observed, dotted– ECMWF data) Cor. cof.=0.55

Figure 34. Time series of observed and simulated wind speed and wind direction at Barrow for 1991. Temporal resolution of the atmospheric fields is 12 hours.

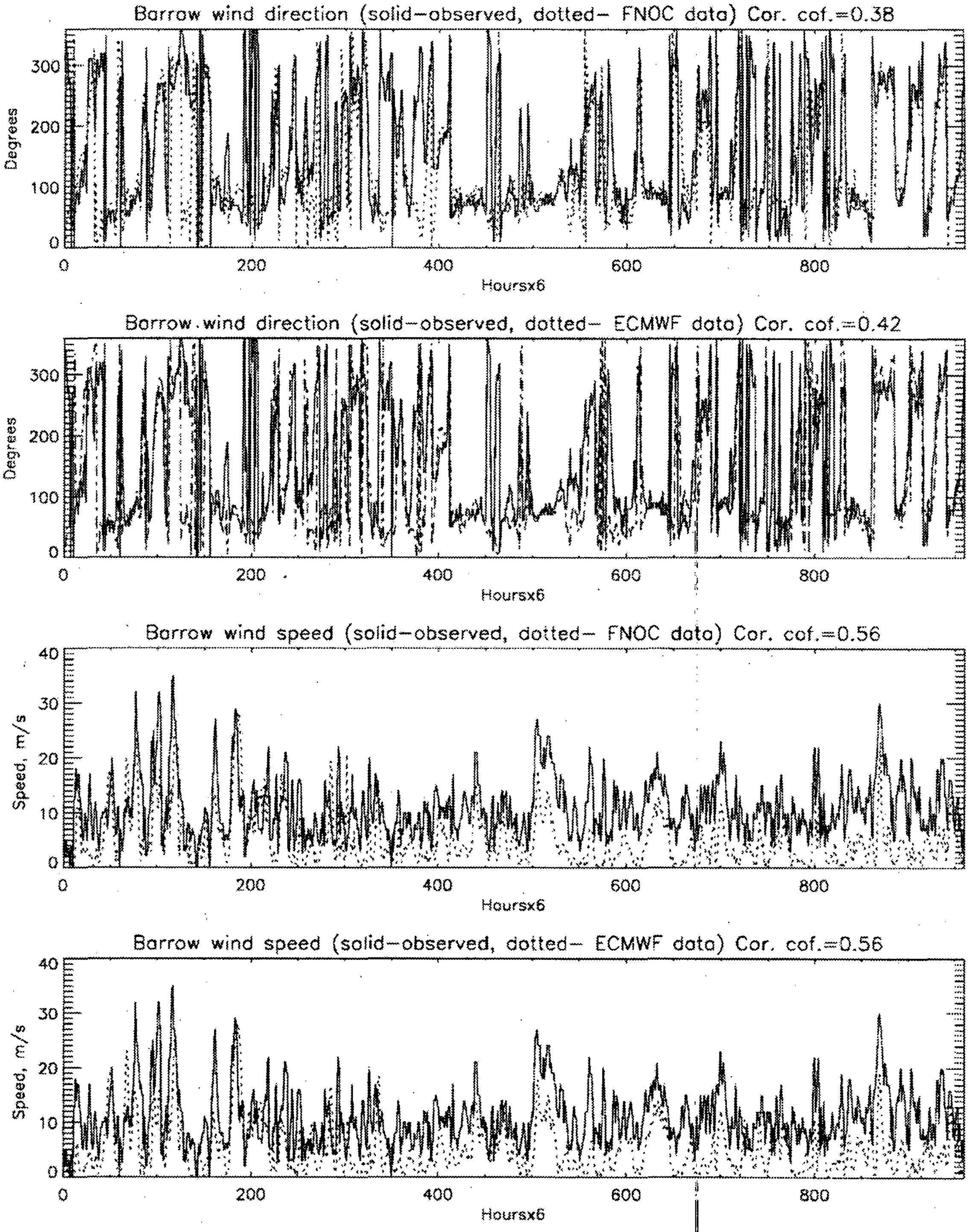

Figure 35. Same as Figure 34 except the temporal resolution between atmospheric fields is six hours.

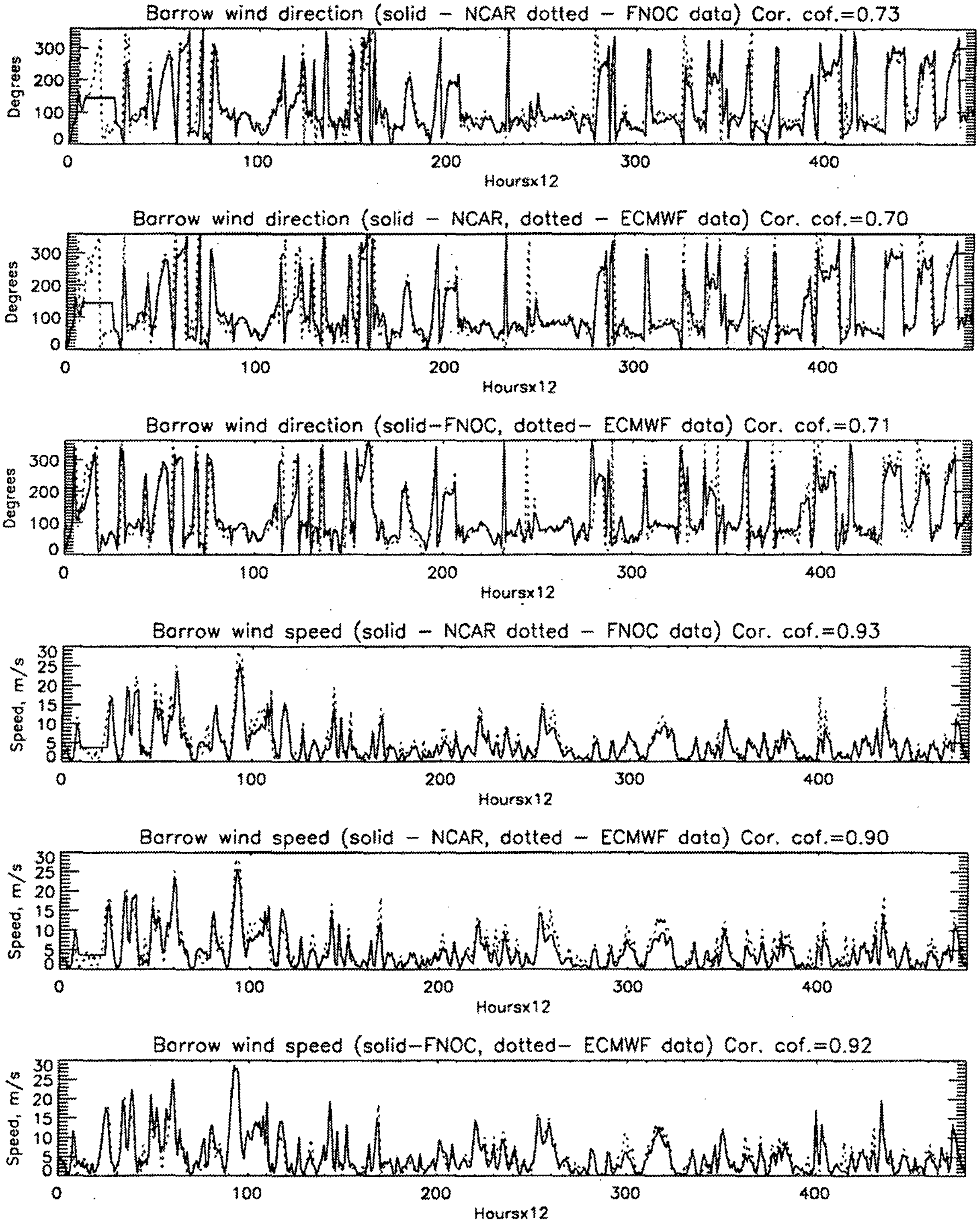

Figure 36. Times series of simulated ECMWF, NCAR, and FNOC wind at Barrow with a 12-hour temporal resolution for 1991.

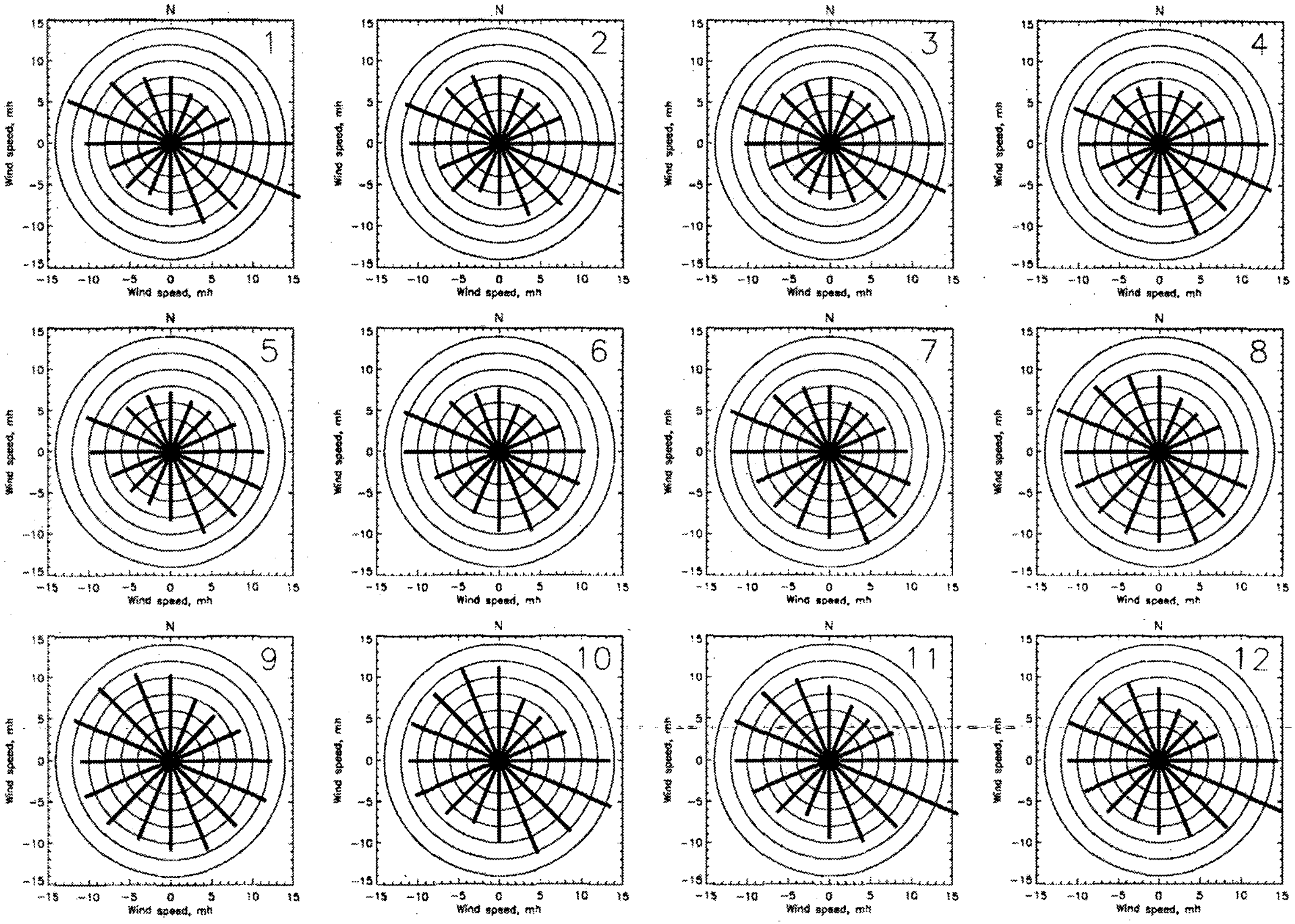

Kotzebue monthly mean wind speed, 1945–1991 — 1, 2, 3 ... 12 – month

Figure 37. Seasonal variability of observed monthly mean wind speed at Kotzebue. Data are averaged for the period from 1945 through 1991. Numbers (1, 2, ... 12) depict months.

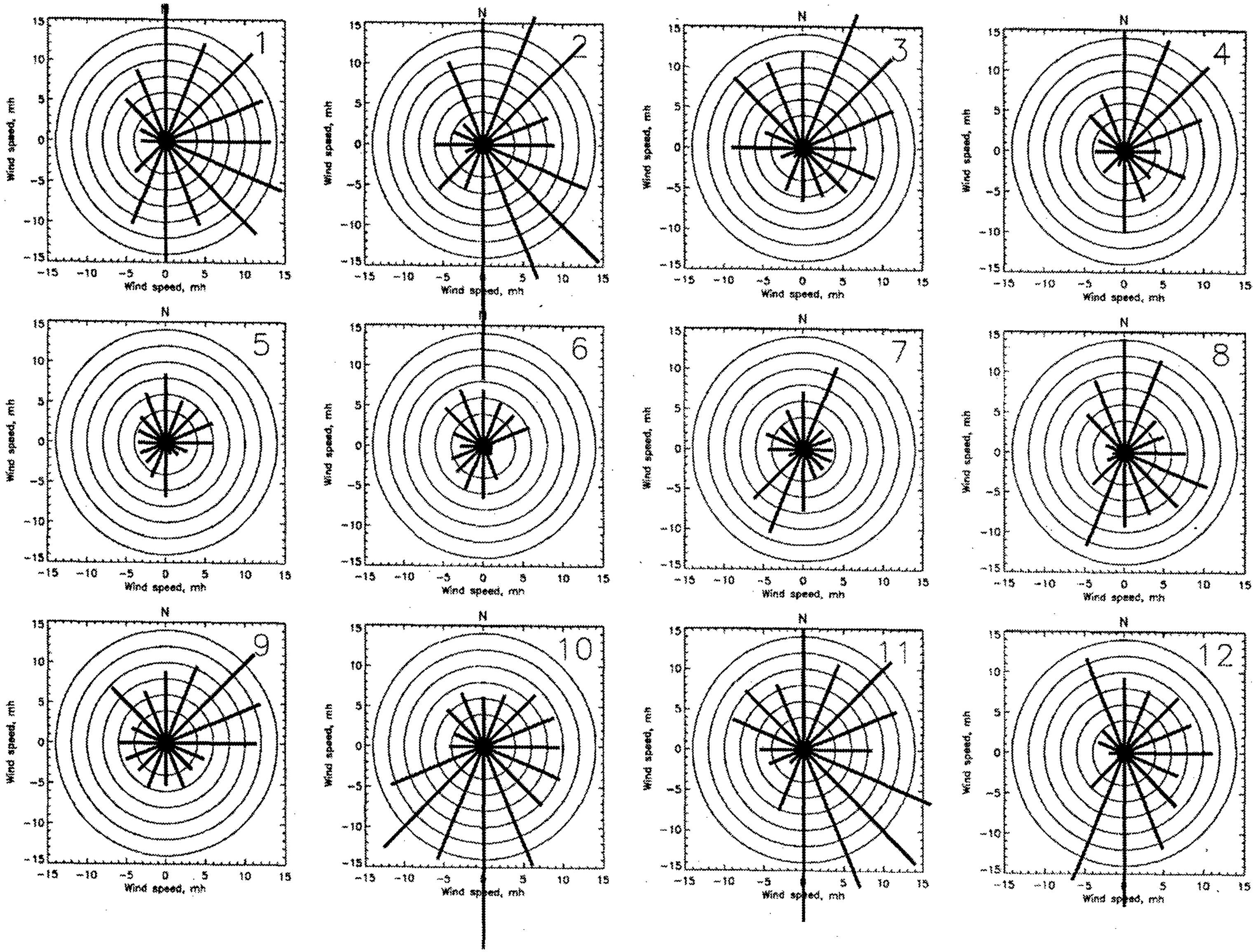

Figure 38. Same as Figure 37 except for ECMWF simulated wind and period from 1991 through 1994.

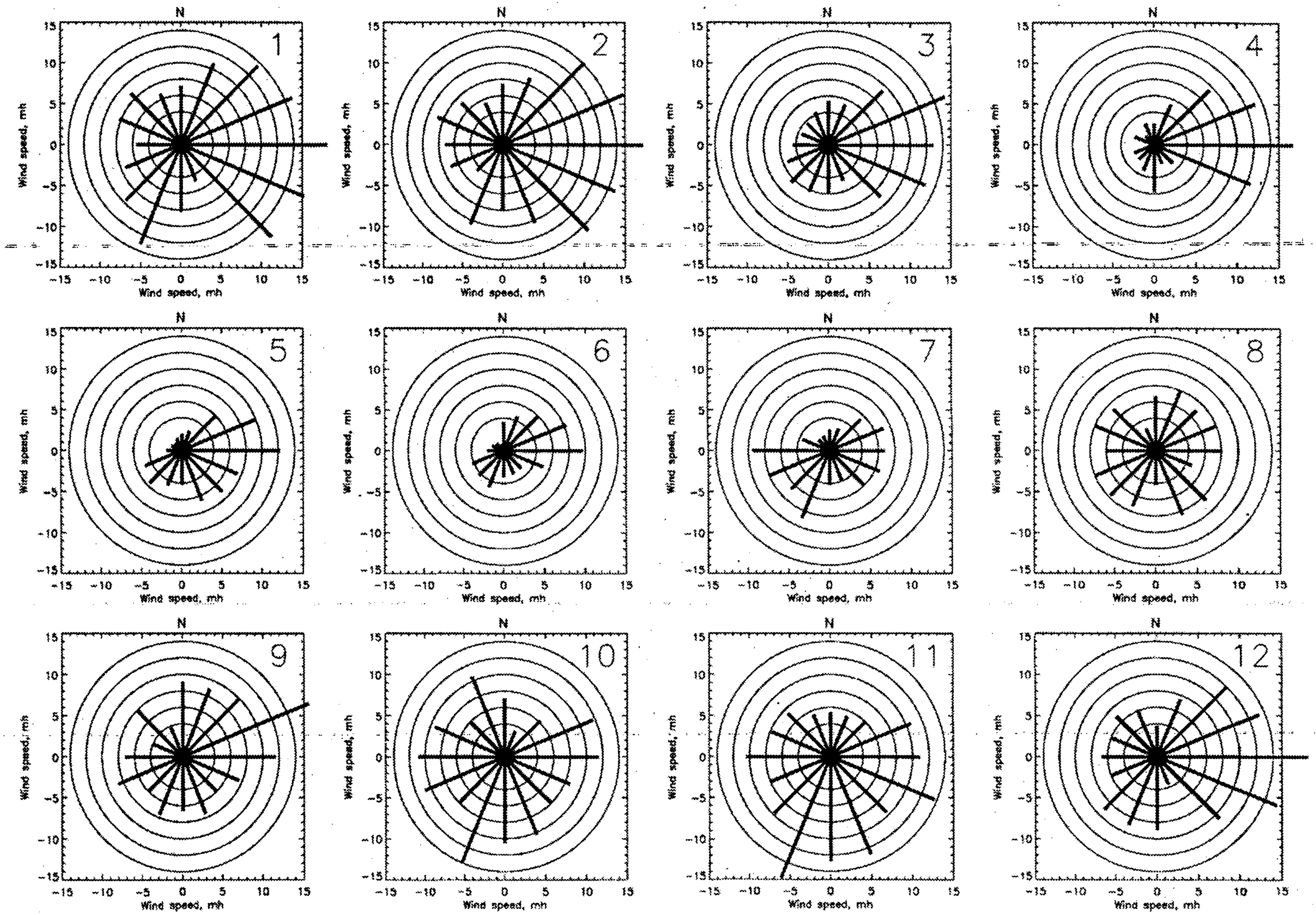

Figure 39. Same as Figure 37 except for FNOC simulated wind and period from 1991 through 1994.

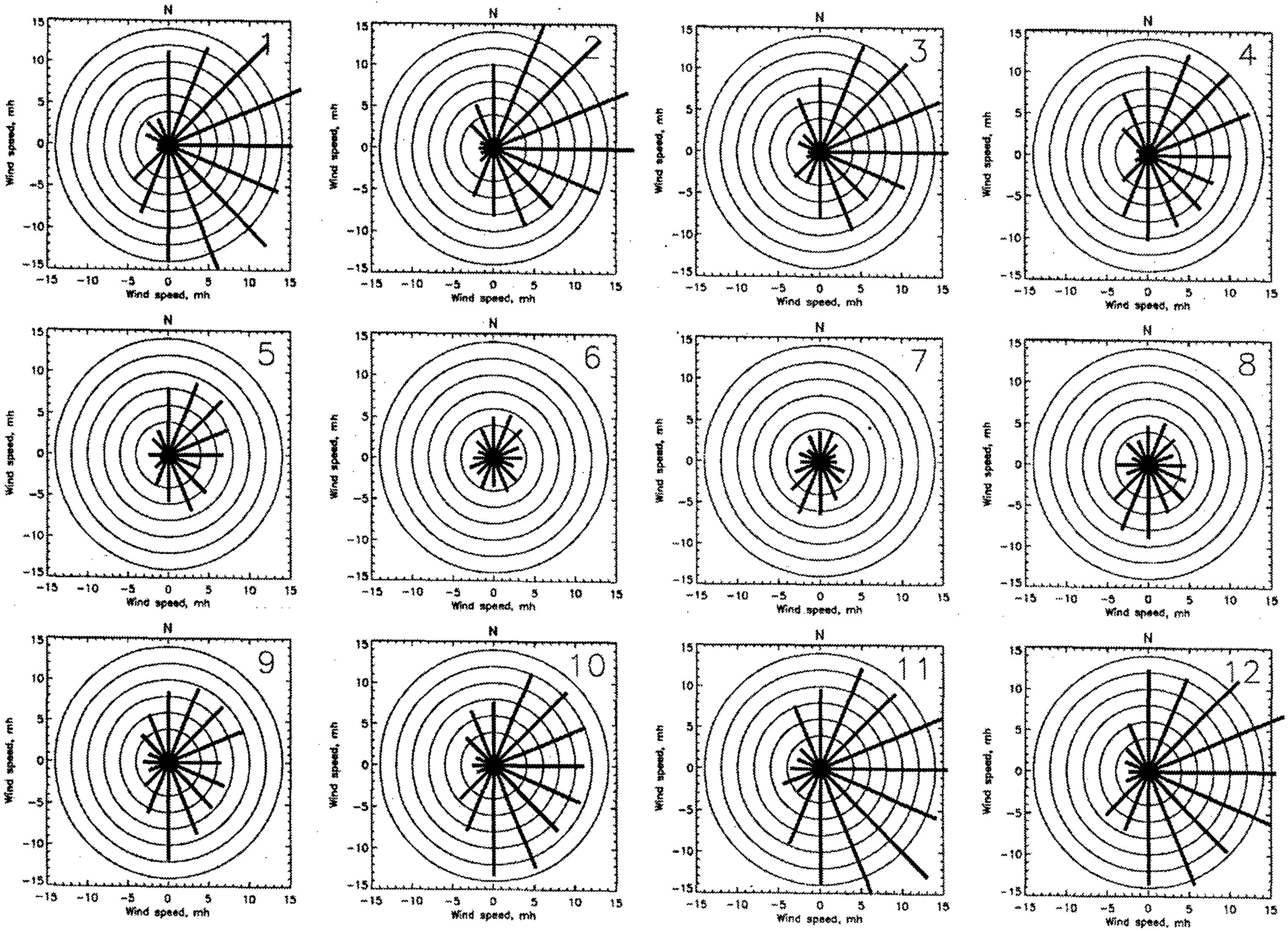

Figure 40. Same as Figure 37 except for NCAR simulated wind and period from 1946 through 1988.

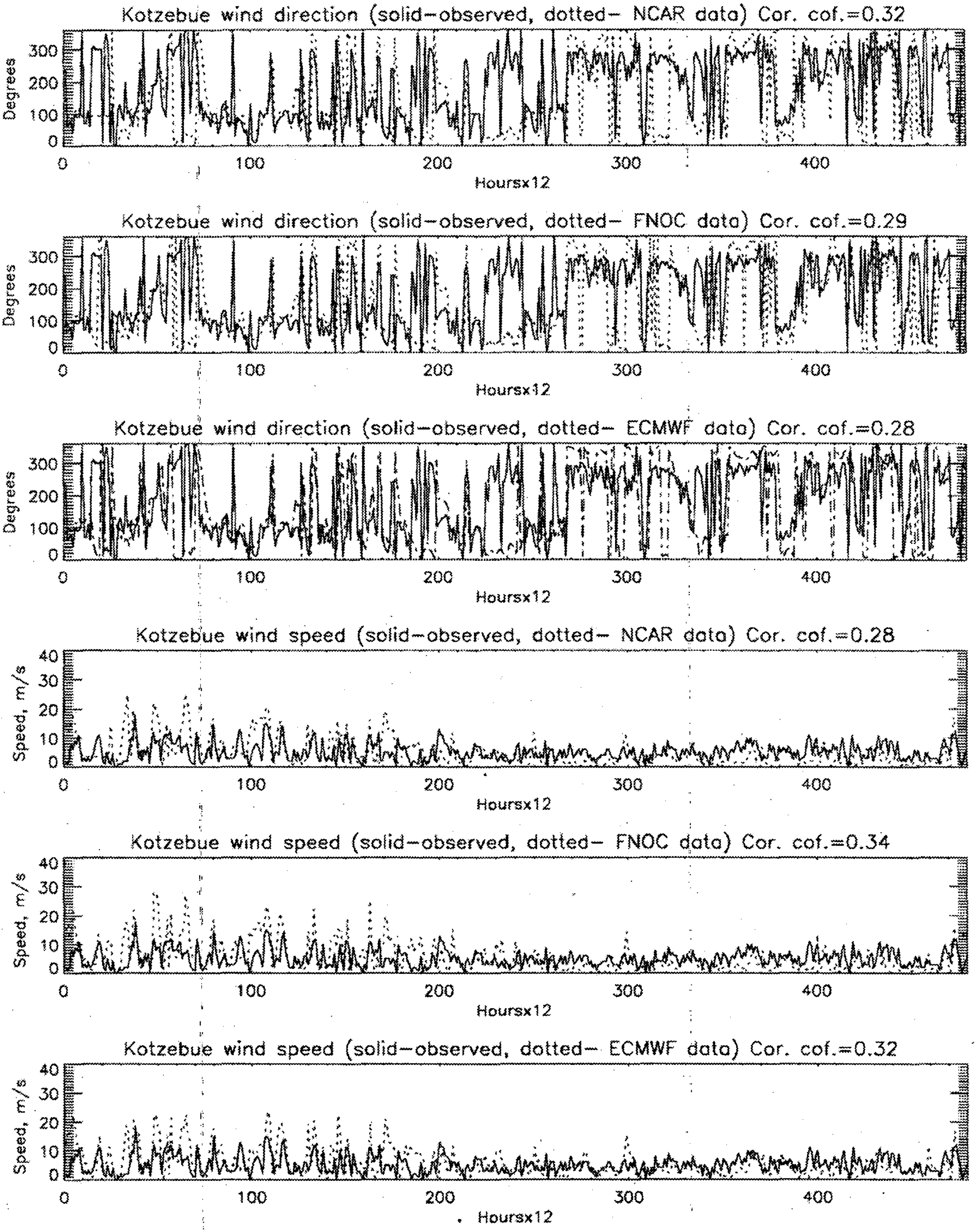

Figure 41. Time series of observed and simulated wind speed and wind direction at Kotzebue for 1991. Temporal resolution of the atmospheric fields is 12 hours.

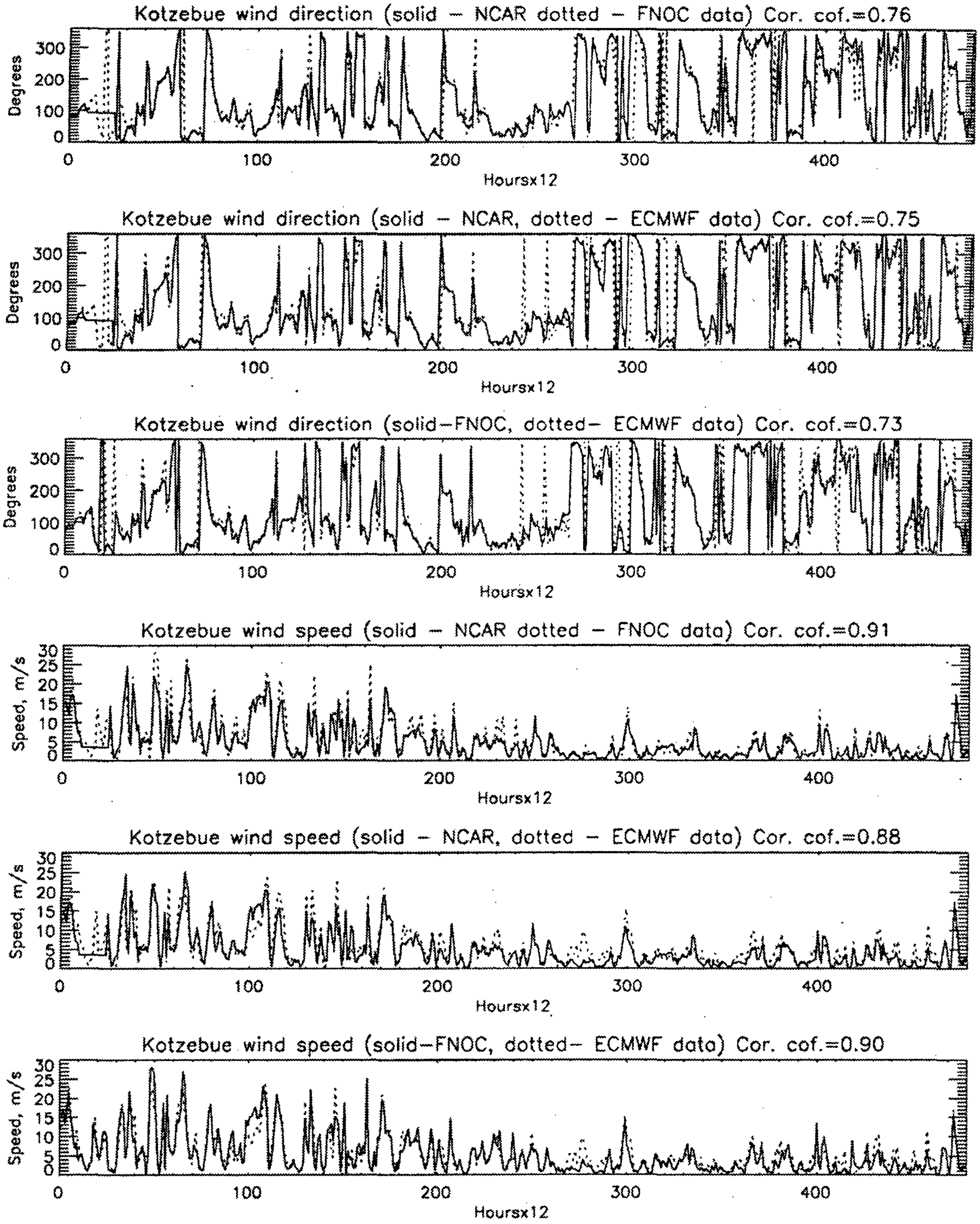

Kotzebue wind direction (solid – NCAR dotted – FNOC data) Cor. cof.=0.76

Kotzebue wind direction (solid – NCAR, dotted – ECMWF data) Cor. cof.=0.75

Kotzebue wind direction (solid–FNOC, dotted– ECMWF data) Cor. cof.=0.73

Kotzebue wind speed (solid – NCAR dotted – FNOC data) Cor. cof.=0.91

Kotzebue wind speed (solid – NCAR, dotted – ECMWF data) Cor. cof.=0.88

Kotzebue wind speed (solid–FNOC, dotted– ECMWF data) Cor. cof.=0.90

Figure 42. Times series of simulated ECMWF, NCAR, and FNOC wind at Kotzebue with a 12-hour temporal resolution for 1991.

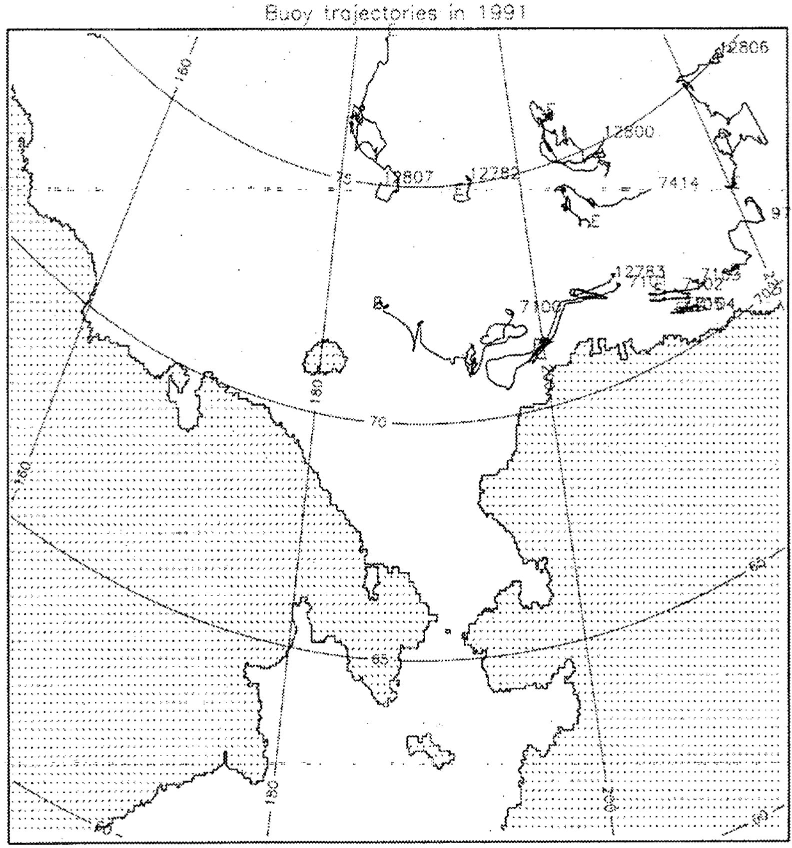

Figure 43. Ice surface buoy (International Arctic Buoy Program) trajectories in the Chukchi and Beaufort Sea in 1991. Numbers show buoy number at the beginning of each trajectory. The end of the trajectory is marked by the letter 'E'.end of the trajectory is marked by the letter 'E'.

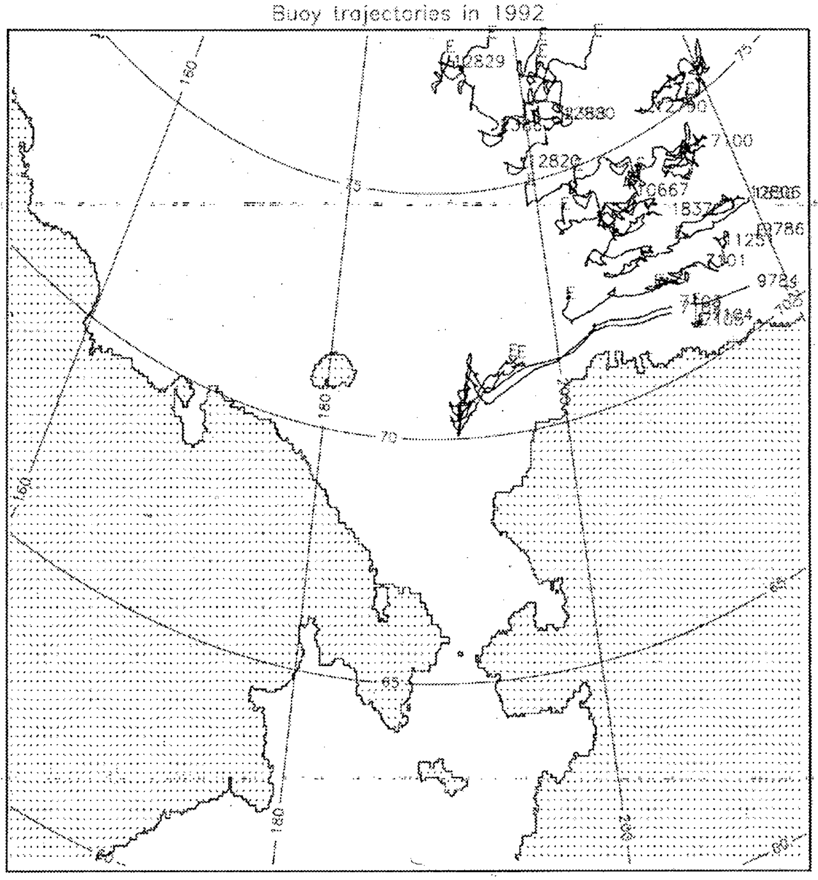

Figure 44. Same as Figure 43 for the year 1992.

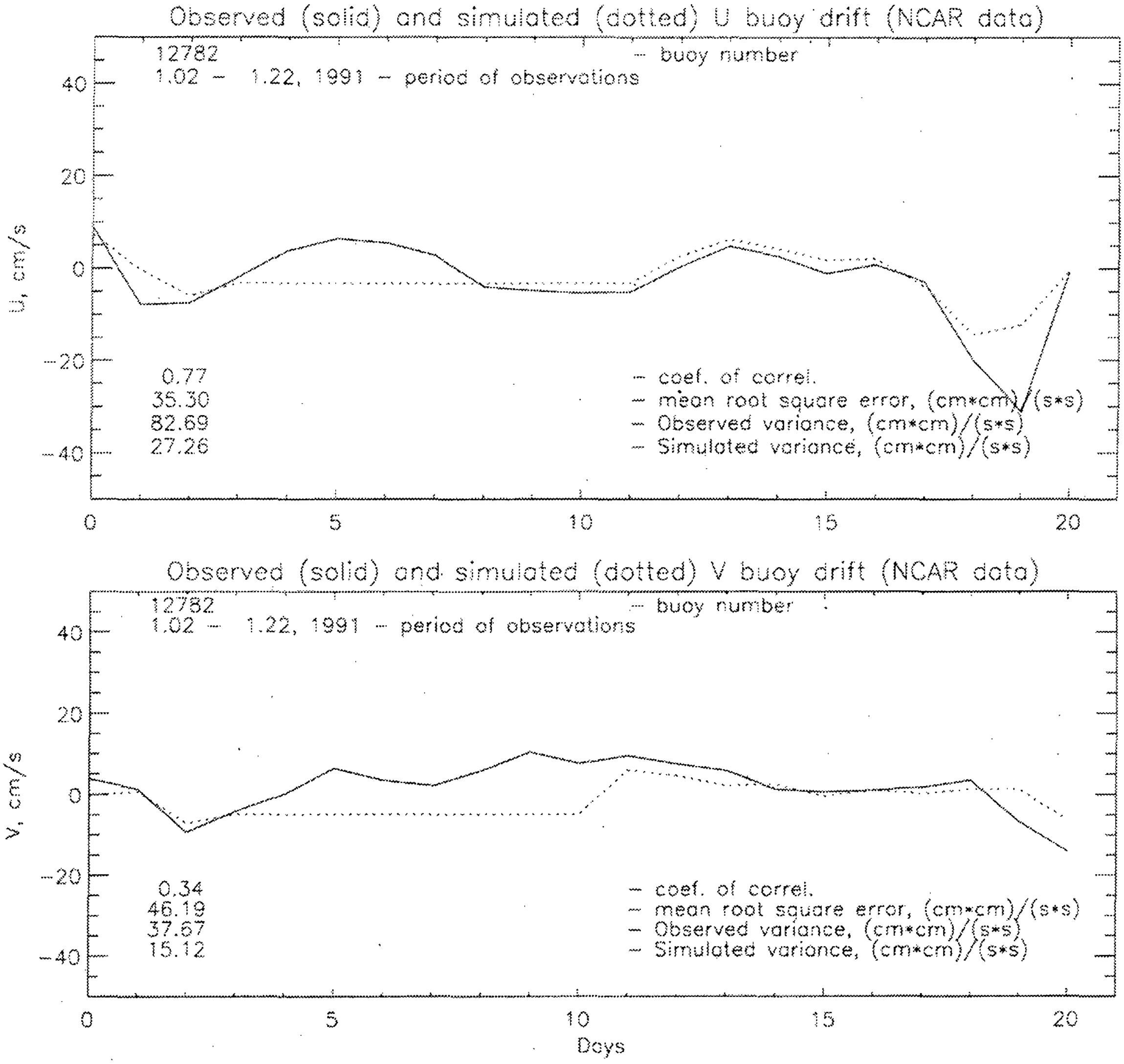

Figure 45. Observed and simulated components of the ice surface buoy drift. Buoy # 12782. Simulated ice drift is based on the Thorndike–Colony empirical model using NCAR atmospheric pressure fields.

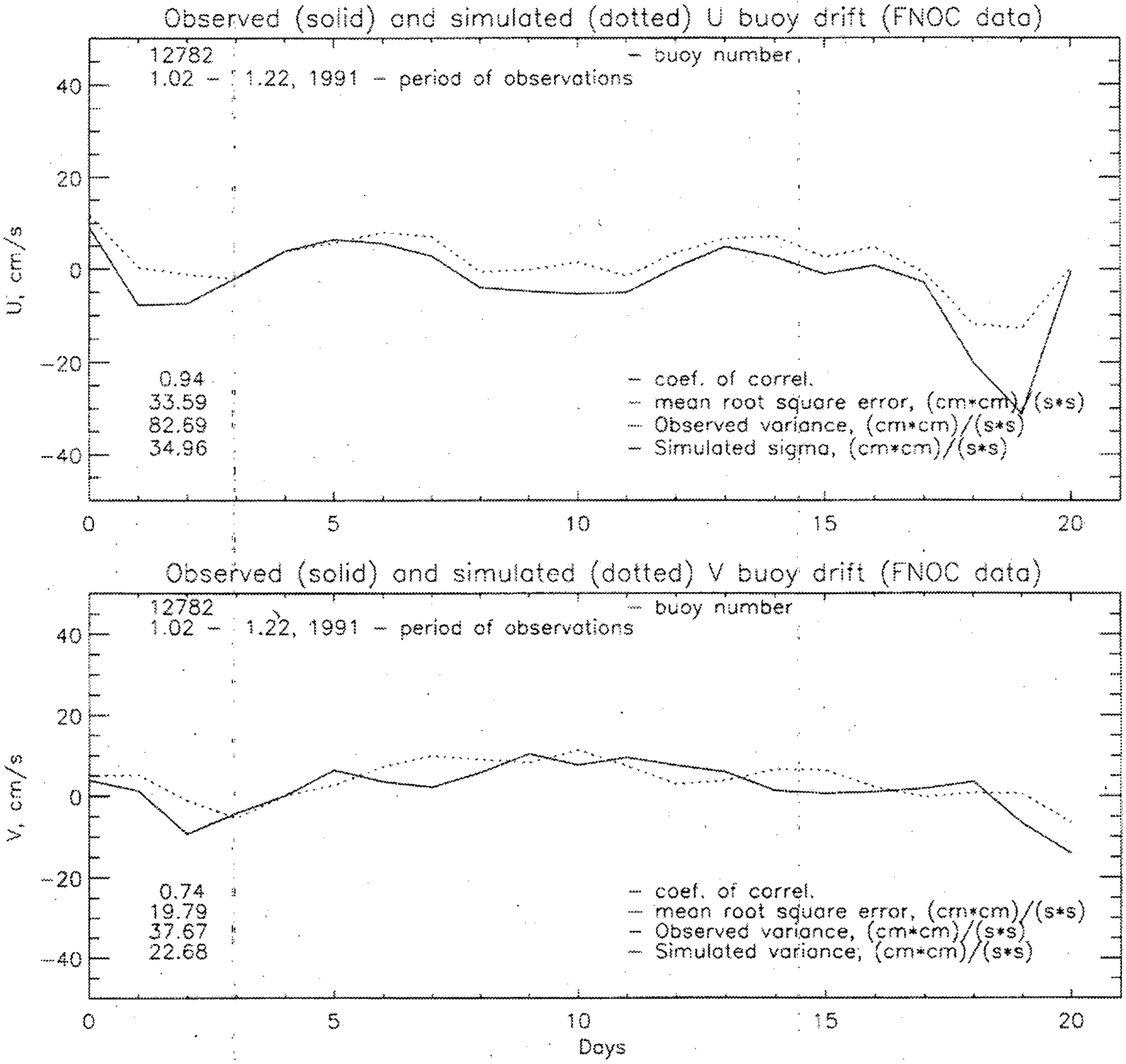

Figure 46. Same as Figure 45 except for FNOC atmospheric pressure data.

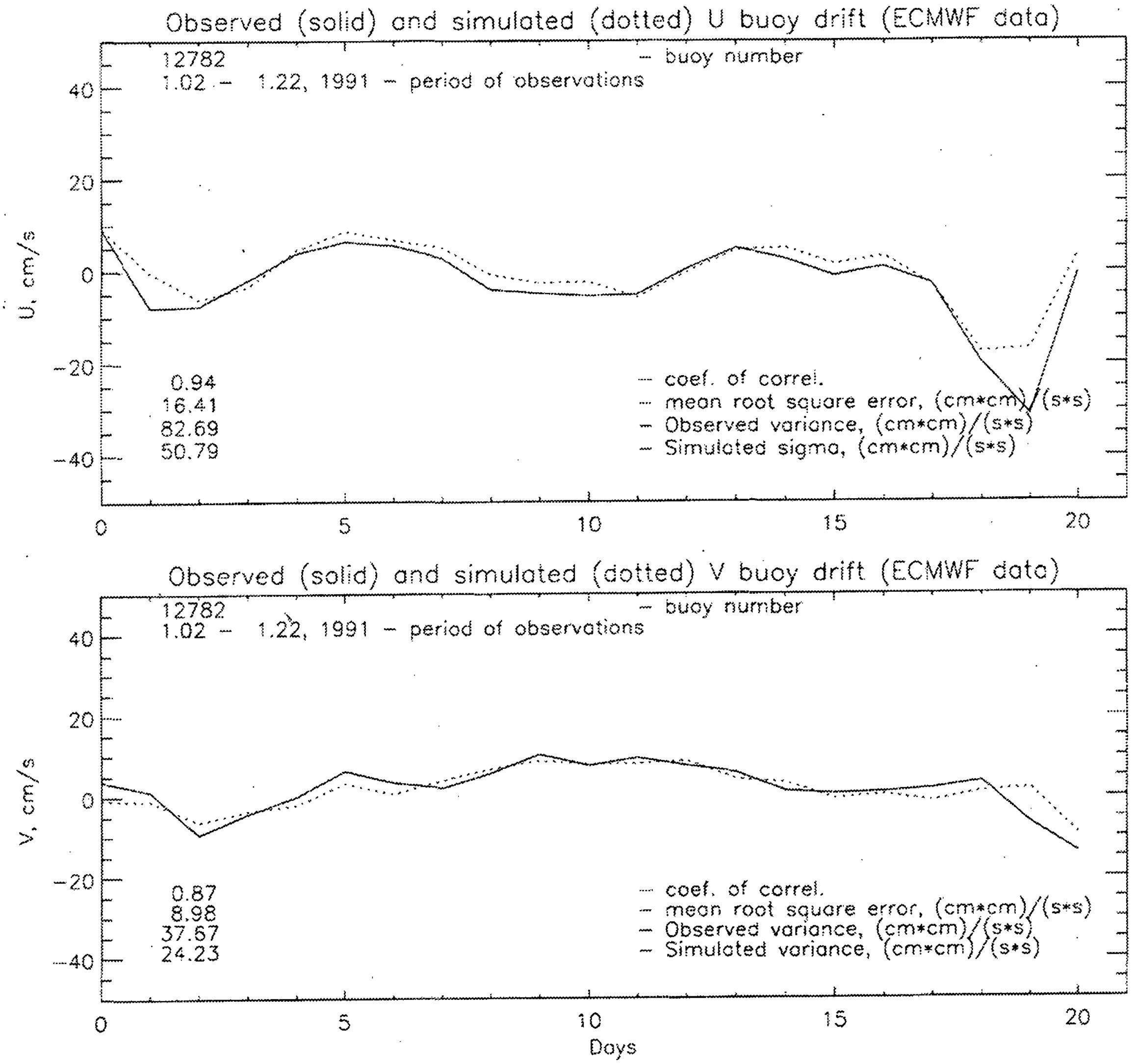

Figure 47. Same as Figure 45 except for ECMWF atmospheric pressure data.

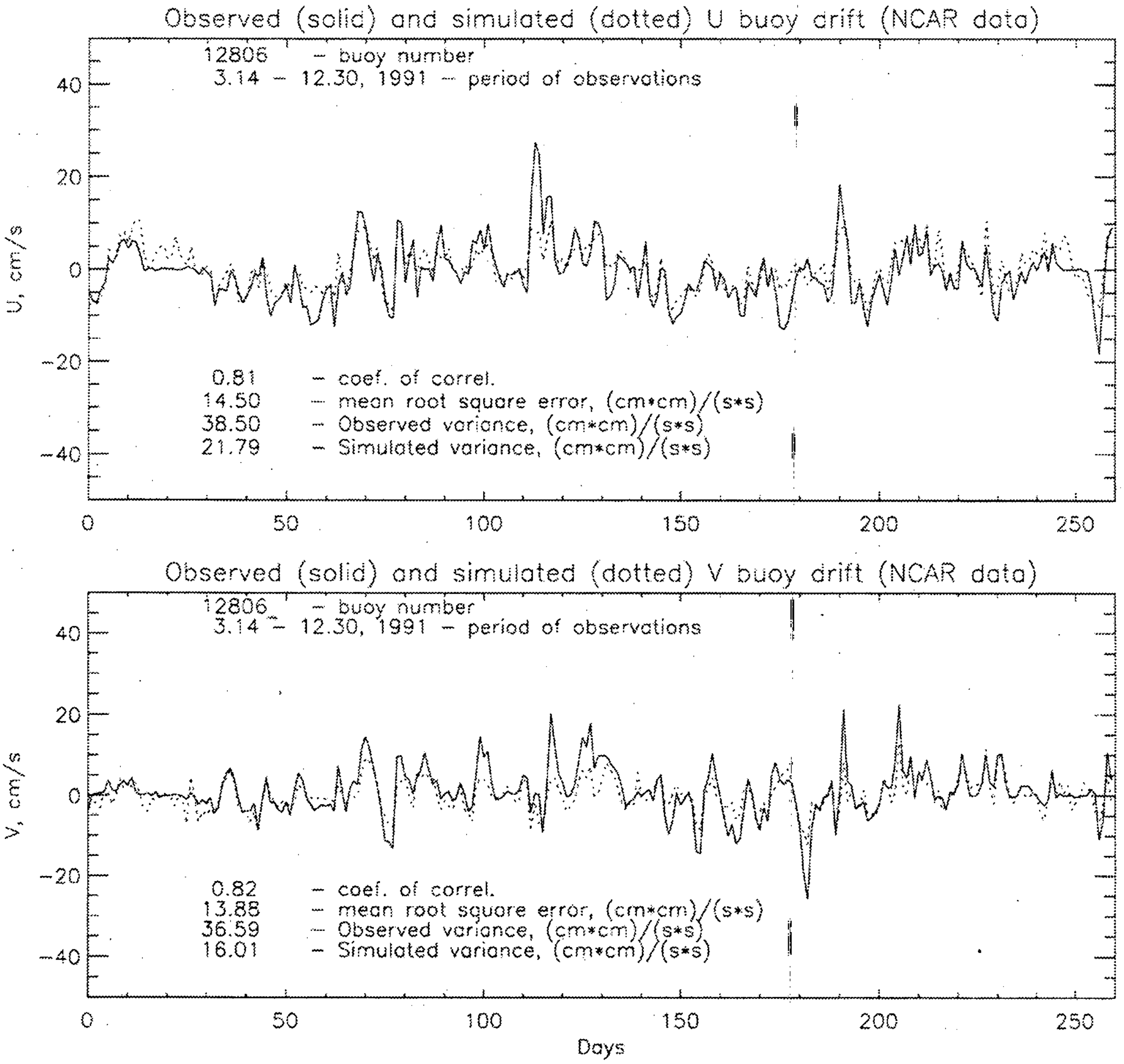

Figure 48. Observed and simulated components of the ice surface buoy drift. Buoy # 12806. Simulated ice drift is based on Thorndike–Colony empirical model using NCAR atmospheric pressure fields.

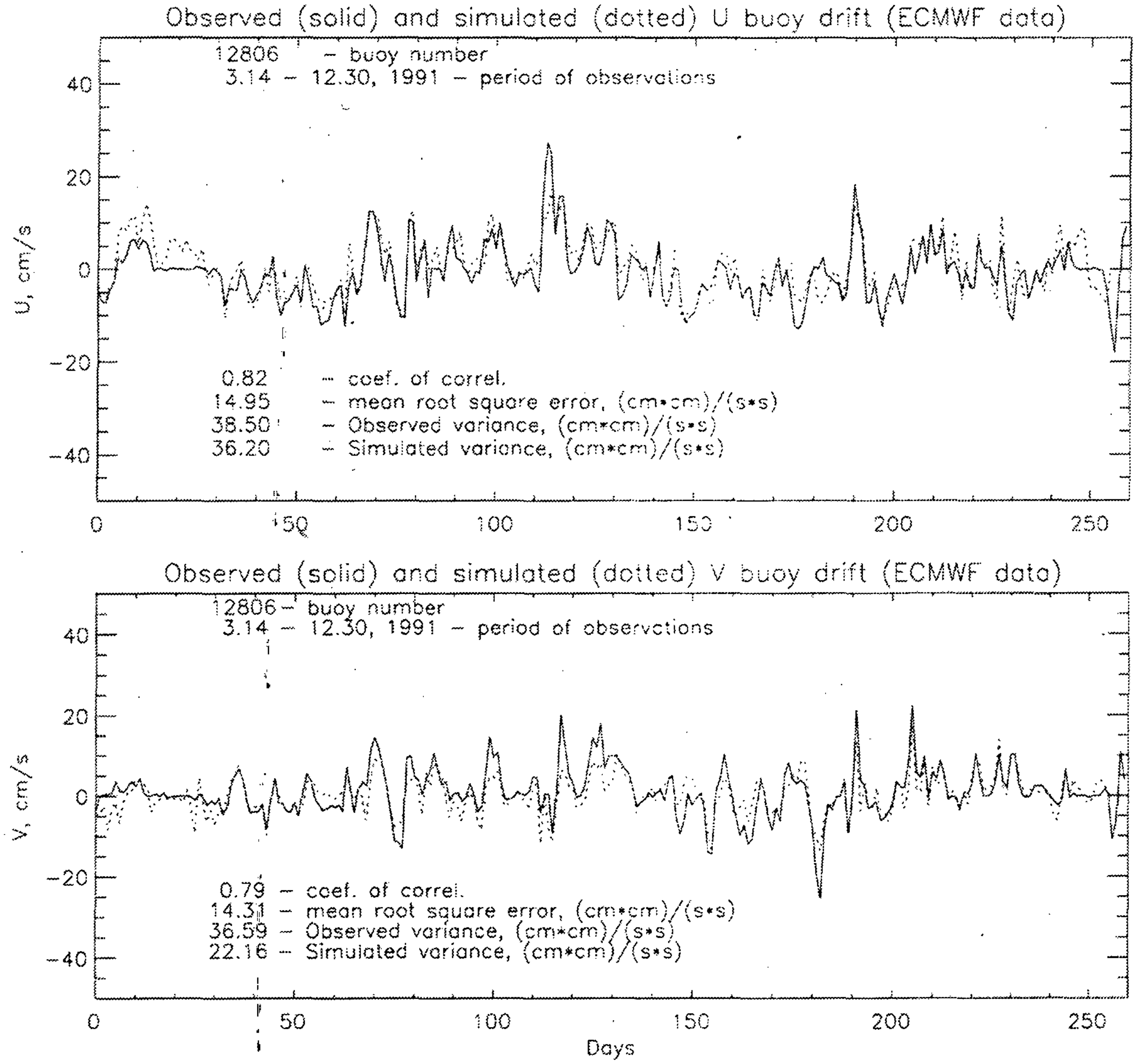

Figure 50. Same as Figure 48 except for ECMWF atmospheric pressure data.

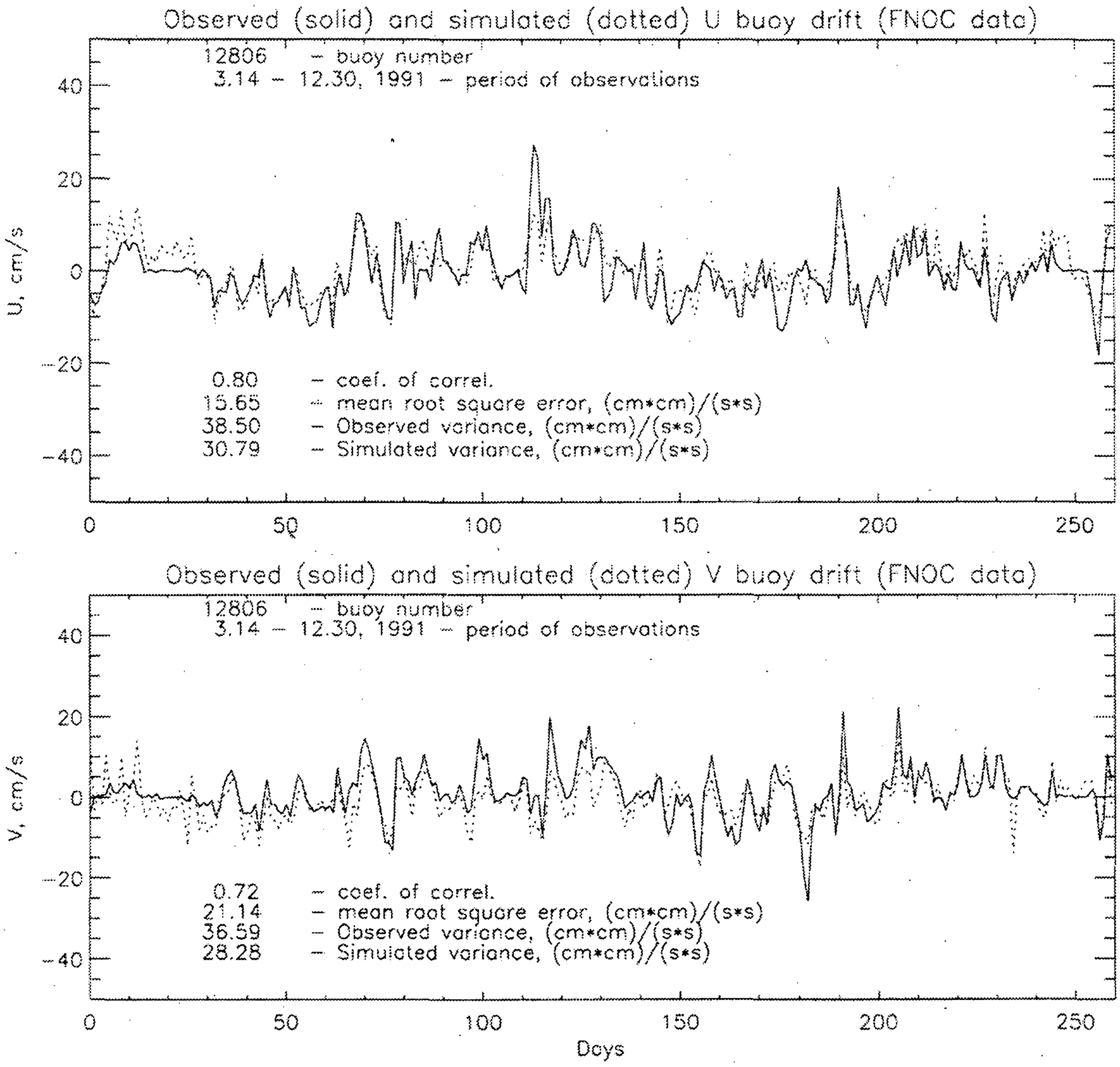

Figure 49. Same as Figure 48 except for FNOC atmospheric pressure data.

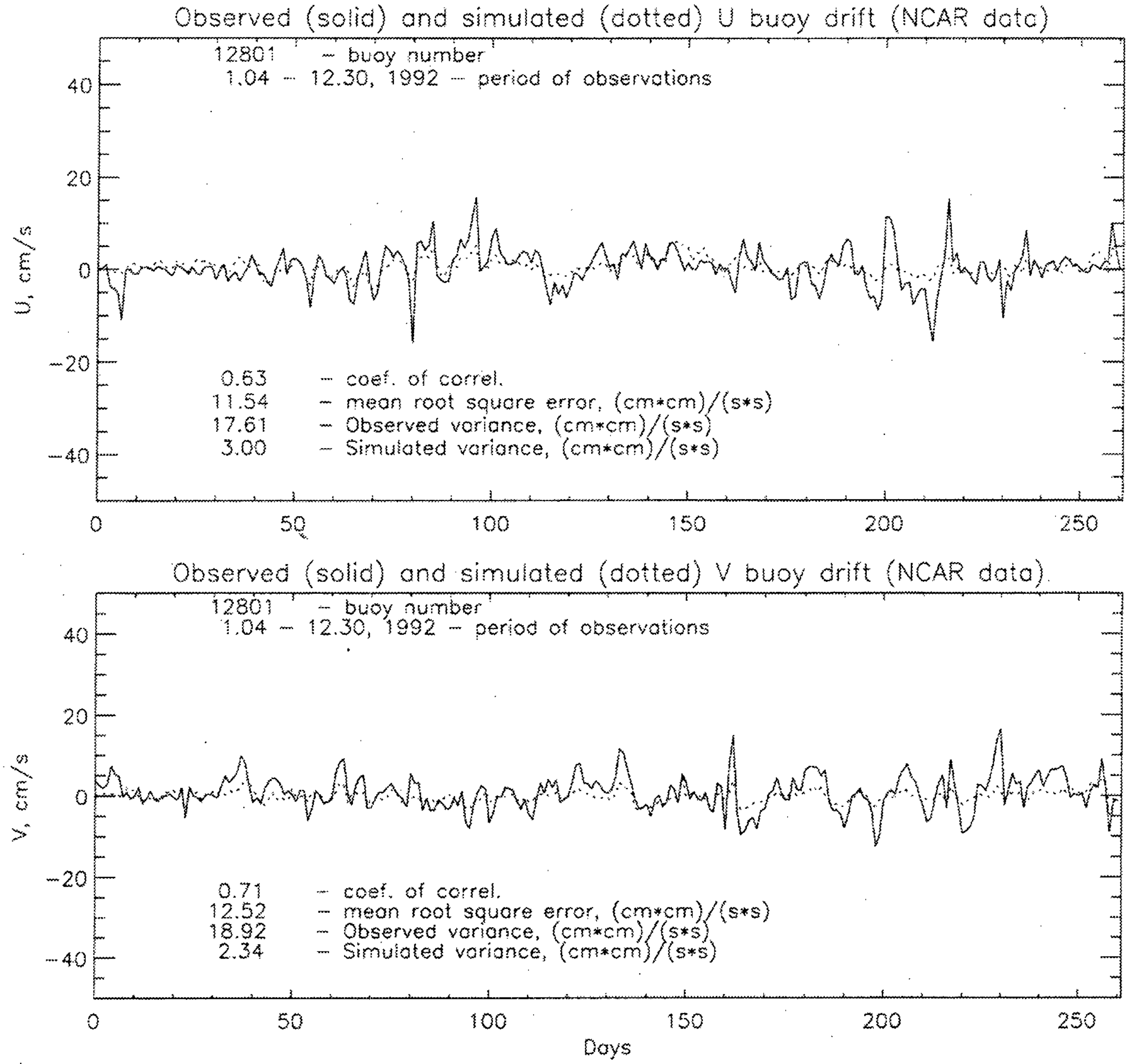

Figure 51. Observed and simulated components of the ice surface buoy drift. Buoy # 12801. Simulated ice drift is based on Thorndike–Colony empirical model using NCAR atmospheric pressure fields.

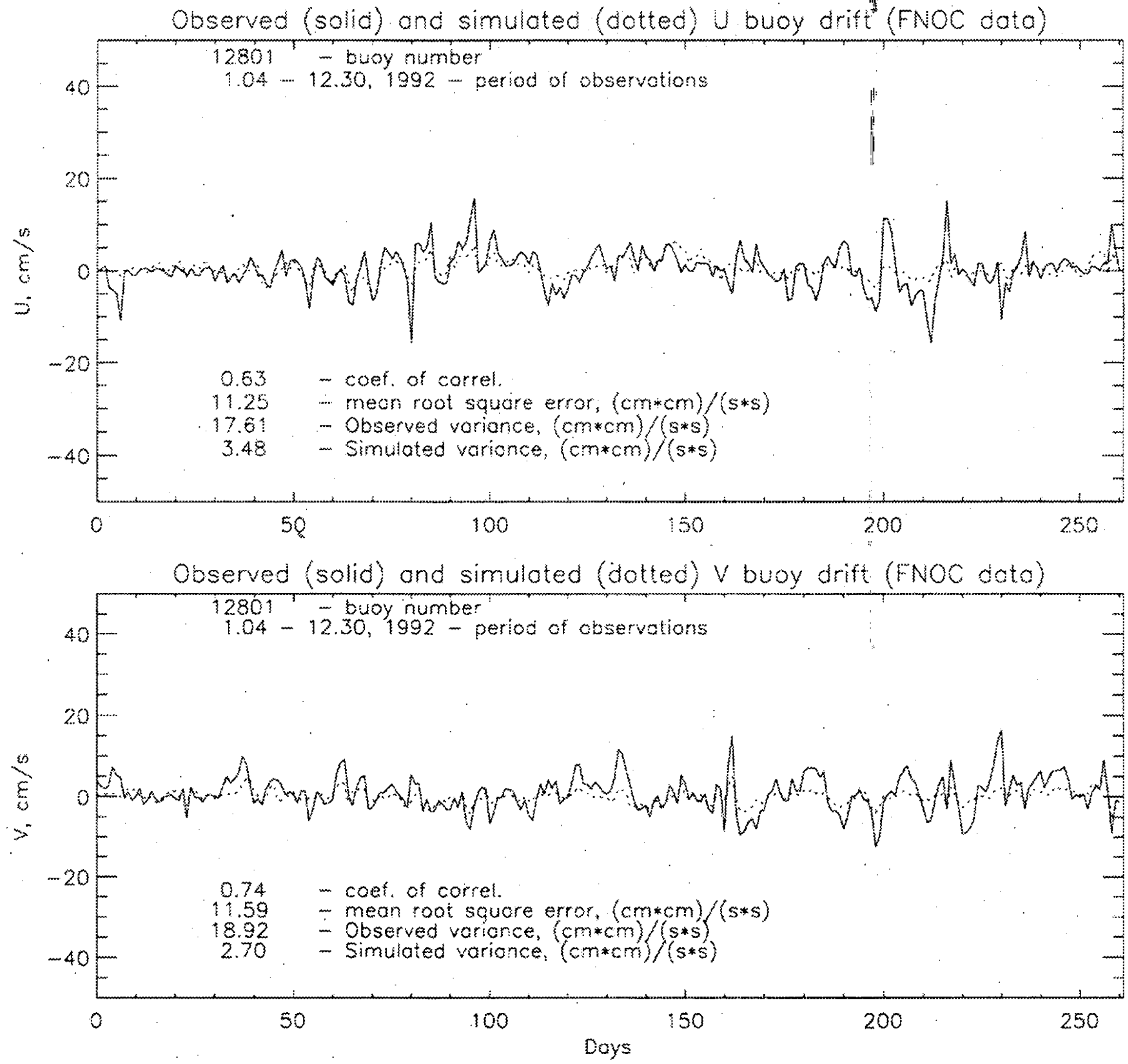

Figure 52. Same as Figure 51 except for FNOC atmospheric pressure data.

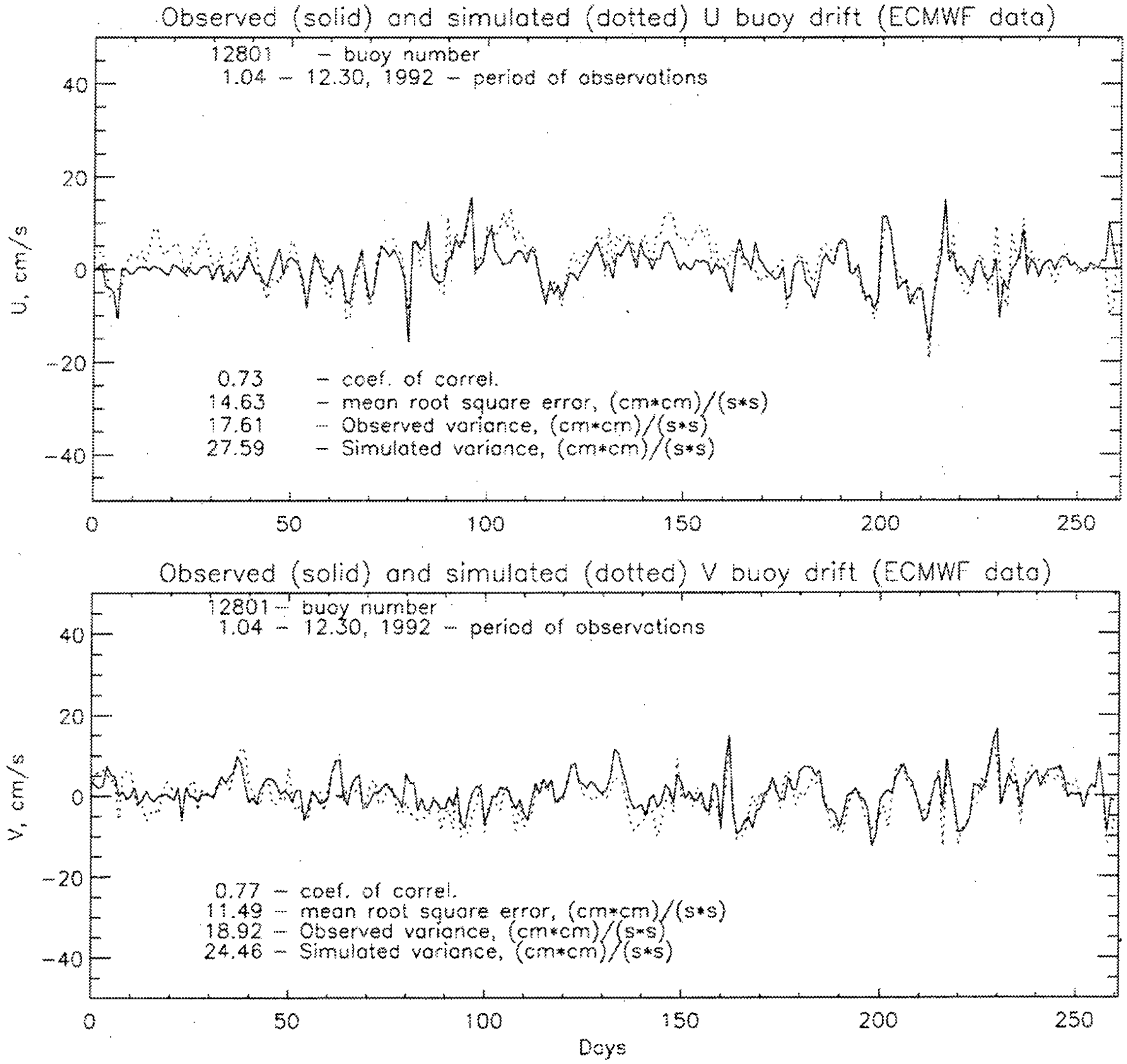

Figure 53. Same as Figure 51 except for ECMWF atmospheric pressure data.

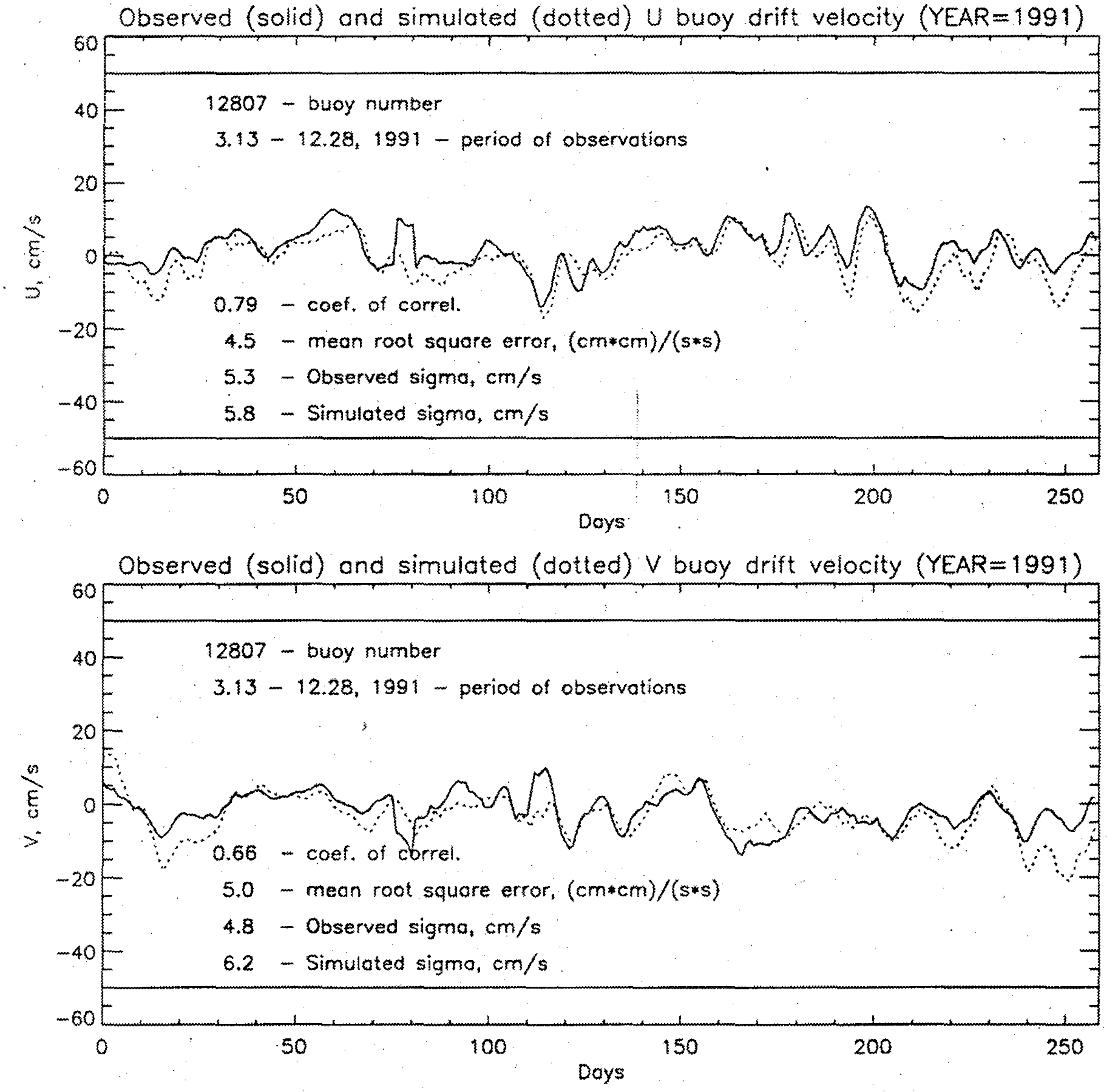

Figure 54. Observed and simulated components of the ice surface buoy drift. Buoy # 12807 in 1991. Simulated ice drift is based on 2-D coupled ice–ocean model using FNOC atmospheric pressure fields.

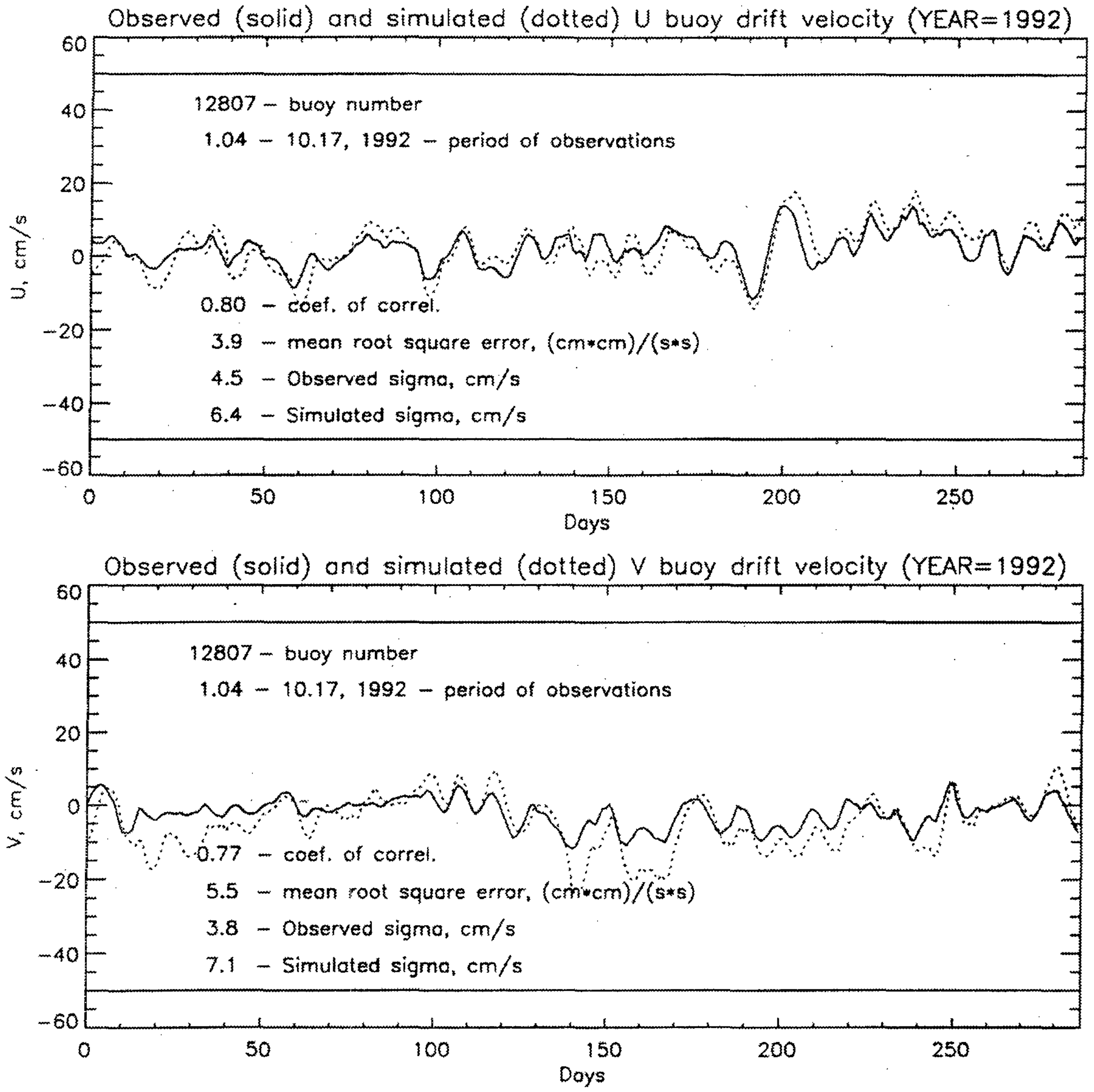

Figure 55. Same as Figure 54 for the year 1992.

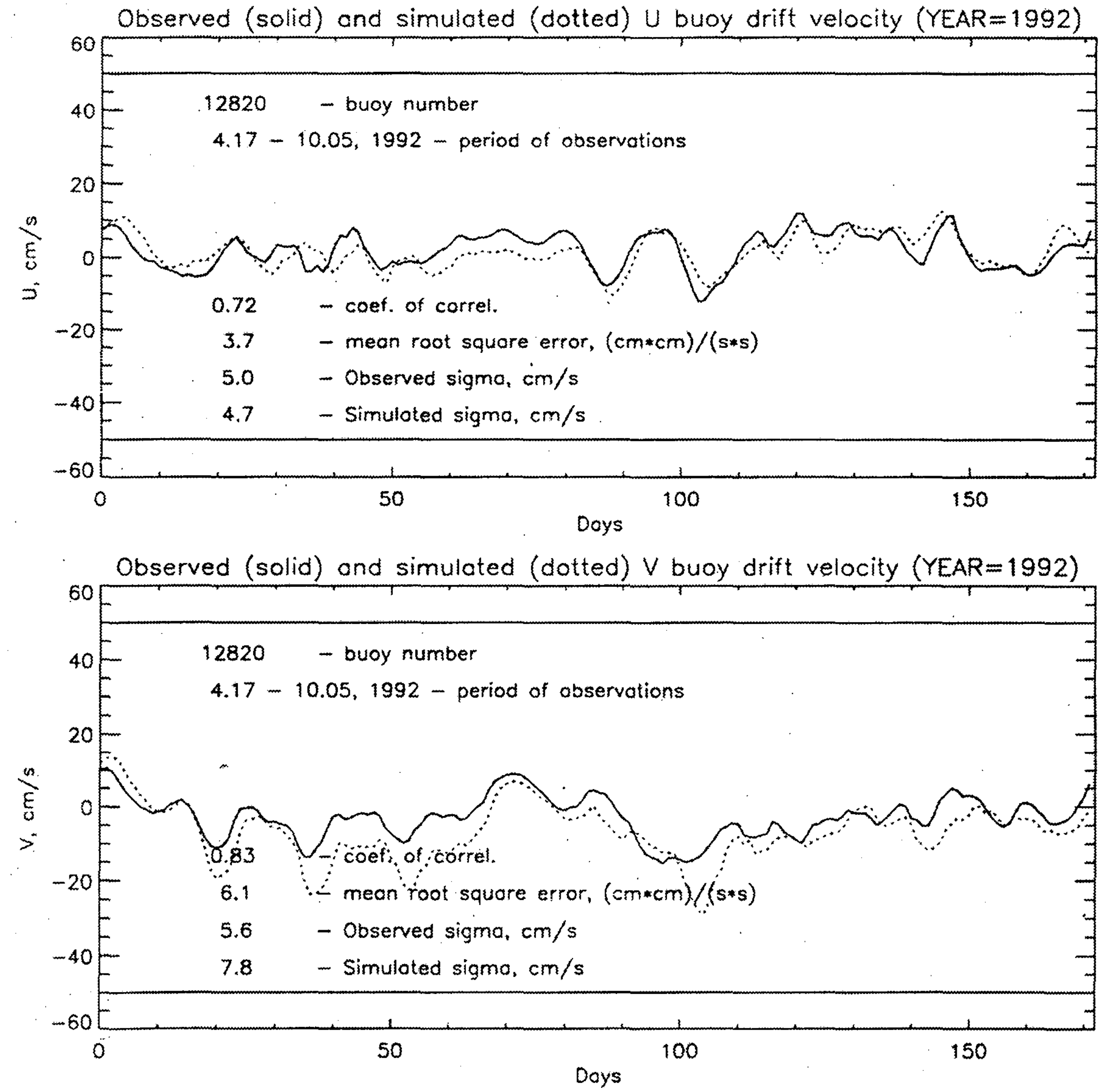

Figure 56. Same as Figure 54 except for buoy # 12820 in 1992.

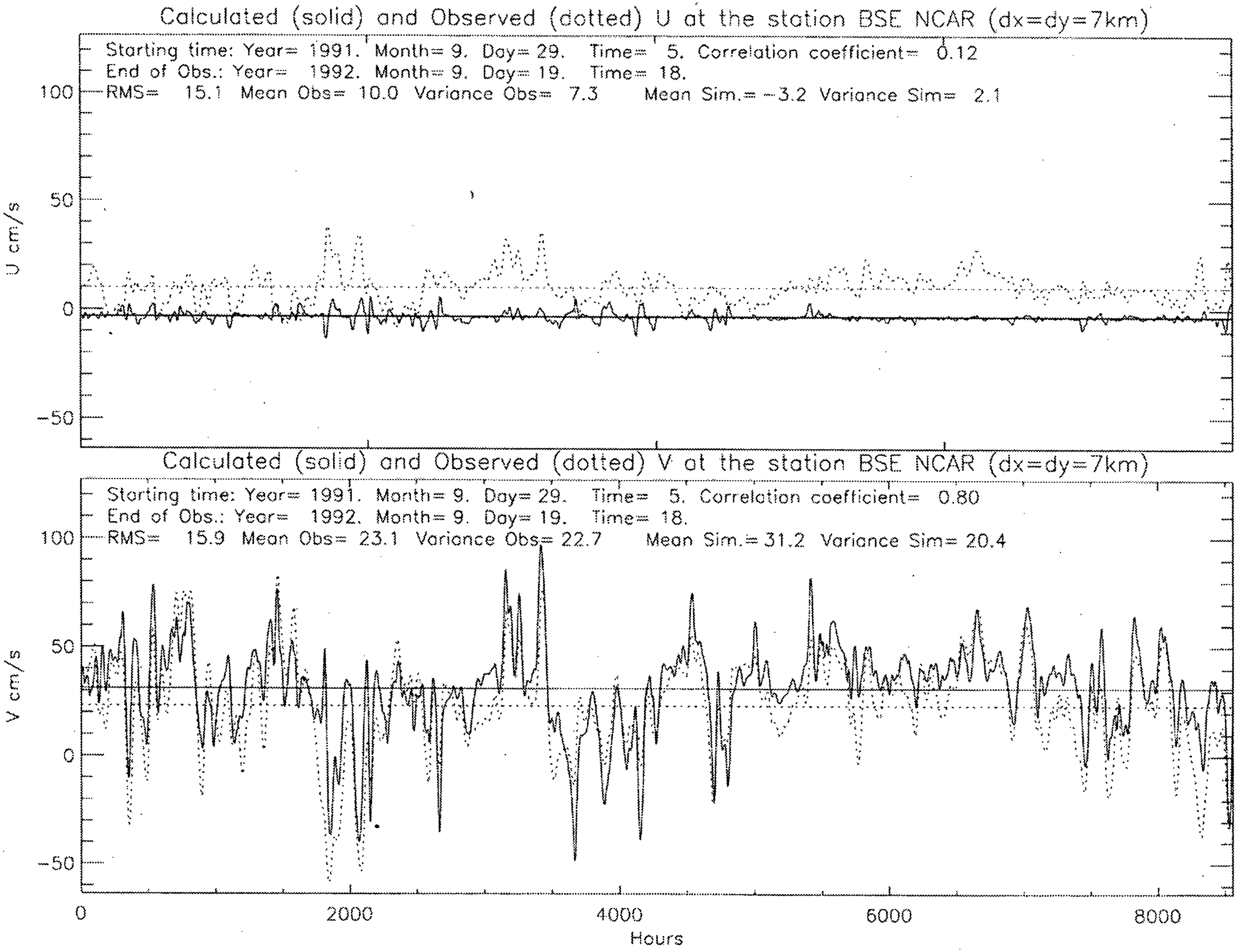

Figure 57. Time series of observed and simulated currents at the mooring BSE. Calculated velocities are obtained using 2-D coupled ice-ocean model and NCAR atmospheric pressure fields.

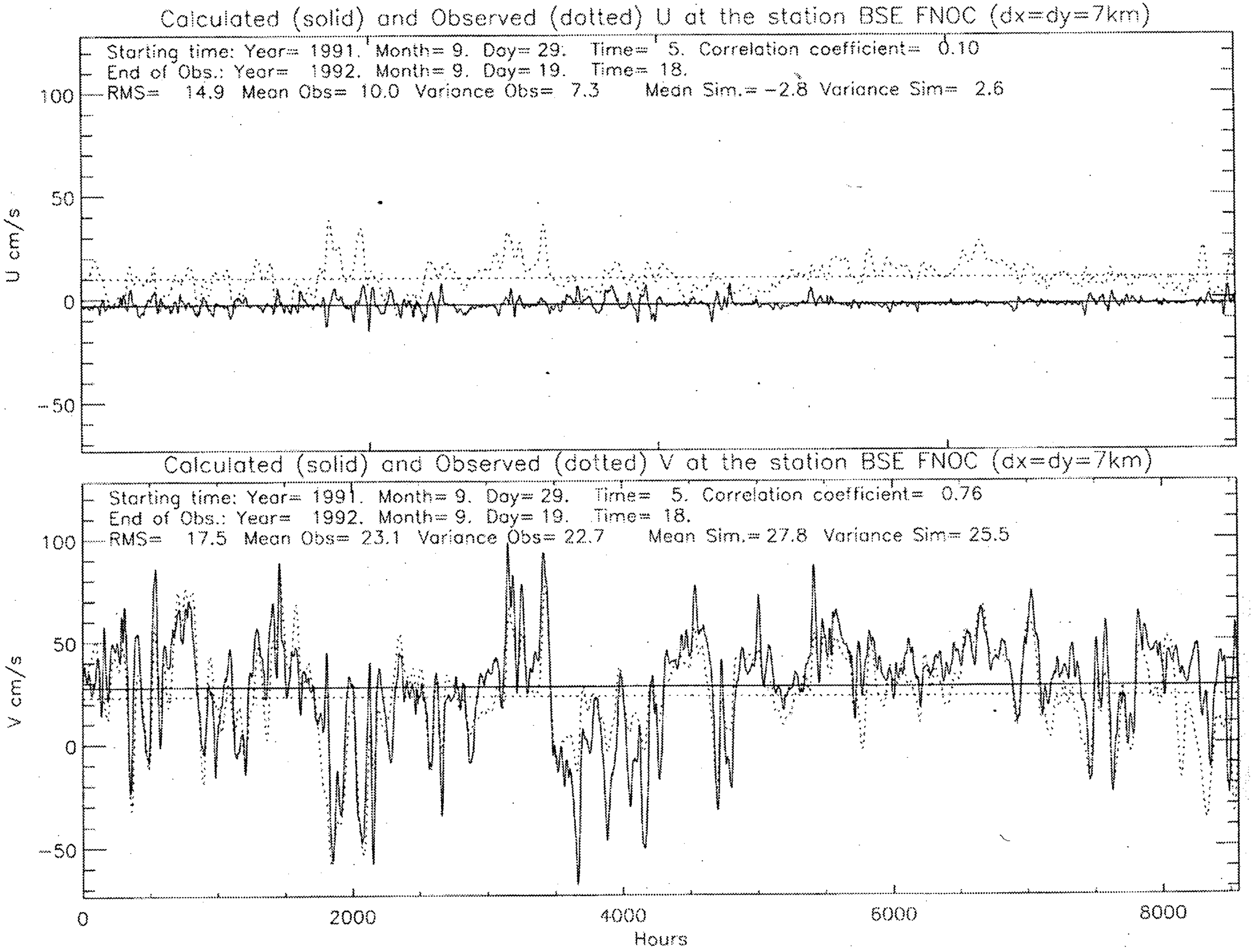

Figure 58. Same as Figure 57 except for the FNOC atmospheric pressure data.

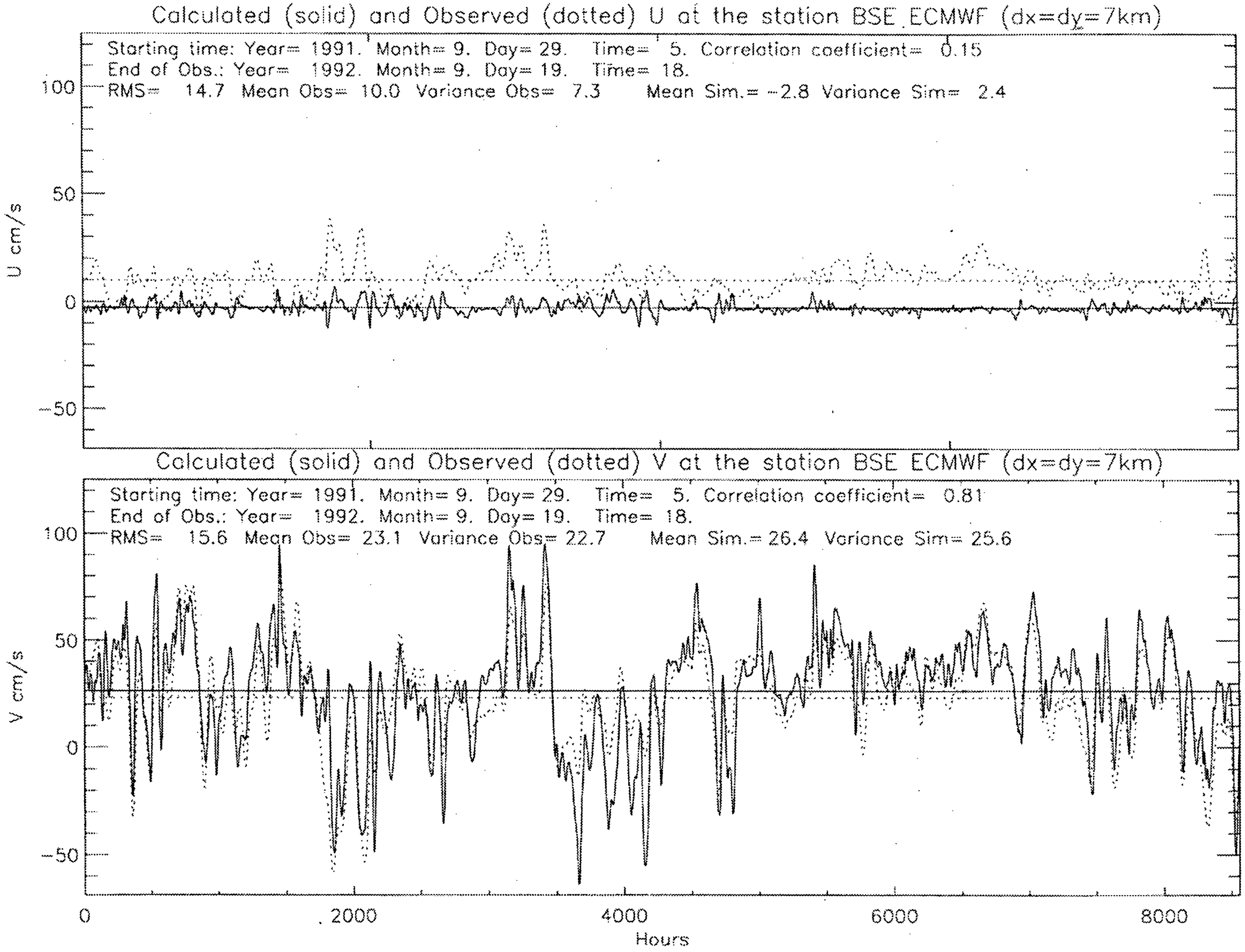

Figure 59. Same as Figure 57 except for the ECMWF atmospheric pressure data.

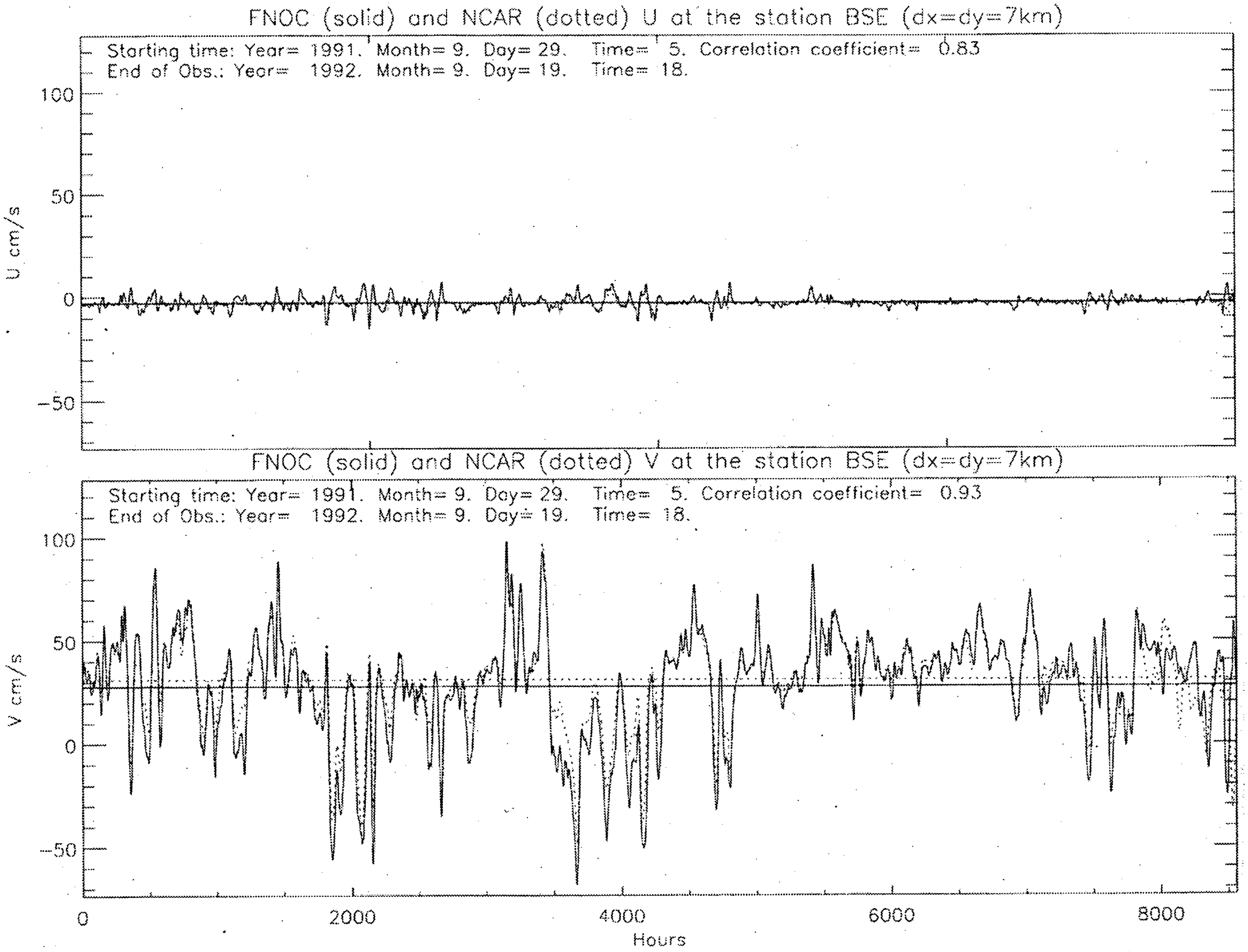

Figure 60. Comparison of FNOC- and ECMWF-based components of currents at mooring BSE.

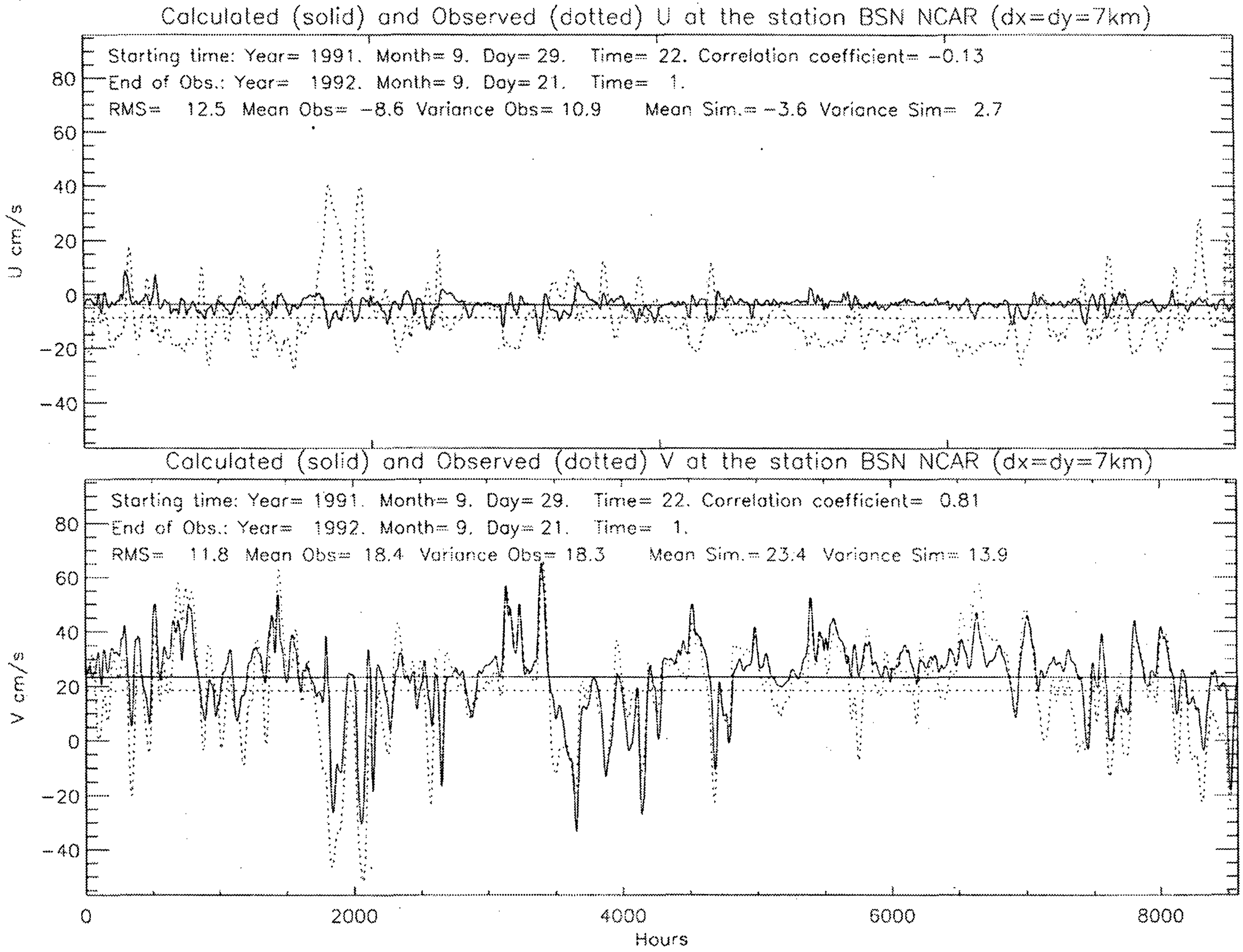

Figure 61. Time series of observed and simulated currents at the mooring BSN. Calculated velocities are obtained using 2-D coupled ice–ocean model and NCAR atmospheric pressure fields.

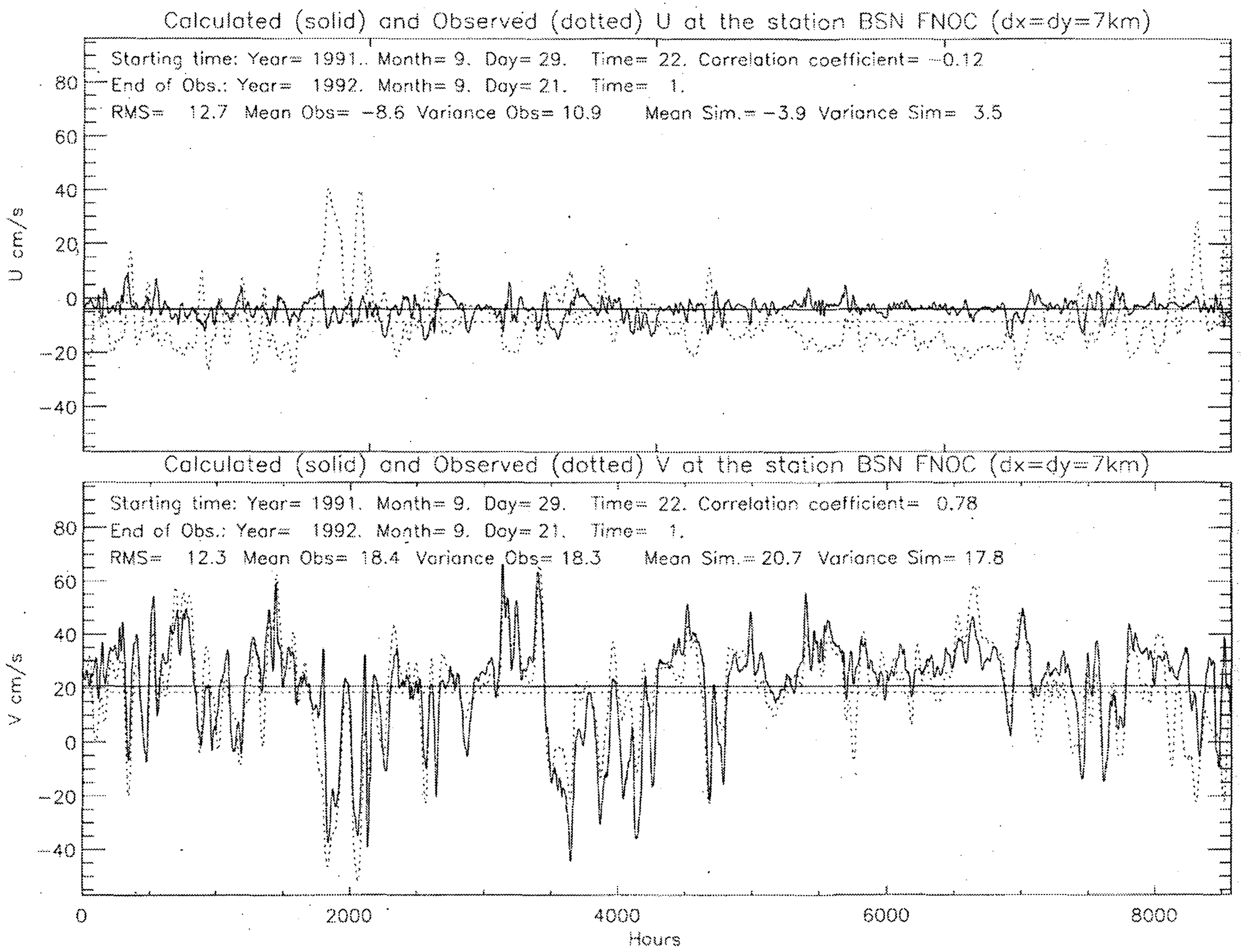

Figure 62. Same as Figure 61 except for the FNOC atmospheric pressure data.

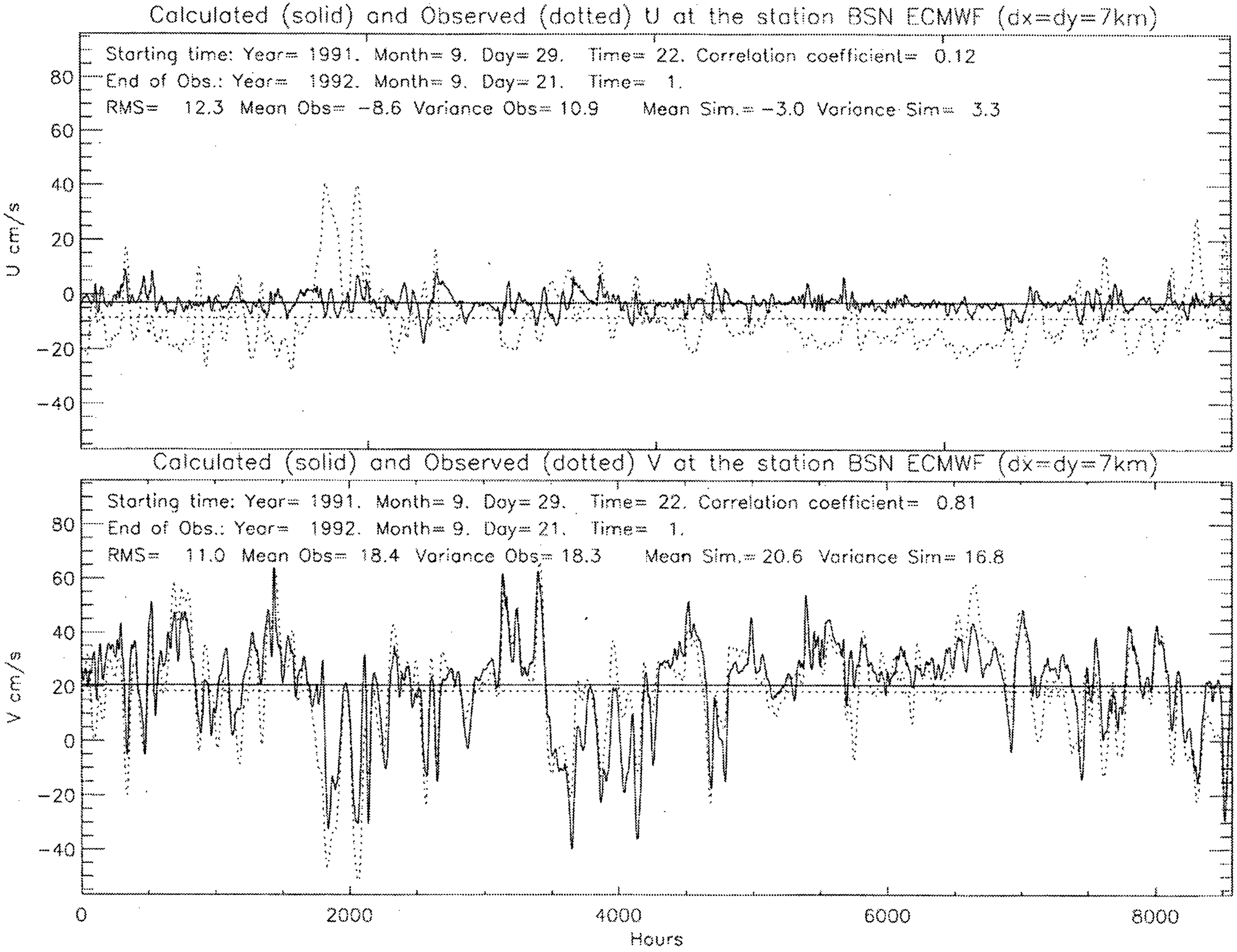

Figure 63. Same as Figure 61 except for the ECMWF atmospheric pressure data.

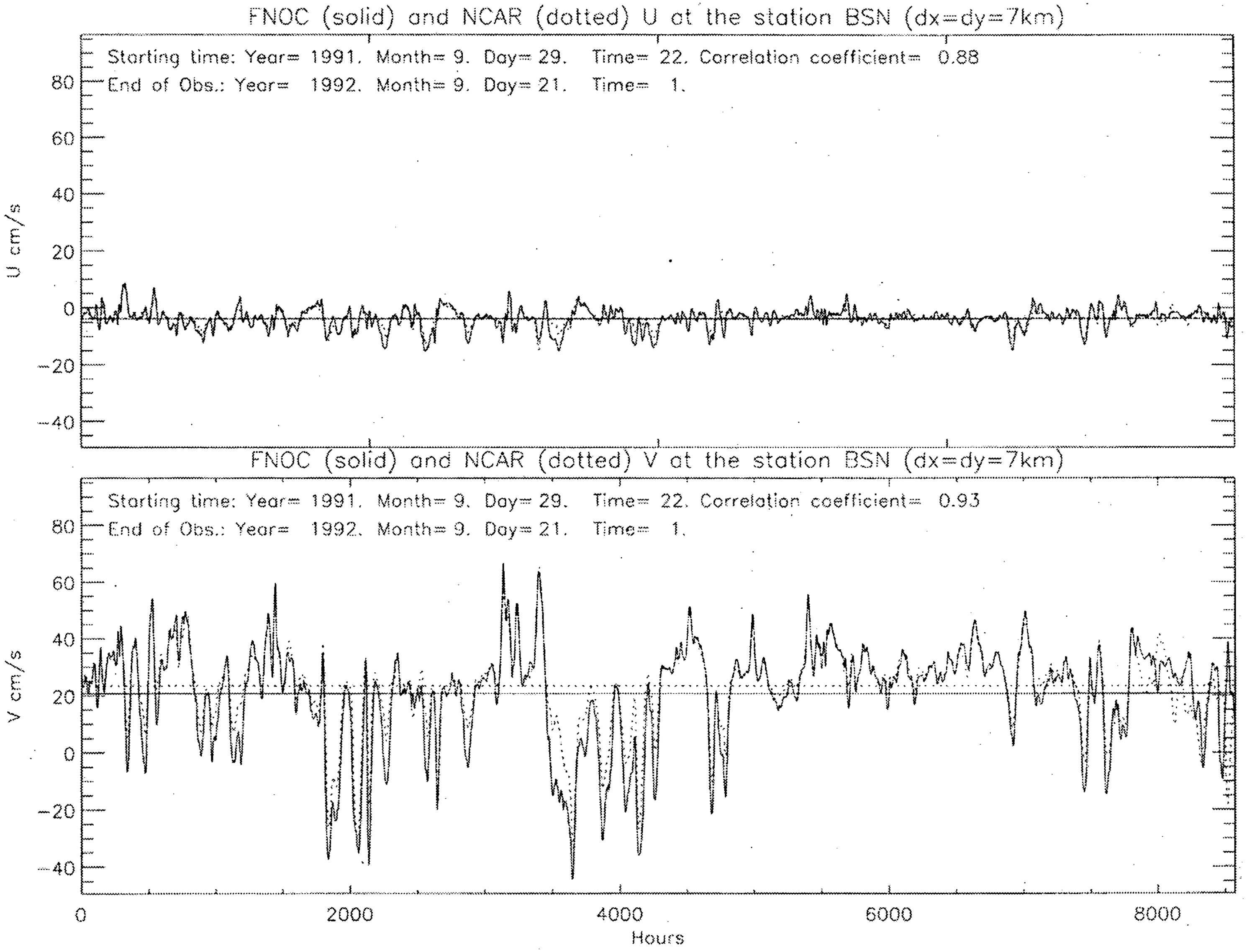

Figure 64. Comparison of FNOC- and ECMWF-based components of currents at mooring BSN.

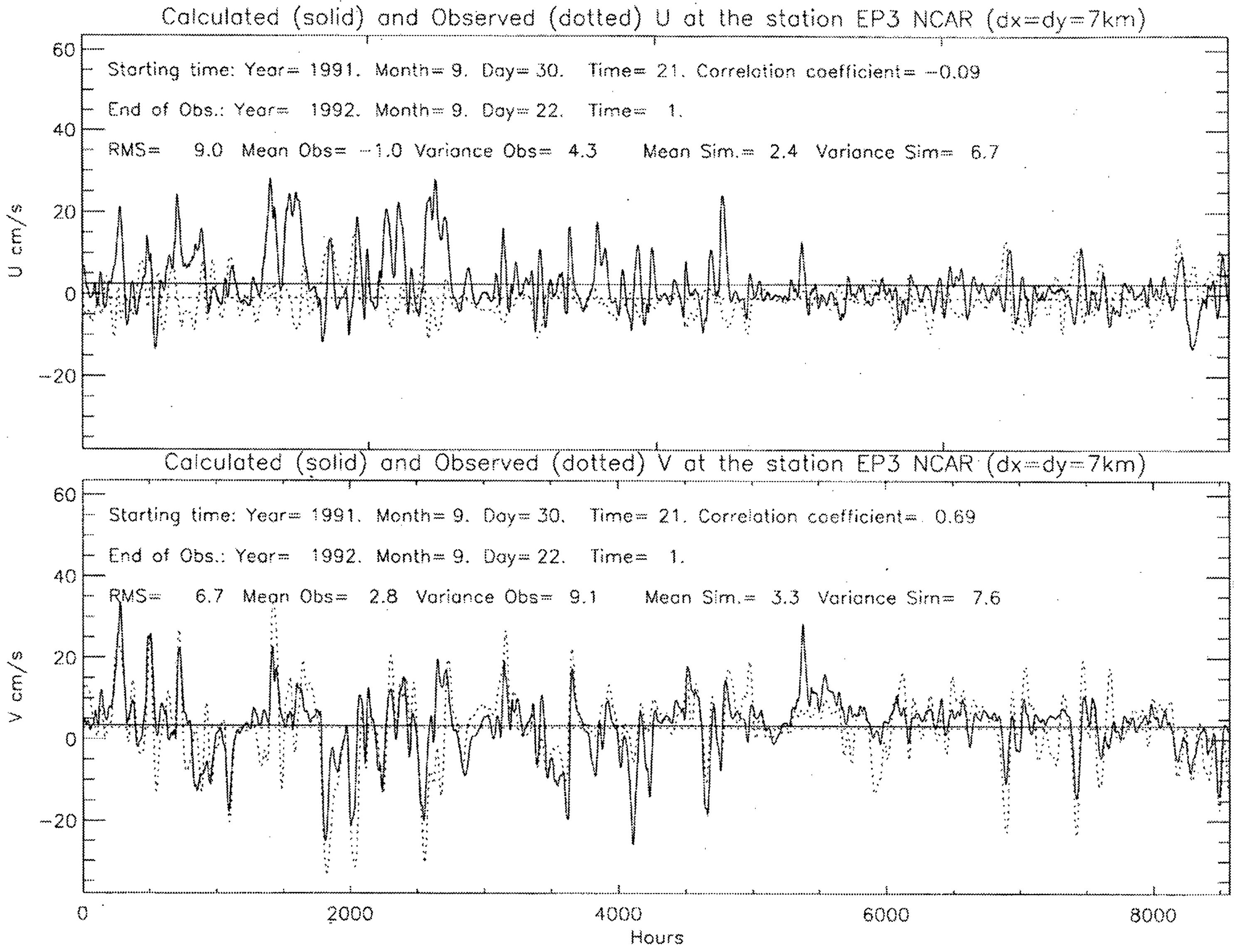

Figure 65. Time series of observed and simulated currents at mooring EP3. Calculated velocities are obtained using a 2-D coupled ice–ocean model and NCAR atmospheric pressure fields.

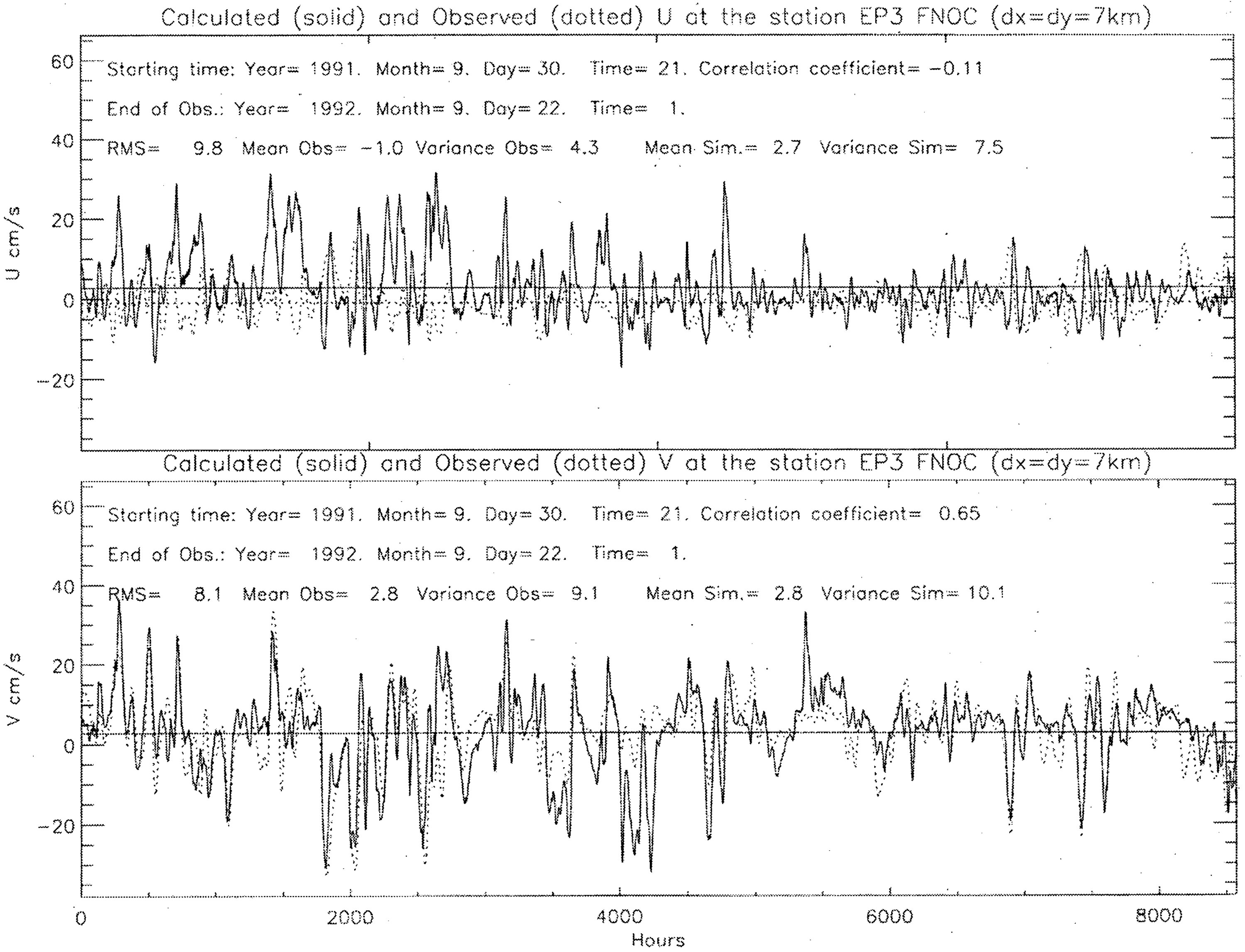

Figure 66. Same as Figure 57 except for the FNOC atmospheric pressure data.

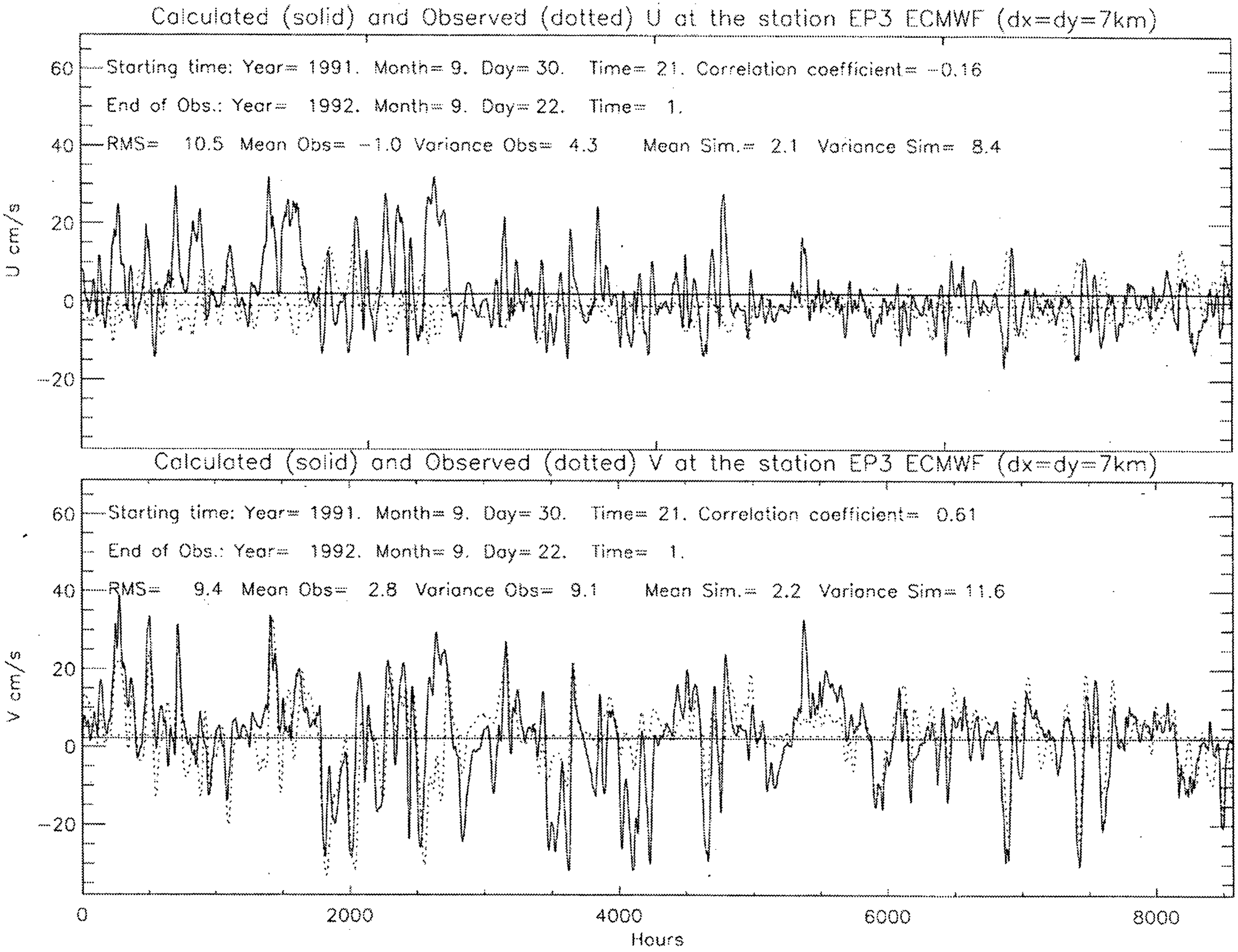

Figure 67. Same as Figure 57 except for the ECMWF atmospheric pressure data.

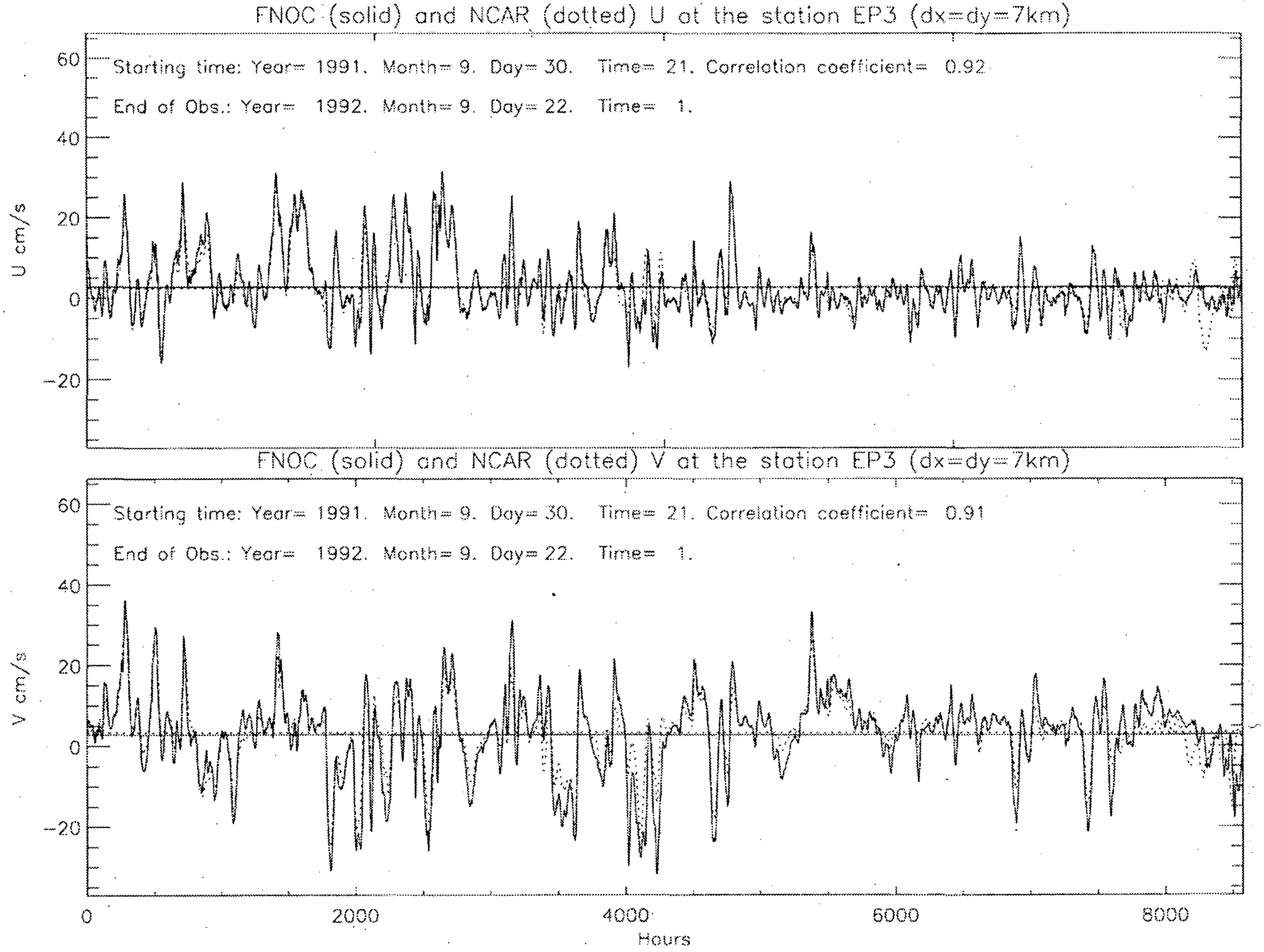

Figure 68. Comparison of FNOC- and ECMWF-based components of currents at mooring EP3.

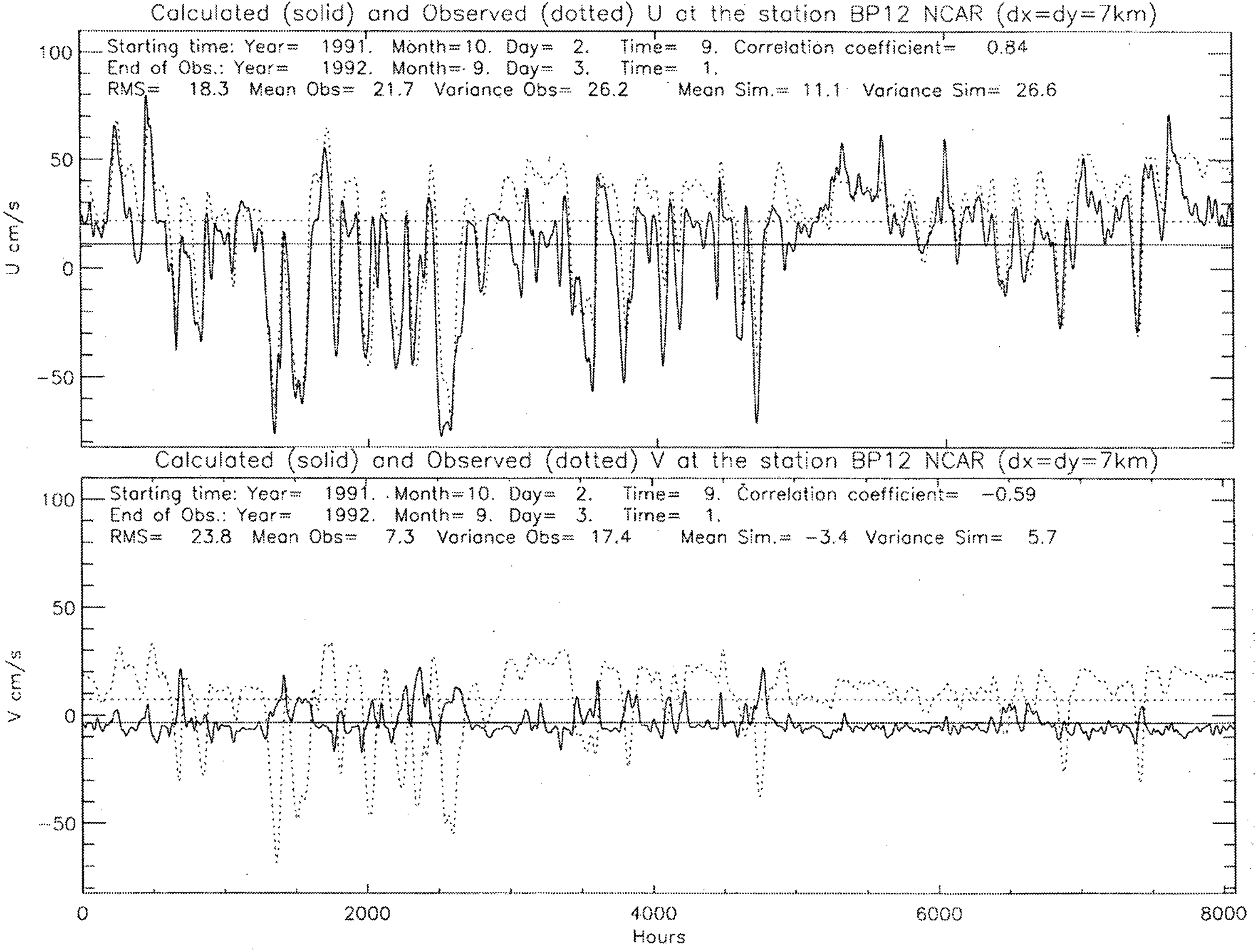

Figure 69. Time series of observed and simulated currents at mooring BP12. Calculated velocities are obtained using a 2-D coupled ice–ocean model and NCAR atmospheric pressure fields.

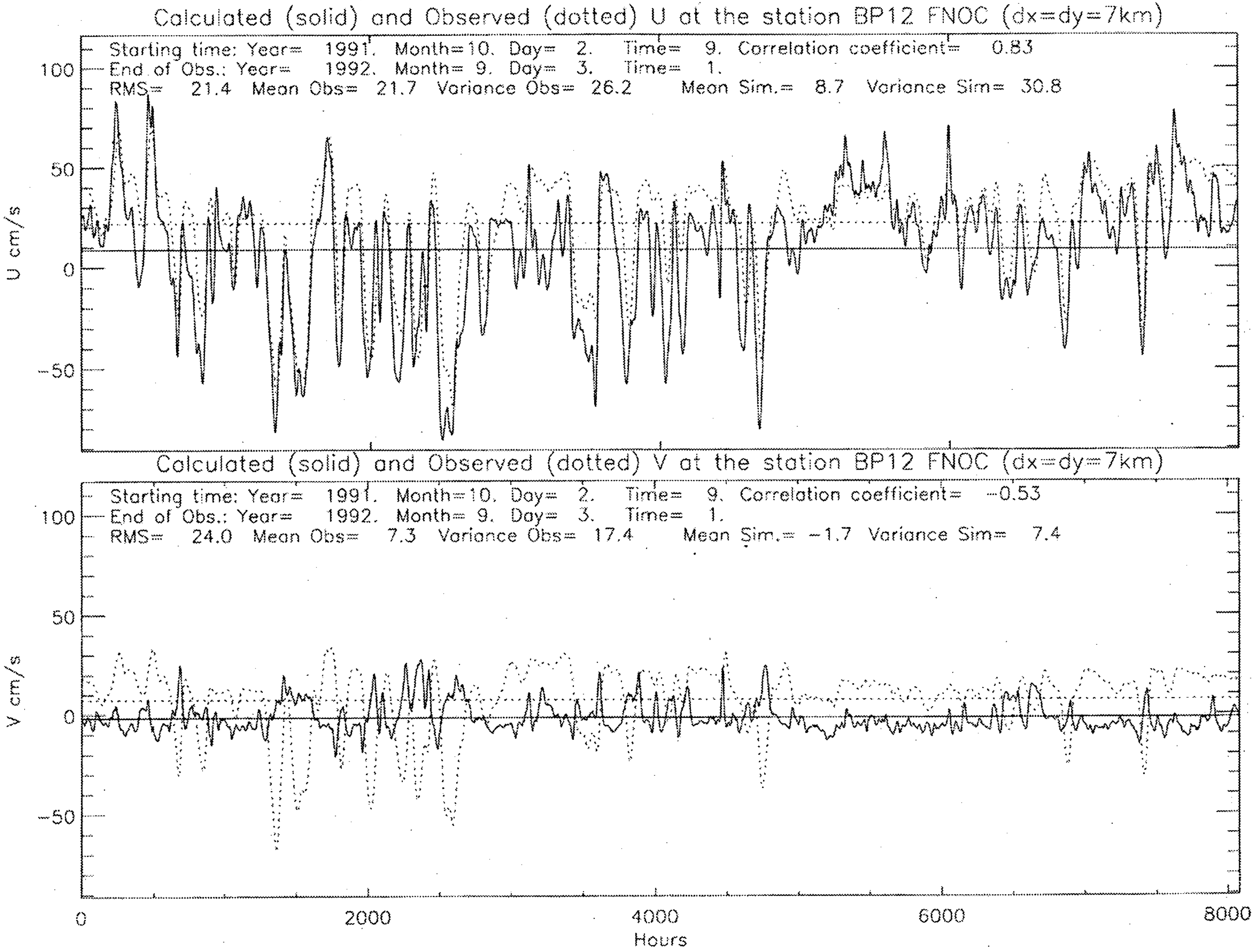

Figure 70. Same as Figure 69 except for the FNOC atmospheric pressure data.

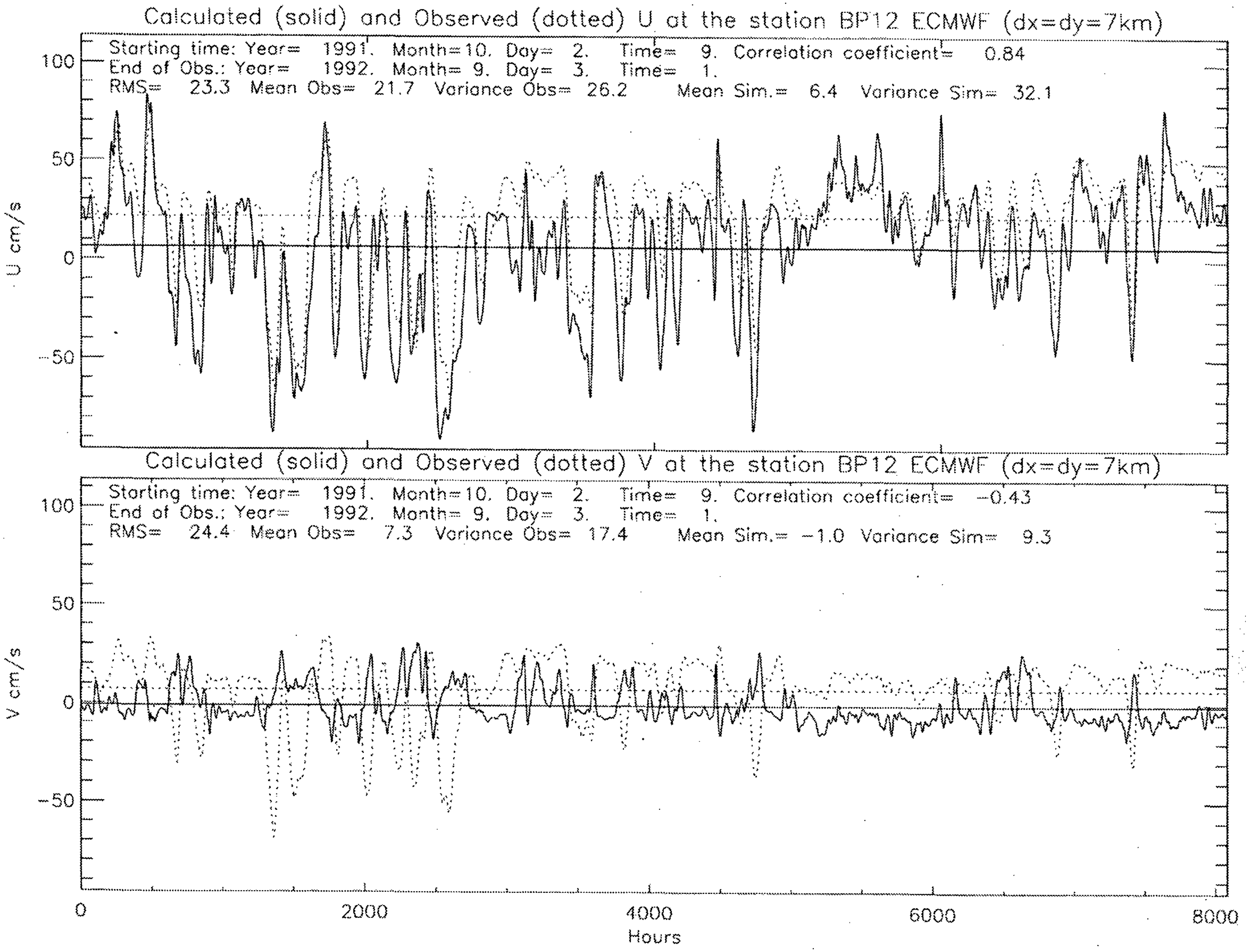

Figure 71. Same as Figure 69 except for the ECMWF atmospheric pressure data.

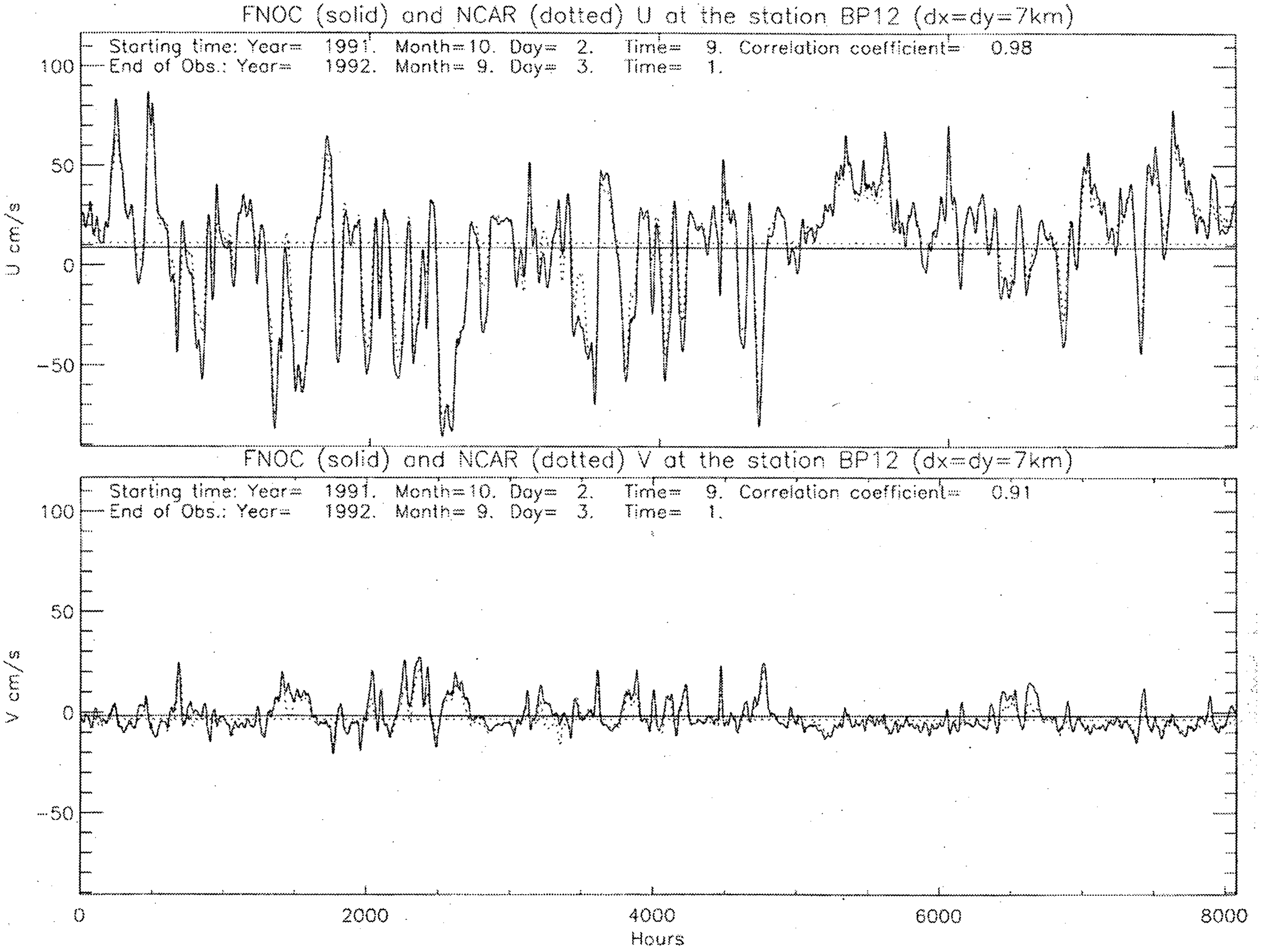

Figure 72. Comparison of FNOC- and ECMWF-based components of currents at mooring BP12.

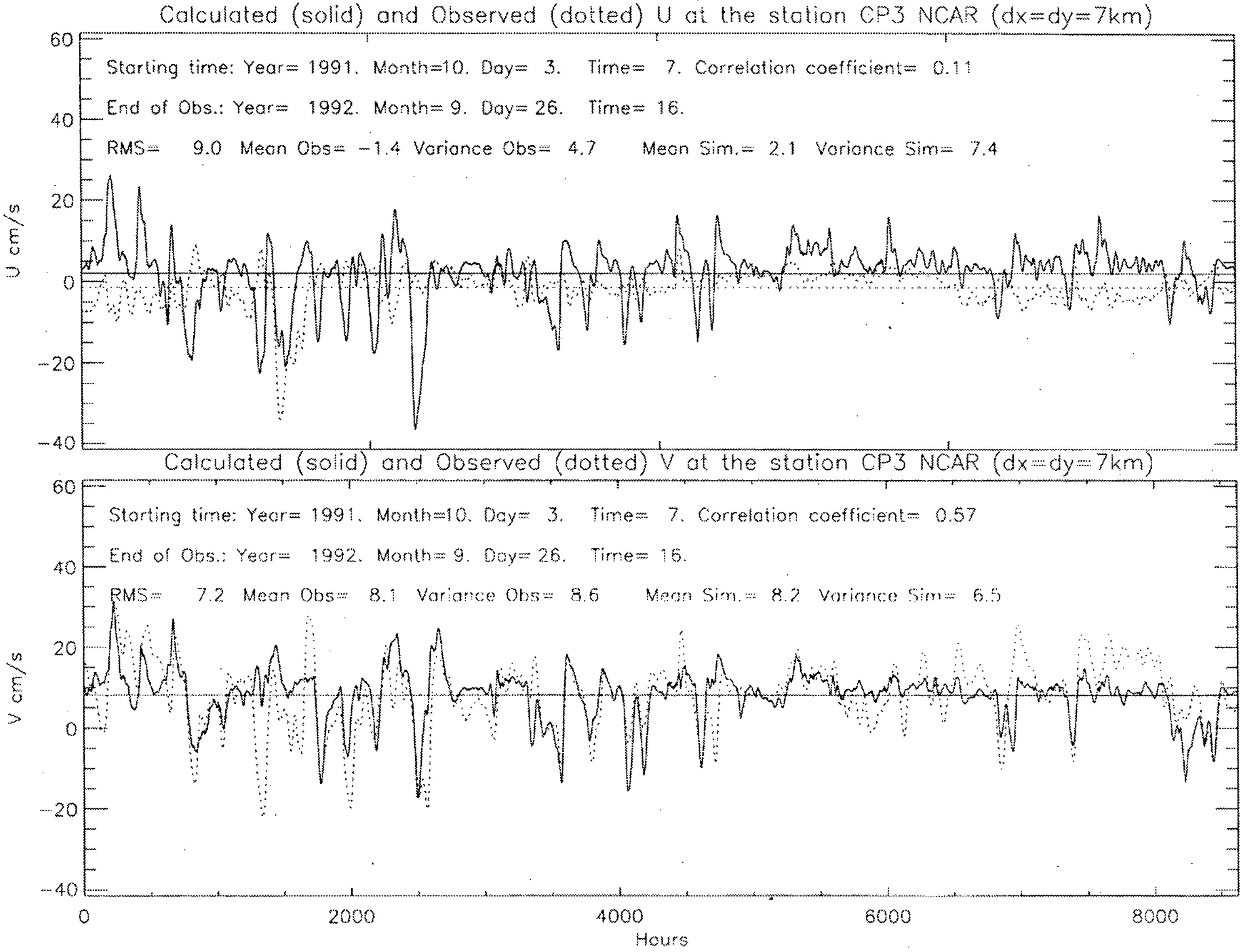

Figure 73. Time series of observed and simulated currents at mooring CP3. Calculated velocities are obtained using a 2-D coupled ice–ocean model and NCAR atmospheric pressure fields.

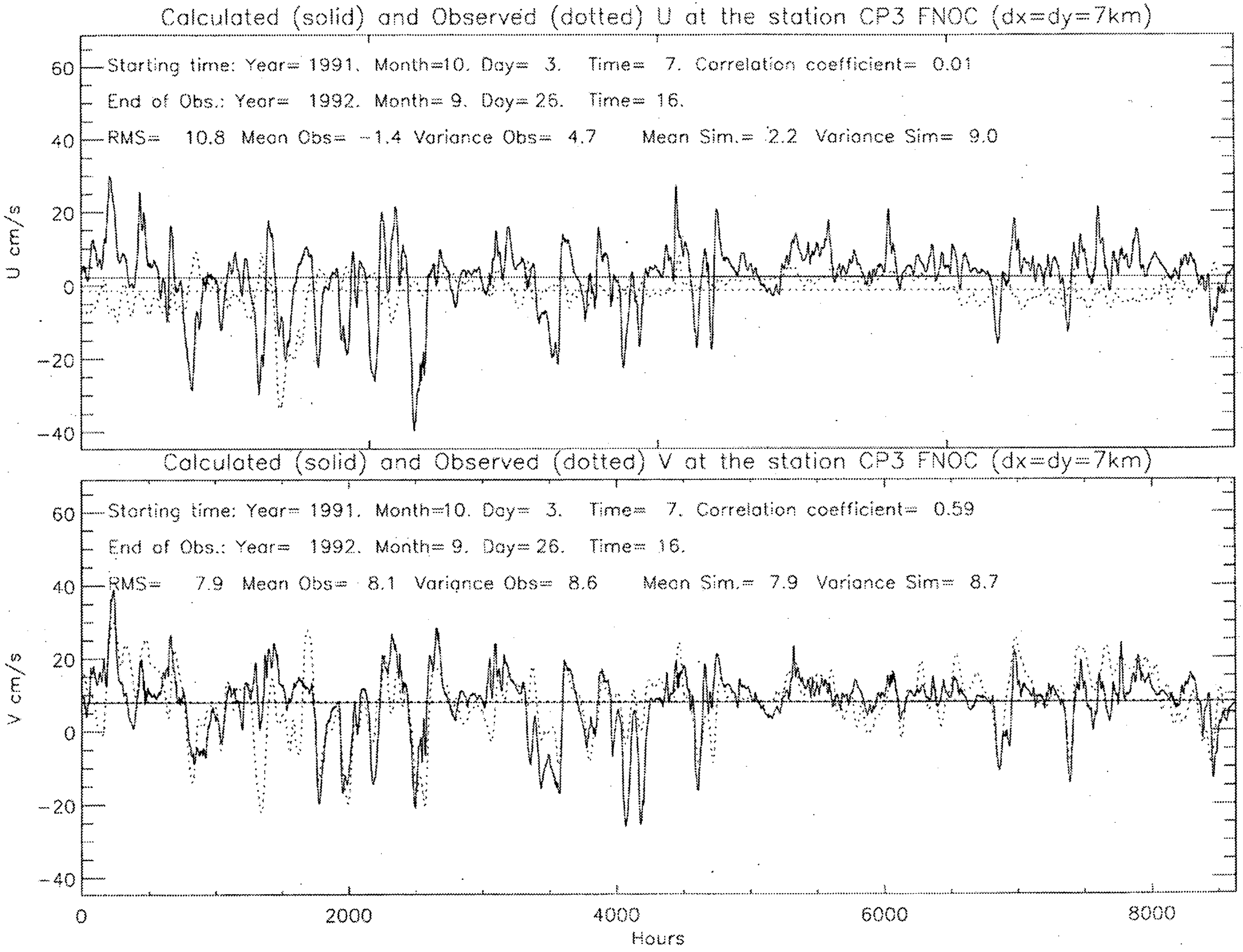

Figure 74. Same as Figure 73 except for the FNOC atmospheric pressure data.

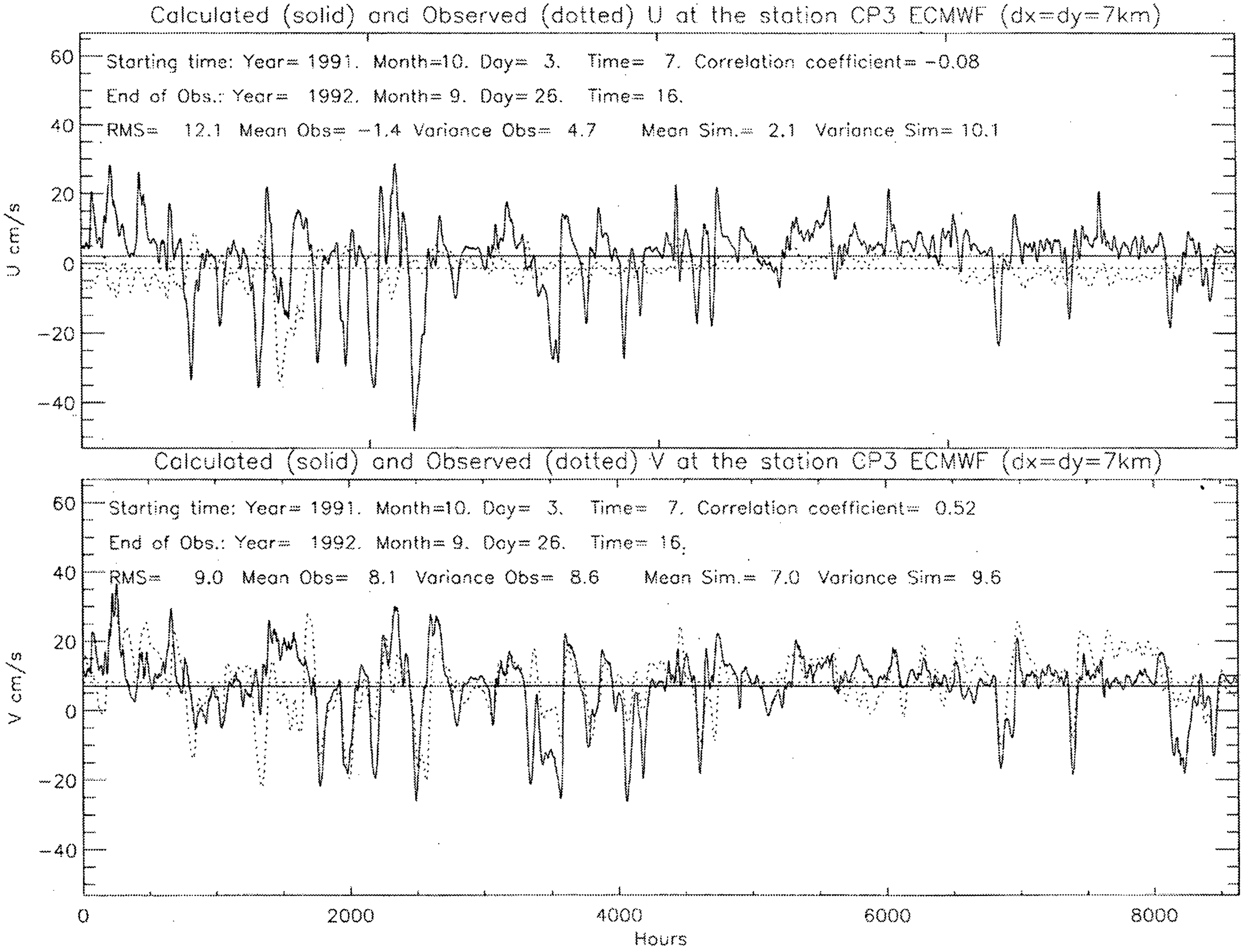

Figure 75. Same as Figure 73 except for the ECMWF atmospheric pressure data.

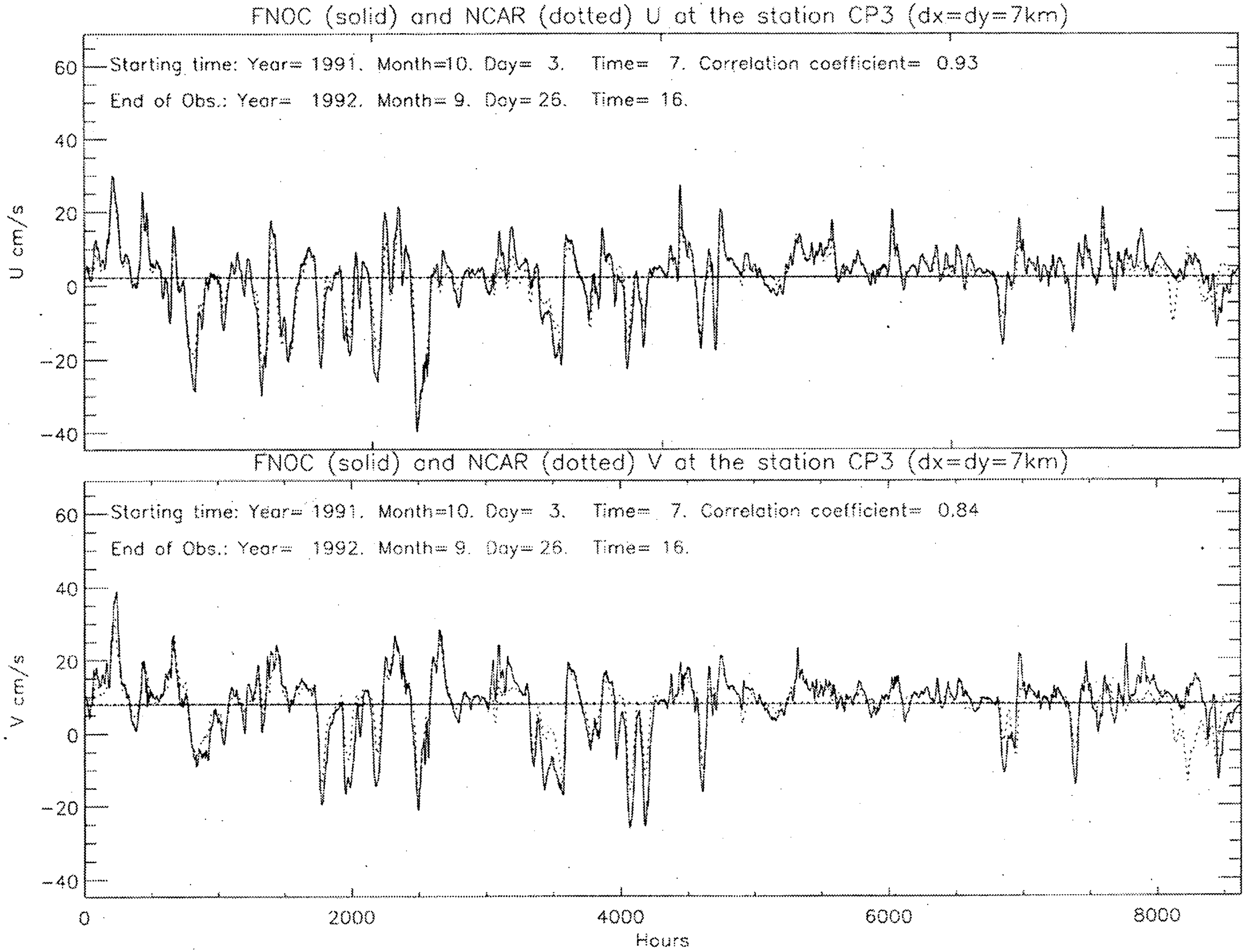

Figure 76. Comparison of FNOC- and ECMWF-based components of currents at mooring CP3.

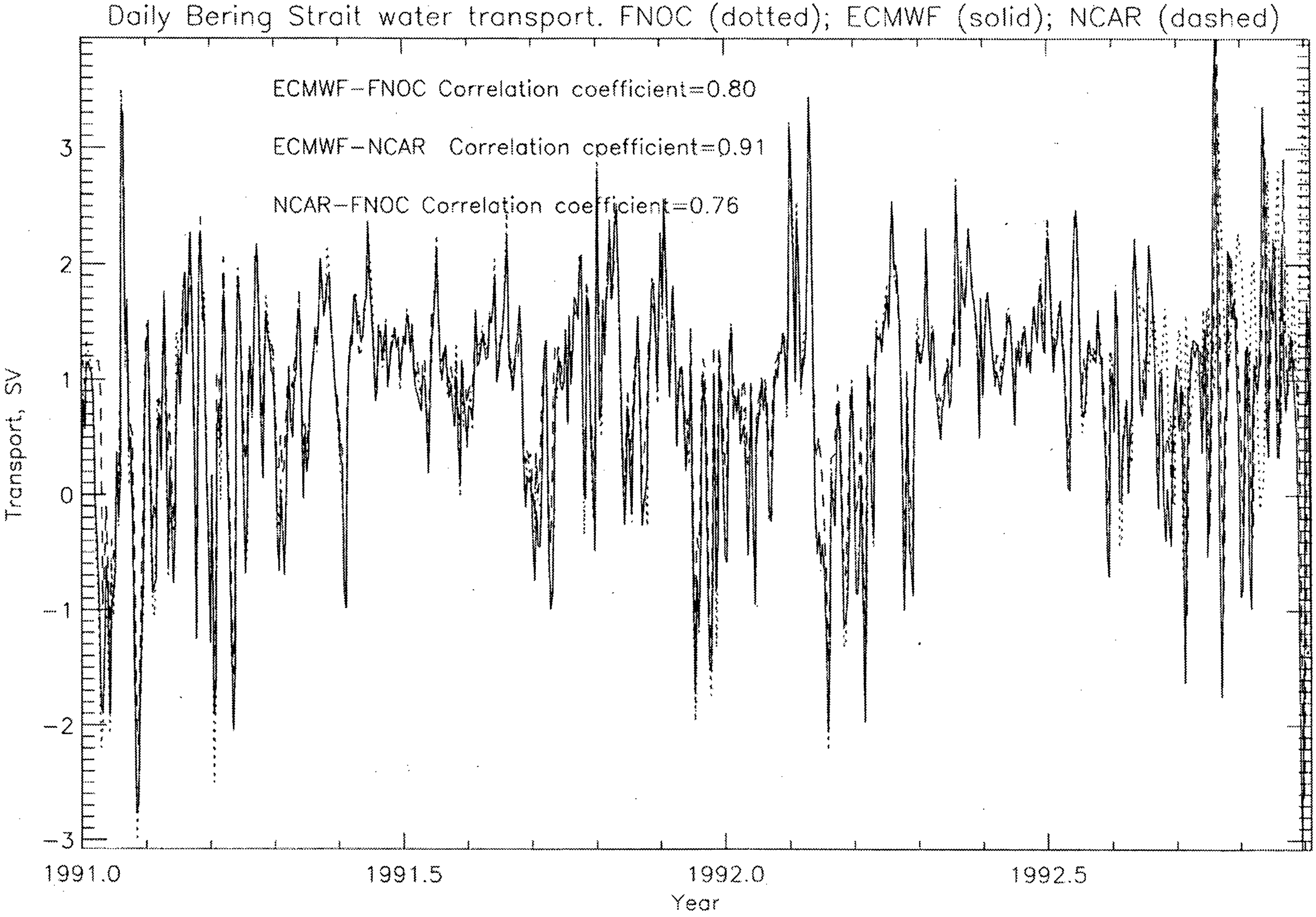

Figure 77. Daily Bering Strait simulated water transport (results of 2-D coupled ice–ocean model) based on ECMWF (solid line), FNOC (dotted line), and NCAR (dashed line) sea level atmospheric pressure fields.

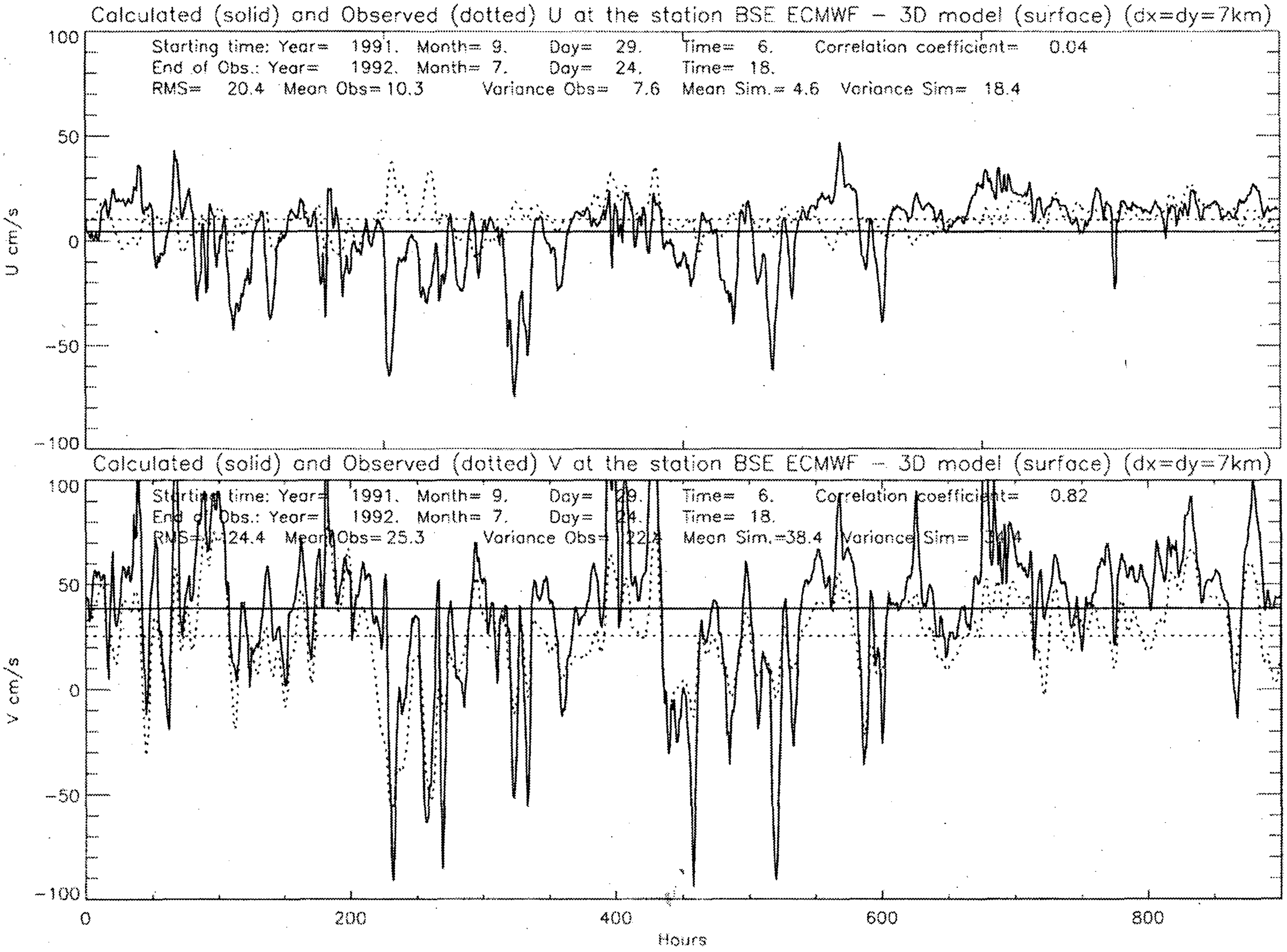

Figure 78. Time series of observed and simulated surface currents at mooring BSE. Calculated velocities obtained using a 3-D ocean barotropic model and ECMWF atmospheric pressure fields.

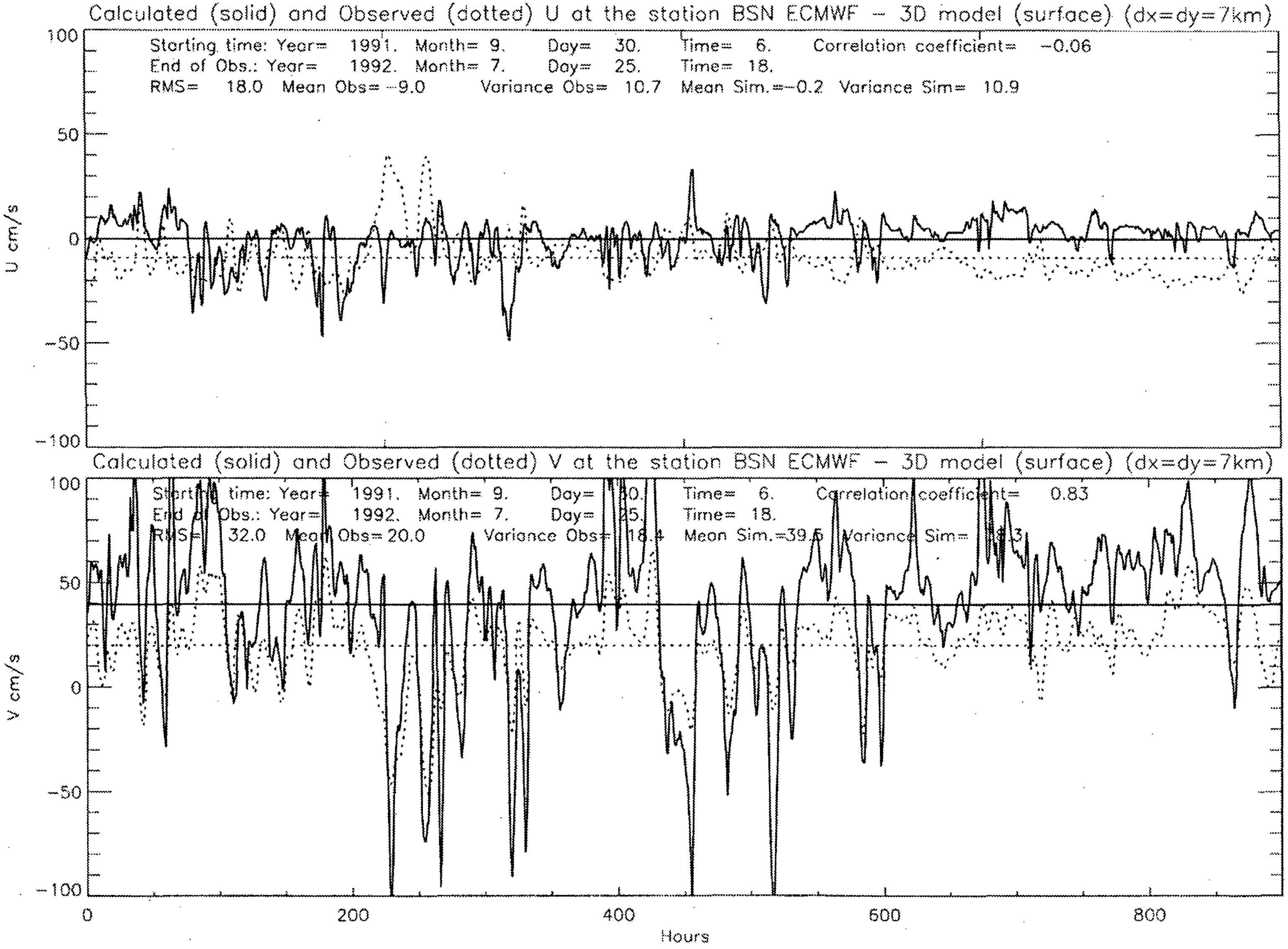

Calculated (solid) and Observed (dotted) U at the station BSN ECMWF – 3D model (surface) (dx=dy=7km)

Calculated (solid) and Observed (dotted) V at the station BSN ECMWF – 3D model (surface) (dx=dy=7km)

Figure 79. Same as Figure 78 for mooring BSN

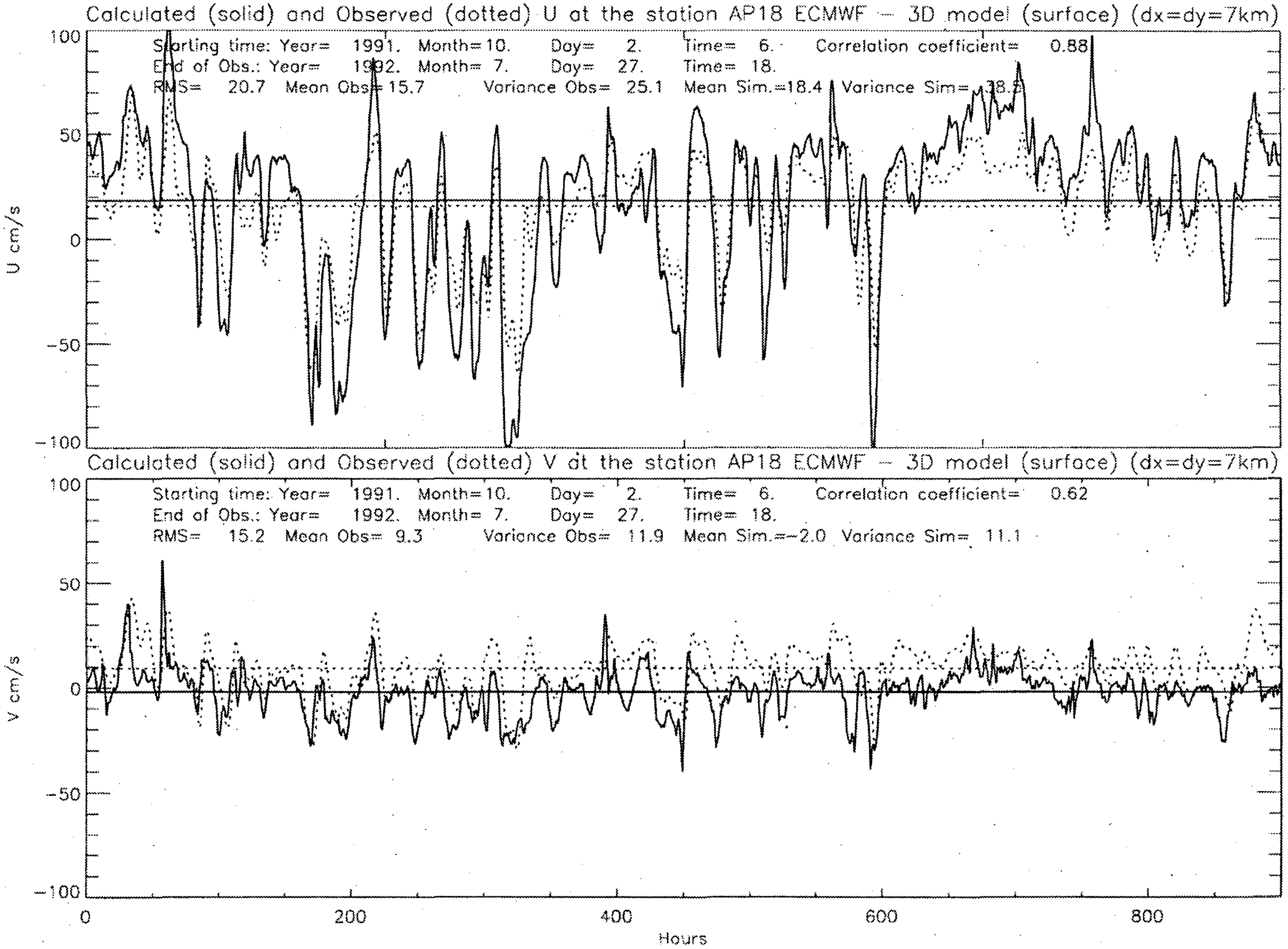

Figure 80. Same as Figure 78 for mooring AP18.

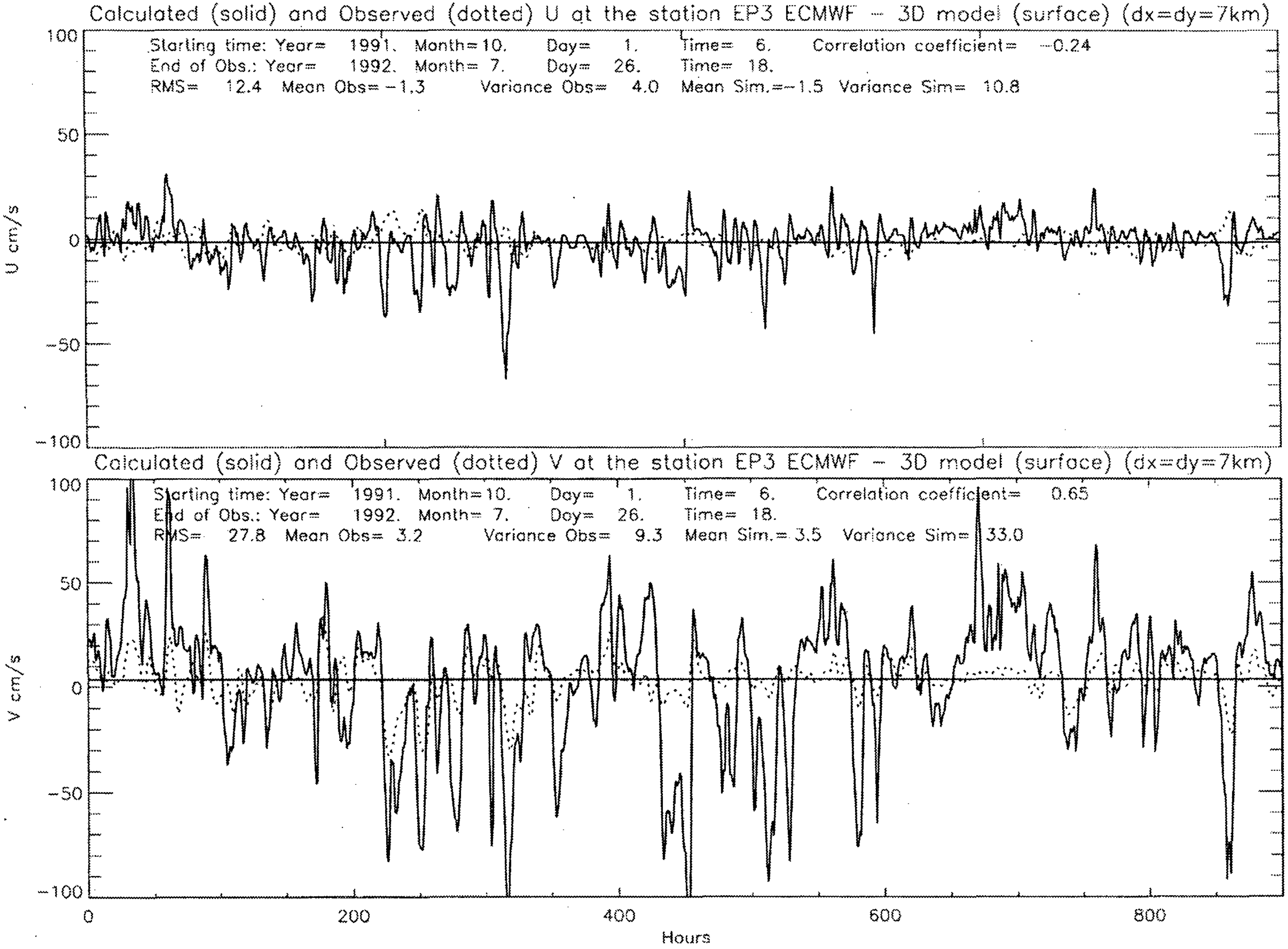

Figure 81. Same as Figure 78 for mooring EP3.

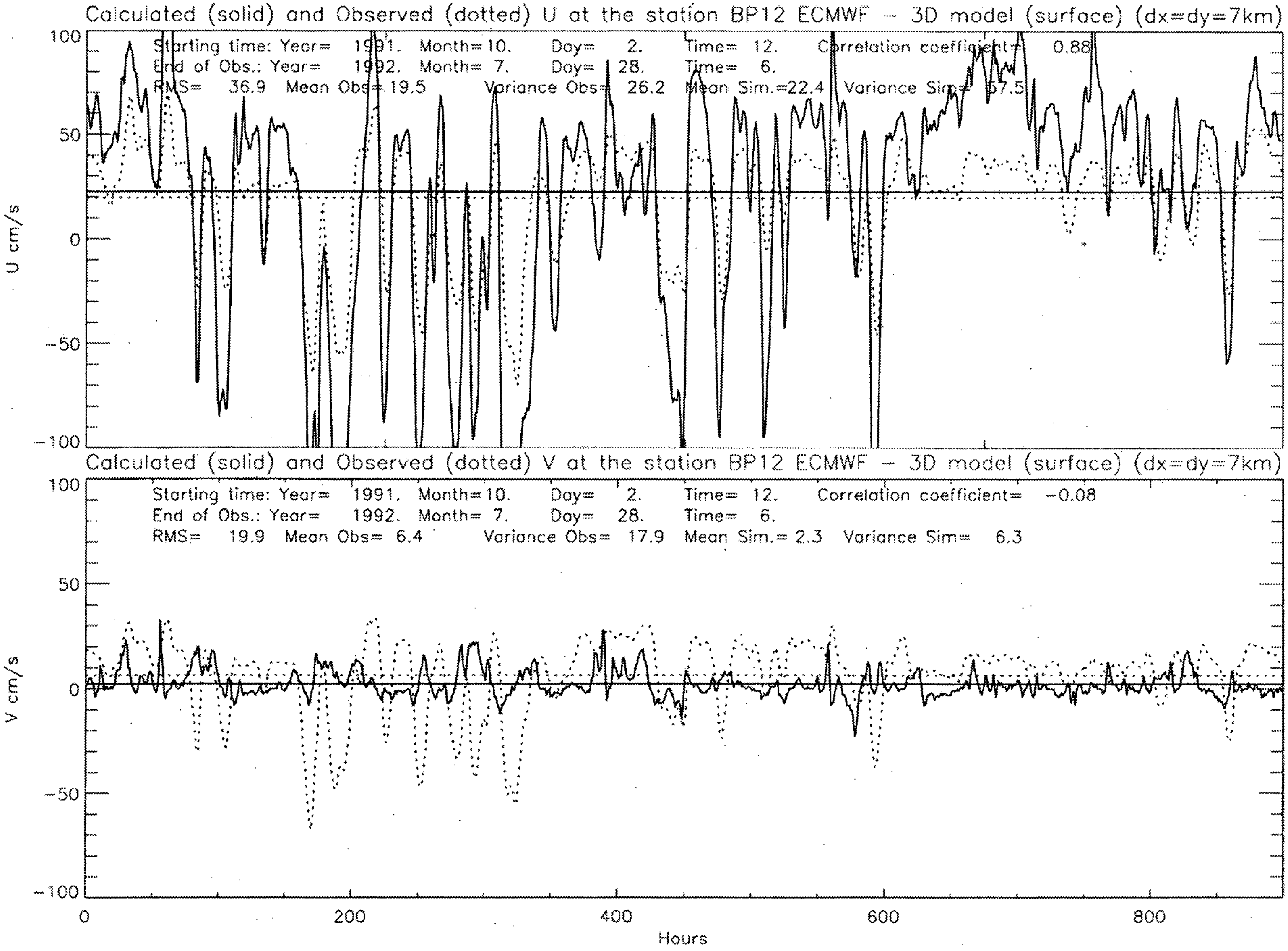

Figure 82. Same as Figure 78 for mooring BP12.

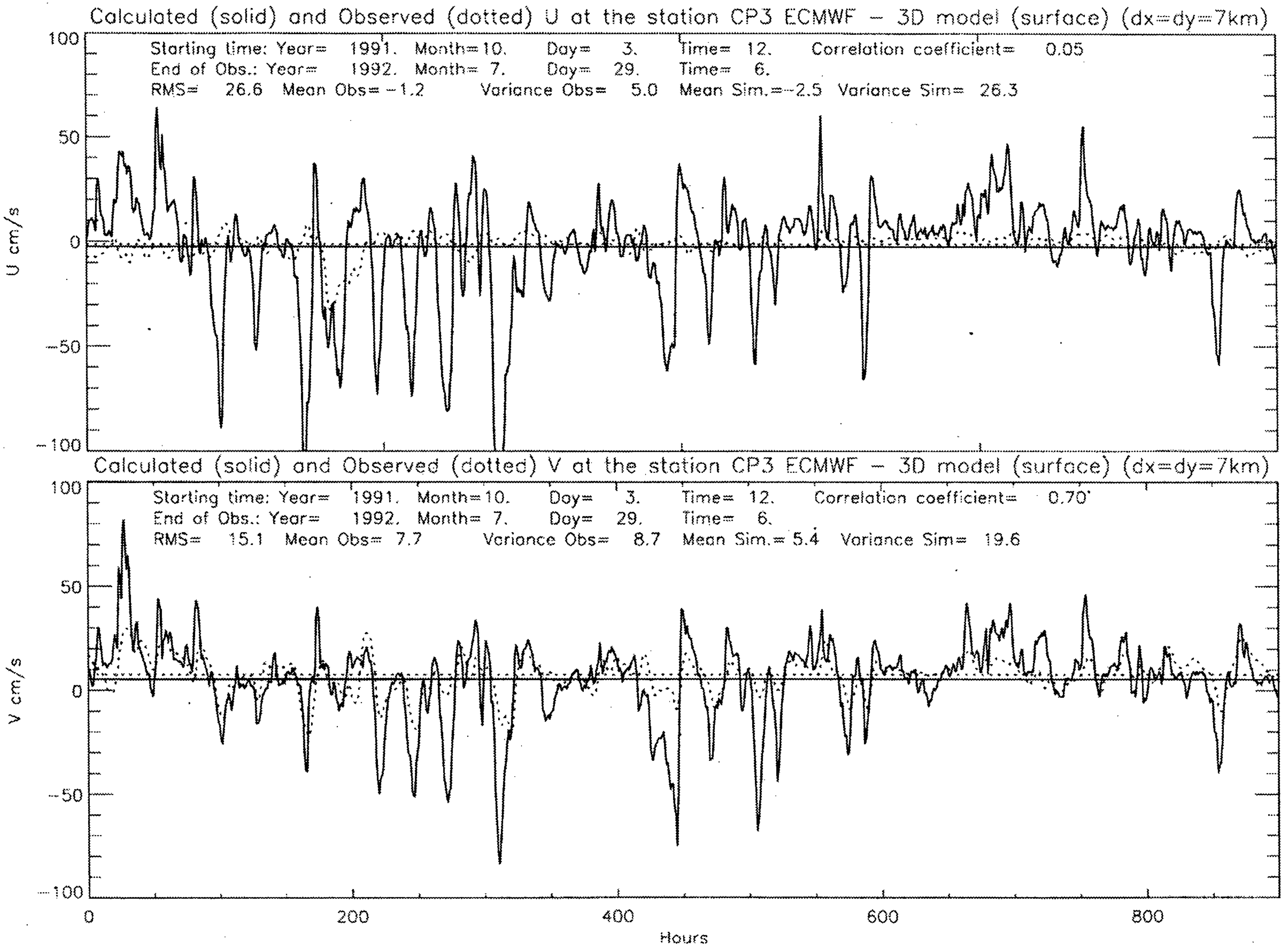

Figure 83. Same as Figure 78 for mooring CP3.

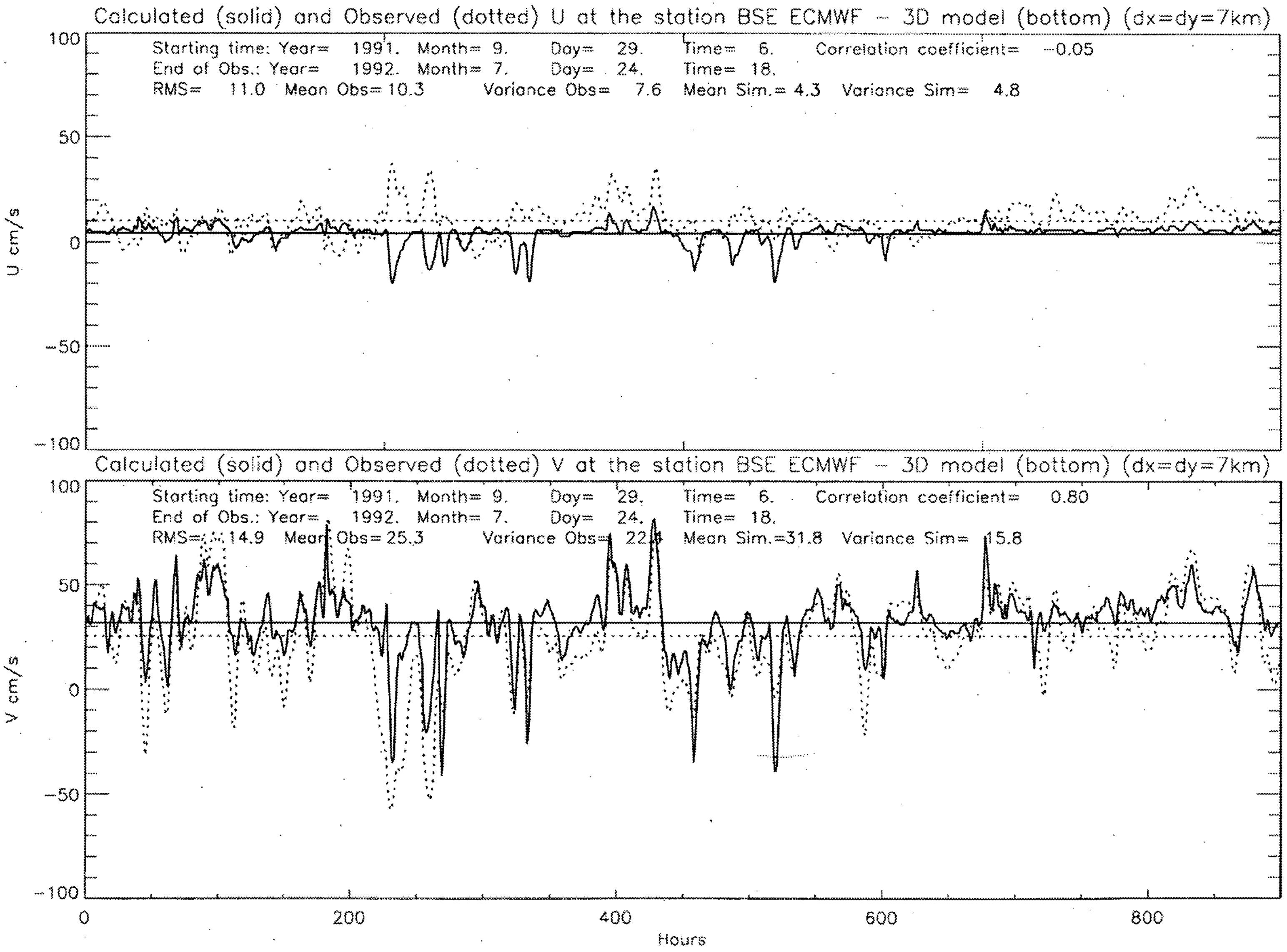

Figure 84. Time series of observed and simulated near bottom currents at mooring BSE. Calculated velocities obtained using 3-D ocean barotropic model and ECMWF atmospheric pressure fields.

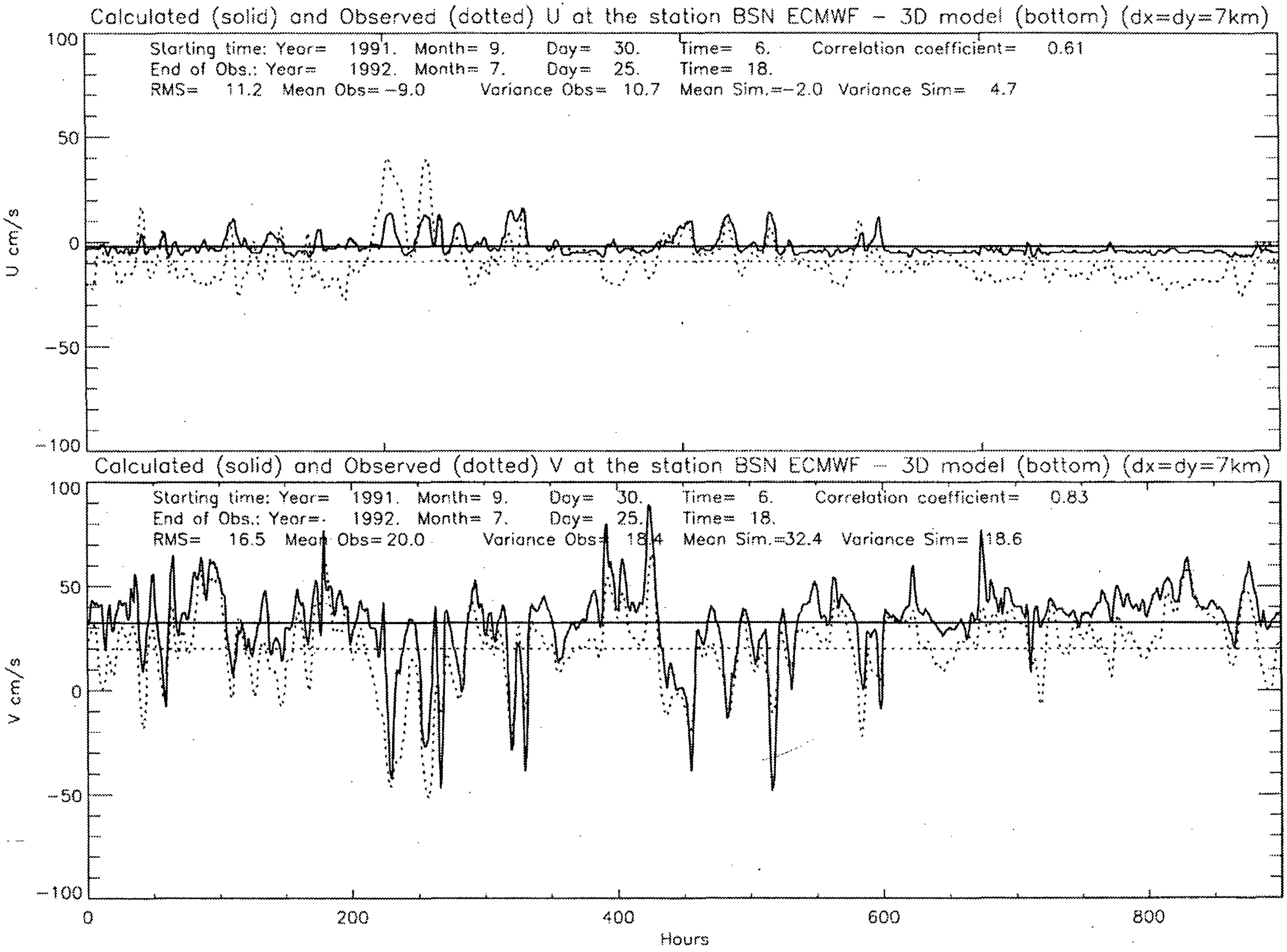

Figure 85. Same as Figure 84 for mooring BSN.

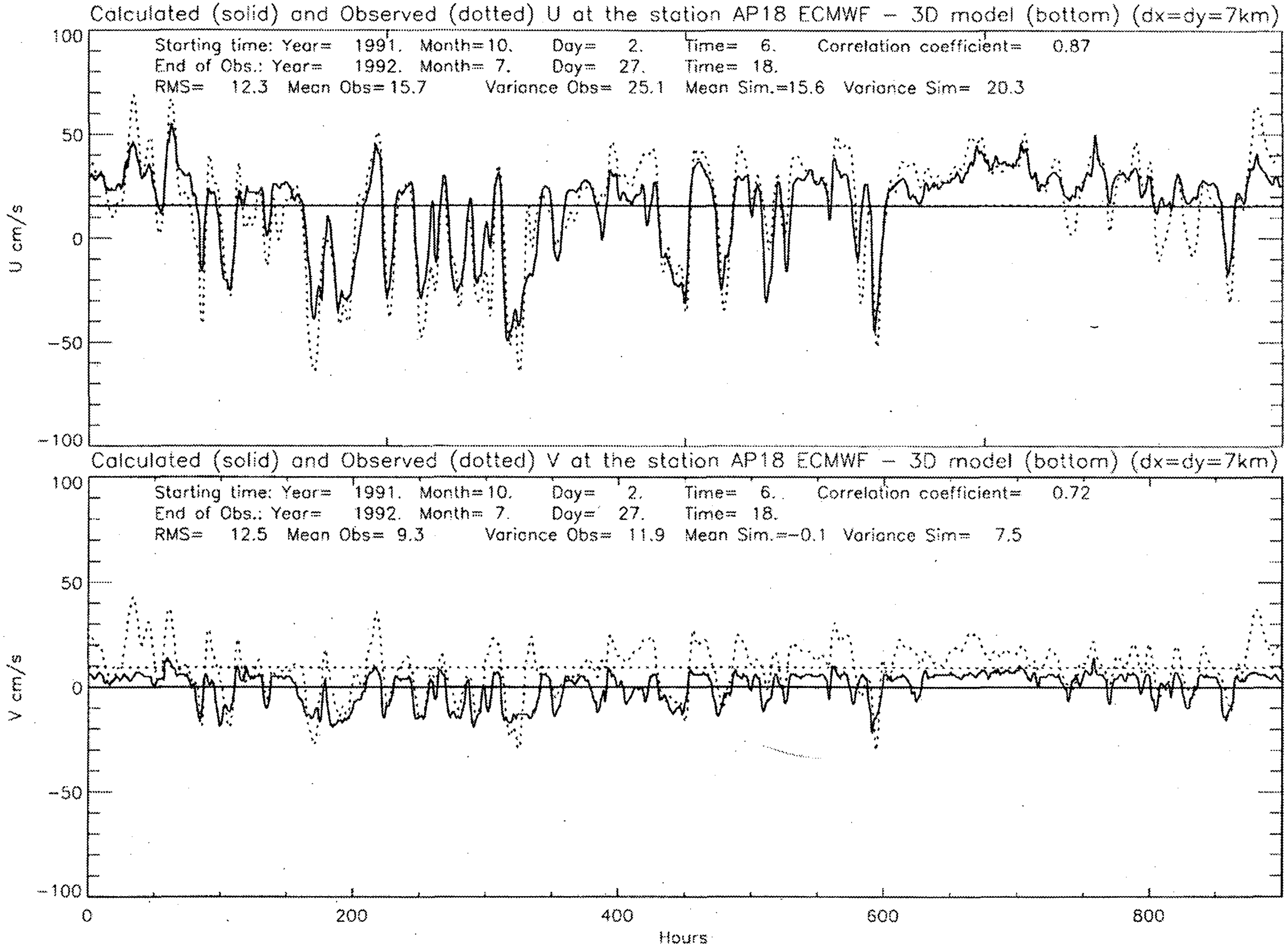

Figure 86. Same as Figure 84 for mooring AP18.

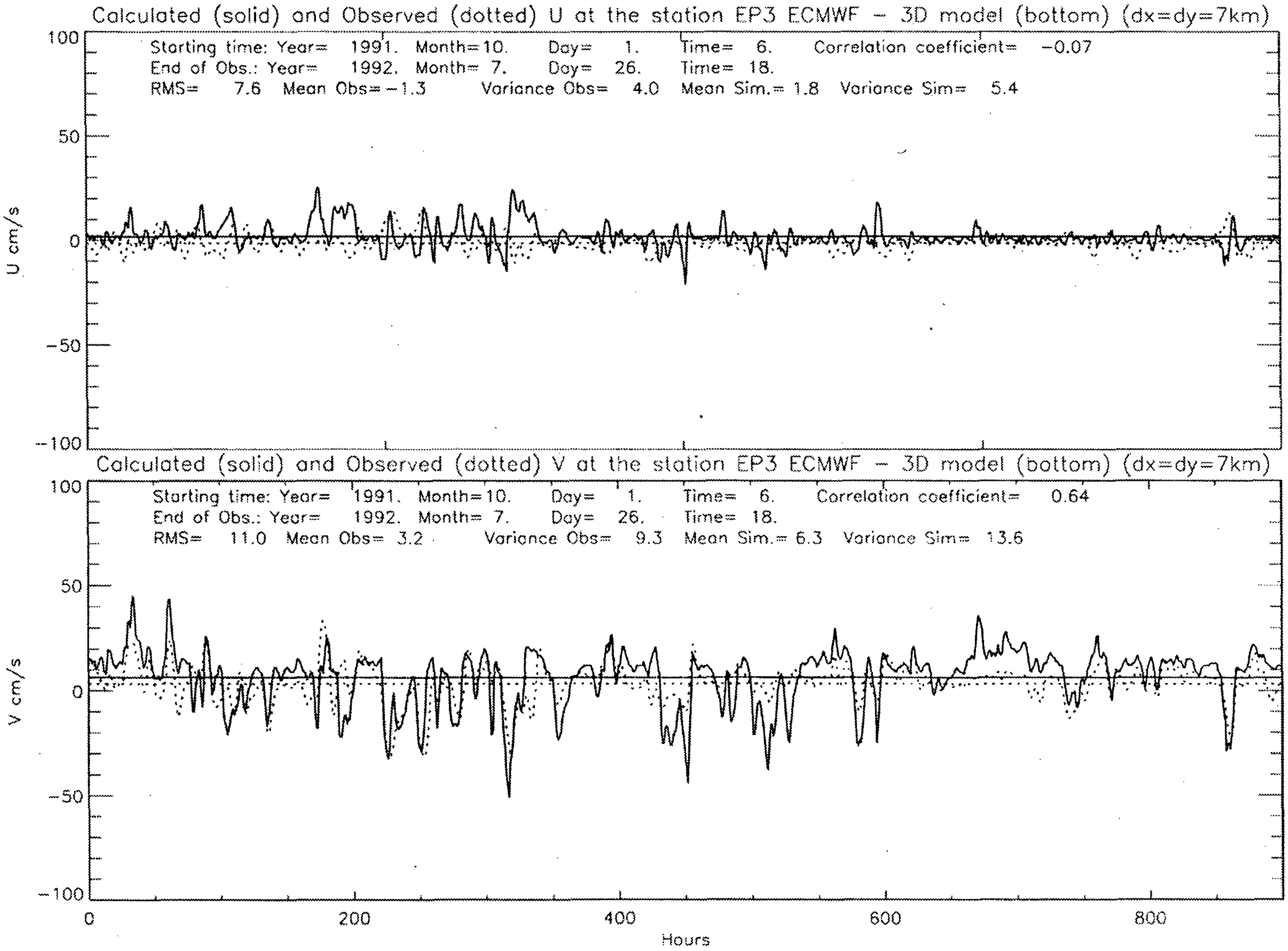

Figure 87. Same as Figure 84 for mooring EP3.

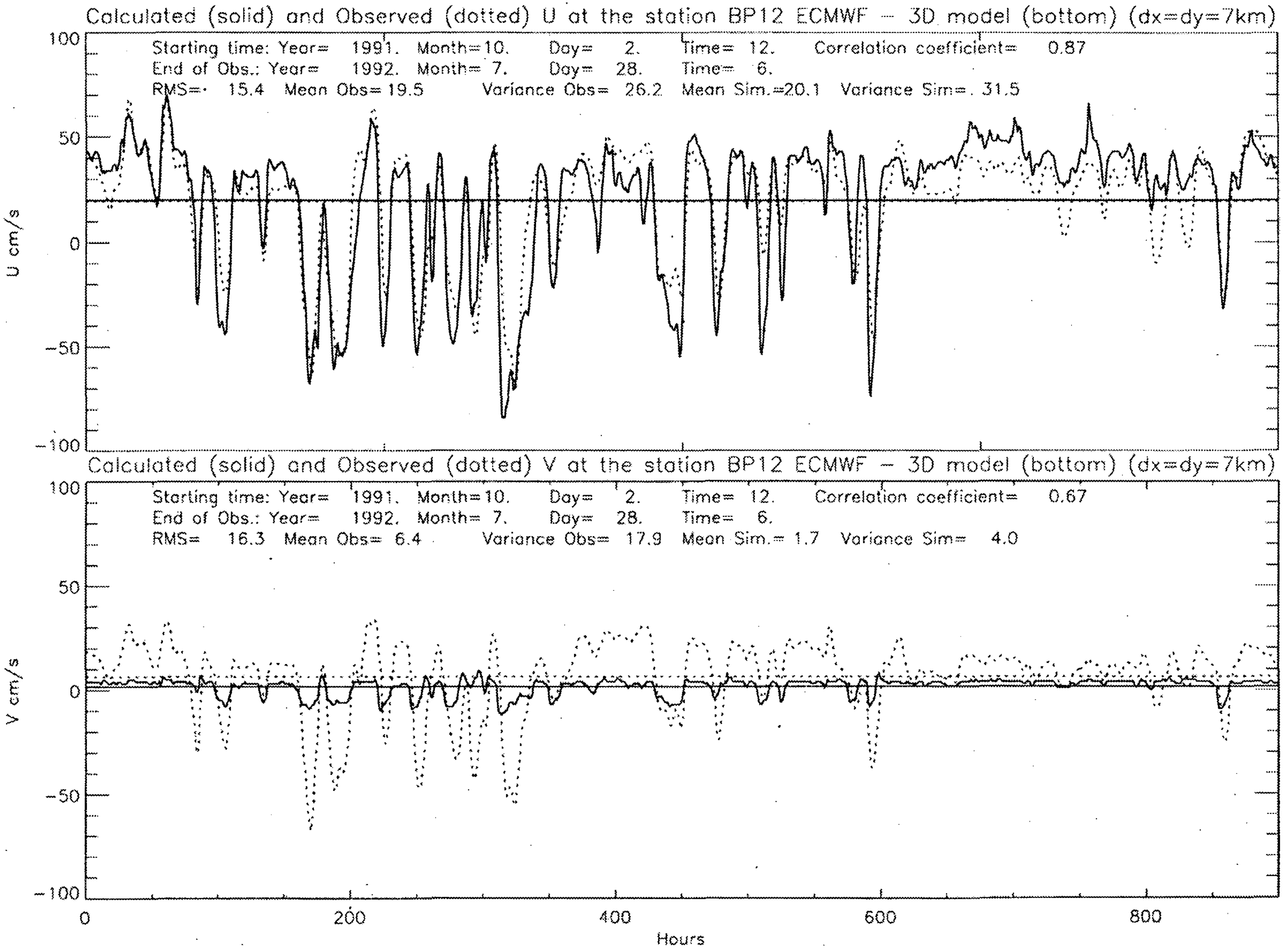

Figure 88. Same as Figure 84 for mooring BP12.

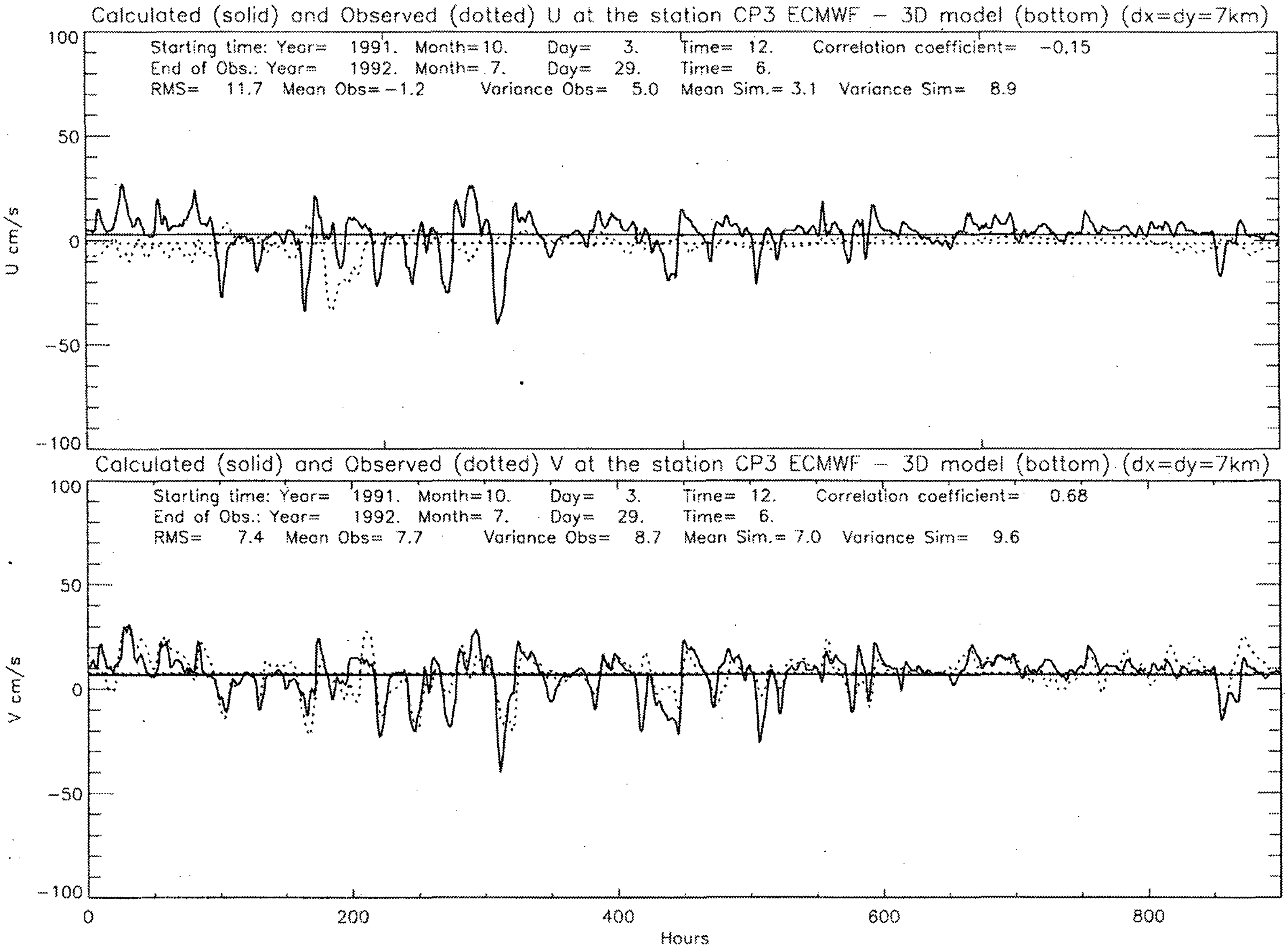

Figure 89. Same as Figure 84 for mooring CP3.

Surface currents (NCAR atmospheric pressure)

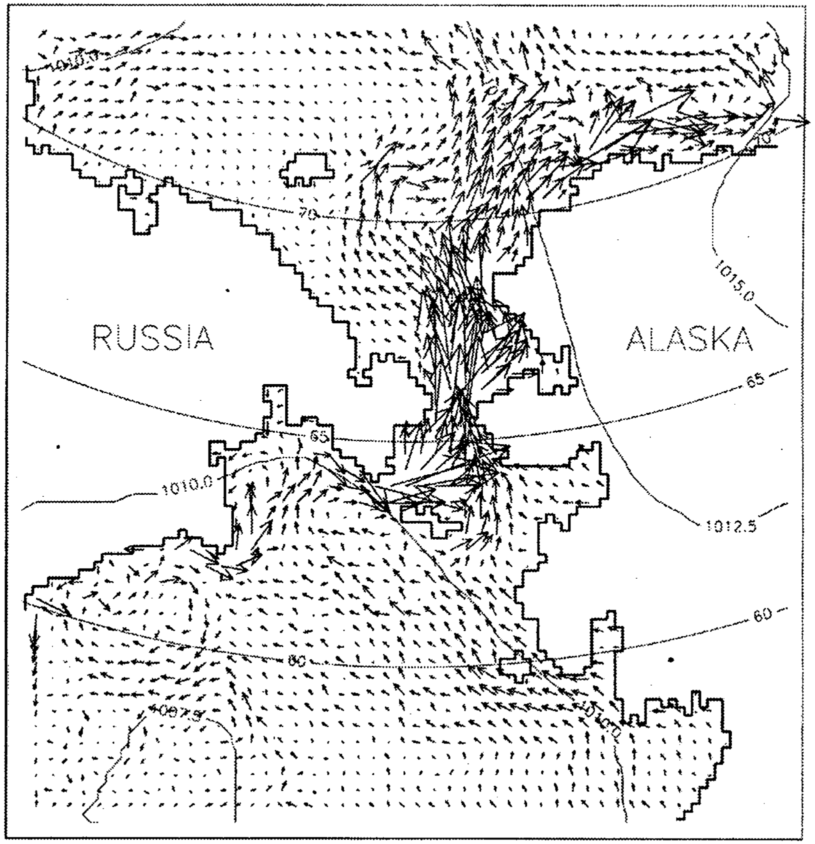

Year = 1991 Month = 10 Maximum vector = 76. cm/s

Figure 90. Surface circulation and atmospheric pressure distribution in the Chukchi Sea in October 1991. Results of simulation using a 3-D barotropic model and NCAR atmospheric pressure data.

Surface currents (FNOC atmospheric pressure)

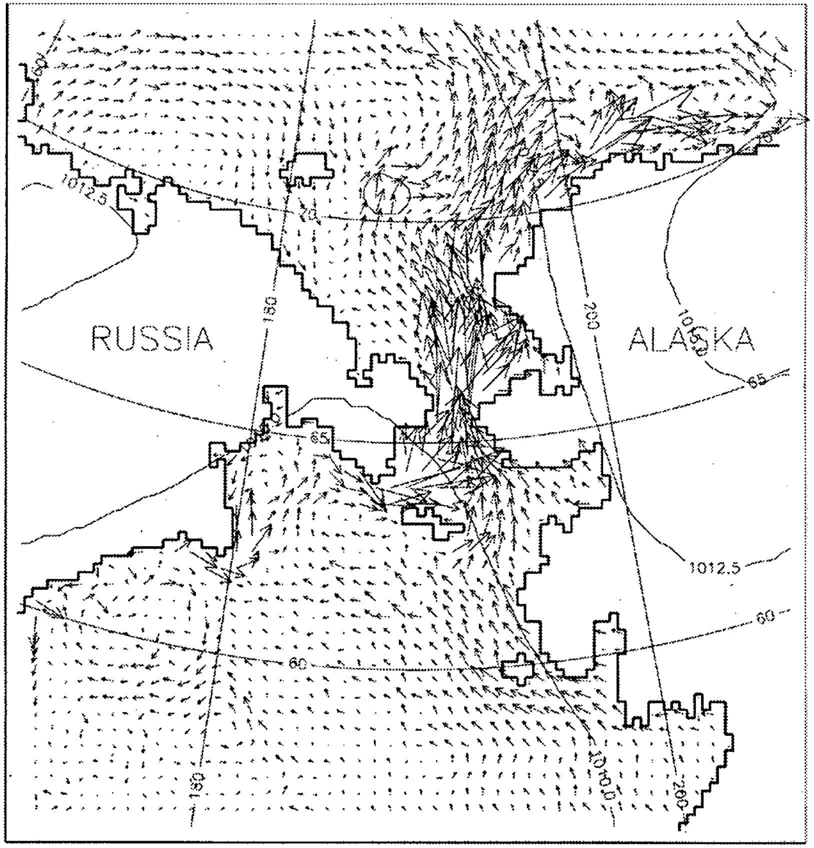

Year = 1991 Month = 10 Maximum vector = 74. cm/s

Figure 91. Surface circulation and atmospheric pressure distribution in the Chukchi Sea in October 1991. Results of simulation using a 3-D barotropic model and FNOC atmospheric pressure data.

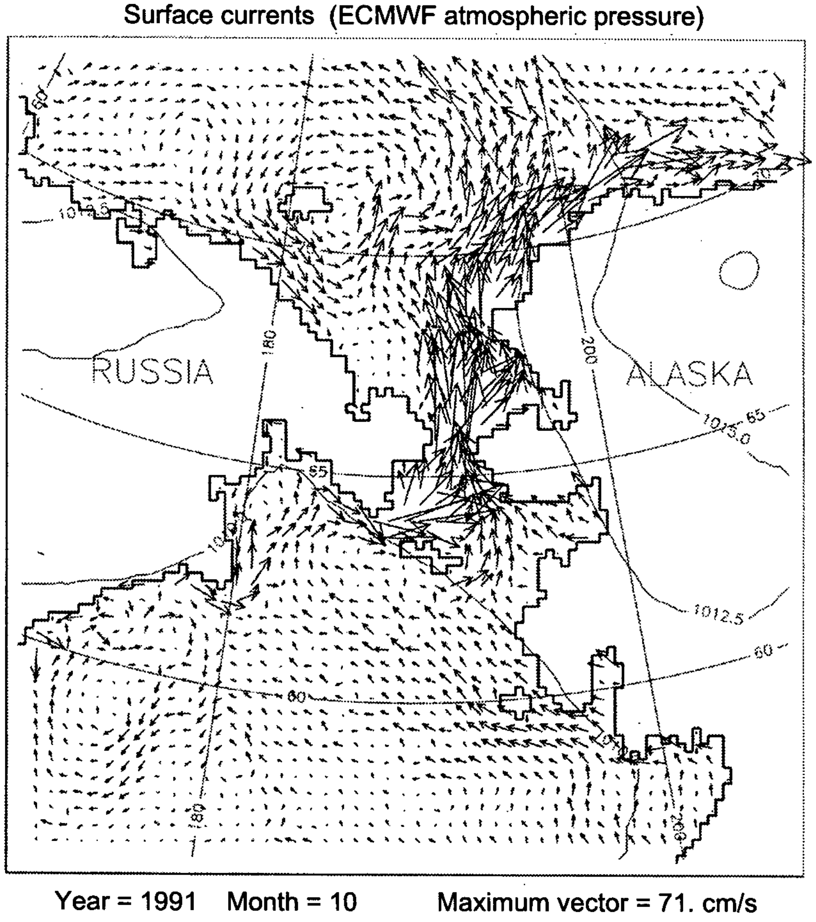

Figure 92. Surface circulation and atmospheric pressure distribution in the Chukchi Sea in October 1991. Results of simulation using a 3-D barotropic model and ECMWF atmospheric pressure data.

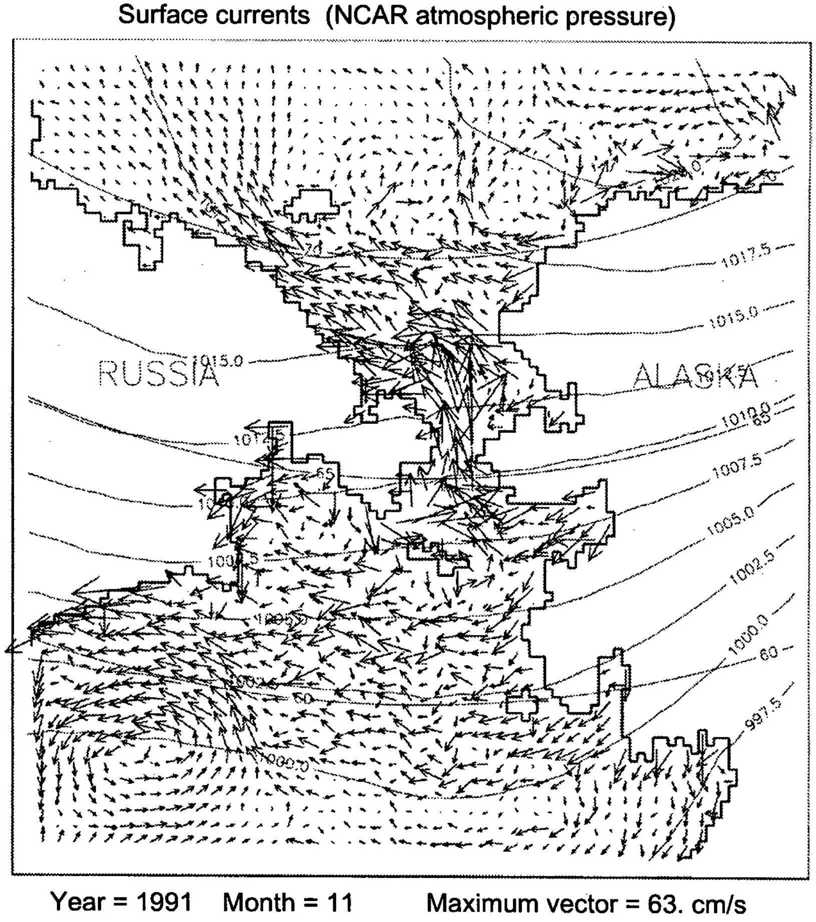

Figure 93. Surface circulation and atmospheric pressure distribution in the Chukchi Sea in November 1991. Results of simulation using a 3-D barotropic model and NCAR atmospheric pressure data.

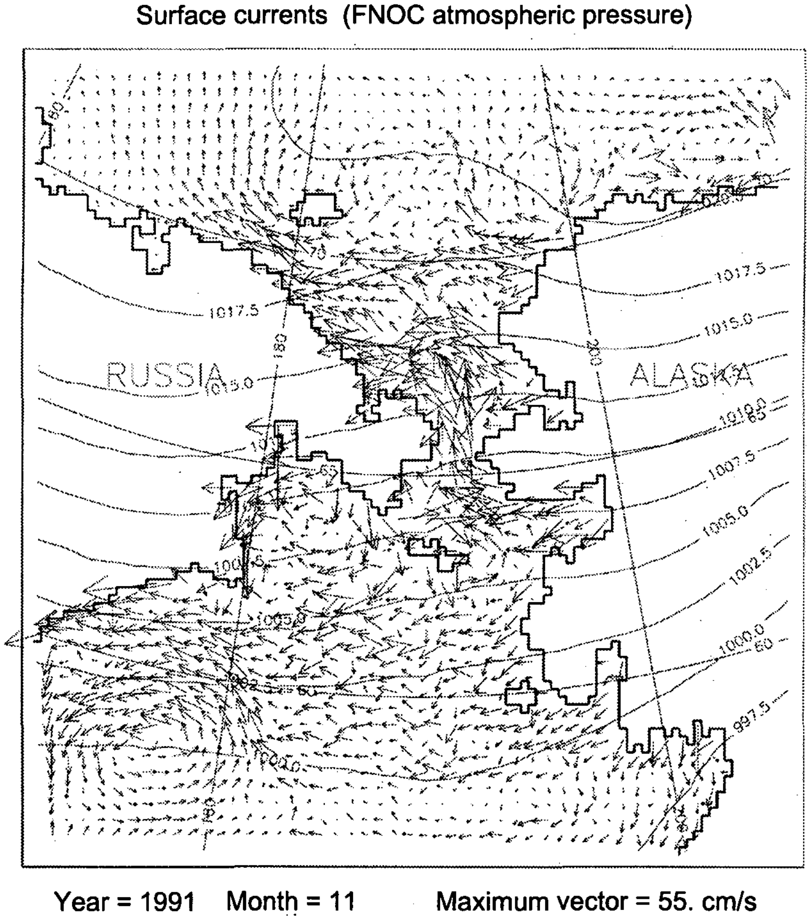

Figure 94. Surface circulation and atmospheric pressure distribution in the Chukchi Sea in November 1991. Results of simulation using a 3-D barotropic model and FNOC atmospheric pressure data.

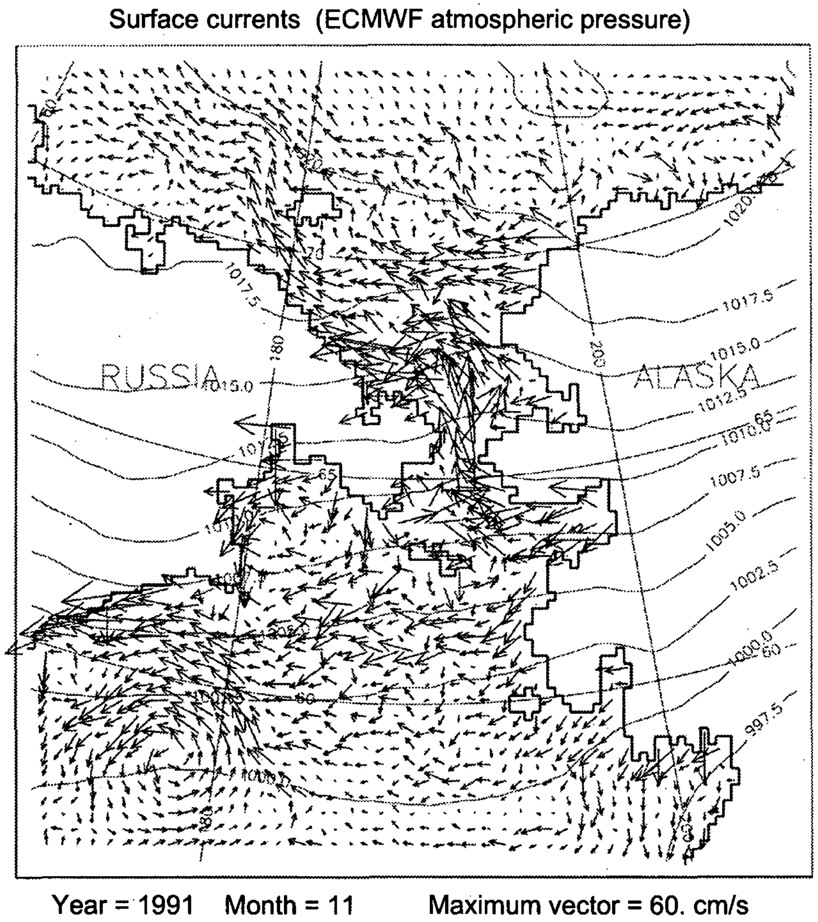

Figure 95. Surface circulation and atmospheric pressure distribution in the Chukchi Sea in November 1991. Results of simulation using a 3-D barotropic model and ECMWF atmospheric pressure data.

Surface currents (NCAR atmospheric pressure)

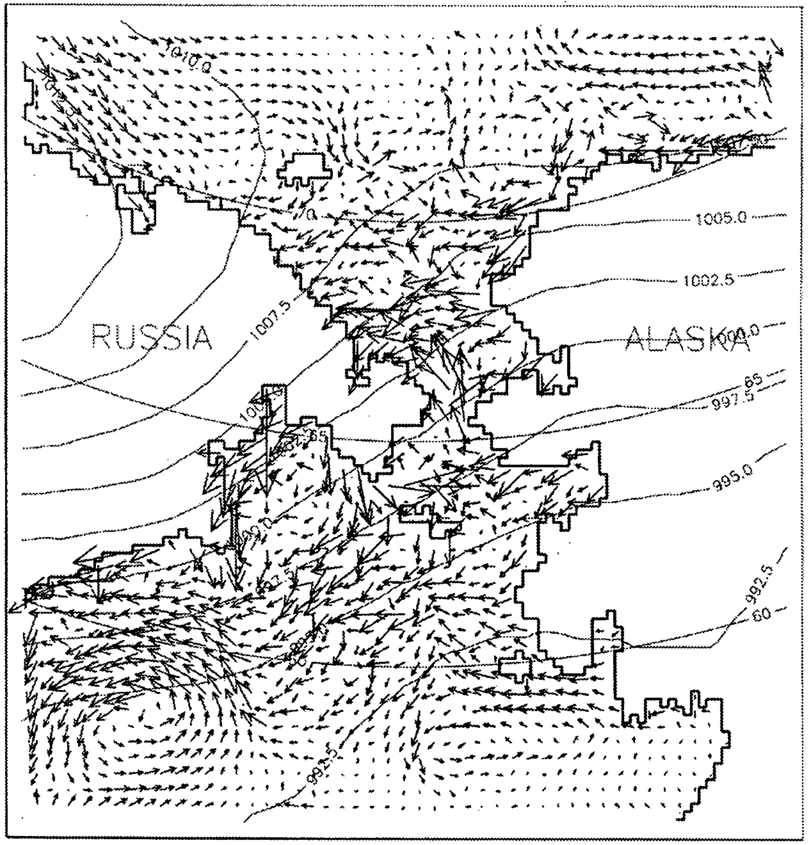

Year = 1991 Month = 12 Maximum vector = 47. cm/s

Figure 96. Surface circulation and atmospheric pressure distribution in the Chukchi Sea in December 1991. Results of simulation using a 3-D barotropic model and NCAR atmospheric pressure data.

Surface currents (FNOC atmospheric pressure)

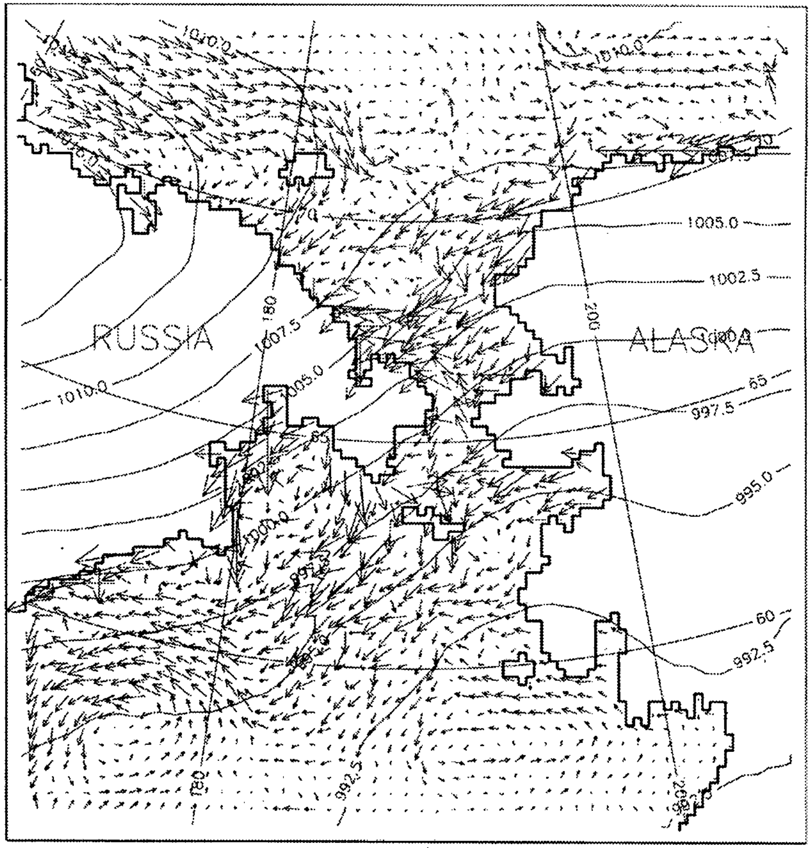

Year = 1991 Month = 12 Maximum vector = 46. cm/s

Figure 97. Surface circulation and atmospheric pressure distribution in the Chukchi Sea in December 1991. Results of simulation using a 3-D barotropic model and FNOC atmospheric pressure data.

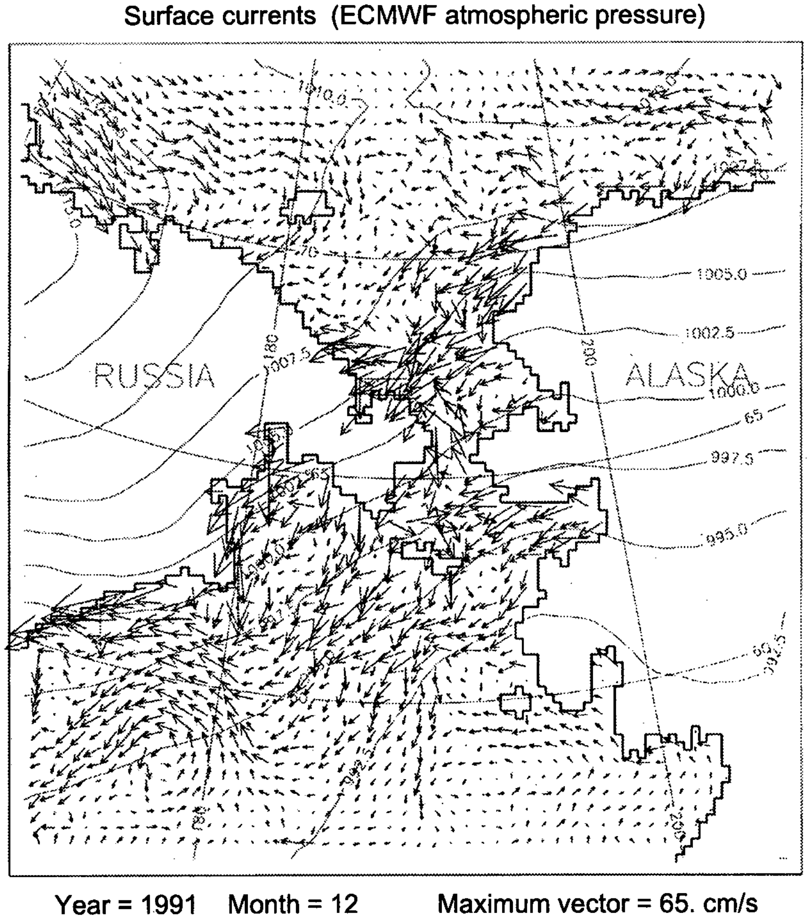
Surface currents (ECMWF atmospheric pressure)

Year = 1991 Month = 12 Maximum vector = 65. cm/s

Figure 98. Surface circulation and atmospheric pressure distribution in the Chukchi Sea in December 1991. Results of simulation using a 3-D barotropic model and ECMWF atmospheric pressure data.

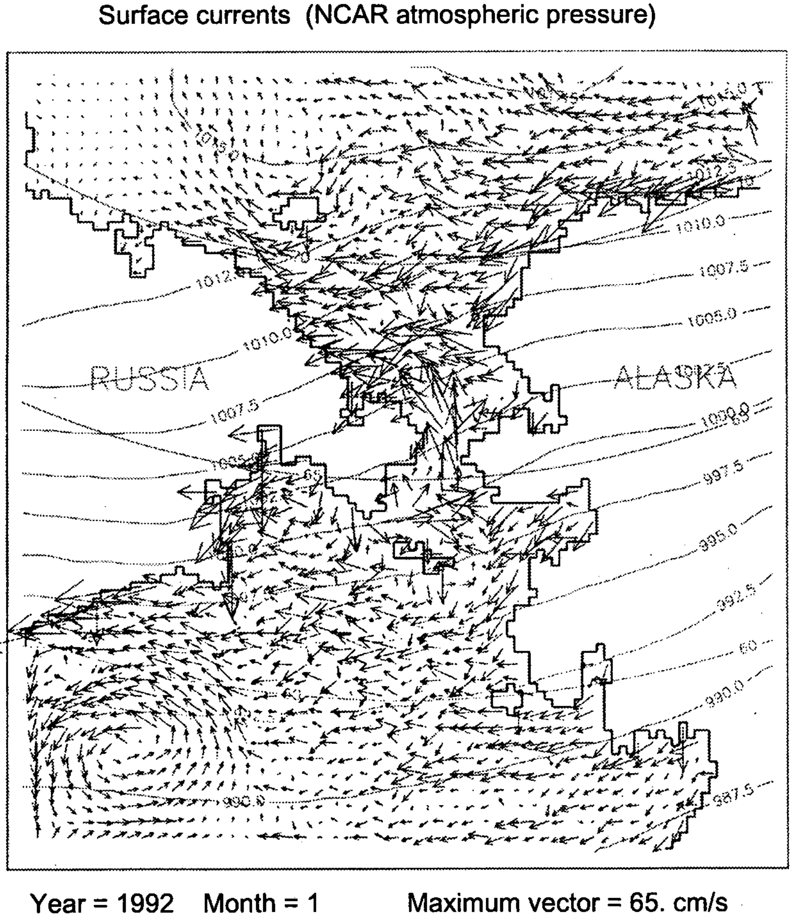
Surface currents (NCAR atmospheric pressure)

Year = 1992 Month = 1 Maximum vector = 65. cm/s

Figure 99. Surface circulation and atmospheric pressure distribution in the Chukchi Sea in January 1992. Results of simulation using a 3-D barotropic model and NCAR atmospheric pressure data.

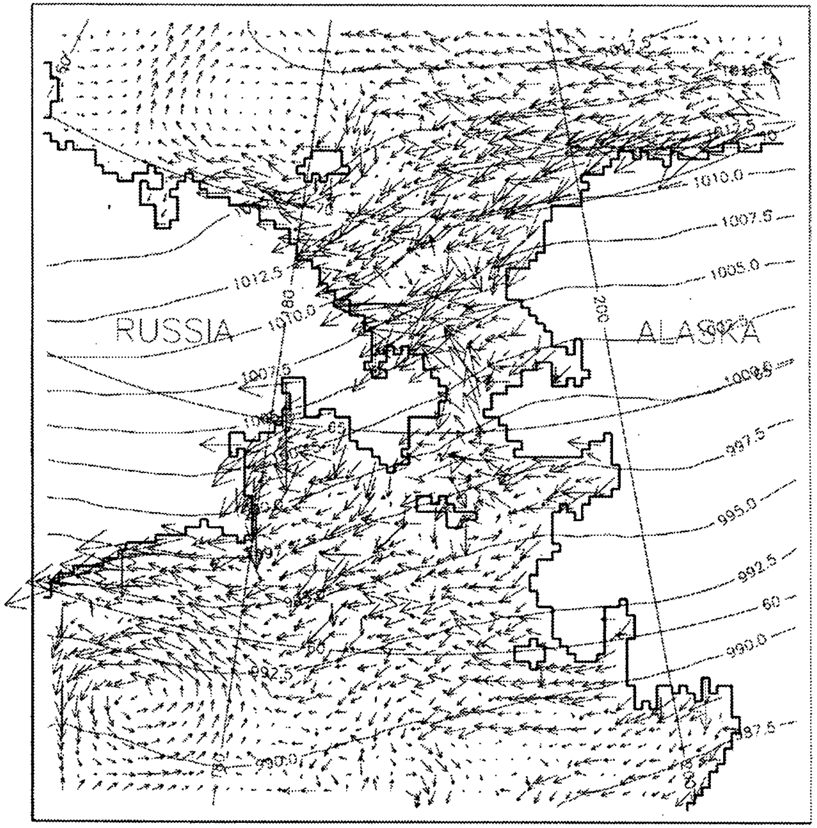

Surface currents (FNOC atmospheric pressure)

Year = 1992 Month = 1 Maximum vector = 71. cm/s

Figure 100. Surface circulation and atmospheric pressure distribution in the Chukchi Sea in January 1992. Results of simulation using a 3-D barotropic model and FNOC atmospheric pressure data.

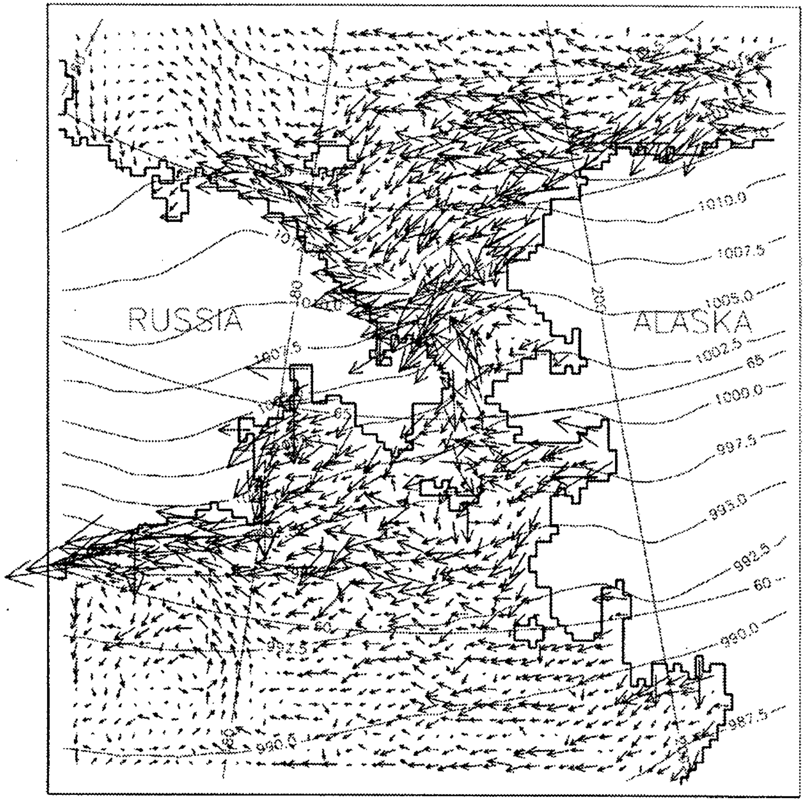

Surface currents (ECMWF atmospheric pressure)

Year = 1992 Month = 1 Maximum vector = 82. cm/s

Figure 101. Surface circulation and atmospheric pressure distribution in the Chukchi Sea in January 1992. Results of simulation using a 3-D barotropic model and ECMWF atmospheric pressure data.

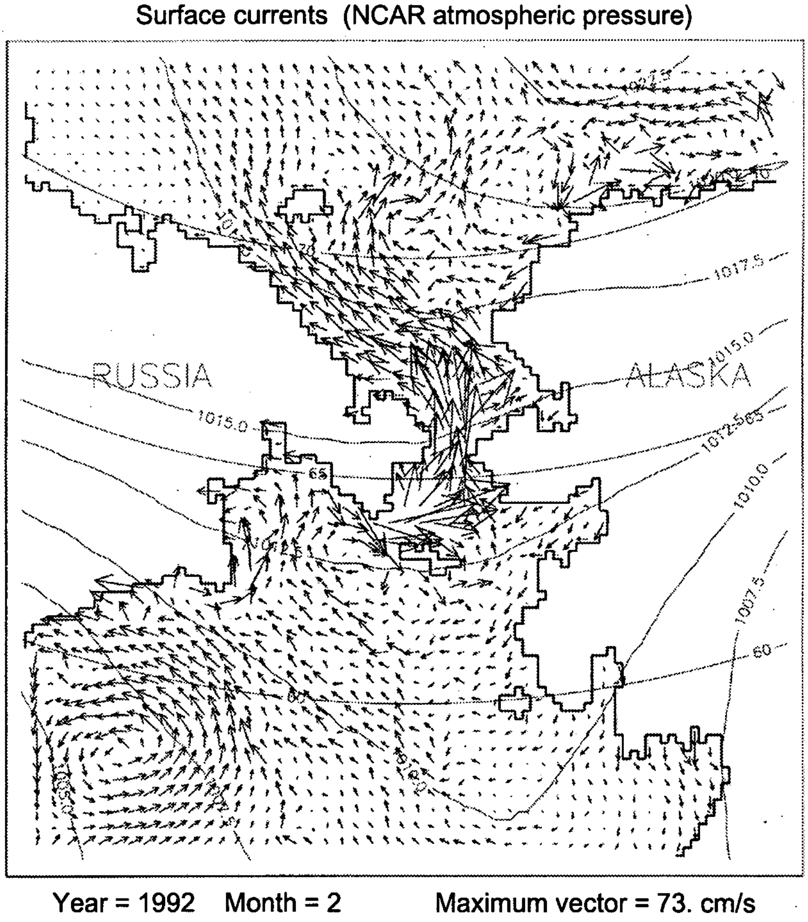
Surface currents (NCAR atmospheric pressure)

Year = 1992 Month = 2 Maximum vector = 73. cm/s

Figure 102. Surface circulation and atmospheric pressure distribution in the Chukchi Sea in February 1992. Results of simulation using a 3-D barotropic model and NCAR atmospheric pressure data.

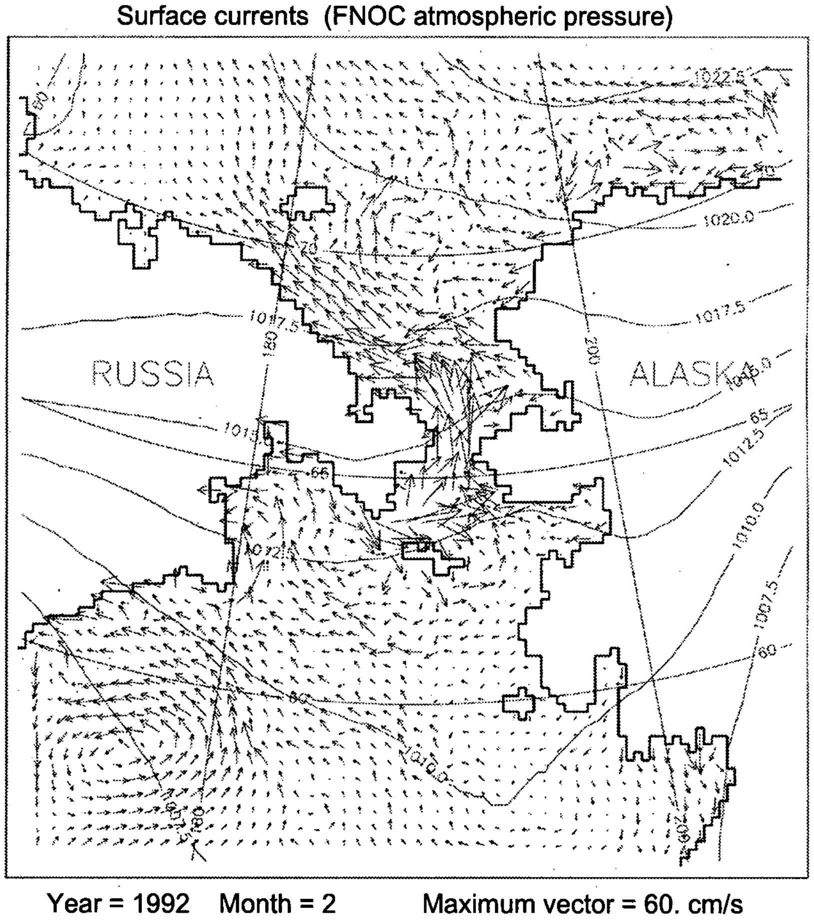
Surface currents (FNOC atmospheric pressure)

Year = 1992 Month = 2 Maximum vector = 60. cm/s

Figure 103. Surface circulation and atmospheric pressure distribution in the Chukchi Sea in February 1992. Results of simulation using a 3-D barotropic model and FNOC atmospheric pressure data.

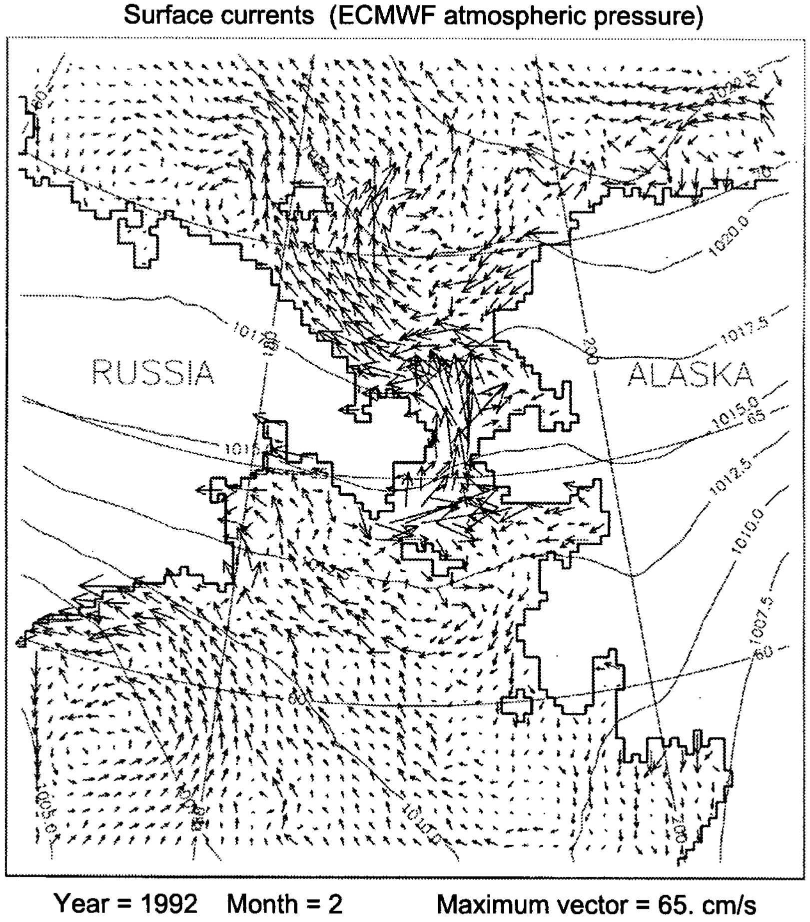

Figure 104. Surface circulation and atmospheric pressure distribution in the Chukchi Sea in February 1992. Results of simulation using a 3-D barotropic model and ECMWF atmospheric pressure data.

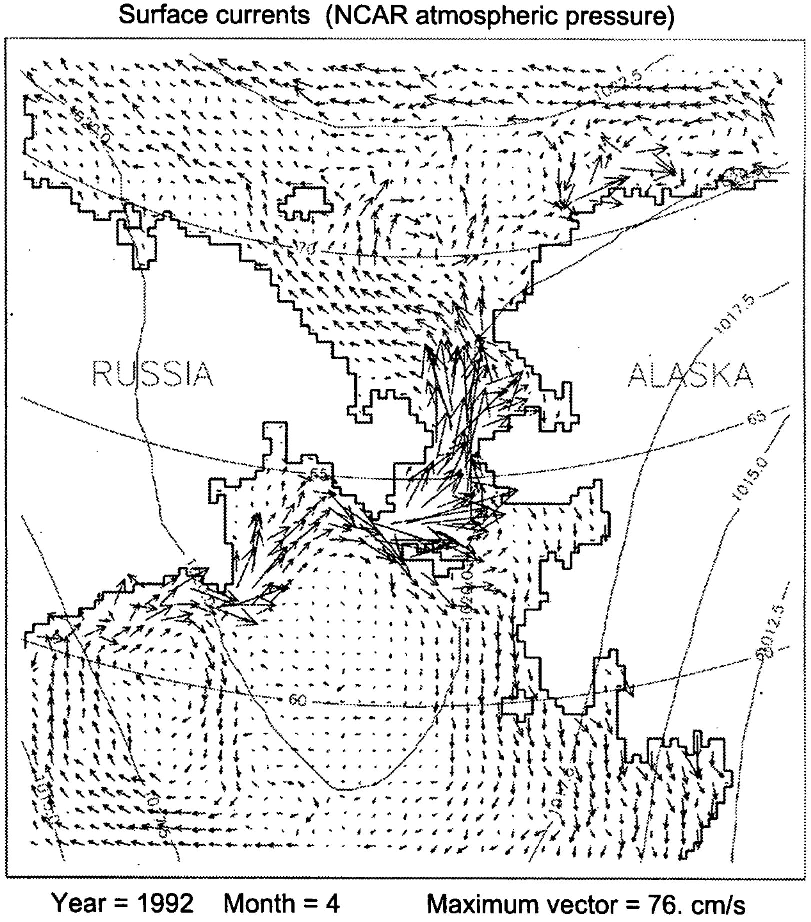

Figure 105. Surface circulation and atmospheric pressure distribution in the Chukchi Sea in April 1992. Results of simulation using a 3-D barotropic model and NCAR atmospheric pressure data.

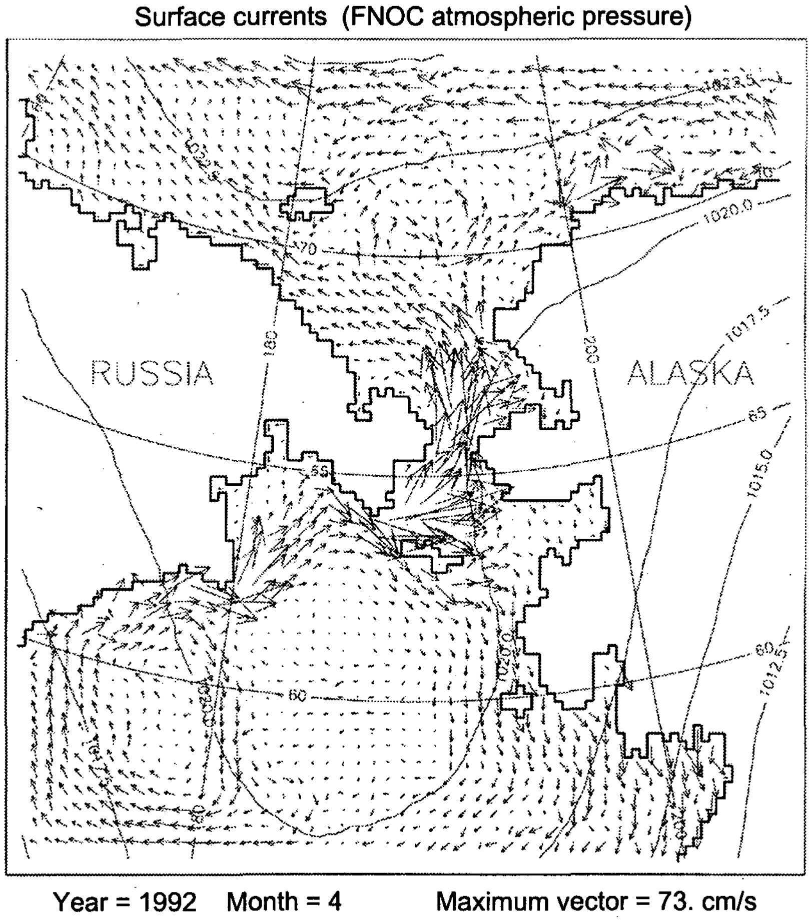
Surface currents (FNOC atmospheric pressure)

Year = 1992 Month = 4 Maximum vector = 73. cm/s

Figure 106. Surface circulation and atmospheric pressure distribution in the Chukchi Sea in April 1992. Results of simulation using a 3-D barotropic model and FNOC atmospheric pressure data.

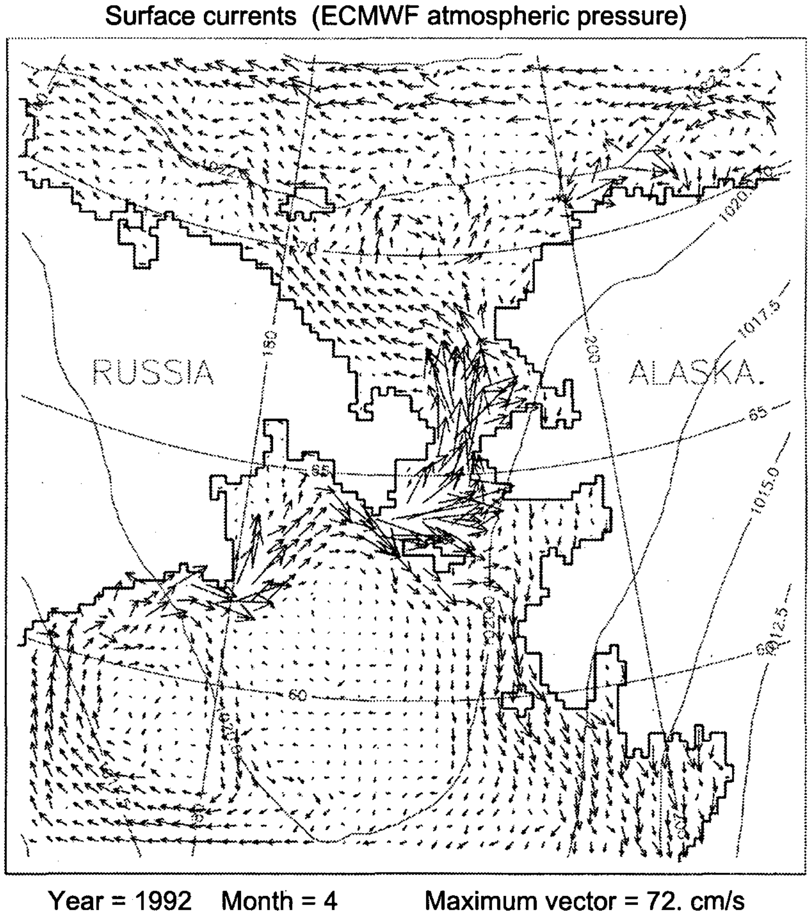
Surface currents (ECMWF atmospheric pressure)

Year = 1992 Month = 4 Maximum vector = 72. cm/s

Figure 107. Surface circulation and atmospheric pressure distribution in the Chukchi Sea in April 1992. Results of simulation using a 3-D barotropic model and ECMWF atmospheric pressure data.

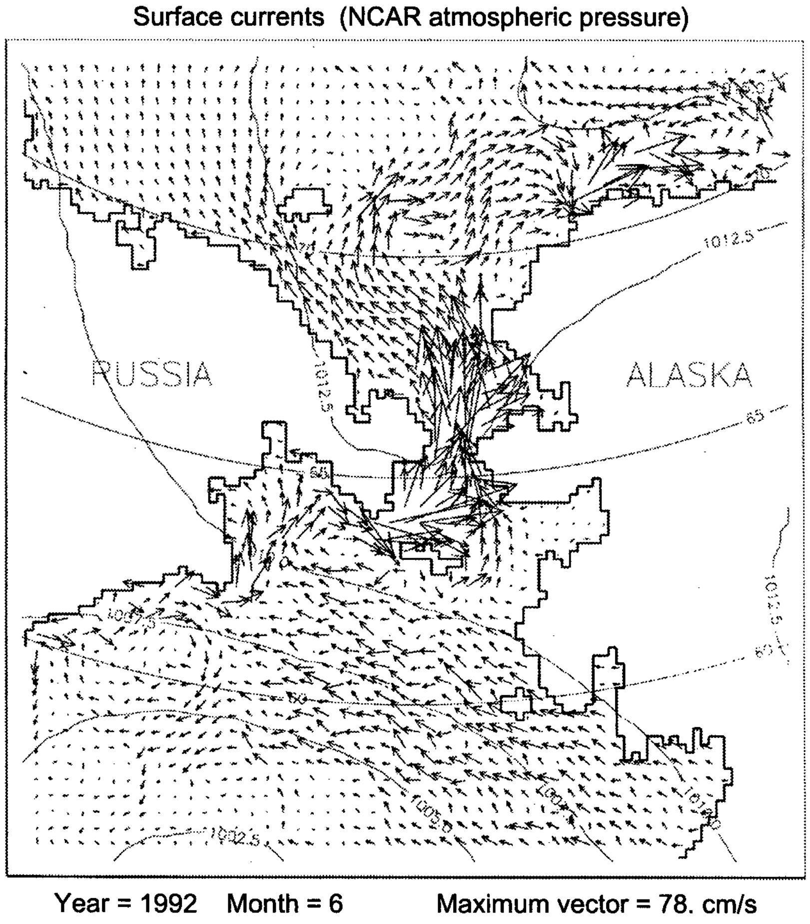

Figure 108. Surface circulation and atmospheric pressure distribution in the Chukchi Sea in June 1992. Results of simulation using a 3-D barotropic model and NCAR atmospheric pressure data.

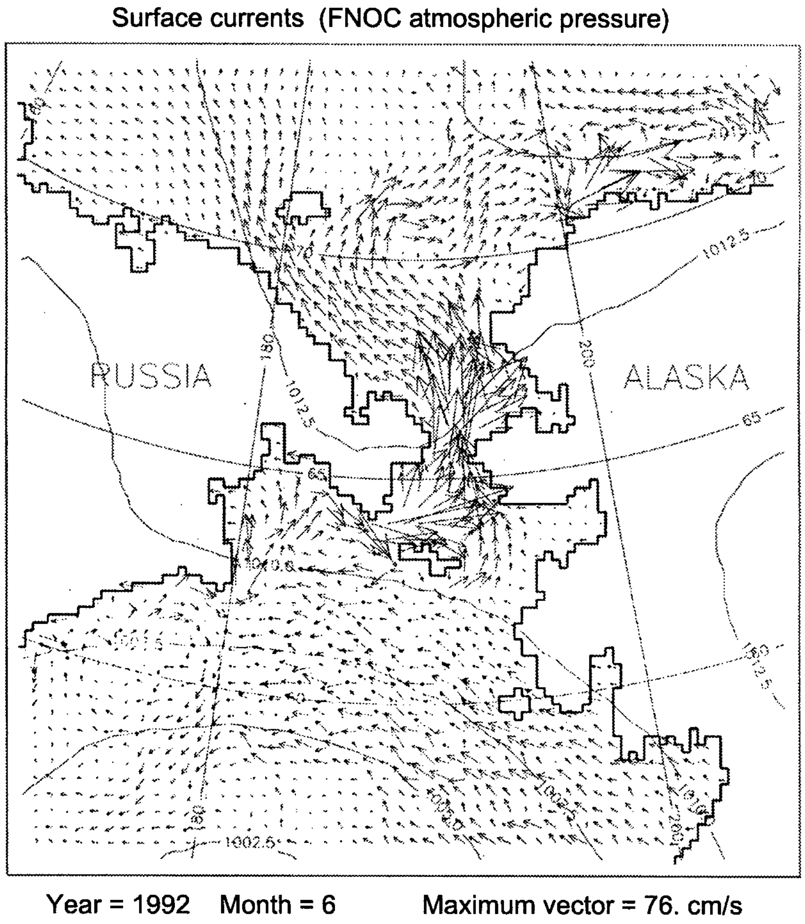

Figure 109. Surface circulation and atmospheric pressure distribution in the Chukchi Sea in June 1992. Results of simulation using a 3-D barotropic model and FNOC atmospheric pressure data.

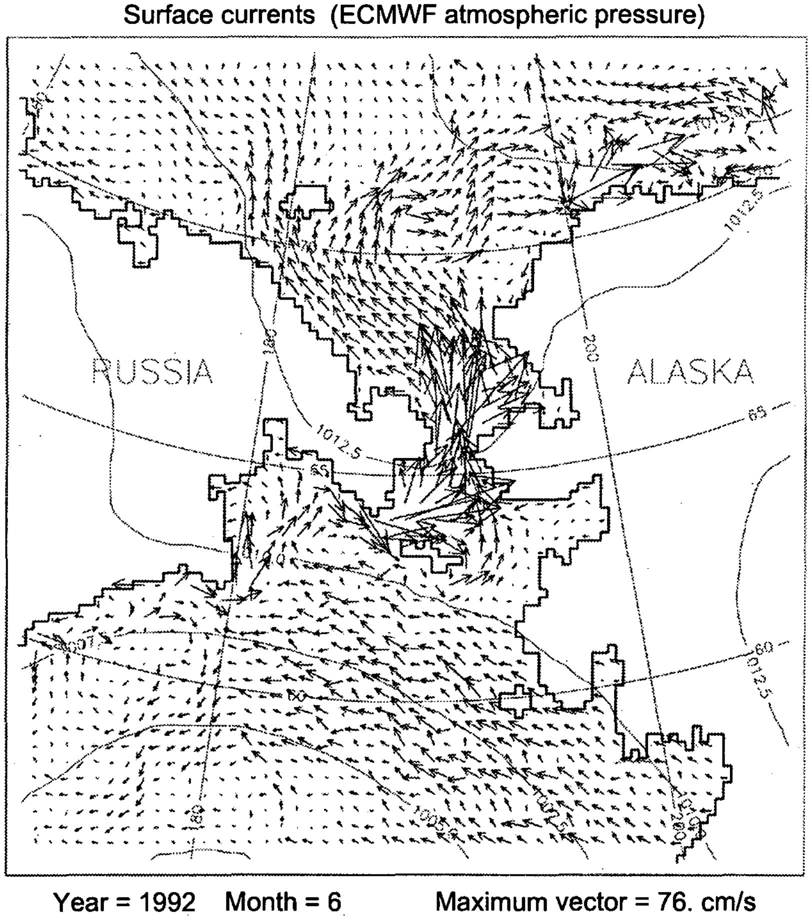

Figure 110. Surface circulation and atmospheric pressure distribution in the Chukchi Sea in June 1992. Results of simulation using a 3-D barotropic model and ECMWF atmospheric pressure data.

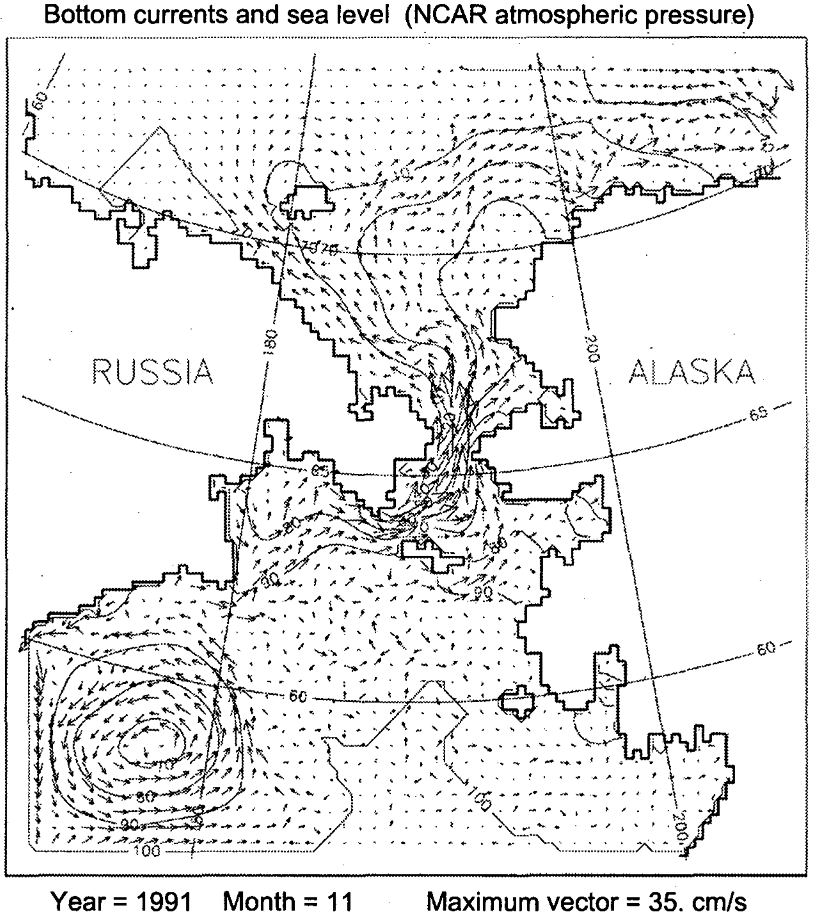

Figure 111. Bottom circulation and sea level (cm) distribution in the Chukchi Sea in November 1991. Results of simulation using a 3-D barotropic model and NCAR atmospheric pressure data.

Bottom currents (FNOC atmospheric pressure)

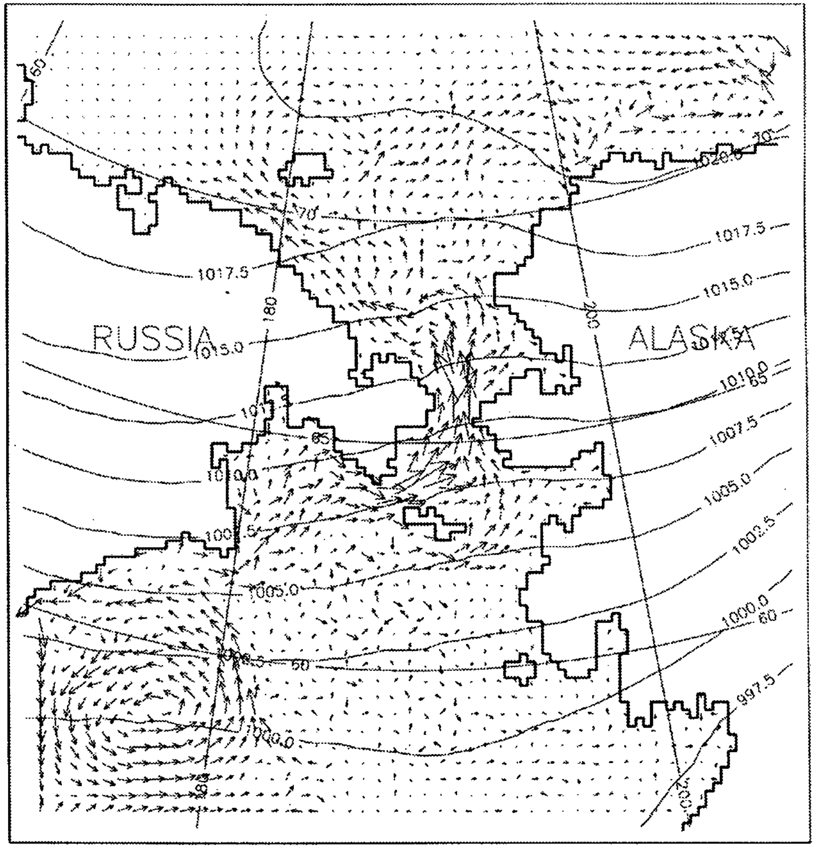

Year = 1991 Month = 11 Maximum vector = 31. cm/s

Figure 112. Bottom circulation and sea level (cm) distribution in the Chukchi Sea in November 1991. Results of simulation using a 3-D barotropic model and FNOC atmospheric pressure data.

Bottom currents and sea level (ECMWF atmospheric pressure)

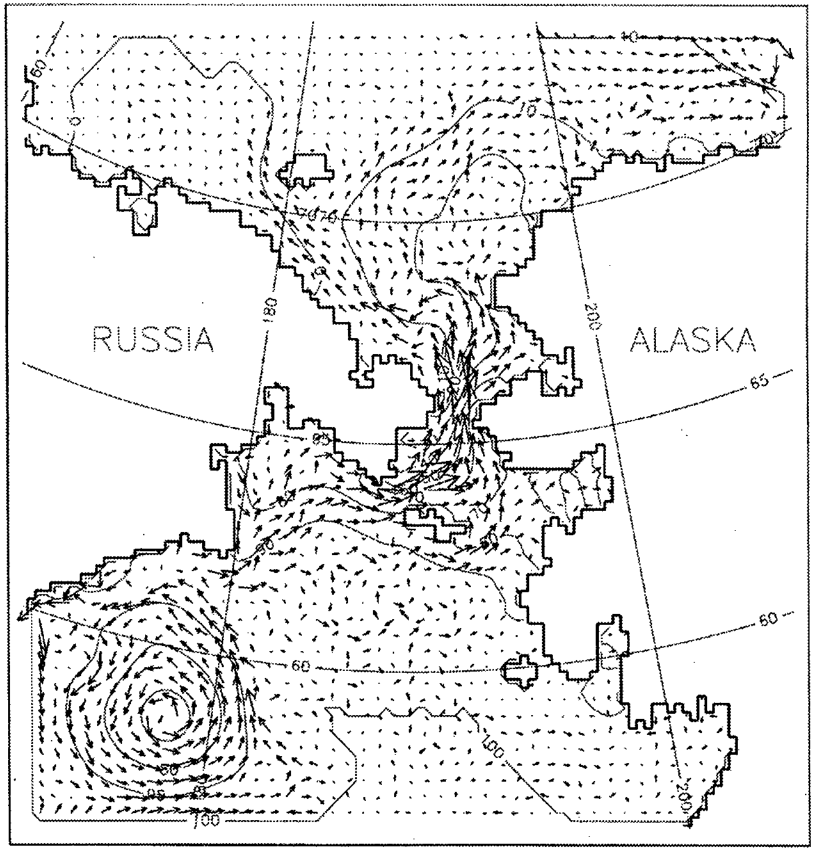

Year = 1991 Month = 11 Maximum vector = 33. cm/s

Figure 113. Bottom circulation and sea level (cm) distribution in the Chukchi Sea in November 1991. Results of simulation using a 3-D barotropic model and ECMWF atmospheric pressure data.

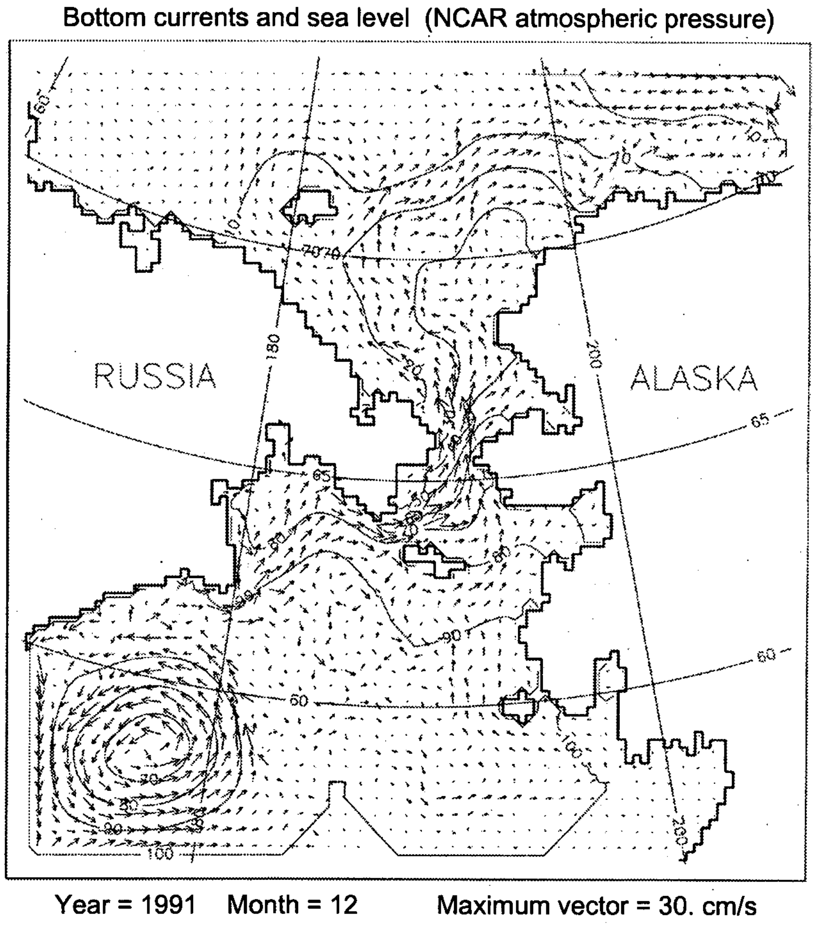

Bottom currents and sea level (NCAR atmospheric pressure)

Year = 1991 Month = 12 Maximum vector = 30. cm/s

Figure 114. Bottom circulation and sea level (cm) distribution in the Chukchi Sea in December 1991. Results of simulation using a 3-D barotropic model and NCAR atmospheric pressure data.

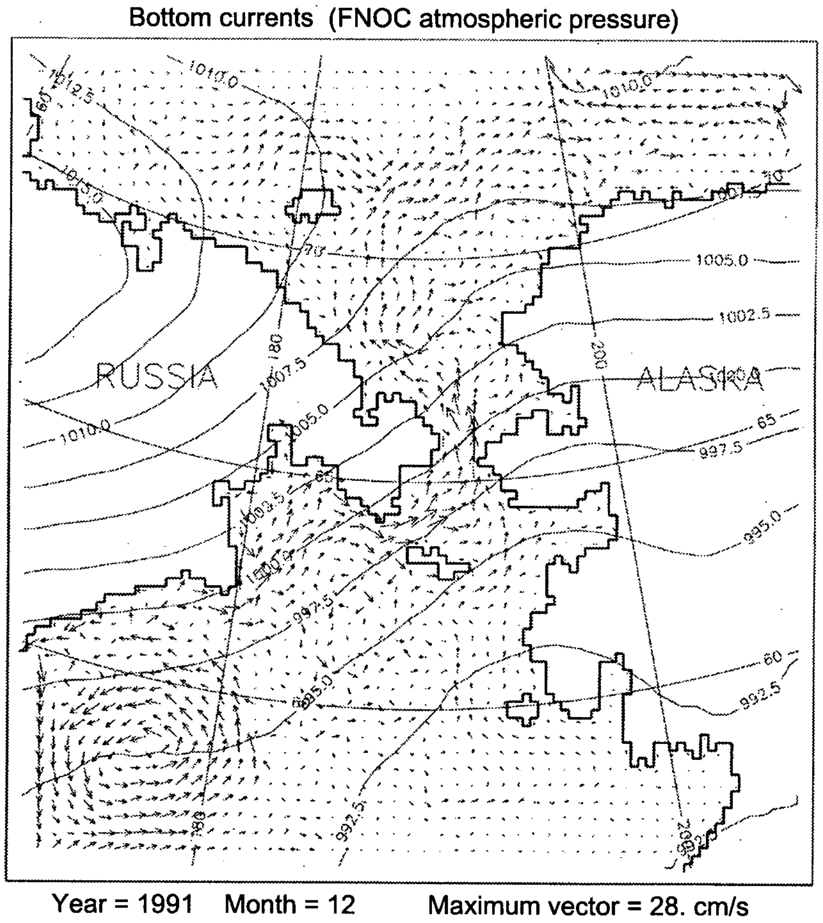

Bottom currents (FNOC atmospheric pressure)

Year = 1991 Month = 12 Maximum vector = 28. cm/s

Figure 115. Bottom circulation and sea level (cm) distribution in the Chukchi Sea in December 1991. Results of simulation using a 3-D barotropic model and FNOC atmospheric pressure data.

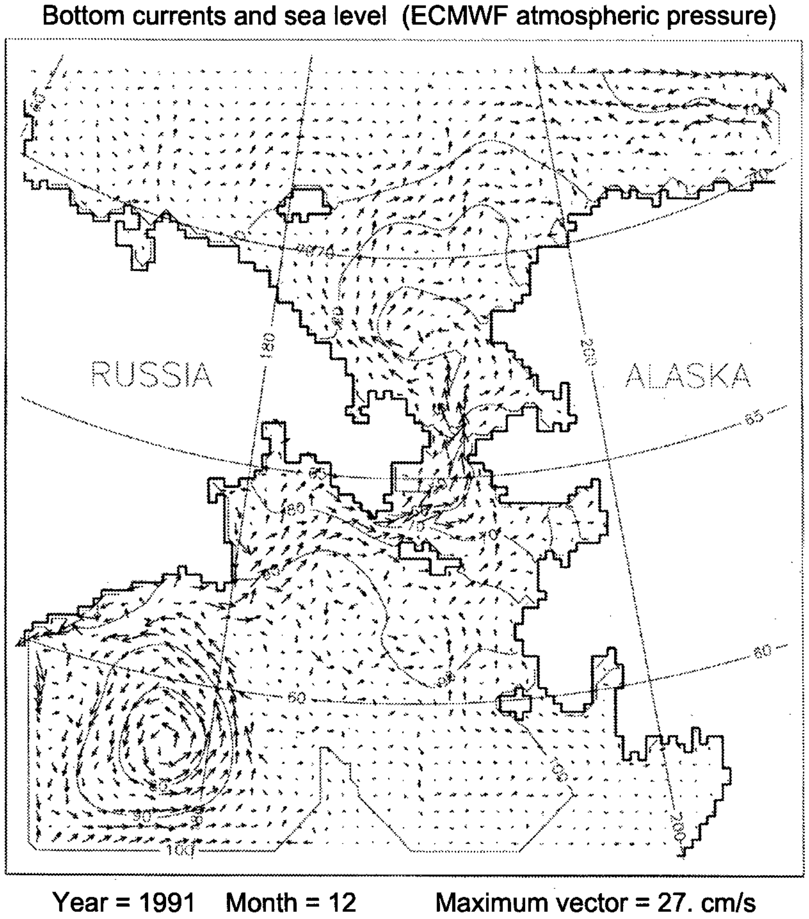

Figure 116. Bottom circulation and sea level (cm) distribution in the Chukchi Sea in December 1991. Results of simulation using a 3-D barotropic model and ECMWF atmospheric pressure data.

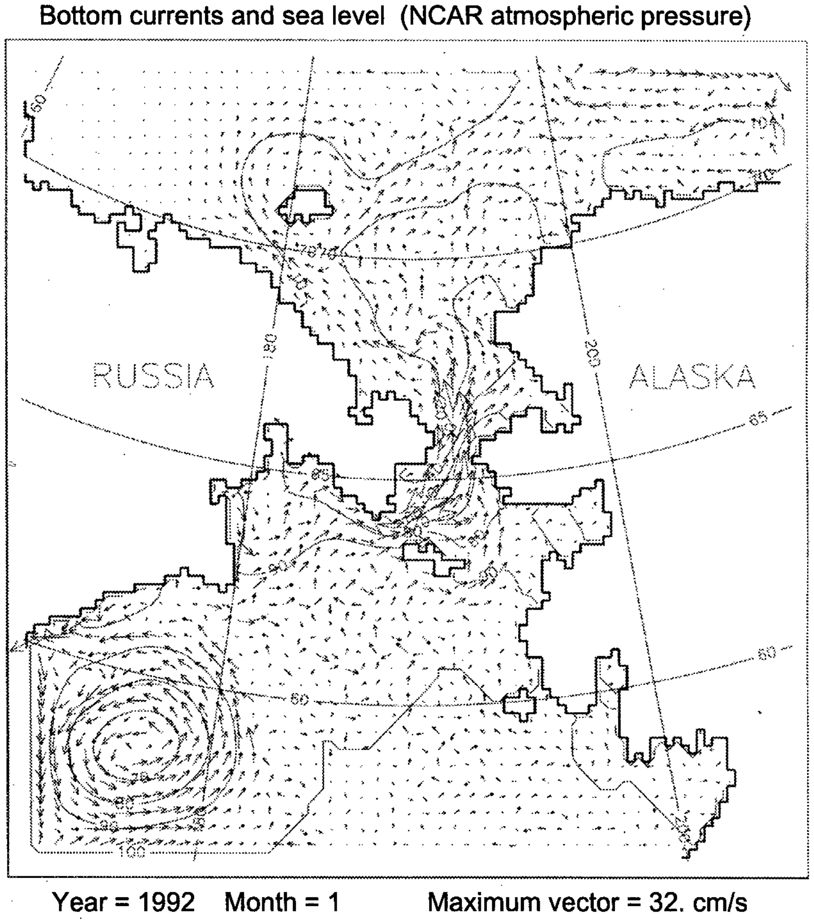

Figure 117. Bottom circulation and sea level (cm) distribution in the Chukchi Sea in January 1992. Results of simulation using a 3-D barotropic model and NCAR atmospheric pressure data.

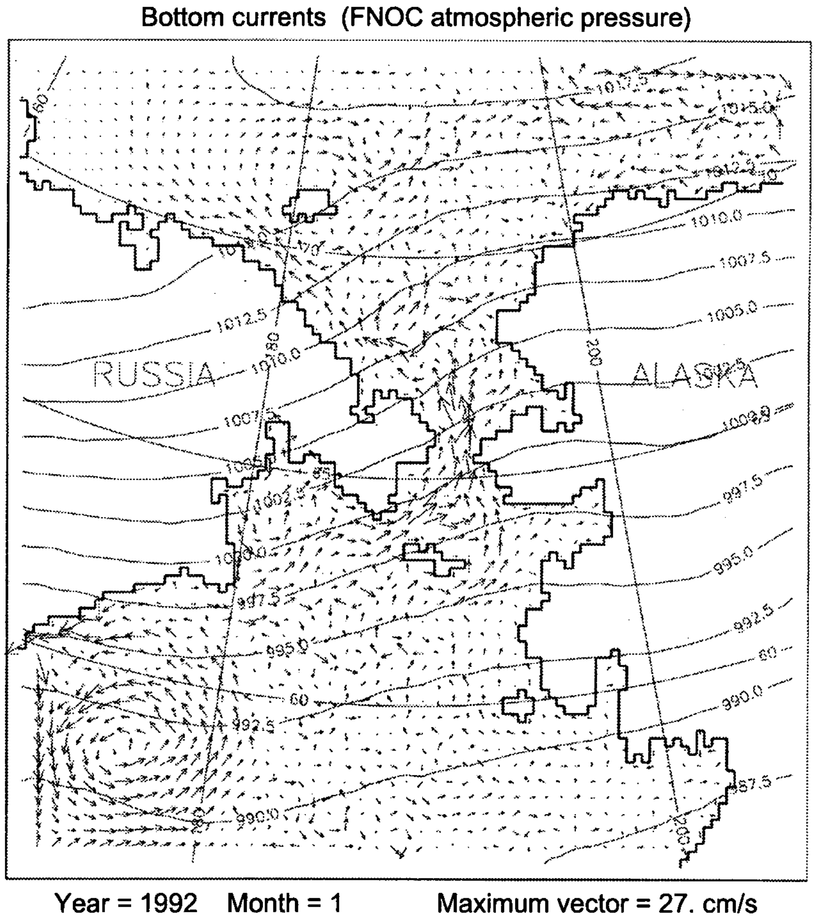

Figure 118. Bottom circulation and sea level (cm) distribution in the Chukchi Sea in January 1992. Results of simulation using a 3-D barotropic model and FNOC atmospheric pressure data.

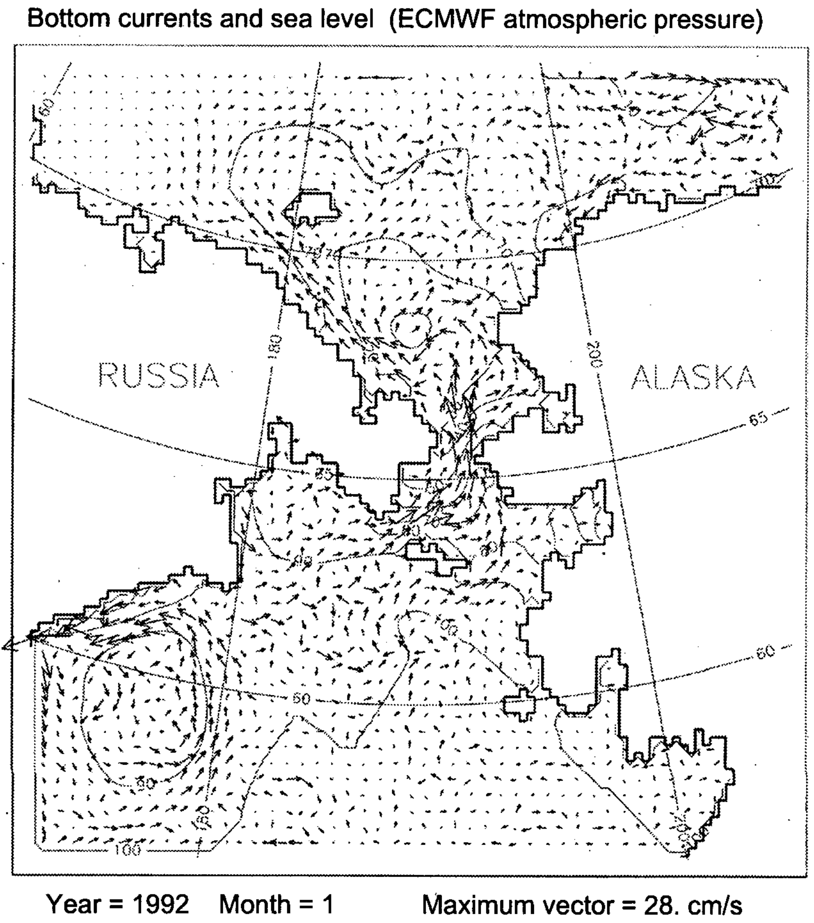

Figure 119. Bottom circulation and sea level (cm) distribution in the Chukchi Sea in January 1992. Results of simulation using a 3-D barotropic model and ECMWF atmospheric pressure data.

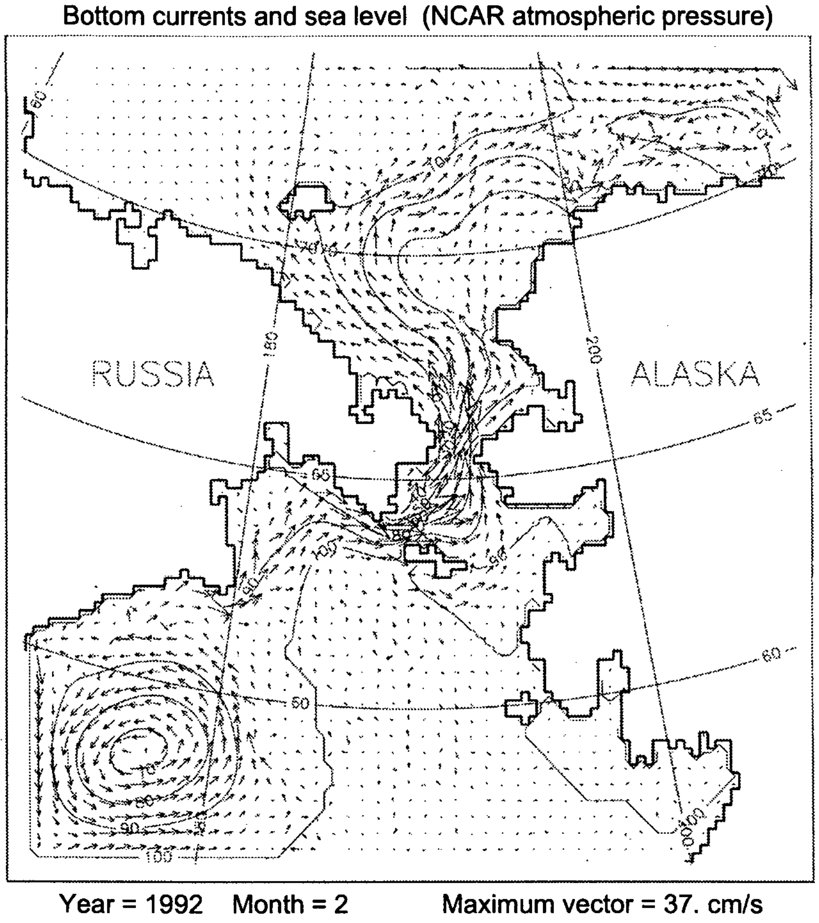
Bottom currents and sea level (NCAR atmospheric pressure)

Figure 120. Bottom circulation and sea level (cm) distribution in the Chukchi Sea in February 1992. Results of simulation using a 3-D barotropic model and NCAR atmospheric pressure data.

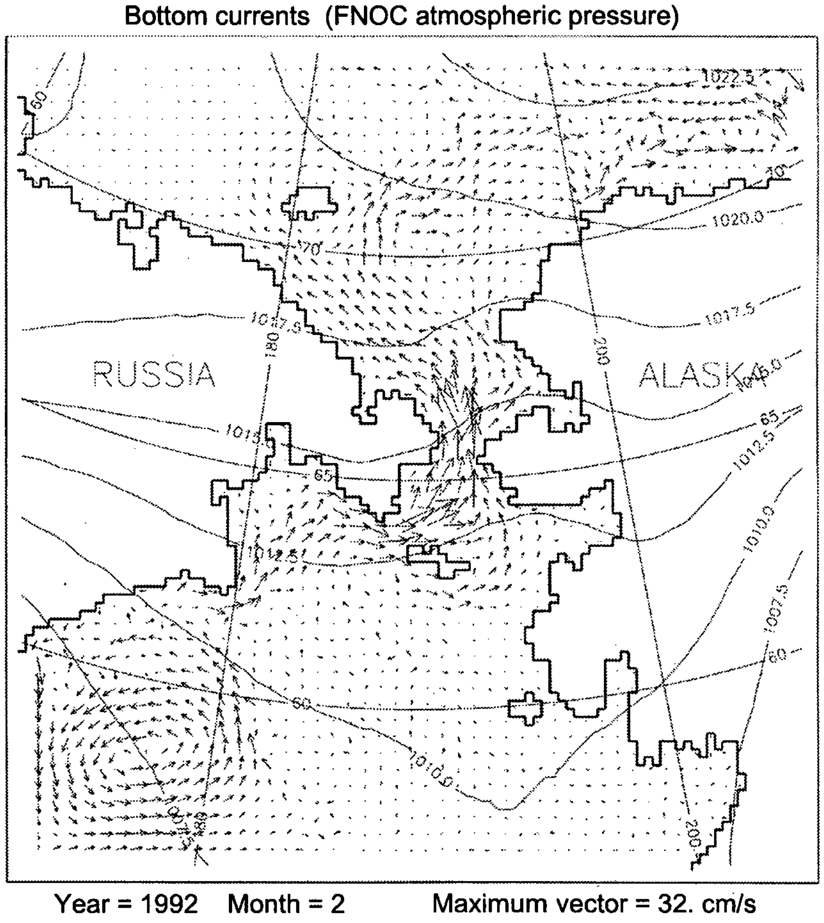
Bottom currents (FNOC atmospheric pressure)

Figure 121. Bottom circulation and sea level (cm) distribution in the Chukchi Sea in February 1992. Results of simulation using a 3-D barotropic model and FNOC atmospheric pressure data.

Bottom currents and sea level (ECMWF atmospheric pressure)

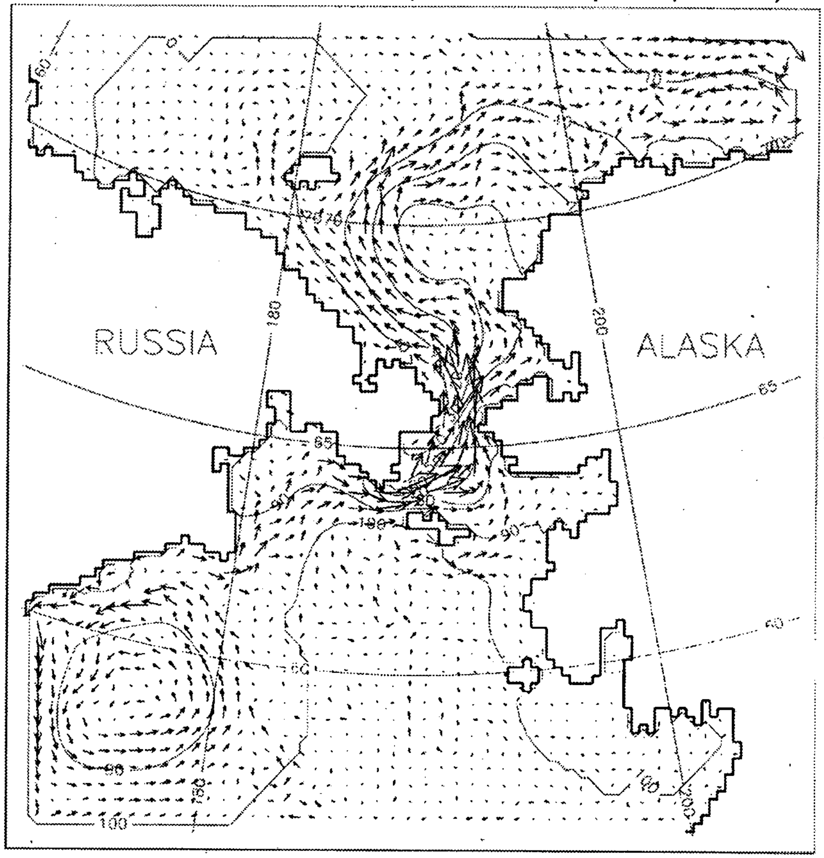

Year = 1992 Month = 2 Maximum vector = 35. cm/s

Figure 122. Bottom circulation and sea level (cm) distribution in the Chukchi Sea in February 1992. Results of simulation using a 3-D barotropic model and ECMWF atmospheric pressure data.

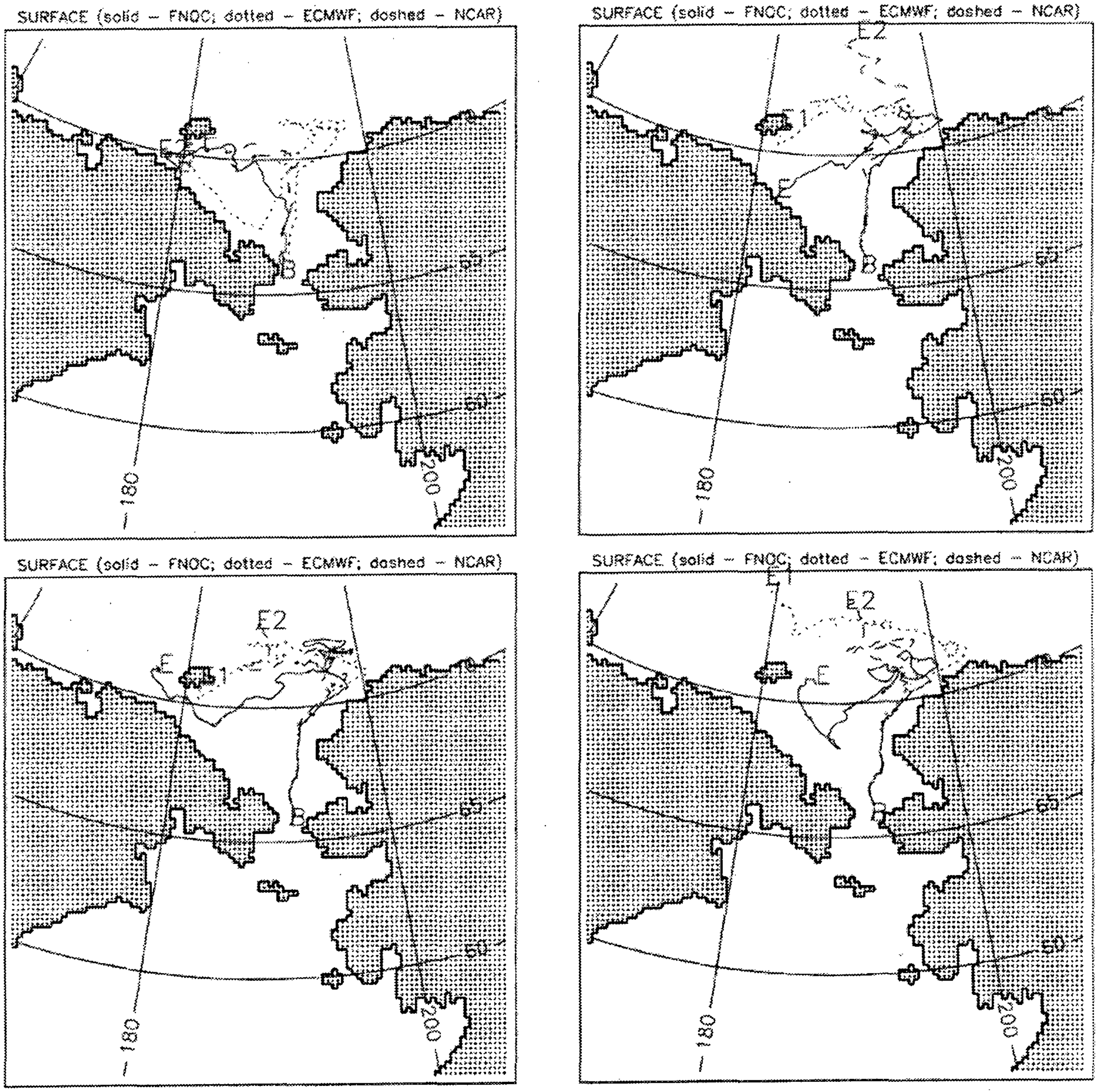

SURFACE (solid – FNOC; dotted – ECMWF; dashed – NCAR)

SURFACE (solid – FNOC; dotted – ECMWF; dashed – NCAR)

SURFACE (solid – FNOC; dotted – ECMWF; dashed – NCAR)

SURFACE (solid – FNOC; dotted – ECMWF; dashed – NCAR)

Figure 123. Simulated trajectories of water particles released in the Bering Strait on October 1, 1991. Solid, dotted, and dashed lines show trajectories of particles simulated using, respectively, FNOC, ECMWF, and NCAR atmospheric pressure data. Trajectories of particles moving with surface currents are shown. B is a releasing point. E, E1 and E2 denote locations of particles on September 29, 1992 for the FNOC, ECMWF and NCAR simulations, respectively.

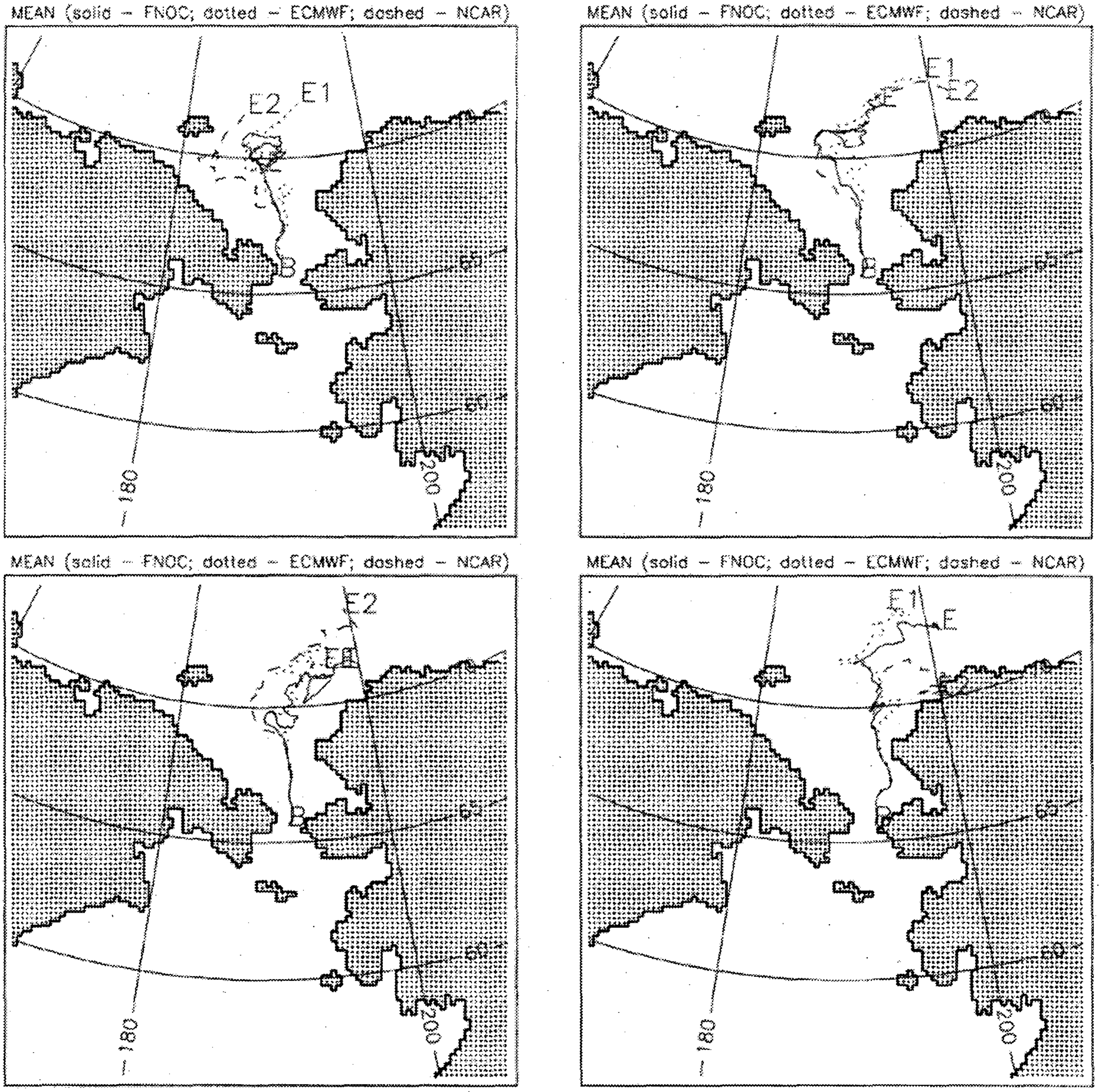
MEAN (solid – FNOC; dotted – ECMWF; dashed – NCAR)

MEAN (solid – FNOC; dotted – ECMWF; dashed – NCAR)

MEAN (solid – FNOC; dotted – ECMWF; dashed – NCAR)

MEAN (solid – FNOC; dotted – ECMWF; dashed – NCAR)

Figure 124. Same as Figure 123, for particles moving with vertically mean currents.

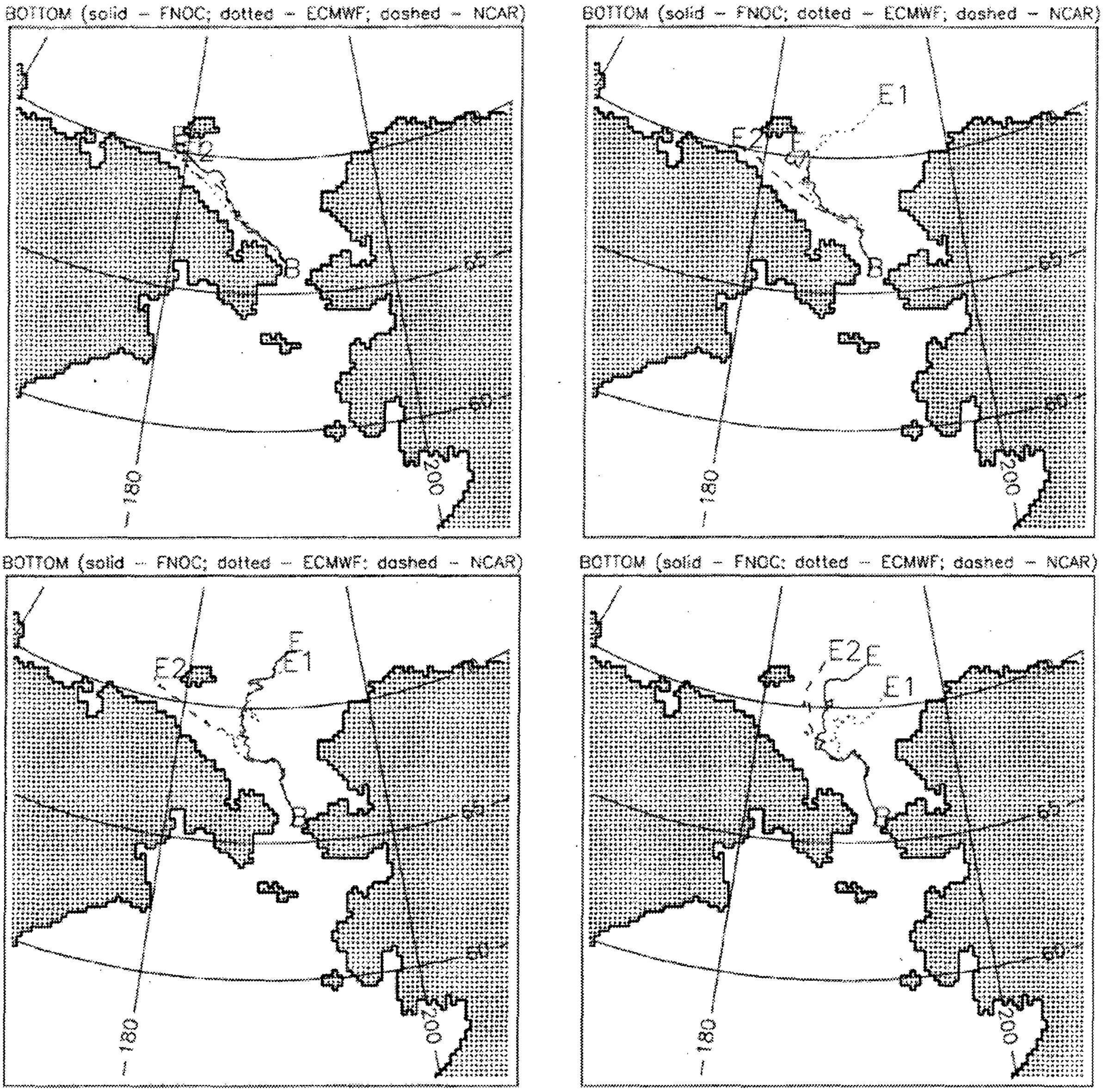

BOTTOM (solid – FNOC; dotted – ECMWF; dashed – NCAR)

BOTTOM (solid – FNOC; dotted – ECMWF; dashed – NCAR)

BOTTOM (solid – FNOC; dotted – ECMWF; dashed – NCAR)

BOTTOM (solid – FNOC; dotted – ECMWF; dashed – NCAR)

Figure 125. Same as Figure 123, for particles moving with bottom currents.

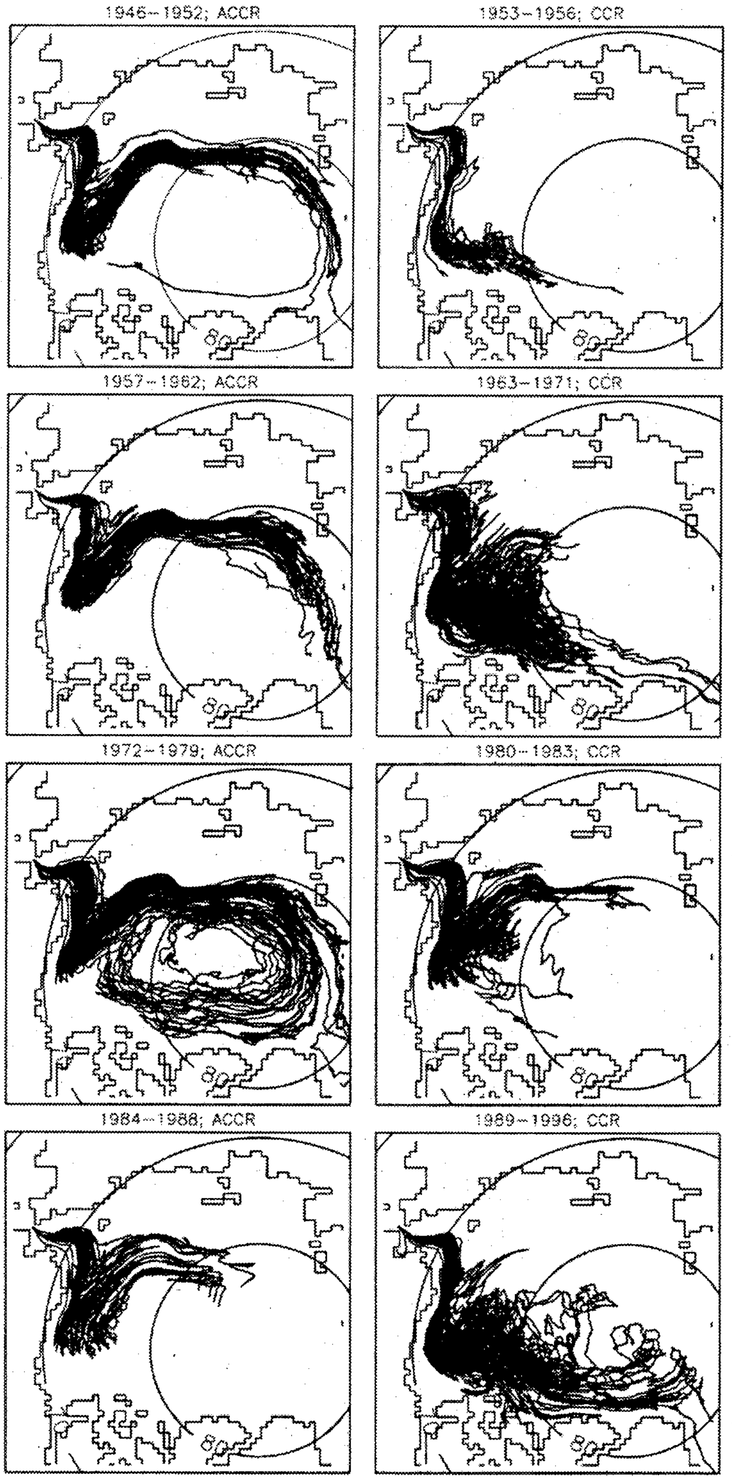

Figure 126. Simulated trajectories of water particles (moving with vertically averaged water velocities) released in the Bering Strait for anticyclonic circulation regimes of circulation (ACCR) in the left column (for years 1946–1952, 1957–1962, 1972–1979 and 1984–1988, respectively). In the right column the trajectories of parcels released in the Bering Strait in the years of cyclonic regime of circulation regime (CCR) are shown (1953–1956, 1963–1971, 1980–1983, and 1989–1996).

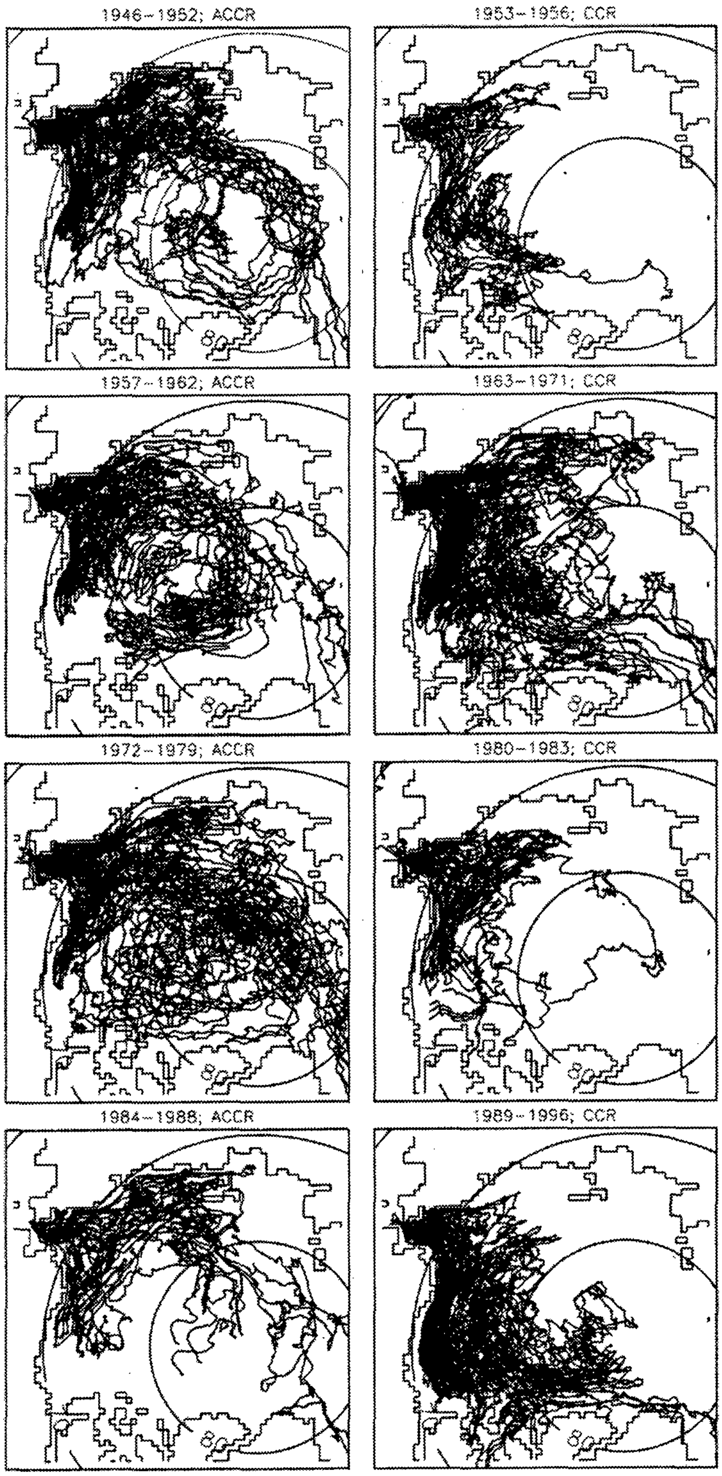

Figure 127. Same as Figure 126, for ice particles.

Appendix. Project-Related Publications and Presentations

Proshutinsky, A.Y. 1998. Wind field representations and their effect of shelf circulation models: A case study in the Chukchi Sea. CMI Annual Research Review, February 24, 1998, University of Alaska Fairbanks.

Proshutinsky, A.Y. 1998. Wind field representations and their effect on shelf circulation models: A case study in the Chukchi Sea. MMS Seminar, March 1998, Anchorage.

Proshutinsky, T.O. and A.Y. Proshutinsky. 1998. Environmental conditions affecting commercial navigation along the Northern Sea Route. 1998 AGU Spring Meeting, May 26–30, Boston.

Proshutinsky, T.O., A.Y. Proshutinsky and T.J. Weingartner. 1998. Numerical modeling of seasonal and interannual variablity of the Chukchi Sea circulation, Poster OS51-A4. 1998 AGU Spring Meeting, May 26–29, Boston, Abstract is published as a supplemental to EOS, April 28, 1998, p. S183.

Proshutinsky, A.Y. 1999. Climate states of the Arctic Ocean. MMS Seminar, January 19–21, 1999, Anchorage.

Proshutinsky, A.Y., T.O. Proshutinsky, and J. Maslanik. 1999. Decadal variability of the Beaufort and Chukchi seas. IUGG99 Meeting, Symposium JSP25, Abstracts B.241, July 19–30, 1999, Birmingham, UK.

Proshutinsky, T.O. and A.Y. Proshutinsky. 1999. Seasonal variability of the Beaufort and Chukchi seas. IUGG99 Meeting, July 19–30, 1999, Birmingham, UK.

MARCH 3, 1849

The Department of the Interior Mission

As the Nation's principal conservation agency, the Department of the Interior has responsibility for most of our nationally owned public lands and natural resources. This includes fostering sound use of our land and water resources; protecting our fish, wildlife, and biological diversity; preserving the environmental and cultural values of our national parks and historical places; and providing for the enjoyment of life through outdoor recreation. The Department assesses our energy and mineral resources and works to ensure that their development is in the best interests of all our people by encouraging stewardship and citizen participation in their care. The Department also has a major responsibility for American Indian reservation communities and for people who live in island territories under U.S. administration.

The Minerals Management Service Mission

As a bureau of the Department of the Interior, the Minerals Management Service's (MMS) primary responsibilities are to manage the mineral resources located on the Nation's Outer Continental Shelf (OCS), collect revenue from the Federal OCS and onshore Federal and Indian lands, and distribute those revenues.

Moreover, in working to meet its responsibilities, the **Offshore Minerals Management Program** administers the OCS competitive leasing program and oversees the safe and environmentally sound exploration and production of our Nation's offshore natural gas, oil and other mineral resources. The MMS **Royalty Management Program** meets its responsibilities by ensuring the efficient; timely and accurate collection and disbursement of revenue from mineral leasing and production due to Indian tribes and allottees, States and the U.S. Treasury.

The MMS strives to fulfill its responsibilities through the general guiding principals of: (1) being responsive to the public's concerns and interests by maintaining a dialogue with all potentially affected parties and (2) carrying out its programs with an emphasis on working to enhance the quality of life for all Americans by lending MMS assistance and expertise to economic development and environmental protection.